Autoassemblage de monocouches organiques à faible température

Lutz Wiegart

Université de Grenoble I
SCIENCES, TECHNOLOGIE, MÉDECINE

THÈSE

présentée à l'Université Joseph Fourier - Grenoble I
Pour le titre de
Docteur de l'UNIVERSITÉ GRENOBLE I

Spécialité: Milieux denses at matériaux
Doctorat: Physique des Matériaux
Ecole Doctorale: Physique

Autoassemblage de monocouches organiques à faible température

par
Lutz WIEGART

soutenue le 2 juillet devant le jury composé de:

J.R. REGNARD	Professeur, Université Grenoble I	Président du Jury
M. GOLDMANN	Professeur, Université Paris 6 et 7	Rapporteur
S. CANTIN	Maitre de Conference, Université Cergy-Pontoise	Rapporteur
M. TOLAN	Professeur, Université de Dortmund	Co-directeur
B. STRUTH	Chercheur, DESY Hamburg	Examinateur
F. RIEUTORD	Chercheur, CEA Grenoble	Directeur de thèse

Thèse financée par
Commissariat à l'Énergie Atomique (CEA) Grenoble
et
Installation Européenne de Rayonnement Synchrotron (ESRF)

Low Temperature Self-Assembly of Organic Monolayers

Acknowledgment

This thesis was the occasion for numerous acquaintanceships and I would like to take the opportunity to acknowledge all the people I came across during this project, either in the field of science or/and in private life.

First of all I'd like to thank my supervisor Bernd Struth for setting up the project, reams of fruitful scientific discussions as well as for his help and support even during weekends, vacation and beamline nightshifts. I admire his scientific ideas, his enthusiasm and his working spirit, turning him into an outstanding example of a scientist.

I am indepted to my thesis director François Rieutord, for fruitful discussions, active support and proofreading of the manuscript. Moreover, his help to organise the thesis defence was indispensable.

Metin Tolan accepted the role of the thesis co-director. I appreciated his helpfulness, being always on the spot if needed, as for example for the adventure of a French thesis defence.

I would like to thank Michel Goldmann and Sophie Cantin for accepting the role of referees, careful reading of the thesis manuscript and the preparation of the reports for the university. At the same time I am indebted to Jean-René Régnard who kindly accepted the role as the president of the Jury.

The "directeurs de laboratoire" at the CEA, Jean-Pierre Traverse and Olivier Diat as well as the corresponding research director at the ESRF, Sine Larson, kindly welcomed me in their groups. At the same time I would like to thank the CEA and the ESRF for the funding of the thesis project.

Christian Riekel as my responsible at the ESRF always kindly offered his help in case of organisational and administrative questions.

Sean O'Flaherty helped during many beamtimes and provided solutions for various Matlab problems. I enjoyed very much both the scientific and the not so scientific discussions with him in and outside the synchrotron world.

The analysis of the XPCS data crucially benefited from many discussions with Christian Gutt, who was also involved in corresponding experiments.

Chiara Caronna did not only help with experiments, but moreover I cherish the numerous coffee breaks with her and the many lines of nonsense spoken between us to keep a balance to the working stress.

Henri Gleyzolle supported the project, amongst others by providing a whole gallery ('the windowsill of fame') of very nice sample chambers. His efforts even during weekends and night times are gratefully acknowledged. In this context I'd like to apologise by an unnamed vendor of 'Richardson' for the confusion we caused with our request for toilet pipes for helium and vacuum conditions.

Pierre Terech did not only offer experimental support, but moreover I always found his door open in case of problems.

Saskia Schmacke and Daniela Lietz from the University of Dortmund are thanked for their help during beamtimes.

Anders Madsen provided support far beyond his local contact duties and experiments crucially benefited from his experience.

I am indebted to the present and former members of the Troika beamline for the integration in the group.

The sample environment group and namely Peter van der Linden, Ricardo Steinmann and Jeroen Jacobs are thanked for their support.
The help of Jean-Paul Gonzales from the ILL with major problems with an orange cryostat is gratefully acknowledged.
The team of Experimental Hall Operators is acknowledged for their 24 hours support, particular Christian Perrin is thanked for his visits during long night shifts and for accomplishing special needs (90% empty He dewars,...).
All my problems and questions in the field of chemistry were always kindly solved by Harald Müller.

All the administrative issues that came along the way were eventually overcome thanks to the help and experience of Josie Poet, Eva Jahn and Elisabeth Perrin.

I had also the pleasure to come across various people with whom I did not only enjoy coffee breaks and philosophical discussions but also mountain outings and other: Irmi, Adeline, Yvonne, Marco, Manuela, Friederike, Yuri, Andrei, Emanuele, Ute,...

Besides my contacts in the scientific world, I thank my parents whose encouragement has been a great support during all the time.

Pour terminer, je voudrais exprimer toute ma gratitude à Agnès, qui m'a non seulement aidé avec la rare substance de Glüberin, les traductions françaises, la brandade de morue et les crêpes, mais qui m'a aussi encouragée dans les jours frustrants. Je te suis très reconnaissant de ta hospitalité, ton réconfort et ta confiance.

Abstract:

At ambient temperature monolayer phases of most alkane chain molecules exhibit phases, characterised by the rotation of the chain around the molecular axis. Consequently, these phases are only weakly ordered rather than crystalline. In order to achieve crystalline ordering, the energy of the system needs to be reduced. New cryo-protective liquid subphases extend the accessible range to much lower temperatures than the freezing threshold of water. Monolayers of common surfactants like fatty acids and phospholipids were prepared under constant volume/constant surface pressure conditions and their phase behaviour was studied upon cooling. First insights into film stability and evolution upon cooling were achieved by Langmuir isotherms and grazing incidence diffuse X-ray scattering (GIXOS), while the in-plane ordering was investigated by grazing incidence X-ray diffraction (GIXD). The molecules were found to adapt crystalline phases by a purely entropy driven self-assembly process, reaching packing densities similar to three dimensional single crystals. The evolution of the structure parameters compare to those of bulk alkanes undergoing the rotator-crystalline phase transition. The characteristic herringbone ordering of the crystalline phase of the fatty acid monolayer was proven by structure factor calculations. X-ray photon correlation spectroscopy (XPCS) was employed to relate the surface dynamics of the system to the appearance of crystalline phases. The phase transition was found to be accompanied by a change of the dynamics from propagating to overdamped capillary waves.

Key words: monolayers on liquid subphases, fatty acids, phospholipids, eicosanoic acid, Dipalmitoyl Phosphatidic Acid (DPPA), low temperature self-assembly, rotator-crystalline phase transition, structure factor calculations, Langmuir isotherms, grazing incidence X-ray diffraction (GIXD), X-ray photon correlation spectroscopy (XPCS)

Résumé:

À température ambiante, la plupart des monocouches constituées de molécules formées de chaînes alcanes présentent des phases caractérisées par la rotation des chaînes autour de leur axe moléculaire. Afin d'obtenir un ordre cristallin, il est impératif de réduire l'énergie du système. De nouvelles sous-phases liquides utilisant des agents cryoprotecteurs permettent d'accéder à des températures plus basses que la température de solidification de l'eau. Les monocouches de surfactants tels que les acides gras (acide eicosanoique) ou les phospholipides (acide dipalmitoyl-phosphatidique) ont été préparées à volume et pression surfacique constants. L'étude de la stabilité des films par refroidissement a été effectuée par des isothermes de Langmuir et par diffusion non spéculaire des rayons X (GIXOS) et celle de l'ordre dans le plan par la technique de la diffraction des rayons X sous incidence rasante (GIXD). Les molécules adoptent des phases cristallines qui sont induites par un processus d'autoassemblage d'origine exclusivement entropique et dont la densité d'empilement est similaire à celle d'un monocristal à trois dimensions. La technique de spectroscopie de corrélation des photons X (XPCS) a enfin été employée pour relier la dynamique de surface du système étudié à la formation des phases cristallines.

Mots clés:

monocouches sur des sous-phases liquides, acides gras, phospholipides, acide eicosanoique, acide dipalmitoyl-phosphatidique (DPPA), autoassemblage à basse température, transition de phase rotateur-cristalline, isothermes de Langmuir, diffraction X sous incidence

rasante (GIXD), spectroscopie de corrélation de photons X (XPCS)

Résumé substantiel:

Cette thèse porte sur l'étude du comportement de phase et de l'auto-organisation de monocouches organiques déposées sur une sous-phase cryoprotective jusqu'à des températures égales à -50 °C. De tels systèmes organiques à deux dimensions présentent de nombreux intérêts : ils constituent à la fois des modèles pour résoudre les problèmes fondamentaux à deux dimensions en physique ou en biologie et sont aussi très employés sur le plan industriel notamment lors de la fabrication de couches moléculaires en électronique. A température ambiante, les phases ordonnées des chaînes alcane sont généralement limitées à quelques sous-groupes d'espèces moléculaires car les interactions intermoléculaires sont suffisantes pour concurrencer les fluctuations perturbatrices. Bien que certaines molécules élémentaires comme les alcools adoptent des phases cristallines caractérisées par une forte compacité et de grandes tailles de cristallites, les molécules plus complexes possèdent souvent des phases très partiellement ordonnées. Dans le cas des acides gras, ces phases sont appelées phases rotateurs et sont matérialisées par la rotation de la chaîne alcane autour de son axe. Les phospholipides correspondent au niveau suivant de complexité et possèdent des modes d'empilement similaires. En volume, les phases rotateurs faiblement ordonnées des systèmes alcane peuvent être transformées en des phases cristallines par refroidissement ce qui augmente les interactions moléculaires effectives. Un point essentiel dans la préparation de ces monocouches est la nécessité d'avoir recours à des sous-phases cryoprotectives pour augmenter la plage accessible des températures qui doivent être inférieures à celle du point de solidification de l'eau.

La thèse est subdivisée en cinq chapitres. Le premier chapitre comprend tout d'abord un résumé sur le comportement de phase des acides gras et sur la formation de leur structure. Puis les sous-phases cryoprotectives, utilisées lors des expériences à basse températures, sont caractérisées et comparées à partir de leurs propriétés physiques pertinentes. Enfin, une étude de la stabilité des monocouches organiques, déduite grâce aux isothermes de Langmuir, en fonction de la sous-phase est décrite.

Le deuxième chapitre commence par introduire les bases théoriques sur la diffusion et la diffraction des rayons X en géométrie de surface. Ensuite, deux modèles sont présentés pour le traitement des données de diffraction sous incidence rasante. Le modèle cylindrique, le plus commun et où les descriptions submoléculaires sont négligées, est particulièrement adapté pour l'analyse des phases rotateurs. Dans le cas des phases cristallines, une méthode de calcul du facteur de structure simplifié est expliquée. Celle-ci permet en effet d'obtenir des informations sur les orientations moléculaires au-delà du modèle cylindrique. Ce chapitre se termine par une description de la diffusion diffuse à des angles très petits et hors plan qui permet de reconstruire le profil de densité des électrons d'une couche.

Les séries de refroidissement des monocouches d'un acide gras et d'un phospholipide sont exposées dans le troisième chapitre. La structure des couches, la stabilité des systèmes, l'ordre dans le plan ainsi que les processus de réorganisation et d'autoassemblage ont été obtenus à l'aide des méthodes de rayon X mentionnées dans le deuxième chapitre. Les résultats ont alors été comparés avec ceux des alcanes et des monocristaux dans une

géométrie de volume ainsi que des monocouches de Langmuir. Ce parallèle a ensuite été effectué en étudiant une monocouche d'acide gras physisorbée sur un substrat solide.

Le quatrième chapitre donne les bases théoriques sur les mesures de la dynamique de surface obtenues par la technique de Spectroscopie de Corrélation de Photons X (XPCS). A partir de la description hydrodynamique de la surface et des fluctuations associées de l'intensité de la lumière diffusée, les résultats ont été adaptés au domaine le régime des rayons X. Les effets de cohérence associés à une résolution finie et leur impact sur les signaux observés sont finalement discutés.

Dans le cinquième et dernier chapitre, les mesures de la dynamique de surface d'une sous-phase avec et sans monocouche sont présentées. La résolution du dispositif utilisé est déduite à partir de mesures de calibrations réalisées avant l'étude de la dépendance de la dynamique de la sous-phase cryoprotective avec la température. Ces résultats sont par la suite comparés à ceux de la dynamique de surface lorsque la monocouche est présente. Le chapitre conclut en faisant le lien entre les informations sur la dynamique et sur les structures statiques.

Dans le cas de l'acide gras, la transition entre une phase faiblement ordonnée et une phase cristalline peut être observée. Les paramètres structuraux de la monocouche sont similaires à ceux des systèmes tridimensionnels comme les alcanes et l'évolution de la maille élémentaire de la monocouche avec le refroidissement ressemble fortement à la transition entre la phase rotateur et la phase cristalline des alcanes en géométrie de volume. Pour la monocouche quasi bidimensionnelle, la transition de phase s'accompagne d'une augmentation de la taille des domaines cristallins et de l'apparition d'ordres supérieurs de réflexion dans les figures de diffraction X. La caractéristique de l'ordre « chevron » de la phase cristalline a été établie par des calculs du facteur de structure grâce au grand nombre d'observables dans les réflexions dans le plan. La transition de phase a été induite en réduisant l'entropie du système via l'énergie thermique. La monocouche a été préparée juste au-dessus de la transition de phase liquide-expansé/liquide-condensé sans appliquer de contraintes externes telles que la compression. Dans ce contexte, la croissance des domaines cristallins peut être considérée comme un réel processus d'autoassemblage à l'équilibre. Ces résultats sur la formation structurale d'une monocouche complètement relaxée ont également conduit à une meilleure compréhension de la région à basse pression et température du diagramme de phase des acides gras. Le principe a été ensuite appliqué à une molécule plus complexe comme le phospholipide dans le but de le généraliser. Les problemes d'empilement résultant du couplage des deux chaînes alcane à la seule tête hydrophile n'ont pu être résolues. En revanche, la compacité du phospholipide à basse température constitue la première observation d'un empilement incompatible avec une phase rotateur. En reliant la dynamique de surface des systèmes étudiés aux données statiques de la structure, il apparaît que l'évolution de la phase cristalline suit le changement de la propagation des ondes capillaires suramorties ce qui souligne le rôle prépondérant de la dynamique de surface sur l'organisation de la couche.

Contents

Introduction

During the last century much has been learned about the polymorphism of monolayers of alkane chain molecules. The interest in such quasi two-dimensional systems of organic molecules ranges from models for two-dimensional physical problems over model systems for biological membranes up to technical applications such as molecular coatings and electronics. At ambient temperature, ordered phases of alkane chain molecules are generally restricted to a subset group of molecular species, for which the intermolecular interactions are sufficient to be able to compete with disturbing fluctuations. While some simple molecules like alcohols adopt crystalline phases, characterised by high packing densities and large sizes of the crystallites, more complex molecules often only posses weakly ordered phases. In the case of fatty acids, these phases are referred to as rotator phases, characterised by a rotation of the alkane chain around its length axis. Phospholipids as the next level of complexity exhibit similar packing modes. For bulk systems of alkanes weakly ordered rotator phases can be transformed into crystalline phases by cooling the system and hence increasing the effective molecular interactions. A goal of this thesis is to apply this principle to organic monolayers on liquid subphases. An essential point for the realisation is the need for cryoprotective subphases for monolayer preparation in order to increase the accessible range towards lower temperatures. Questions arising amongst other in this context are: Is the rotator-crystalline phase transition achievable upon cooling for molecular species which do not adopt a crystalline phase at temperatures down to the freezing point of water? What happens at such temperatures in terms of stability, self-assembly, nucleation and growth of crystallites? What is the influence of the subphase's viscosity and the molecular mobility? A large viscosity damps surface fluctuations but on the other hand reorganisation processes are hampered by the reduced mobility of the molecules within the surface plane. A physisorbed monolayer on the surface of a solid substrate is the extreme case compromising between surface fluctuations and mobility. In order to address these questions, monolayers of a fatty acid (eicosanoic acid) and a phospholipid (Dipalmitoyl Phosphatidic Acid (DPPA)) were investigated on a cryoprotective subphase at temperatures down to -50°C. The techniques used comprise macroscopic measurements like Langmuir isotherms, giving a first insight in phase behaviour and stability of the system. The layer structure normal to the surface is explored by means of diffuse X-ray scattering, while surface sensitive diffraction is employed to determine the in-plane organisation of the molecules. X-ray photon correlation spectroscopy was applied for the first time to organic monolayers to study the change in surface dynamics accompanied with the appearance of the crystalline phase.

The thesis is subdivided into five chapters. The first chapter comprises a short summary of the phase behaviour of fatty acids and their structure formation. Moreover, the cryoprotective subphases used for the low temperature experiments are characterised and compared in terms of their relevant physical properties. A first investigation by Langmuir pressure area isotherms of the stability of the organic monolayers on selected subphases is described.

The second chapter is devoted to the theoretical background of surface sensitive X-ray scattering and diffraction. For the analysis of the grazing incidence diffraction data two models are presented. The commonly used cylinder model is most adapted for the analysis

of rotator phases, where submolecular details are smeared out. For the crystalline phase a simplified structure factor calculation method is described, in order to obtain information about molecular orientations beyond the limits of the cylinder model. The chapter closes with a description of the diffuse scattering at very small out of plane angles, from which the electron density profile of a layered system can be reconstructed.

Cooling series of monolayers of a fatty acid and a phospholipid on a liquid substrate are described in chapter three. The layer structure and stability of the systems as well as the in-plane ordering, re-organisation and self-assembly processes are monitored by the X-ray methods outlined in chapter two. The obtained results are compared to bulk systems like alkanes and single crystals as well as to Langmuir monolayer studies. The comparison is completed by the investigation of a fatty acid monolayer physisorbed onto a solid substrate.

The fourth chapter expounds the theoretical background of the surface dynamic measurements by XPCS. From a hydrodynamic description of the surface and the accompanied intensity fluctuation of scattered light in the framework of dynamic light scattering, the results are then adapted to the X-ray regime. Coherence effects associated with a finite resolution of the scattering vector and their impact on the observed signal are discussed.

In the fifth chapter the surface dynamic measurements on bare and monolayer covered subphases are presented. The resolution of the used setup is explored by calibration measurements, prior to the investigation of the temperature dependent dynamics of the bare cryoprotective subphase. These results are compared to the changes in the surface dynamics in the presence of a monolayer. The chapter concludes by relating the information obtained about the dynamics to the static structure data.

Chapter 1

Subphases and Thermodynamic Measurements

The following chapter is devoted to the characterisation of possible subphases for monolayer experiments below 0°C. In addition, some Langmuir pressure area isotherm experiments will be presented that demonstrate the feasibility of monolayer preparation on these subphases. The experiments also give first insights into possible changes in the thermodynamic behaviour of the films induced by cooling and/or the interaction with the subphase. A short description will be also given on the fabrication of Langmuir-Blodgett (LB) films which were afterwards investigated by X-ray diffraction. A short overview about some experimental techniques applicable to monolayers on liquid an solid substrates, the phase behaviour and structures of monolayers will be given as an introduction.

1.1 Langmuir Monolayer: A brief Overview

1.1.1 Experimental Techniques

The first experiments on monolayers on liquid subphases [69] measured the surface tension by means of a film balance like described in section 1.3. From these measurements it is possible to draw conclusions on the phase behaviour of the monolayer from features like kinks in the pressure-area isotherms which indicate a phase transition. To date, a rich variety of techniques is available to study monolayers on liquid subphases and supported on solid substrates. Without seeking for completeness, in the following some of the commonly used techniques will be presented.

In order to study the polymorphism of Langmuir layers, it is of great interest to map the boundaries of the phase diagram. Two techniques have been proven to be particularly suited for this purpose: Polarized Fluorescence Microscopy (PFM) and Brewster Angle Microscopy. The first technique uses small quantities of a fluorescent dye which is incorporated into the layer and afterwards detected by the microscopy technique. The principle is based on the dye being squeezed out of the dense parts of the monolayer and accumulating at the domain boundaries which can hence be easily detected. Phase coexistence is with this technique observable due to the contrast arising from the different solubility of the dye in the different phases. Due to the polarization of the excitation

light, the fluorescence emission depends on the dye orientation and hence the method is sensitive to the molecular tilt organisation within the film. The BAM principle is based on reflection of *'s'* polarised light under the Brewster angle at an interface between two media with different refraction indices. By using *'p'* polarised light, phases with different densities (and refractive indices) are visible due to spatial variations of the surface reflectivity. By using an analyzer, the technique is also sensitive to in-plane anisotropy such as induced by molecular tilt [96]. In contrast to PFM no dye needs to be added to the sample. Other optical methods applicable to Langmuir monolayers are ellipsometry, probing the layer structure normal to the surface and infrared spectroscopy, giving access to the characteristic vibration modes of the different chemical groups. After the transfer of the Langmuir layer from the liquid subphase to a solid substrate by the Langmuir-Blodgett, Langmuir-Schaefer or related techniques, the mono or multilayers can also be investigated by direct image techniques, like e.g. Atomic Force Microscopy (AFM) [118] providing information on the nanoscale even for very thin flat lying films (see e.g. [26]). Scanning Tunneling Microscopy (STM) [93] can provide a resolution down to atomic length scales but requires in general the transfer to a specific substrate (usually conductive). In order to study in-plane ordering of systems on liquid or non-conductive substrates, surface sensitive diffraction techniques as described in chapter 2.1 are powerful tools.

1.1.2 The Phase Diagram of Fatty Acids

Ställberg-Stenhagen and Stenhagen [111] presented a surface pressure – temperature phase diagram for behenic (C22) acid, obtained from pressure-area isotherm studies (see figure 1.1 a)). It turned out to be 'generic' in a way such as phase sequences upon compression hold for a wide range of fatty acids, if the temperature axis is scaled by 5°C to 10°C for each additional CH_2 group of the alkane chain and minor adjustments on the surface pressure axis are taken into account. These findings reflect the fact that the interaction energy of rod-like molecules is dominated by the long-range van der Waals attraction between hydrocarbon chains and their short-range repulsion, which are both proportional to the chain length of the molecule [55]. Later on, a new low temperature, low pressure phase was added to the phase diagram by Lundquist [74]. Gracing incidence X-ray diffraction allowed for the determination of the microscopic structure of the identified phases. While these diffraction measurements are very time consuming, optical techniques like BAM and PFM made the mapping of the phase diagram and in particular the determination of phase boundaries possible. Overbeck and Möbius found a new high temperature phase at intermediate pressure [83] using BAM that was shortly afterwards confirmed by Schwarz and Knobler [101] employing PFM as well as by X-ray diffraction [29]. Figure 1.1 b) shows the phase diagram obtained by Rivière and co-worker for eicosanoic (C20) and behenic (C22) acid by a combined study of BAM and PFM [96]. The data for the two fatty acids have been scaled in temperature to overlap and the temperature axis corresponds to the phase diagram of behenic acid. In the following a short summary about the observed phase transitions will be given. Rivière et al. observed the phase transitions leading to the phase diagram shown in figure 1.1 b) mostly at constant temperatures and successively increasing the surface density of the molecules upon compression. Temperature scans at constant surface pressure were performed at the Ov-L2 phase boundary. In a later work,

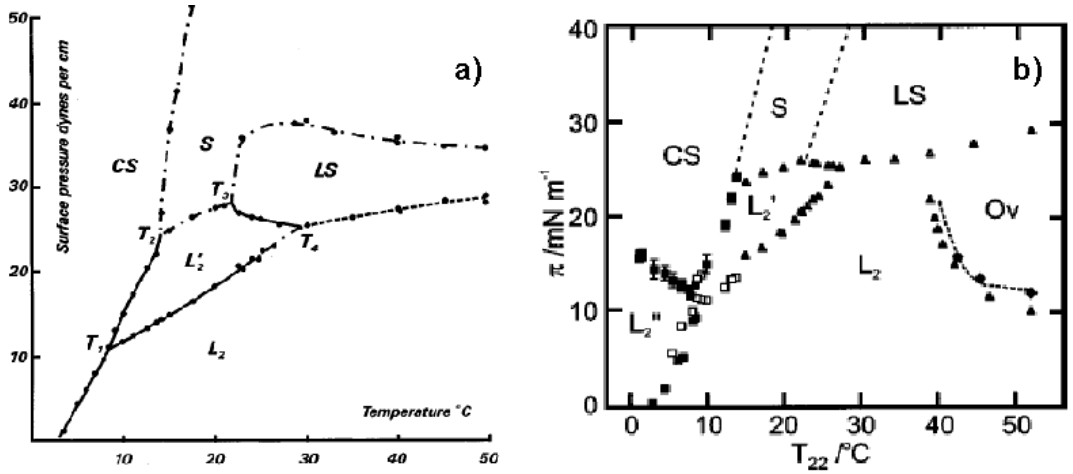

Figure 1.1: Generic phase diagrams: a) according to Ställberg-Stenhagen and Stenhagen (adopted from [54]), the temperature axis corresponds to behenic acid. b) according to Rivière et al., filled symbols: behenic acid, open symbols (scaled in temperature): eicosanoic acid (adopted from [54]).

Rivière-Cantin and co-workers studied also by BAM the L_2-L_2'-L_2" triple point and the L_2"-CS phase transition [97]. For the latter transition observed under compression, they found evidence for a continuous reduction of the tilt angle from a finite value to zero accompanied by a possible variation of the area per molecule. The phase diagram of eicosanoic acid has been explored by Bibo and Peterson [9] using pressure-area isotherms in the temperature range from 10°C to 35°C and by Durbin et al. [30] by means of GIXD along isotherms in the temperature range from -5°C to 15°C. The latter temperature range was accessible in the study due to the use of HCl at pH 2 as a subphase and is one of the rare studies, where Langmuir monolayers have been investigated at temperatures slightly below the freezing point of water. While Bibo and Peterson only report the existence of an LS, L_2' and L_2 phase, Durbin et al. found a phase with intermediate tilt between the L_2 and L_2' phase, at a surface pressure of about 15mN/m and triple point with the L_2 and L_2' phase at about 10°C.

Like fatty acids, phospholipids exhibit a rich polymorphism [5]. While for fatty acids mainly the length of the alkane chain determines the phase behaviour, the situation is more complex for phospholipids, were usually two alkane chains are connected to a hydrophilic headgroup via a backbone. Different head groups exist, which in combination with the length of the alkane chains modify the phase behaviour.

1.1.3 Structure Formation

The variety of phases of fatty acids on a pure water subphase arises from the structure of the hydrocarbon chains (planar and Zig-Zag) and the van der Waals interaction between them. In addition, the interaction between the polar headgroups themselves and the headgroups and the polar liquid subphase can be taken into account. However, from the scaling behaviour found in the generic phase diagram, for fatty acids on pure water

the headgroup interactions seem to be negligible compared to the chain contribution. A different situation is met if ions are present in the subphase: the polar headgroup layer favours the nucleation of an inorganic ion layer at the headgroup-subphase interface. The ion layer in return can alter the organisation of the organic monolayer due to ionic constraints. Parameters that determine the phase behaviour in this case are the nature and concentration of the cations, the pH of the subphase and the nature of the counterions. Experimental findings point in this case towards the existence of a generic phase behaviour that is strongly dependent upon the interactions of the polar headgroups [16]. The topological features of the phase diagram can be reproduced by simulations (see e.g. [23]) taking effective chain interactions and chains stiffness (this stiffness of a chain can chemically be varied by fluorination) and head-chain size mismatch into account. In particular the tilting transitions between the condensed phases are driven by an interplay between the head size, the chain diameter and the surface pressure. Experimental findings show that despite the generic phase behaviour there exist fundamental differences in the tilt ordering for surfactants with different chemical structure, e.g. the L_2 phase was found to be absent in the phase diagrams for alcohols and esters [114]. Similar effects as above described for fatty acids determine also the phase behaviour of phospholipids. In addition, the headgroups of these surfactants are in general more bulky and exert a larger influence on the phase behaviour. Due to the coupling of more than one alkane chain to one headgroup via a backbone additional packing restrictions arise.

The essential molecular degrees of freedom are the tilt angle between the surface normal and the length axis of the rod-like molecule and the orientations of the molecular backbone. While the less dense packed phases of fatty acids are supposed to be characterised by a rotation of the molecule around its molecular axis (similar to the rotator phases of bulk alkanes), for phospholipids this rotation is believed to be rendered impossible by the coupling of two or even more alkane chains to one headgroup and backbone. Nevertheless, the packing densities and the structure parameters like lattice vectors are very well comparable to rotator phases.

From a symmetry point of view the most symmetrical observed phase in a Langmuir monolayer is the hexatic phase (see figure1.2 a)). Such a phase possesses sixfold orientational order of the intermolecular bonds connecting neighbouring molecules, while the translational order is short range [54]. The tilt in the hexatic phase is related to the azimuth. Two symmetry related tilt directions are along hexatic bonds towards the nearest neighbour or in between them towards the next nearest neighbour. In addition, an intermediate tilt direction is also possible. Hindered rotation of the molecule upon decreasing the temperature gives rise to a defined orientation of its backbone plane. Possible backbone orientations have been determined from interaction energy (Lennard-Jones interaction potential) calculations by Buzano et al. [14]. The three minima in the interaction energy were found to correspond to a parallel alignment of backbone planes [90], pseudo herringbone order (see figure 1.2 b)) and herringbone order (see figure 1.2 c)). The two type of herringbone order differ not only in the typical dimensions of the two-dimensional rectangular unit cell. The most distinct difference is the relative orientation $\Delta\phi$ of the backbones of the two molecules in the unit cell, being 90° in the case of herringbone and 40° in the case of pseudo-herringbone ordering, respectively. The different structural features of the phases of the generic phase diagram were identified by X-ray

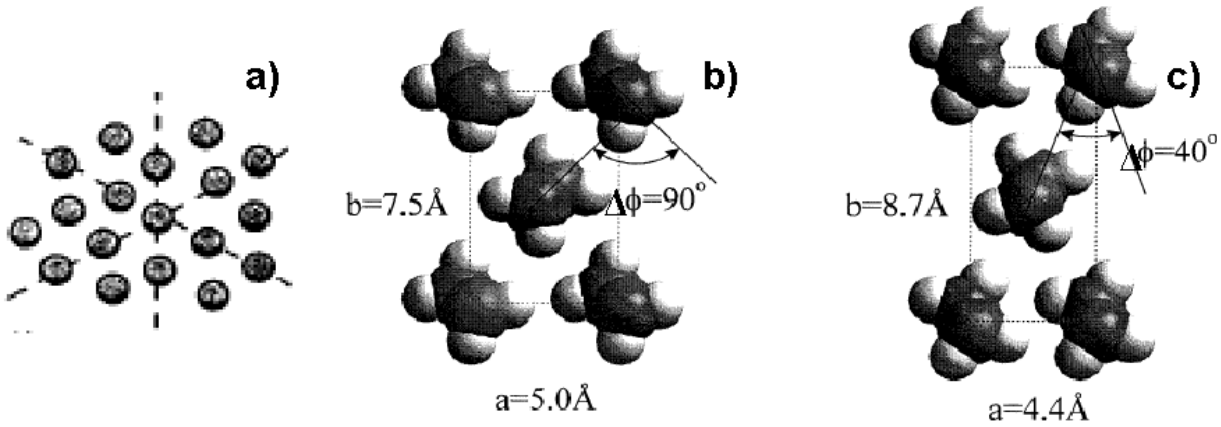

Figure 1.2: a) hexatic 2d ordering (adapted from [54]); b) herrinbone ordering; c) pseudo-herringbone ordering adapted from [67])

diffraction. In addition to the phases in the phase diagram (figure 1.1 b)), symmetry requirements of the Landau theory require a subdivision of the phase L_2 into two phase L_{2d} and L_{2h}, which posses disordered and herringbone ordered backbone planes at high and low temperatures, respectively [53, 54]. Contrary, experimental evidence for long range herringbone order in the L_{2h} phase was not experimentally observed [31]. In the following the phases of the fatty acids will be described in more detail and special attention will be drawn to their structural features on sub-microscopic length-scales as accessible by GIXD. At low temperatures there exist two crystalline phases L_2" at low surface pressure and CS at higher surface pressure. Both phases exhibit a rectangular unit cell and herringbone ordering of the alkane chain backbones. While in the CS phase the chains are upright with respect to the surface, in the L2" phase they exhibit a tilt in the direction of the nearest neighbour (n.n.). The CS phase displays all the characteristics of a two-dimensional crystal: a very low compressibility and long-range positional order [97]. CS and L_2" are the only two crystalline phases in the phase diagram, while all the other phases are mesophases. The high pressure phases are all untilted, these are the LS phase at high temperature and the S phase at intermediate temperature, exhibiting hexagonal and rectangular unit cells, respectively. At lower surface pressures the tilted mesophase are Ov, L_2 and L_2'. All of them exhibit a rectangular unit cell. The tilt directions of the Ov and L_2' phase are towards the next nearest neighbour (n.n.n.), whereas the tilt direction of the L2 phase is n.n.. The only difference between the L_2' and the Ov phase is that the molecules in the Ov pack into a hexagonal lattice, while the molecules in the L_2' phase pack into a distorted hexagonal (rectangular) one. An overview about the different phases of the generic phase diagram and their structural features is given in table 1.1.

1.2 Subphases for Monolayer Preparation

To date, most studies of monolayers on liquid surfaces employ water or water based buffers as a subphase. Consequently, the low temperature cut-off for these experiments is given by

phase		unit cell	tilt	herringbone ordering
S	mesophase	rectangular	-	-
LS	mesophase	hexagonal	-	-
CS	crystalline	rectangular	-	long range
L_2"	crystalline	rectangular	n.n.	long range
L_2'	mesophase	rectangular	n.n.n.	-
L_{2d}	high T mesophase	rectangular	n.n.	-
L_{2h}	low T mesophase	rectangular	n.n.	short range
Ov	mesophase	rectangular*)	n.n.n.	-

Table 1.1: Summary of the properties of the monolayer phases. *) the packing in a plane normal to the chain axis is hexagonal

the freezing point of water at 0°C. Although ultra pure water can be supercooled to much lower temperatures (about -30°C) it was found for alcohols that the presence of a surfactant monolayer at the surface induce ice nucleation already at much higher temperatures (e.g. about -8°C for a C22 alcohol) [91]. In order to investigate the phase behaviour, morphology, cooling induced self-assembly and reorganisation processes of amphiphilic monolayers at temperatures far below the limit of the freezing threshold of pure water, novel subphases need to be explored. The subphase requirements for the preparation of amphiphilic monolayers at low temperatures can be summarised as the following:

- a freezing point distinct lower than 0°C, preferably without supercooling
- a surface tension sufficiently high at ambient temperatures for the preparation of well defined monolayers

The main compromise is thereby given by the first point, as most pure substances which exhibit low freezing points are quite volatile with a surface tension of only about 20mN/m or less. For obvious reasons pure solvents like ethanol or methanol are also not considered. The focus is hence given to aqueous solutions of water with a cryo-protectant like e.g. alcohol or glycerol, were the surface tension of the mixture benefits from the relatively high surface tension of the water content (72.8 mN/m at 20°C). A sketch of a phase diagram of a binary mixture is shown in figure 1.3 a). Depending on the fraction x_B of liquid B in liquid A and the temperature T, the mixture is liquid, liquid plus solid content of either component B or A. At temperatures below the freezing point of the eutectic mixture, for all possible mixing ratios both substances A and B are in a solid state. The eutectic mixture has a composition for which complete liquefaction occurs at a lower temperature than for any other composition. This principle and the term 'eutectic' originally arises from metallurgy but is much the same when applied to other materials that crystallise, such as glycerol, water and salt. The differences arise from the bonding types: metallic bonding on the one hand and hydrogen bonding and ionic bonding on the other. As a consequence, the solid phases of water/salt mixtures are pure crystalline phases of water and salt instead of the composites formed by for instance an eutectic lead/tin mixture.

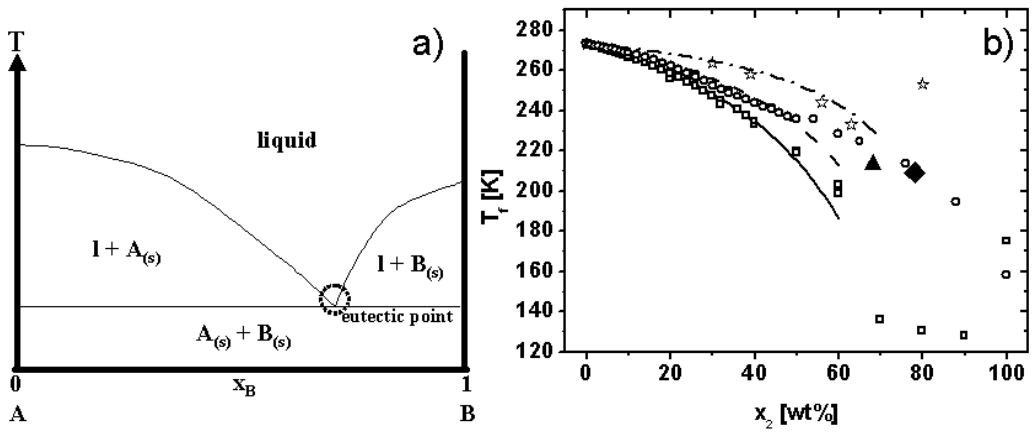

Figure 1.3: a) sketch of a phase diagram of a binary mixture. b) freezing point depression for mixtures of water and several cryo-protectants: open squares and solid line: water/methanol, open circles and dashed line: water/ethanol, open stars and dashed dotted line: water glycerol. Filled square: freezing point of the ternary system NaCl/water/glycerol (the x-axis referes to the glycerol content). Filled triangle: freezing point of an eutectic water/DMSO mixture. All symbols are literature values, while the curves were created using equation 1.1.

For ideal mixtures, where each component behaves as it would in the absence of other chemical species, the freezing point depression of a binary mixture can be calculated as

$$\Delta T_f = E_f \cdot m_2, \tag{1.1}$$

where ΔT_f is the freezing point depression relative to the freezing point of the pure solvent, E_f is the cryoscopic constant of the solvent and m_2 is the molality (moles of solute per kilogram solvent). The cryoscopic constants are 1.86 K kg mol^{-1} for water and 3.56 K kg mol^{-1} for glycerol [2].

In the case of interactions between the different chemical species present in the mixture, the mixture will be non-ideal, which holds in particular for polar substances and substances with different functional groups. Mixtures containing the polar substances water and glycerol are therefore non-ideal, but as comparison with literature data shows (see figure 1.3 b)), equation (1.1) can nevertheless be used to estimate freezing temperatures over a wide composition range, although eutectic behaviour (increase of the freezing point for solute concentrations higher than corresponding to the eutectic composition) cannot be reproduced. In the following, some properties of the binary mixtures water/ethanol, water/methanol, water/glycerol and water/DMSO (Dimethylsulfoxid) will be revealed. Some relevant properties of the pure substances are summarised in table 1.2. The eutectic mixture of water and glycerol is 33/67 wt% and exhibits a freezing point of -46°C (227.15K). In combination with sodium chloride (NaCl) the freezing point of the ternary mixture NaCl/water/glycerol (5/22/73 wt%) is lowered to -64°C (209.15K). The freezing temperatures for the eutectic mixtures hold thereby for low cooling rates, while faster cooling results in supercooling and freezing at even lower temperatures. For a water/ethanol mixture (45/55 wt%) the freezing point is lowered to -37.6°C (235.55K),

	formula	T_f [°C]	T_f [K]	σ[mN/m]	ρ [g/cm^3]	η [mPas]	M_w
water	H_2O	0	273.15	72.73 (20°C)	0.998 (20°C)	1.002 (20°C)	18.02
glycerol	$C_3H_8O_3$	0*)	273.15*)	63.0 (20°C)	1.261 (20°C)	934 (25°C)	92.09
ethanol	C_2H_6O	-115	158.15	23.22 (10°C)	0.789 (20°C)	1.074 (25°C)	46.07
methanol	CH_4	-98.3	174.82	22.67 (20°C)	0.792 (20°C)	0.918 (20°C)	32.04
DMSO	C_2H_6SO	18.5	291.6	43.53 (20°C)	1.099 (25°C)	1.987 (25°C)	78.13

Table 1.2: Properties of the pure solvents used in this work: freezing point T_f, surface tension σ, density ρ and viscosity η. *)the melting point of pure glycerol is 17.8°C (290.95K) [1], but due to its tendency to supercool, it crystallises after prolonged cooling at 0°C

at higher ethanol contents the phenomenon of supercooling occurs. The freezing point of a water/methanol mixture (50/50 wt%) is -53.9°C (219.25K). The eutectic mixing ratio for water and DMSO is 31.9/68.1 wt% with a freezing point of about -60°C (213.15K).

As the further investigations of cooled monolayers on liquid subphase by X-ray scattering and diffraction focus on the eutectic mixture of water and DMSO as a subphase, the evolution of the surface tension and the bulk viscosity of this mixture will be discussed in more detail. These parameters play in particular an important role in the analysis of the measurements of the surface dynamics by X-ray photon correlation spectroscopy (see chapter 5). The surface tension of the DMSO/water mixture was determined using a tensiometer (Nima ST 9002) and a Pt/Ir du Noüy-ring. The du Noüy-ring geometry allows the determination of the surface tension for liquids, where the contact angle between the liquid and the probe (ring, plate,...), which depends on the wetting behavior, is unknown. The force acting on the tensiometer balance is given by the weight of the ring, the uptrust when the ring is immersed into the liquid and the surface tension. The weight of the ring can easily be determined by a measurement with the ring pulled out of the liquid. The uptrust is reduced to zero when to ring is pulled out of the liquid and the ring is on the same level as the liquid level. The surface tension is then given by the measured force F, divided by the perimeter of the ring:

$$\sigma = F/(\pi d + \pi(d - 2t)), \tag{1.2}$$

with the outer diameter d and thickness t of the ring. However, for this measuring geometry the apparent surface tension needs to be corrected: one source of errors is the appearance of a meniscus at the outer and the inner diameter of the ring. Both contact angles reduce to zero but not simultaneously. The second source of error are buoyancy forces on the ring. Build-in software (Nima) was used to correct for the two effects. The two parameters needed are the effective ring perimeter and the relative density of the liquid with respect to the air. The effective ring perimeter is commonly determined by measuring a test liquid with known surface tension and relative density (in this case water was used). The relative density of the DMSO/water mixture at various temperatures can be found in reference [98]. Measurements of the surface tension used a sealed test vessel containing the liquid, immersed into the cooling bath of a chiller. The temperature of the liquid was directly monitored by a Pt100 temperature sensor immersed into the liquid. A thin silver wire entering the test vessel by a 1mm diameter fit-through was used to connect

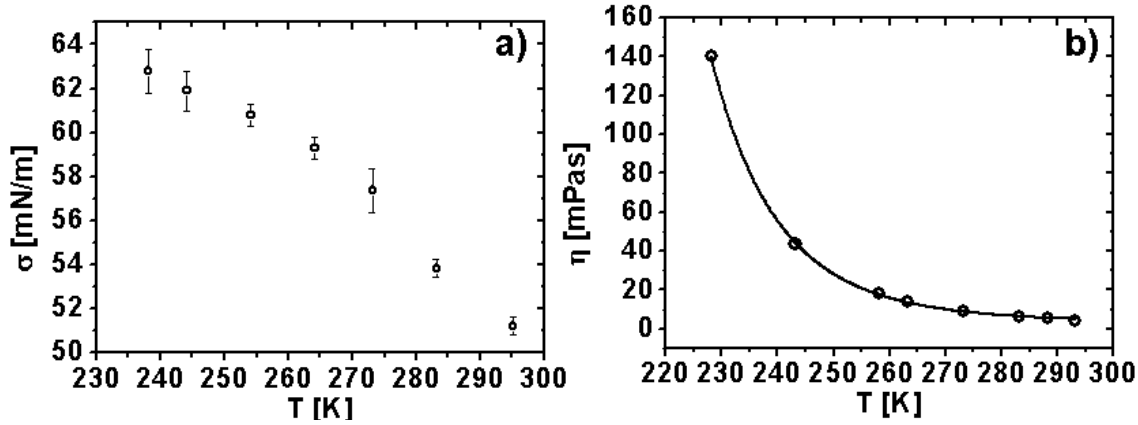

Figure 1.4: a) surface tension of an eutectic mixture of water/DMSO as a function of temperature. Symbols are mean values from three independent measurements and the error bars denote the associated standard error. b) viscosity as a function of temperature: data points were taken from reference [98], the solid line is a fit according to equation 1.3.

the du Noüy-ring and the balance. At low temperatures the fit-through was flushed with dry nitrogen gas to avoid any condensation of humidity. The obtained values for the corrected surface tension as a function of temperature are shown in figure 1.4 a), data points are average values from three independent measurements and the error bars denote the standard error. The viscosity of the water/DMSO mixture in the eutectic composition was investigated by Schichman et al. using a falling ball viscometer. The reported data is shown as open circles in figure 1.4 b), the solid line is a fit to the Arrhenius model

$$\eta = A \exp\left(\frac{E_\eta}{RT}\right), \tag{1.3}$$

which holds for the description of the temperature dependence of the viscosity for systems like e.g. dilute polymer solutions. Here A is a prefactor, E_η is the activation energy for viscous flow, R is the universal gas constant and T is the temperature in Kelvin. Equation (1.3) together with the obtained parameters $A = 2.65 \cdot 10^{-9} Pa\ s$ and $E_\eta = 33724.3 J/mol$ can be used to interpolate the viscosity at the temperatures of interest.

1.3 Langmuir Pressure-Area Isotherms

First insights in the properties and stability of monolayers prepared on the above described subphases were obtained by measurements of Langmuir pressure-area isotherms. In these experiments the surface tension of the subphase is measured as a function of the surfactant coverage. A detailed explanation about the phenomenon of surface tension can be found in [4]. A molecule in the bulk of a liquid is in a lower energetic state, if it is in contact with neighbouring molecules. A molecule at the surface of the liquid has fewer neighbours and is hence in a higher state of energy. In order to minimise its energetic state, the liquid must therefore minimise the number of molecules at the surface, which is identical to a

minimisation of the surface area. The surface tension σ can hence be defined as the work necessary to increase the surface of a liquid by an amount δA, which is given by $\sigma \cdot \delta A$. The corresponding excess energy is the surface free energy. Intermolecular interactions are strongest for polar liquids, where water has an exceptional high surface tension and is used as a standard subphase for the preparation of Langmuir monolayers.

Surface active agents (surfactants) in general consist of a hydrophilic (water soluble) and a hydrophobic (water insoluble) part. This amphiphilic nature of the surfactant dictates the orientation of the molecules at the liquid/gas interface. For the case of a lipid or fatty acid the polar headgroup is immersed in the liquid while the hydrocarbon chains are pointing towards the gas phase. The driving force behind the association of the surfactants is the reduction of the free energy of the system. As a consequence, a surfactant accumulating at the liquid/gas interface causes a decrease in the surface tension.

If the area per molecule for a surfactant film on a liquid subphase is sufficiently small enough, the molecules start to exert a repulsive effect on each other. This two-dimensional analogue of a pressure is referred to as surface pressure π which is linked to the surface tension σ by the relation:

$$\pi = \sigma_0 - \sigma, \tag{1.4}$$

where σ_0 is the surface tension of the subphase without and σ in the presence of a surfactant. The surface pressure π is also the first derivative of the surface free energy with respect to the area per molecule A [77]. The surface pressure as a derivation of a thermodynamic potential is therefore adequate to indicate phase transitions which appear as kinks and plateaus in the pressure-area isotherms.

Measurement of pressure-area isotherms were performed using a conventional Langmuir trough with a Wilhelmy paper plate equipped micro-balance (Nima, model 312D with surface pressure sensor PS4). The temperature of the subphase was adjusted to ± 0.1°C by circulating a cooling agent from a chiller through the metal support plate of the PTFE trough. The subphase temperature was monitored by a Pt100 temperature sensor immersed directly into the subphase. For experiments at low temperatures the trough was housed in a polystyrene box for thermal insulation. Condensation of humidity inside the box during cooling was avoided by the presence of hygroscopic silica particles. Water serving as a subphase either pure or as aqueous solutions with cryo-protectors was of ultra pure grade (Elga, *Purelab Classic*).

Two different amphiphilic molecules were investigated: eicosanoic (arachidic) acid ($CH_3(CH_2)_{18}COOH$) and dipalmitoyl-phosphatidic acid (DPPA, $C_{35}H_{68}O_8PNa$). The first amphiphile is a fatty acid, consisting of small hydrophilic headgroup and a methyl group terminated hydrophobic alkane chain. The second surfactant molecule is a phospholipid consisting of two alkane chains connected to a single phosphatidic acid group by a glycerol backbone. While single chain molecules like fatty acids are well studied simple model systems, phospholipids are not only the basic constituents of biological membranes but also a step towards amphiphilic polymers which in general consist of hydrophobic side chains linked by a hydrophilic backbone [54]. Sketches of the two molecules are shown in figure 1.5 a). Arachidic acid and 1,2-Dipalmitoyl-sn-glycero-3-phosphate sodium salt were purchased at $\geq$99% purity from Sigma Aldrich. Spreading solutions were obtained

	H_2O	H_2O/DMSO	H_2O/glycerol	H_2O/glycerol/NaCl
$A_{\text{lift-off}}$ [Å^2]	25	35	>50	40
$A_{5\text{mN/m}}$ [Å^2]	23.8	28.3	28.7	26.6
$A_{25\text{mN/m}}$ [Å^2]	19.4	20.6	19.0	20.9

Table 1.3: Lift of area $A_{\text{lift-off}}$ and area requirement per molecule at surface pressures of 5mN/m and 25mN/m, $A_{5\text{mN/m}}$ and $A_{25\text{mN/m}}$, respectively, for the different investigated subphases.

by dissolving arachidic acid in pure chloroform and DPPA in a mixture (3:1) of chloroform and methanol (both from Sigma Aldrich, ≥99.8% purity). Spreading of the monolayers was performed using a Hamilton microliter syringe.

Figure 1.5 b) displays the pressure area-isotherms for eicosanoic acid monolayers on pure water for four different subphase temperatures between 22.5°C and 2.0°C. All isotherms were measured with a compression speed of 3cm^2/minute. At 22.5°C and 15.0°C one distinct kink in the isotherm was observed, separating two phases labelled as L_2 and LS, respectively in accordance with the phase diagram given in reference [9]. A detailed dicussion of the phase diagram for fatty acids including their microstructure as derived by X-ray diffraction experiments will be given in section 3.4.2. Both phases are liquid condensed phases, while a liquid expanded phase as observed e.g. for shorter chain length is absent. At lower temperatures a second kink appears in the isotherm (indicated by an arrow in figure 1.5 b)). The phase sequences are in this case L_2-L_2'-LS and L_2-L_2'-S, respectively, according to reference [30]. In contrast to the sharp kinks in the isotherms on pure water, the phase transitions are much more washed out in the isotherms measured on subphases of DMSO/H_2O in the eutectic mixing ratio (figure 1.5 c)). The collapse pressure of all isotherms are lower compared to pure water as a consequence of the lower surface tension of the subphase. The lift-off area is increased by about 10-15Å^2 and the slope of the isotherm is similar to the liquid expanded phases found e.g. in isotherms of hexadecanoic acid [9]. However, the characteristic two phase coexisting region between the liquid expanded and the liquid condensed phase is absent. The most distinct difference between the isotherm measured at 20.4°C and the one at -11.3°C is the position of the kink with respect to to the surface tension, which reduces from about 20.7mN/m to 15.8mN/m. For the isotherms measured on subphases of eutectic mixtures of glycerol/water (figure 1.5 d)) and glycerol/water/NaCl (figure 1.5 e)) sharp kinks in the isotherms are completely absent. For subphases of water/ethanol and water/methanol no stable monolayers could be prepared at solvent contents higher than 20-25 Vol%, probably due to the rather low surface tension of these mixtures and the high solubility of the surfactants in the solvents. The possible mixtures correspond to subphase freezing points of -10 to -15°C and were hence not further investigated. Table 1.3 lists the lift-off areas and the area requirement per molecule at surface pressures of 5 and 25mN/m at ambient temperatures for the investigated monolayers of eicosanoic acid. It strikes out that both in the presence of glycerol and DMSO both the lift-off areas and the area requirement at low surface pressures are drastically increased. At higher surface pressures the shift of the isotherm is smaller for DMSO/H_2O and H_2O/glycerol/NaCl and even negative for H_2O/glycerol. These findings may be partially attributed to the interaction

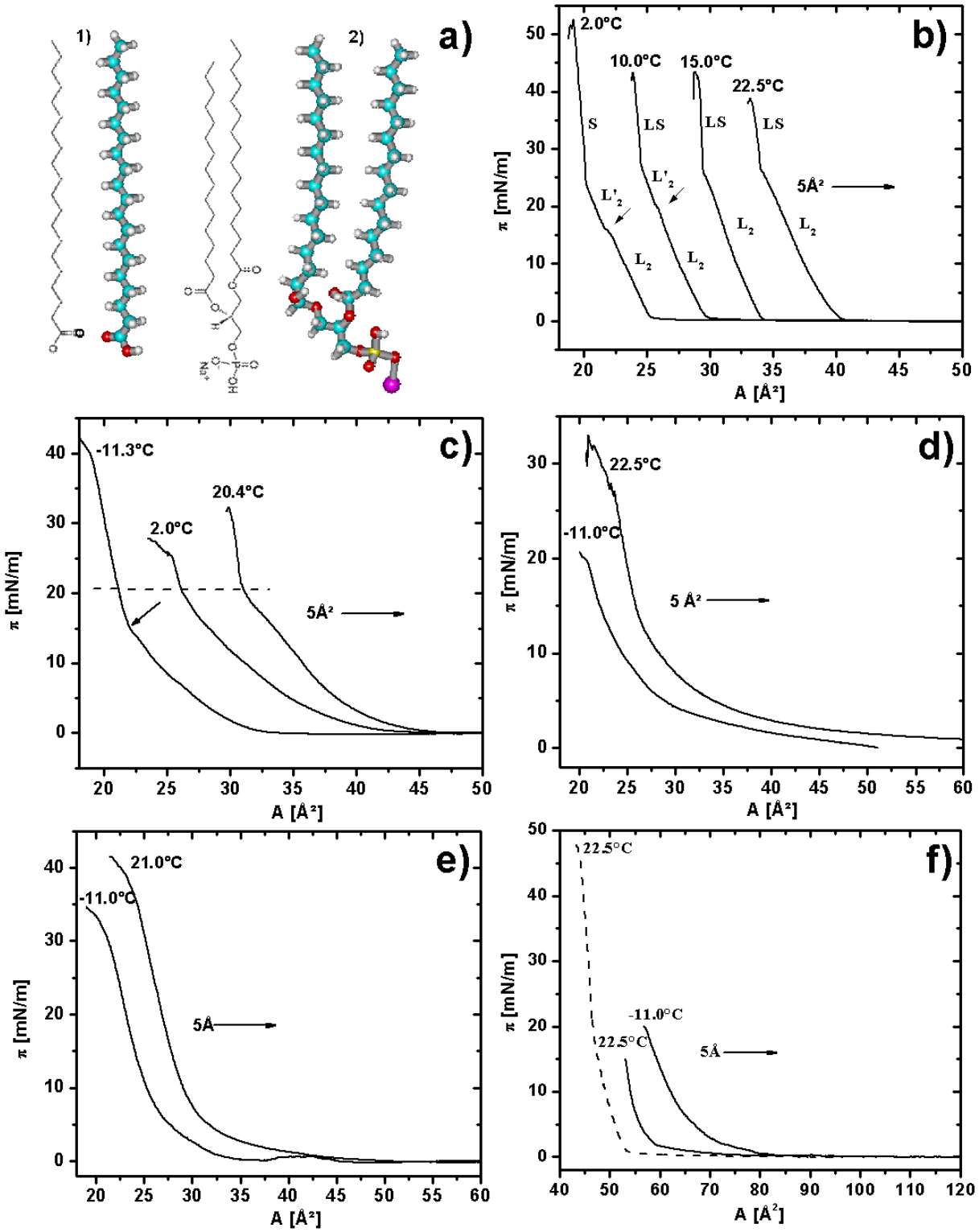

Figure 1.5: a) sketch of the two investigated surfactant molecules 1) eicosanoic (arachidic) acid, 2) DPPA (sketches from [48]); b) isotherms for eicosanoic acid on a water suphase; c) eicosanoic acid on a subphase of the eutectic mixture of DMSO and water; d) eicosanoic acid on a subphase of water and glycerol; e) eicosanoic acid on a subphase of H_2O/glycerol/NaCl; f) dashed line: DPPA on water, solid lines: DPPA on DMSO/H_2O; Isotherms have been successively shifted by 5Å^2 along the x-axis for clarity.

of the cryo-protectors with the surfactant layer. Glycerol and DMSO are commonly used cryo-protectors used in cooling and vitrification processes of biological tissues and cells. Their interaction with surfactant molecules was therefore mainly studied for vesicles and lamellar phases of phospholipids. Orädd et al. [82] investigated the liquid crystalline lamellar phase of DOPC in glycerol water mixtures by nuclear magnetic resonance, electron paramagnetic resonance and fluorescence spectroscopy. They find that the increase of the macroscopic viscosity arising from the addition of glycerol in the polar region of the membrane affects the dynamics of the molecules. The motional friction in the interface of the lipid aggregates is increased and hampers both the alkane chain motion and the translational diffusion of the molecules. Moreover, the same group reported in an earlier X-ray diffraction study an increase of the head group area with increasing glycerol content [52]. DMSO is able to make hydrogen bonds and competes with water for a direct interaction with the membrane surface. Gordeliy and co-workers found for lamellar systems of DPPC in DMSO/H_2O mixtures a stronger interaction between DMSO and the membrane surface than compared to water [39]. Wide angle X-ray scattering experiments revealed that the area per polar head of the lipid molecule and the tilt angle are increasing in the presence of DMSO. DMSO is adsorbing to the polar part of the membrane, displacing water molecules and is presumably forming a network of hydrogen bonds that stabilises the membrane. These findings for the influence of glycerol and DMSO on the membrane structure of phospholipids, in particular the increased area requirement, are in qualitative agreement with the above described results for the Langmuir monolayers of eicosanoic acid. In the following, the experiments will focus on DMSO/H_2O as a liquid subphase: the main goal of the present work is the study of the influence of temperature on monolayer phase behaviour and structure. Upon cooling changes in the physical characteristics of the subphases like for instance the viscosity are obviously inevitable. The temperature dependency of the mixture of DMSO/H_2O was discussed in section 1.2. Over the temperature range from 20°C to -45°C the viscosity of the eutectic mixture is increasing by approximately a factor of 35, while according to the data given in reference [18] the viscosity of the eutectic mixture of glycerol and water varies by even one and a half orders of magnitude more. In addition, the absolute value of the viscosity is generally lower for the DMSO/H_2O mixture. This plays an important role, as a restricting parameter for the lateral mobility of the amphiphiles, which is needed for reorganisation processes, depends on viscous coupling to the aqueous subphase [59]. The same argument about the viscosity holds for the eutectic mixture of water/glycerol/NaCl, but in addition the effect of ions and an altered pH value on the monolayer structure would have to be taken into account and separated from the effects due to cooling and an increased viscosity. At this stage DMSO/H_2O was chosen as the more easier system to study, as it does not contribute additional ions and its pH value was found to be 7.1, hence identical to a reference measurement on pure water. Figure 1.5 f) shows isotherms for DPPA on pure H_2O and on DMSO/H_2O at ambient temperature and at -11.1°C. While the lift-off areas are slightly increased in the presence of DMSO, at ambient temperature and low surface pressure the isotherms on pure H_2O and DMSO/H_2O superimpose. At -11.0°C the area requirement per molecule at low surface pressure is distinct larger than compared to DPPA on H_2O. It is noteworthy that in contrast to the collapse pressures suggested by the isotherms, DPPA films could be prepared at higher surface pressure by spreading. These monolayers

were found to be stable by monitoring the surface tension on time scales of a few hours.

Langmuir-Blodgett films [89] of eicosanoic acid were transferred at a surface pressure of 4mN/m from a subphase containing $5{\cdot}10^{-4}$M cadmium chloride (pH 6) [87] to a $15{\times}15\text{mm}^2$ silicon substrate (Wacker Chemie AG). The monolayer was organised at the liquid surface by conventional compression and the dipper speed for the upstroke of the silicon substrate was set to 3mm/minute. The silicon substrate was cleaned and made hydrophilic in the following way:

- bathed in a 50/50 Vol% mixture of water and methanol for about 30 minutes
- washed repeatedly and sonicated in ultra pure water
- bathed in a 70/30 Vol% mixture of sulfuric acid and water for about 30 minutes
- washed repeatedly and sonicated in ultra pure water

The first step provides cleaning of the wafer surface from organic residuals. The treatment with sulfuric acid renders the hydrophobic SiO_2 surface hydrophilic. The wafers were prepared prior to use and inserted into the subphase before spreading the monolayer. Analysis of the transfer ratio from dipper position versus trough-area plots revealed typical transfer ratios of $\geq$90%.

Chapter 2

Surface Sensitive X-ray Scattering and Diffraction

The theoretical basis of the surface sensitive X-ray scattering and diffraction techniques, GIXOS (Grazing Incidence X-ray scattering Out of the Specular plane) and GIXD (Grazing Incidence X-ray Diffraction), will be derived in the following chapter. A simplified way to model the diffraction peak intensities by structure factor calculations will be described.

The information obtained by means of GIXD and GIXOS is somehow complementary in a way that the two techniques probe different parts of the structure factor, according to different projections of the monolayer structure. GIXD measurements probe the projection of the two-dimensional lattice onto the xy-plane, while the so-called 'Bragg rod scans' (out-of-plane GIXD measurements) provide information about the three-dimensional alignment of the scatterer in the two-dimensional unit cell. Complementary, GIXOS probes the projection of the electron density of a quasi two-dimensional system onto the z-axis, thus perpendicular to the surface. In the case of, for instance, a heterogenous monolayer, another distinct difference between the two techniques is given by the part of the layer they probe: while by GIXD only the ordered parts can be investigated, for GIXOS only a contrast in the electron density normal to the surface is necessary. For such a system the packing and layer thickness obtained by GIXOS present an average over the probed surface area, while the corresponding values extracted from GIXD only hold for the ordered domains. So the information obtained by the two techniques are complementary rather than identical.

2.1 Grazing Incidence X-ray Diffraction (GIXD)

2.1.1 Interaction of X-rays with Matter

The classical goal of an X-ray diffraction experiment is to determine the structure of a crystal and the position of the scatterers (atoms, ions or molecules) in the unit cell. A common definition of a crystal is a periodic translation of a pattern of scatterers. Correspondingly, a crystal is mathematically described as the folding of a lattice with the content of the unit cell. The symmetry operations inversion, reflection and rotation create in three dimensions seven crystal systems and 32 point groups. In combination with the

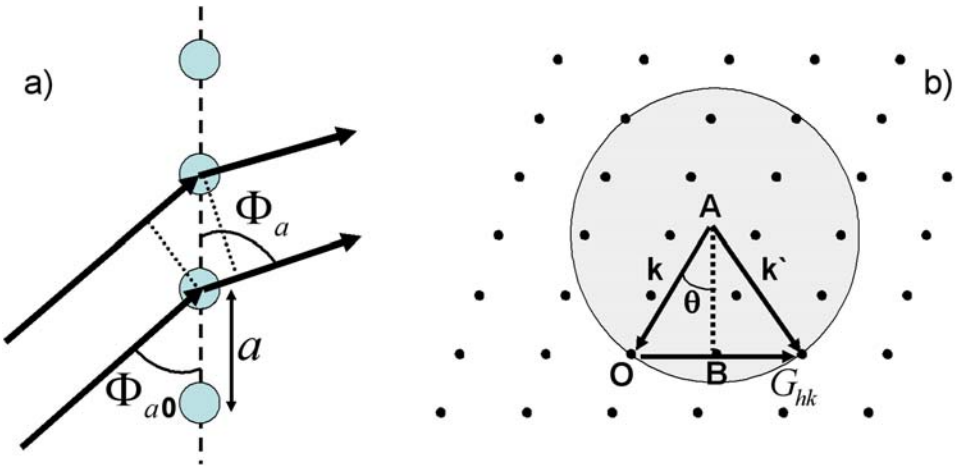

Figure 2.1: a) interference of two electromagnetic waves at a one-dimensional lattice according to Laue. b) Ewald construction in two dimensions, the dashed line AB indicates the lattice plane perpendicular to the reciprocal lattice vector G_{hk}.

translation symmetries *glide plane* and *screw axis* one obtains the 14 Bravais lattices and 230 space groups [63]. In two dimensions the number of plane groups is reduced to 17 [43].

The following section will present the principles of the diffraction of X-rays at a periodic structure (crystal) within the kinematical (first Born) approximation. The simplifying approximation of this theory is that only single scattering effects are taken into account. Therefore, the amplitude of the incident electromagnetic wave is the same at all points within the sample, with only the phase changing from point to point. Despite the disregard of the scattered wave amplitude, the kinematical approximation is widely used in structural crystallography and holds as long as the crystals are not too perfect and not too large, cases where dynamic scattering theory would have to be applied [99].

Scattering of an electromagnetic wave at a periodic lattice may lead to interference effects and a characteristic diffraction pattern which contains information about the structure. Therefore, the wavelength of the incoming wave has to be of the same order of magnitude as the distances between the scattering centres of the investigated structure. Hence X-rays or neutrons are common tools to probe periodic structures on atomic length scales and to obtain information about the lattice and the scatterer, respectively. The Laue equations (2.1) [70] describe the diffraction of a plane wave at a (three-dimensional) lattice. Each scattering center which is hit by the plane wave becomes the origin of a secondary spherical wave. Two of these waves originating from different scattering centers can interfere constructively only if the path length difference is an integer multiple of the wavelength (see figure 2.1 a)). Therefore in three dimensions the three Laue equations

$$\begin{aligned} a(\cos\Phi_a - \cos\Phi_{a0}) &= h\lambda \\ b(\cos\Phi_b - \cos\Phi_{b0}) &= k\lambda \\ c(\cos\Phi_c - \cos\Phi_{c0}) &= l\lambda \end{aligned} \tag{2.1}$$

have to be fulfilled simultaneously. The angle between the propagation direction of the

incoming and the diffracted wave are denoted by $\Phi_{a0}, \Phi_{b0}, \Phi_{c0}$ and Φ_a, Φ_b, Φ_c, respectively. The lattice vectors in real space are a, b, c, while the integers h, k, l are the Laue indices. The Laue equations can be combined to a vector equation:

$$\mathbf{q} = \mathbf{k}' - \mathbf{k} = \mathbf{G}_{hkl}. \tag{2.2}$$

Equation (2.2) illustrates that constructive interference will only occur provided that the wavevector transfer $\mathbf{q}$ is equal to a reciprocal lattice vector $\mathbf{G}_{hkl}$. The reciprocal lattice vector is thereby defined in the usual way as $\mathbf{G}_{hkl} = h\mathbf{a}^* + k\mathbf{b}^* + l\mathbf{c}^*$, with the integer values h, k, l and the primitive reciprocal lattice vectors $\mathbf{a}^*, \mathbf{b}^*, \mathbf{c}^*$. In the framework of the elastic scattering theory the moduli of the wavevector of the incident and the diffracted wave are identical: $k' = k$. The condition for constructive interference can equally be described by the Bragg equation [12]:

$$2d \sin\theta = n\lambda \tag{2.3}$$

Here d_{hk} denotes the lattice spacing, θ the angle between the incident wave and the lattice plane and n the order of the reflection. The wavelength λ is linked to the modulus of the incident wavevector by $k = 2\pi/\lambda$.

The Ewald construction [33, 8] (see figure 2.1 b)) illustrates the occurrence of a reflection according to the Laue equation (eq. 2.2). In reciprocal space, the wavevector $\mathbf{k}$ of the incident wave is oriented accordingly to the direction of the incident beam, the tip of this vector coincides with a reciprocal lattice vector. A circle (a sphere in three dimensions) with the radius $|\mathbf{k}|$ around the incident wavevector represents the elastic condition $k' = k$. The Laue condition (2.2) is fulfilled for each intersection of the circle with a reciprocal lattice point. The corresponding wavevector is $\mathbf{k}'$ and the wavevector transfer is a two-dimensional reciprocal lattice vector $\mathbf{G}_{hk}$. This reciprocal lattice vector is normal to some set of lattice planes and has the length

$$G_{hk} = \frac{2\pi}{d_{hk}} \tag{2.4}$$

where d is the interplanar spacing for this set of lattice planes. In the Ewald construction AB is the lattice plane normal to $\mathbf{G}_{hk}$ and θ is the angle between the direction of the incident wave and this lattice plane. Therefore, the Ewald construction allows for a given wavelength and incident direction the determination of the lattice planes which will diffract. The construction also illustrates the limit for useful wavelengths in a diffraction experiment: If a denotes the shortest distance between two lattice points, a circle with the radius $k < \frac{1}{2}2\pi/a$ will have no intersection points with the reciprocal lattice. Hence the maximum wavelength must not exceed $2a$.

The description of the diffraction conditions so far holds for single crystals and for single crystalline domains, respectively. However, many samples cannot be synthesised as single crystals of sufficient size and quality, but only as 'powders'. That is a large number of small crystallites randomly oriented with respect to each other. This holds in particular for organic monolayers on liquid or solid substrates, indicated by diffraction peaks being independent of sample rotation [65]. In the case of powder diffraction, the randomly oriented crystal axes of the individual crystallites produce a diffraction pattern

equivalent to a combination of the diffraction pattern for all possible orientations of a single crystal. The main difference compared to single-crystal diffraction is the impossibility to resolve separately the diffraction pattern for each orientation. This leads to an overlap of reflections originating from lattice planes with the same d-spacing. Organic monolayers form a quasi two-dimensional powder, where the quasi two-dimensional crystallites are randomly oriented in the monolayer plane. For a diffraction experiment using a monochromatic X-ray beam at fixed orientation with respect to the sample, the Ewald circle is fixed. The random orientation of the individual crystallites has the same effect as the rotation of a single crystal: the reciprocal lattice points are rotated on a circle around the origin of the reciprocal space. Thus each reciprocal lattice point traverses a circle and constructive interference occurs wherever the path of such a point intersects with the Ewald circle. The corresponding Bragg reflection can be detected at the Bragg angle θ with respect to the fixed direction of the incident beam.

The following section is a brief description of the interaction of X-rays with matter as the basis for scattering phenomena. Far away from absorption edges, the dominant scattering process is Thompson scattering. Within a classical framework, the scattering process is described as the electrons of an atom being accelerated by an impinging electromagnetic wave and emitting dipole radiation. The amplitude of the far-field radiation at a distance R from the source under an angle ψ with respect to the incident beam is given as

$$E_R = -r_0 E_0 \frac{e^{ikR}}{R} \cos\psi \tag{2.5}$$

where E_0 is the amplitude of the incident wave. The Thompson scattering length $r_0 = 2.82 \cdot 10^{-5}$ $\mathring{A}$ is thereby a measure for the ability of an electron to scatter an electromagnetic wave. The scattering from an atom with Z electrons is described by the number density of the electrons $\rho(\mathbf{r})$, where $\int \rho(\mathbf{r}) d\mathbf{r} = Z$. Each volume element of the atom contributes with $-r_0 \rho(\mathbf{r}) d\mathbf{r}$ to the total scattering amplitude. Summing up all contributions and accounting for the phase shifts leads to a total scattering length for one atom of $-r_0 \cdot f(\mathbf{q})$, where the atomic form factor $f(\mathbf{q})$ is given by

$$f(\mathbf{q}) = \int \rho(\mathbf{r}) e^{i\mathbf{q}\cdot\mathbf{r}} d\mathbf{r}. \tag{2.6}$$

Equation (2.6) shows that the atomic form factor is the Fourier transform of the electron density of the atom. In the case of the X-ray energy being close to atomic absorption edges, the atomic form factor has to be corrected for absorption and resonant scattering. For a molecule consisting of N atoms at positions $\mathbf{r}_n$ the molecular form factor can be written in the form

$$F(\mathbf{q}) = \sum_{n=1}^{N} f_n^0(\mathbf{q}) e^{i\mathbf{q}\cdot\mathbf{r}_n} \tag{2.7}$$

where $f_n^0(\mathbf{q}) = -r_0 f(\mathbf{q})$. If the molecules form a crystal whose lattice is defined by the lattice vectors R_n, the correct magnitude of the scattering amplitude is given by

summing up the molecular contribution while taking the phase factors into account. For the required phase factors equation (2.7) needs to be multiplied by the lattice sum $\sum_{\mathbf{R}_n} e^{i\mathbf{q}\cdot\mathbf{R}_n}$. By inserting the the Laue equation (2.2) into the equation for the molecular form factor (2.7), the structure factor for a three dimensional structure can be written in the form

$$F_{hkl}(\mathbf{q}) = \sum_j f_j^0(\mathbf{q}) e^{2\pi i(hx_j + ky_j + lz_j)} \tag{2.8}$$

where the x_j, y_j, z_j denote the positions of the atoms in the unit cell in units of the lattice vectors and the sum is extended over all atoms in the unit cell. In X-ray measurements it is not the scattering amplitude which is experimentally accessible, but the intensity of the scattered wave which is proportional to the absolute squared of the scattering amplitude:

$$I(\mathbf{q}) \propto |F_{hkl}(\mathbf{q})|^2 . \tag{2.9}$$

It is this absolute squared which causes the so-called 'phase problem ', rendering the reconstruction of the sample's electron density from the diffraction pattern by a simple Fourier transformation impossible due to the loss of the phase information. From equation (2.8) Friedel's law [78] follows immediately: $|F_{hkl}(\mathbf{q})|^2 = |F_{-h-k-l}(\mathbf{q})|^2$, indicating that the intensities of a wave diffracted at the front-side and the backside of a lattice plane are in general identical.

2.1.2 The Scattering Geometry

Grazing incidence diffraction is a powerful tool for the structural investigation of thin films on liquid and solid surfaces due to its surface sensitivity. The latter arises from the phenomenon that at incident angles below the critical angle for total external reflection an evanescent wave is established, which is travelling parallel to the surface and whose penetration into the bulk is exponentially damped. Below the critical angle the $1/e$ penetration depth is typically of the order of 50 $\mathring{A}$ [32] so that bulk scattering is suppressed in contrast to scattering from the surface. Typical experiments use incident angles of 60 to 80% of the critical angle α_c, the latter being about 0.15° and 0.25° for water and a silicon wafer at an X-ray energy of 8 keV, respectively.

The scattering geometry for GIXD and the notation for wavevector and angles are shown in figure 2.2. The surface of the sample is located in the horizontal xy-plane, normal to the z-direction. The incident wave with wavevector k_i impinges on the sample surface under an angle α_i smaller than the critical angle. For the investigation of the structure of a quasi two-dimensional powder, the incident direction is fix with respect to the sample. The scattered wave with a wavevector k_f is detected under an exit angle α_f normal to the sample surface and under an in-plane scattering angle 2θ. By using a position sensitive detector (PSD), at each in-plane angle 2θ the scattering for several α_f can be recorded simultaneously on different channels of the PSD. For an in-plane scan the scattering angle 2θ is varied and the scattered intensity is integrated over the channels of the PSD. An out-of-plane scan is obtained as the spectrum of the PSD at fixed scattering angle α_f. As the integration over the channels of the PSD is performed by a software after saving the channel resolved data, during a 2θ-scan both types of measurements are

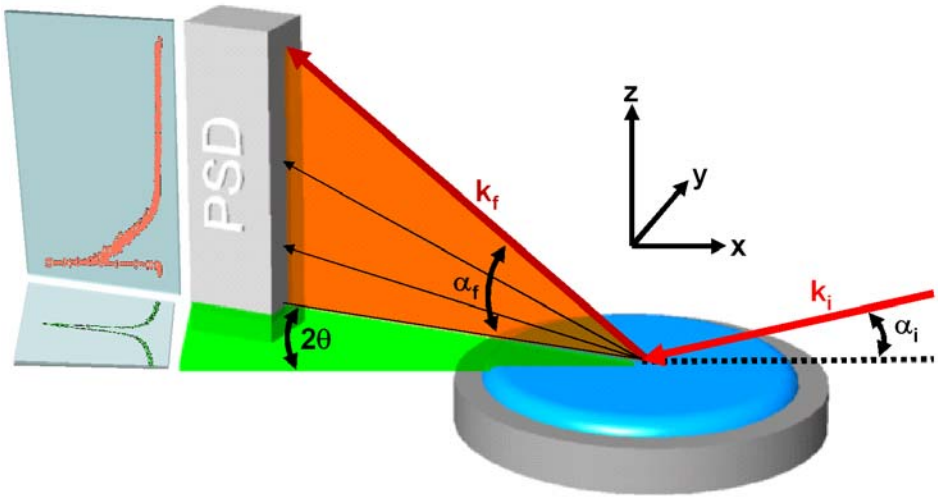

Figure 2.2: Scattering geometry for GIXD from a liquid surface. The incident wavevector and the incident angle are denoted with k_i and α_i, respectively. k_f and α_f denote the wavevector of the scattered wave and the exit angle, respectively. The in-plane scattering angle is 2θ. By using a position sensitive detector (PSD) in-plane measurements and out-of-plane measurements are performed simultaneously.

performed simultaneously, leading to a map of the scattering distribution in reciprocal space.

The wavevector transfer is given as $\mathbf{q} = \mathbf{q}_x + \mathbf{q}_y + \mathbf{q}_z = \mathbf{k}_i - \mathbf{k}_f$, with the boundary condition $k_i = k_f$ for elastic scattering. The components $\mathbf{q}_x$ and $\mathbf{q}_y$ are combined to the lateral wavevector transfer $\mathbf{q}_{xy}$. The remaining two components of the wavevector transfer for the given scattering geometry can then be calculated as:

$$q_{xy} \approx k\sqrt{1+\cos^2\alpha_f - 2\cos\alpha_f\cos 2\theta} \approx 2k\sin\frac{2\theta}{2} \tag{2.10}$$

$$q_z = k(\sin\alpha_i - \sin\alpha_f) \tag{2.11}$$

The first approximation in equation 2.10 holds for $\alpha_i \ll 1$, while the second one also assumes that $\alpha_f \ll 1$.

The separate detection of the in-plane wavevector transfer q_{xy} and the out-of-plane wavevector transfer q_z allows for splitting the structure factor (eq.2.8) into two parts. For the two-dimensional case, the in-plane wavevector transfer corresponds for constructive interference to the two-dimensional reciprocal lattice vector: $q_{xy} = G_{hk}$. Equation 2.8 can thus be rewritten in the form

$$F_{hk}(\mathbf{q}) = \sum_j f_j^0(\mathbf{q}) e^{iq_z\cdot r_z^j} e^{i\mathbf{q}_{xy}\cdot\mathbf{r}_{xy}^j} \equiv F_{str.}(\mathbf{q}_{xy})\cdot F_{form.}(\mathbf{q}_{xy}, q_z) \tag{2.12}$$

where the two-dimensional structure factor $F_{str.}(\mathbf{q}_{xy})$ describes the in-plane lattice, while $F_{form.}(\mathbf{q}_{xy}, q_z)$ describes the from factor of the scatterer. Because in two-dimensions there is no Laue condition for the q_z-direction, the q_z values in the form factor are continuos

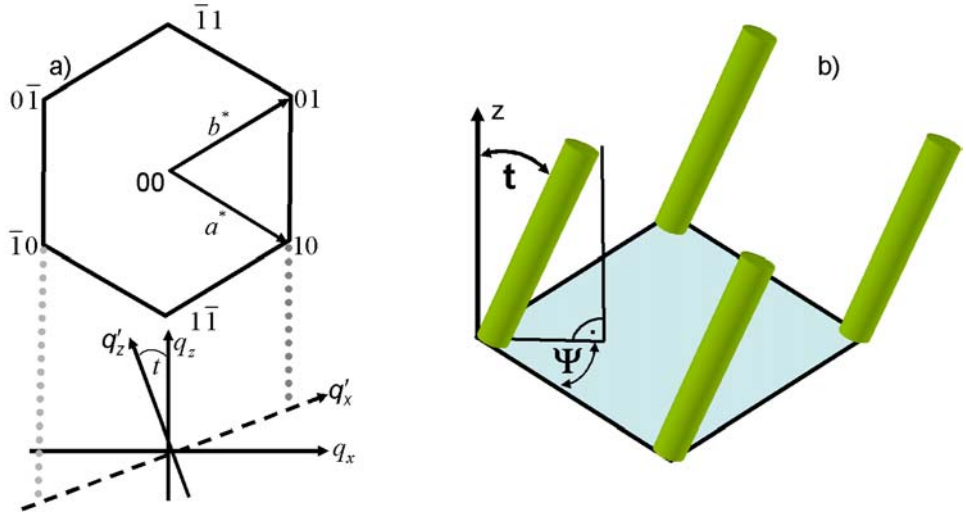

Figure 2.3: a) Intersection of the 2d structure factor and the molecular form factor in the case of tilted and untilted alkane chains. In the case of untilted chains the intersection points for all reflection are located at $q_z = 0$, while for tilted chains the intersection points for e.g. the reflections $0\overline{1}$, 11 and 01 are located at $q_z < 0$, $q_z = 0$ and $q_z > 0$, respectively. b) definition of the tilt angle t of the alkane chain relative to the surface normal and the tilt direction Ψ relative to a lattice vector.

and not restricted by a diffraction condition, in contrast to $\mathbf{q}_{xy} = \mathbf{G}_{hk}$. Therefore, it is possible to access on an in-plane Bragg reflection of a two-dimensional lattice directly the from factor of the scatterer by an out-of-plane scan.

2.1.3 Out-of-plane Measurements: Bragg Rods

In the following paragraph the above general description of GIXD will be concretised towards the diffraction from a two-dimensional lattice formed by the alkane chains of organic surfactants. Two approaches to model the molecular form factor of such scatterers will be introduced and discussed.

As it is apparent from the Laue equations (2.2), the scattering from a two-dimensional periodic structure is concentrated in 'so-called' Bragg rods, defined by $\mathbf{q}_{xy} = \mathbf{G}_{hk}$ along the q_z-direction. The convolution of the structure with a unit pattern of scatterers determines where in reciprocal space the diffracted intensity can be found and which reflections can be observed. The intensity distributed along the direction of a reciprocal lattice vector is maximal where it coincides with the molecular form factor (see figure 2.3 a)). If the tilt angle t of the alkane chain with respect to the surface normal is zero, the intersection points are located in the q_xq_y-plane. For tilted chains the intensities of the $01, 10$ reflections peak at $q_z > 0$, while the intensities of the $1\overline{1}$, $\overline{1}1$ reflections still peak at $q_z = 0$. For the $0\overline{1}$ and $\overline{1}0$ reflection the maxima in intensity are shifted towards $q_z < 0$, rendering the observation of these reflections impossible, because their position is below than the

scattering horizon defined by the surface of the substrate[1]. It is noteworthy that the reflections, which are according to figure 2.3 a) well separated with respect to q_x, might completely overlap in a two-dimensional powder diffraction experiment where only the total in-plane wavevector transfer q_{xy} is resolved.

In the case of tilted alkane chains a new coordinate system (denoted with primes in figure 2.3 a)) can be introduced, that relates the wavevector transfers in the tilted system of the molecule to the wavevector transfers of the untilted laboratory system. If the q_x-axis is chosen along the tilt direction m of the chains (see figure 2.3 b)), i.e. along the projection of the chain long axis onto the $q_x q_y$-plane, the new coordinates q'_z and q'_{xy} can be calculated as [70]:

$$\begin{aligned} \mathbf{q}'_z &= (q_z \cos t - q_x \cos(\pi/2 - t))\mathbf{e}'_z \\ \Longrightarrow\ & q'_z = q_z \cos t - q_x \sin t \qquad (2.13) \\ \mathbf{q}'_{xy} &= (q_x \cos t + q_z \cos(\pi/2 - t))\mathbf{e}'_x + q_y \mathbf{e}'_y \\ \Longrightarrow\ & q'_{xy} = \sqrt{q_y^2 + (q_x \cos t + q_z \sin t)^2}. \qquad (2.14) \end{aligned}$$

Here the components q_x and q_y of the in-plane wavevector transfer can be calculated as

$$q_x = G_{hk} \cos \Psi^*_{hk} \qquad (2.15)$$

$$q_y = G_{hk} \sin \Psi^*_{hk}, \qquad (2.16)$$

where G_{hk} is the modulus of the reciprocal lattice vector of the Bragg reflection where the Bragg rod is measured and Ψ^*_{hk} being the angle between that reciprocal lattice vector and the tilt direction m. By choosing the tilt direction of the chains as a reference direction for the decomposition of the wavevector transfer, equations 2.15 and 2.16 hold independently of a particular lattice symmetry.

One possibility to model a measured Bragg rod is to calculate the molecular form factor from the overall shape of the molecule, thus neglecting atomic details. This approach seems to be particularly suited to model the Bragg rods of alkane chains in a rotator phase. In such a state the carbon atoms that constitute the chains exhibit a large freedom of movements and thus a flexible model based only on the shape of the scattering molecule is adapted. A model considering in particular the rotation of the chains around their length axis, the so-called 'cylinder model', has been introduced by [70]. The model substitutes the alkane chains by stiff cylinders, where the electron density of the chains is smeared out over a cylindrical shell. As a further simplification, the CH_2 groups, which form the alkane chains, are substituted by only one atom with the same number of electrons (oxygen) located at the position of the center of mass of the CH_2 group. The distance of this atom from the axis of rotation defines the radius R of the cylinder. The radius can be calculated using the length of the CH_2-CH_2 bonding (1.54 $\mathring{A}$) and the included angle between them (110°) as $R = \frac{1}{2} \cdot 1.54\ \mathring{A} \cdot \cos\left(\frac{110°}{2}\right) \approx 0.44\mathring{A}$. Assuming all-trans configuration for the alkane chain, the length L of the embedding cylinder can be calculated as $L = (n + \frac{9}{8}) \cdot 1.265\ \mathring{A}$. Here n denotes the number of CH_2 groups in the

[1] With a typical X-ray energy of about 8keV, the absorption by the liquid subphase is too large to observe these reflections.

chain, while the second term in brackets takes into account the slightly longer CH_3 group terminating the chain. The molecular form factor for a rod-like particle is given by [92]:

$$F_{\text{cylinder}}(\mathbf{q}) = f^0(\mathbf{q}) \int dV \cos(\mathbf{q} \cdot \mathbf{r}) \tag{2.17}$$

where the integration is extended over the volume of the particle. The integral can be separated into two parts, the axial molecular form factor

$$S(q_z') = \int_{-L/2}^{L/2} dz \cos(q_z' \cdot z) = 2\frac{\sin(\frac{1}{2}L \cdot q_z')}{q_z'} \tag{2.18}$$

and the radial molecular form factor

$$R(\mathbf{q}_{xy}') = \int_0^{2\pi} d\varphi \int_0^R dr \left\langle \cos(\mathbf{q}_{xy}' \cdot \mathbf{r}) \right\rangle_{2d}. \tag{2.19}$$

Using the identity $\left\langle \cos(\mathbf{q}_{xy}' \cdot \mathbf{r}) \right\rangle_{2d} \equiv J_0(q_{xy}' \cdot r)$, [3] for the two-dimensional average of the phase factor leads to the final expression for the radial molecular form factor

$$R(q_{xy}') = 2\pi \frac{R \cdot J_1(R \cdot q_{xy}')}{q_{xy}'}, \tag{2.20}$$

where J_0 and J_1 are Bessel functions of zeroth and first order, respectively. The primes denote the coordinates with respect to a tilt angle of the lipid chains relative to the surface normal as given by equations 2.13 and 2.14. The total molecular form factor is then described by $F_{\text{cylinder}}(\mathbf{q}) = S(q_z') \cdot R(q_{xy}')$.

A different approach to model a measured Bragg rod is to calculate the intensity distribution using the structure factor (eq. 2.12) and the position of the atoms of the alkane chain. This model neglects the large mobility of the atoms in the rotator phase and is hence more appropriate for a crystalline phase where the rotation of the alkane chain around its length axis is stopped. Using the Laue condition for q_{xy}, equation 2.12 can be rewritten in the form

$$F_{hk}(\mathbf{q}) = \sum_j f_j^0(\mathbf{q}) e^{2\pi i(hx_j + ky_j)} e^{iq_z \cdot z_j \cdot c} \tag{2.21}$$

where the atomic positions x_j, y_j and z_j are in units of the corresponding lattice parameters. As there is no periodicity in the z-direction, the 'lattice spacing' c is given by the height of the chain with respect to the xy-plane, thus $c = L \cos t$. Due to their weak scattering ability, the hydrogen atoms have been neglected in structure factor calculations. The measured intensity of a Bragg rod is proportional to the absolute squared of the molecular form factor. In addition, for the grazing incidence geometry the transmission functions for the incident and the scattered beam have to be taken into account. The measured intensity of a Bragg rod as a function of the out-of-plane wavevector transfer can then be written in the form

$$I(\mathbf{q}) \propto |T_i(\alpha_i)|^2 |F(\mathbf{q})|^2 |T_f(q_z)|^2 \tag{2.22}$$

where the molecular form factor is calculated according either to the cylinder model or from the atomic positions of the atoms constituting the alkane chain. T_i and T_j denote the transmission functions of the incident and the scattered wave, respectively. As the incident angle α_i is fixed in the GIXD geometry, the corresponding transmission function is just a constant factor which might be neglected if the scattered intensity is not measured in absolute units. Contrary, as the scattering intensity is recorded at the same time for a whole range of q_z values (and hence exit angles α_f of the scattered wave), the transmission function of the scattered beam varies with q_z. Within the framework of the kinematical approximation, thus neglecting the refraction of the scattered waves, the transmission function T_f leads to the so-called Vineyard peak [121] defined as

$$V(q_z) = T_f(q_z) = \begin{cases} 2x & 0 < x < 1 \\ 2x/\left(x + \sqrt{(x^2-1)}\right) & x > 1 \end{cases} . \tag{2.23}$$

The abbreviation x in equation (2.23) denotes thereby the ratio between the perpendicular wavevector transfer q_z and the critical wavevector transfer q_c: $x = q_z/q_c$. The critical wavevector transfer q_c is linked to the critical angle α_c by $q_c = 2k \sin \alpha_c$.

A comparison of the Bragg rods for C20 alkane chains calculated with the cylinder and the atomic model respectively is shown in figure 2.4. Panel a) depicts the shape of the Bragg rods at small out-of-plane wavevector transfers q_z. For untilted chains ($t = 0°$) it is evident that the shape of the Bragg rod in the atomic model (open circles) and in the cylinder model (solid line) are identical and thus the two curves superimpose. The very sharp feature in the Bragg rod at $q_z \approx 0.02$ $\mathring{A}^{-1}$ is due to the Vineyard peak. It is noteworthy that the shape of the Bragg rod for untilted chains in the atomic model does not depend upon the orientation of the carbon sheets around the long axis of the chain, that is so to say the state at which the rotation is frozen in. In contrast, there is a distinct difference between the two models in the case of tilted alkane chains ($t = 20°$ and $\Psi^* = 60°$).The position of the maximum with respect to q_z as well as the width of the Bragg rod is larger for the cylinder model (dashed line) as compared to the atomic model (dotted line). In the case of tilted chains the shape of the Bragg rod in the atomic model also depends on the twist angle of the chain (see 2.1.5). The almost complete absence of the sharp Vineyard peak for the Bragg rod calculated within the framework of the cylinder model becomes clear by considering equation (2.22): as the molecular form factor exhibits a minimum at small q_z, the Vineyard peak is multiplied with almost zero and hence almost vanished.

Figure 2.4 panel b) shows the Bragg rods calculated according to the two different models for untilted chains extended to larger q_z. For the atomic model (solid and dotted line) distinct interference pattern attributed to the CH_2-CH_2 repeat distance appear, with a constructive interference maximum at the position of the tenth fringe for a C20 alkane chain. For the cylinder model (dashed line) such interference pattern are absent, due to the conceptional negligence of the sub-molecular details of the alkane chain. Only very weak side maxima arising from the slit-function-like axial molecular form factor (eq. 2.23) are present up to intermediate q_z. The observability of the interference fringes of the atomic model depends however on two factors: the typical background level in the measured data (indicated by a solid horizontal line in figure 2.4 b)) and the surface roughness. The latter

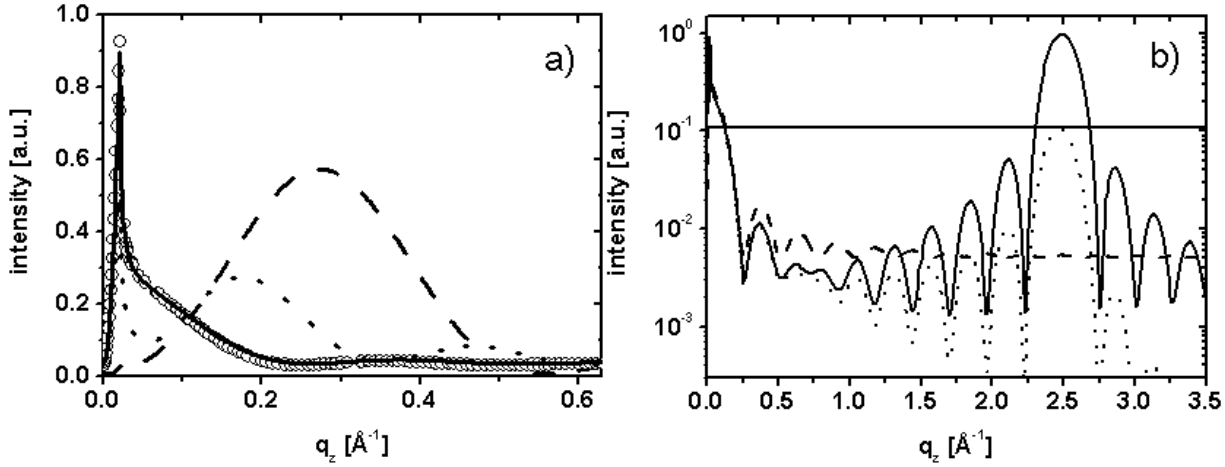

Figure 2.4: Comparison of the Bragg rod shapes from the cylinder and an atomic model. a) at small q_z: For untilted chains the cylinder model (solid line) and the atomic model (open circles) superimpose. For tilted chains the shape of the Bragg rod in the atomic model (dotted line) and the cylinder model (dashed line) differ. b) Bragg rods from the cylinder model (dashed line, $\sigma = 0$) and the atomic model (solid line: $\sigma = 0$, dotted line: $\sigma = 0.6$ $\AA$) extended to larger q_z. Horizontal line: typical level of background scattering.

one gives rise to diffuse scattering and its impact on the intensity of a measured Bragg rod can be described by a Debye-Waller like roughness term [6]:

$$I(\mathbf{q}) \propto |F(\mathbf{q})|^2 \, |T_f(q_z)|^2 \, e^{-q_z^2 \cdot \sigma^2} \tag{2.24}$$

with the surface roughness σ. It is evident, that the surface roughness plays an important role for the intensity of a Bragg rod especially at larger q_z. This fact is demonstrated by the dotted curve in figure 2.4 b) where a surface roughness of $\sigma = 0.6$ $\AA$ has been taken into account, rendering the intensity of the interference maximum of the Bragg rod comparable to the background level. In conclusion, differences between the two models in the shape of the rods appear only for tilted chains or if interference fringes between sub-molecular repeat units become observable, while no differences appear for untilted chains at small q_z.

In contrast to the shape, the intensity of a Bragg rod differs between the two models. Within the framework of the cylinder model, the C-C carbon plane of the alkane chain is replaced by a smearing of the corresponding electron density over a cylindrical shell. The alignment of this plane with respect to the unit cell is consequently no parameter in this model, contrary to the atomic one. Here the alignment of the C-C carbon plane is described by a twist angle ϕ of the alkane chain around its longitudinal axis (see 2.1.5 for a detailed definition). By varying this twist angle at fixed position of the tilt angle of the chain and fixed tilt direction, the positions of the carbon atoms in the unit cell are altered. The influence of the twist angle on the intensity of the Bragg rod of an untilted alkane chain is shown in figure 2.5 a). The periodic change of the intensity of the Bragg rod as a function of ϕ is even more evident in figure 2.5 b), where the intensity is shown integrated along q_z. This dependency of the structure factor intensity upon the position

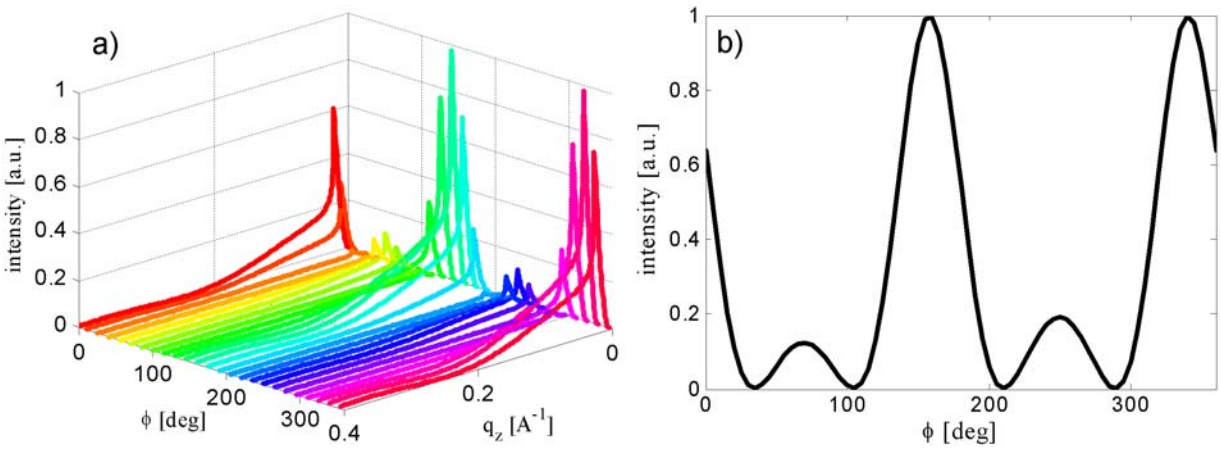

Figure 2.5: a) Bragg rods calculated using the atomic model for different twist angles. b) Corresponding integrated intensities

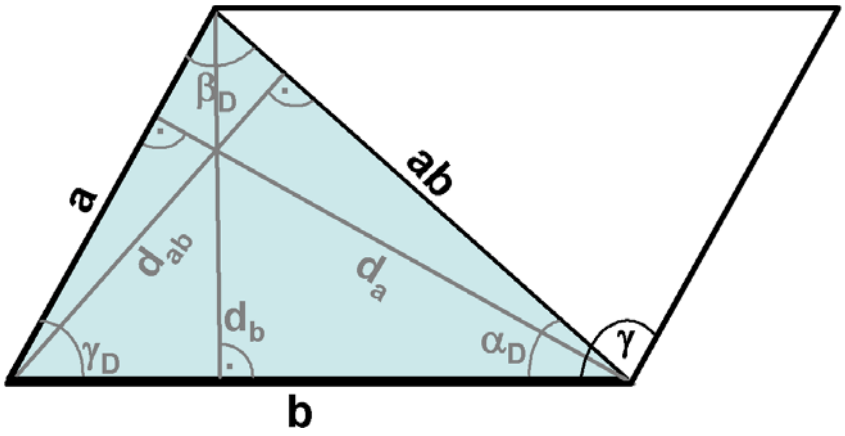

Figure 2.6: Definitions for lattice spacings, angles and lattice vectors in two dimensions for the most general case of an oblique unit cell.

of the individual atoms within the unit cell will be the basis for the quantitative analysis of the Bragg peak intensities which will be described in section 2.1.5.

2.1.4 In-plane Measurements: 2d Unit Cells

In the following, the possible unit cells for a quasi-two-dimensional lattice and their determination from a GIXD diffraction pattern will be introduced. Combining the information of the out-of-plane and the in-plane measurements, not only information about the unit cell dimension but also about the alignment of the scatterer within this unit cell are accessible.

The two-dimensional unit cell is defined by the modulus of the two lattice vectors and their including angle. This is depicted in figure 2.6 for the most general case of an oblique unit cell. The quadrangular unit cell is composed of two congruent triangles whose sides

are denoted as a, b and ab. The vectors **a** and **b** are thereby the lattice vectors in real space and γ is their including angle. For crystallographic convention $a \leq b \leq ab$ and $\gamma \geq \frac{\pi}{2}$ holds. Note that the third side of the triangle is referred to as ab rather than c in order to clearly indicate the restriction of the unit cell to two dimensions. As a consequence, the three vectors **a**, **b** and **ab** are linear dependent, in contrast to the three linear independent lattice vectors **a**, **b** and **c** in the three dimensional case. The heights of the hatched triangle in figure 2.6 correspond to the three lattice spacings d_a, d_b and d_{ab}. These lattice spacings are related to the in-plane wavevector transfer q_{xy} at a Bragg reflection by

$$d_{a,b,ab} = \frac{2\pi}{q_{xy}^{a,b,ab}} \tag{2.25}$$

where $q_{xy} = G_{hk}$. The heights, sides and angles of the hatched half of the unit cell are linked by the relations

$$\sin\alpha_D = \frac{d_{ab}}{b} = \frac{d_b}{ab} \tag{2.26a}$$

$$\sin\beta_D = \frac{d_{ab}}{a} = \frac{d_a}{ab} \tag{2.26b}$$

$$\sin\gamma_D = \frac{d_b}{a} = \frac{d_a}{b} \tag{2.26c}$$

so that the relations between the heights and the sides

$$ab = \frac{d_a}{d_{ab}}a \tag{2.27a}$$

$$b = \frac{d_a}{d_b}a \tag{2.27b}$$

$$a = \frac{d_b}{d_a}b \tag{2.27c}$$

follow. According to equation (2.26c) the modulus of the first lattice vector a can be calculated as

$$a = \frac{d_b}{\sin\gamma_D} \tag{2.28}$$

where the angle γ_D can be expressed in terms of the lattice spacings as

$$\gamma_D = \arccos\left[\frac{d_b}{2d_a} + \frac{d_a}{2d_b} - \frac{d_a d_b}{2d_{ab}^2}\right]. \tag{2.29}$$

The angle γ included by the two lattice vectors **a** and **b** is according to figure 2.6 given by

$$\gamma = \alpha_D + \beta_D. \tag{2.30}$$

Thus, combining the equations (2.28), (2.29), (2.27b), (2.26a), (2.26b) and (2.30), the basic unit cell parameters a, b and γ can be related to the three lattice spacings d_a, d_b and

d_{ab}. These lattice spacings are directly accessible from a GIXD in-plane measurement as shown by equation (2.25). In order to relate a series of measured Bragg reflections to the correct lattice spacings, from the equations (2.26a) and (2.26b) together with the crystallographic convention $a \leq b \leq ab$ the relationship $d_a \geq d_b \geq d_{ab}$ can be derived. Taking the reciprocal relationship (equation 2.25) between the lattice spacings in real space and the wavevector transfers into account, the assignment of the Bragg reflections as $q_a \leq q_b \leq q_{ab}$ is evident. By going from the two-dimensional oblique unit cell to more symmetric ones, two or even all three lattice spacings and thus the corresponding Bragg reflections might be degenerated. If the unit cell is chosen as a primitive one, each lattice spacing results in a corresponding Bragg reflection. By introducing a non-primitive unit cell, the area of the unit cell is increased to an integer multiple of the corresponding primitive cell, thus containing a larger number of lattice spacings. As a consequence, systematic extinction of reflections occur as the number of observable Bragg reflections cannot depend on the arbitrary choice of the unit cell. The intensities of Bragg reflections depend on the scattering contributions of the atoms or molecules in the unit cell and particularly on whether they are in phase with each other or not. Therefore, for centred lattices systematic extinction of reflections occur, while there are no restricting reflection conditions for primitive unit cells containing only one scatterer. The systematic extinctions can be derived directly from the structure factor (eq. 2.12). For instance, for the non-primitive centred rectangular lattice the reflection conditions follow from the position of the scatterers in the unit cell. With a basis consisting of two scatterers located at positions $(0,0)$ and $(\frac{1}{2},\frac{1}{2})$ (in terms of lattice vector units), the sum over the first exponential function in equation 2.12 leads to the term $1+e^{2\pi i(\frac{1}{2}k+\frac{1}{2}h)}$. This term is equal to zero for $h+k=2n+1$, where n is an integer.

The Miller indices for a Bragg reflection can be calculated from the lattice spacings $d_{hk}=\frac{|\mathbf{G}_{hk}|}{2\pi}$, taking possible extinction rules for non-primitives unit cells into account. In two-dimensions the length of the reciprocal lattice vector is in the most general case of an oblique lattice given as

$$|\mathbf{G}_{hk}| = \sqrt{h^2a^{*2} + k^2b^{*2} + 2hka^*b^*\cos\gamma^*}, \tag{2.31}$$

where the angle γ^* between the reciprocal lattice vectors $\mathbf{a}^*$ and $\mathbf{b}^*$ is the same as the angle between the vectors $\mathbf{a}$ and $\mathbf{b}$ in real space: $\gamma^* = \gamma_D$. The three smallest reciprocal lattice vectors for an oblique lattice and hence the corresponding reflections of lowest order are the pairs of reflections $(01),(0\overline{1})$; $(10),(\overline{1}0)$ and $(1\overline{1}),(\overline{1}1)$. In the case of tilted alkane chains the indexing of the diffraction pattern needs to be examined in terms of the observability of the reflections as described in section 2.1.3.

Besides the oblique one, there are three other possible unit cells in two dimensions, namely the rectangular cell, which exists both as a primitive (p) and a centred cell (c), the square unit cell and the hexagonal unit cell. An overview of this unit cells is given in figure 2.7. The two-dimensional plane groups summarise the symmetries created by one of the four unit cells in combination with the translational symmetries of the lattice and the ten crystallographic point groups (see [43]) in two dimensions. A crystallographic point group is a group of symmetry operations that maps a point lattice onto itself. Consequently, operations including translations are excluded and the n-fold rotation points are restricted to the cases n=1,2,3,4,6. The resulting symmetries of the plane groups are -besides from

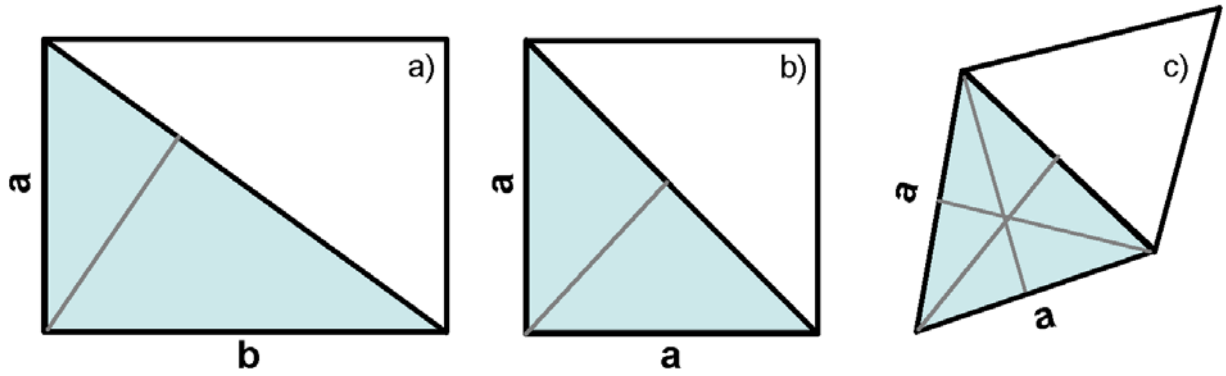

Figure 2.7: overview of the remaining two-dimensional unit cells (apart from the oblique one shown in figure 2.6): a) rectangular, b) square and c) hexagonal

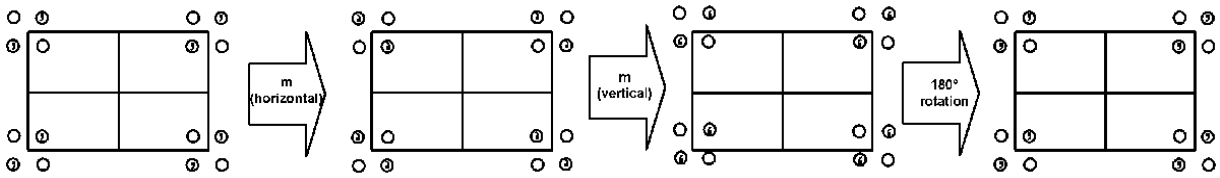

Figure 2.8: The symmetry elements in the plane group p2mm: horizontal and vertical mirror lines and 2-fold rotation axes whose fixed points lie at intersections of axes of reflection. Circles with and without symbol denote mirror images of each other, so that each of the symmetry operations can be carried out separately without changing the pattern.

rotation points- mirror lines (m) and glide lines (g). A glide line is thereby a combination of a reflection at a mirror line and a translation by $\frac{1}{2}\mathbf{a}$ of $\frac{1}{2}\mathbf{b}$. By convention only the minimum symmetry elements of a group are indicated, while the ones that can be derived from the basic ones are suppressed. An overview of the possible unit cells, plane groups and the general reflection condition is given below. An example of the symmetry elements in a rectangular cell (plane group p2mm) is depicted in figure 2.8.

- Oblique: possible plane groups: p1, p1, no general reflection conditions
- Rectangular: possible plane groups (corresponding reflection conditions): p1m1, p1g1 (0k: k=2n) , c1m1 (hk: h+k=2n, h0:h=2n, 0k: k=2n), p2mm, p2mg (h0: h=2n), p2gg (h0:h=2n, 0k: k=2n), c2mm (hk: h+k=2n, h0:h=2n, 0k: k=2n)
- Square: possible plane groups (corresponding reflection conditions): p4, p4mm, p4gm (h0:h=2n, 0k: k=2n)
- Hexagonal: possible plane groups: p3, p3m1, p31m, p6, p6mm

As sketched in section 2.1.3, the intersection of the molecular form factor with the two-dimensional lattice structure factor leads to a relationship between the maxima of a Bragg

reflection with respect to q_{xy} and q_z. This relationship is of the form $q_z = q_{xy} \cos \Psi^* \tan t$ [6, 64] and allows for the determination of the tilt angle t and the tilt direction Ψ^* in reciprocal space. For the most general case of an oblique lattice, the relation is expanded to a system of equations of the form [113, 112]

$$q_z^a = q_{xy}^a \cos \Psi_a^* \tan t \tag{2.32a}$$

$$q_z^b = q_{xy}^b \cos \Psi_b^* \tan t \tag{2.32b}$$

$$q_z^{ab} = q_{xy}^{ab} \cos \Psi_{ab}^* \tan t. \tag{2.32c}$$

It is evident, that there is only one tilt angle with respect to the surface normal and the tilt directions are bounded by the two-dimensional unit cell as sketched in figure 2.3. Therefore, the Bragg rods of the individual Bragg reflections cannot be modeled separately, but the parameters have to fulfill certain boundary conditions. One boundary condition is the demand that the largest out-of-plane wavevector transfer can be calculated as the sum of the two other ones [125]:

$$q_z^a = q_z^b + q_z^{ab}. \tag{2.33}$$

As another boundary condition

$$\Psi_a^* = \Psi_b^* + \gamma_D \tag{2.34}$$

holds, were the angle γ_D between the lattice vector $\mathbf{a}$ and $\mathbf{b}$ can be calculated according to equation (2.29) using only the information from the in-plane measurements. The tilt direction of the chains in reciprocal space is then fully determined by calculating the angle Ψ_b^* according to

$$\Psi_b^* = \arctan \left\{ \frac{1}{\sin \gamma_D} \left[\cos \gamma_D - \frac{q_z^a q_{xy}^b}{q_z^b q_{xy}^a} \right] \right\}. \tag{2.35}$$

With this result, the combination of the equations (2.32a) and (2.32c) leads to

$$\Psi_{ab}^* = \arccos \left[\frac{q_z^{ab} q_{xy}^b \cdot \cos \Psi_b^*}{q_z^b q_{xy}^{ab}} \right]. \tag{2.36}$$

and the tilt angle t of the chains with respect to the surface normal can then be calculated from each of the equations 2.32a-2.32c:

$$t = \arctan \left[\frac{q_z^i}{q_{xy}^i \cdot \cos \Psi_i^*} \right], \; i = a, b, ab. \tag{2.37}$$

The general approach to interpret a GIXD diffraction pattern of an alkane chain monolayer is therefore to first determine the position of the Bragg peaks with respect to the in- and out-of-plane wavevector transfers q_{xy} and q_z. Afterwards, the two-dimensional unit cell can be determined from the in-plane measurements. This information can then be used for the determination of the chain alignment within the unit cell, by solving the equation

system for q_{xy} and q_z as described above. The last step is to cross-check the proposed structure by modeling the measured Bragg rods using the calculated tilt angle and tilt directions.

The angle between the tilt direction and the lattice vectors in real space are linked to the ones in reciprocal space by

$$\Psi_b = \Psi_a^* - \pi/2 \tag{2.38}$$

$$\Psi_a = \Psi_b + \gamma = \Psi_a^* - \pi/2 + \gamma \tag{2.39}$$

$$\Psi_{ab} = \Psi_b + \alpha_D = \Psi_a - \beta_D. \tag{2.40}$$

As the alignment of the chains is fully determined by one angle Ψ^* of the tilt direction and the geometry of the unit cell, the corresponding angles for additional reflections follow from pure geometric considerations.

2.1.5 Quantitative Analysis of Bragg Peak Intensities

The following section is devoted to the quantitative analysis of the Bragg peaks, that is the modelling of the measured peak intensities by structure factor calculations. The goal of this analysis is to go beyond the limitations of the cylinder model and to obtain information about the alignment of the alkane chains within the two-dimensional unit cell on sub-molecular length scales. The first part of this section describes how to extract Bragg peak intensities from a measured diffraction pattern while the second part deals with the modelling of these intensities.

Extracting peak intensities from a diffraction pattern

The general approach of treating a diffraction pattern consists of data smoothing, background subtraction, peak localisation and lineshape fitting in order to obtain the integrated intensity of a Bragg reflection. Counting of photons in a detector is a random process. The associated counting statistical process as well as the (white) electronic noise of the amplifier are the origin of random fluctuations in the raw data. Depending upon the amplitude of the random fluctuations, the original signal disappears in the collected data at a noise amplitude of about 50% of the maximum signal intensity (see figure 2.9). In contrast, the mean value of the fluctuation contributes to the data as a constant, but does not degrade the signal to noise ratio. The goal of data smoothing is therefore to remove as much as possible the statistical fluctuations from the data. By reducing the fluctuations, a better definition of the peak shape is achievable as well as a smoother background which could more easily be subtracted. Criteria that have to be considered upon applying a smooth to the raw data are the sharpness and uniqueness of the individual diffraction peaks as well as the number of points associated with each of them. The most commonly applied filter is the so called "Savitzky-Golay" filter: a polynomial of a certain degree is fitted to a span of data points and the point in the middle of the span is replaced by the interpolation value. As the span moves along the recorded data, the filter gets applied to all data points. Although this method is less destructive to peak features like other adjacent averaging techniques, nevertheless attention must be drawn to a possible broadening of peaks which might result in overlapping reflection becoming

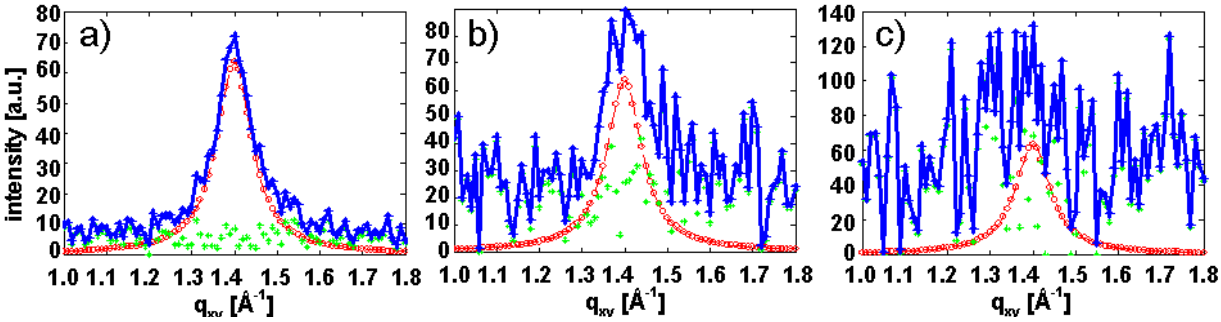

Figure 2.9: Influence of white noise on the measured diffraction signal for different values of the variance of the white noise (open circles: intrinsic diffraction signal, stars: white noise, crosses: measured signal corresponding to the superposition of the intrinsic signal and the white noise). a) variance equal to 5% of the intrinsic peak maximum; b) variance equal to 20%; c) variance equal to 50%

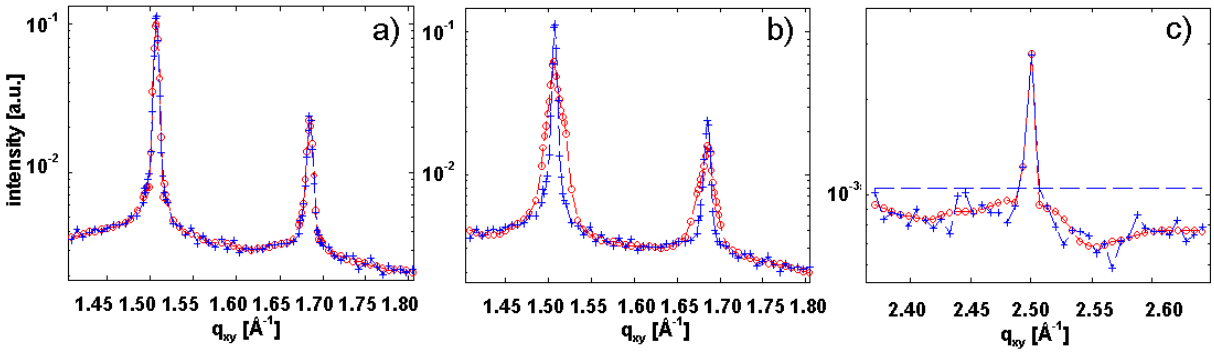

Figure 2.10: a) smoothing of raw data using a Savitzky-Golay filter of second order and a span of seven data points; b) same as a) but with a span of 15 data points: peak broadening and loss of peak intensity are evident; c) smoothing of background points below a threshold level (indicated by the dashed horizontal line)

indistinguishable. Another inherent problem is the suppression of peak intensity by interpolating a polynomial of low order over a large span. A favorable situation for the smoothing technique is given by five up to 15 individual data points above the FWHM of the peak. However, for diffraction peaks of organic monolayers at large in-plane wavevector transfers this condition is not easy to meet due to the very low scattering intensity, requiring long acquisition times per data point. The corresponding high radiation dose might in return cause almost uncorrectable problems with sample degradation. Figure 2.10 a) and b) show two examples for the described situations: both scattering pattern have been smoothed using a Savitzky-Golay filter with a second order polynom and spans of five and 15 data points, respectively. While in panel a) due to the sufficient number of data points on the peaks the widths and peak intensities remain unchanged, the broadening of the peak and the loss in peak intensity is evident in panel b). In the latter case it can be interesting to smooth only the well resolved tails of the reflection and the

background in order to facilitate its subtraction in a later step of the data treatment. Therefore, the data points of the diffraction pattern representing an intensity larger than a threshold value $\sigma_{th} \cdot \langle I \rangle_{pattern}$ are not smoothed. The result is shown in panel c) of figure 2.10: while the few points of the peak remain unchanged, the statistical fluctuations in the tail part of the diffraction pattern are clearly reduced.

After smoothing, the next step in the data pre-treatment is the subtraction of an (estimated) background to linearise the diffraction pattern. For the GIXD geometry a separate measurement of the background is not practical due to the very limited penetration depth of the X-rays into the sample. Therefore, subtracting for instance a scattering curve from a pure subphase from a scattering curve of the subphase covered by a monolayer is not possible. In this case the subtraction of an estimated background is the only possibility to obtain the true Bragg peak intensities of the monolayer. The term 'background' denotes in this context all scattering contributions other than the diffraction peaks originating from the monolayer. Main origins of background scattering are air scattering which is most important at small scattering angles, diffuse and amorphous scattering of the subphase. The latter contribution arises for a liquid subphase, like for instance water, from the next nearest neighbour distance of the molecules which constitute the liquid. In the case of a water subhase this broad and low intensity feature is referred to as the 'water peak'[36]. The different scattering contributions are shown schematically in figure 2.11. A commonly used method for background subtraction is the subtraction of a polynomial fit to data points that have been identified as belonging to the background rather than to a diffraction peak. A search algorithm for these 'background points' works as follows [110]: the diffraction pattern is divided into intervals Δq_{xy} and the intensity minimum $I_i^{\min}$ in each interval i is determined. If $I_{i+1}^{\min} > I_i^{\min}$, then $I_{i+1}^{\min}$ is supposed to belong to a diffraction peak and is hence suppressed from the list of minima. The remaining points are fitted to a polynomial of the form $\sum_{i=0}^{n} a_i x^i$ which describes the background and can be subtracted from the data.

The most reliable method to obtain peak intensities from a diffraction pattern is a whole pattern fit rather than the individual fitting of diffraction peaks. While the latter method provides good results for well separated diffraction peaks, it has conceptional problems with partially overlapping peaks. The goal of a whole pattern fit is the iterative minimization of the expression [108]:

$$R = \sum_{q_{xy}} \left\{ I_{obs}(q_{xy}) - \sum_{G_{hk}} [I(G_{hk}) P_0(q_{xy})] - \sum_{i=0}^{n} a_i \cdot q_{xy}^i \right\}^2 . \tag{2.41}$$

Here I_{obs} describes the observed intensity as a function of the in-plane wavevector transfer q_{xy}, $I(G_{hk})$ is the intensity belonging to the reciprocal lattice vector G_{hk}, which is smeared out in reciprocal space by the peak shape function P_0. The last term describes a polynomial approximation of the background as discussed above. The peak shape function is given as the convolution of the resolution function of the instrument and the intrinsic profile of the diffraction peak. For quasi two-dimensional powders consisting of organic monolayers it has been theoretically shown that the expected intrinsic peak profile is a Lorentzian [46]. Assuming the instrumental resolution function to be a Gaussian, the cor-

responding convolution of resolution and intrinsic peak function leads to a Voigt function, which can be represented as

$$V_o(q_{xy}) = A\frac{2\ln 2}{\pi^{3/2}}\frac{w_L}{w_G^2}\int_{-\infty}^{\infty} dt \frac{e^{-t^2}}{\left(\sqrt{\ln 2}\frac{w_L}{w_G}\right)^2 + \left(\sqrt{4\ln 2}\frac{q_{xy}-G_{hk}}{w_G} - t\right)^2}. \tag{2.42}$$

Despite its rather numerical realisation, the advantage of the use of the Voigt function over approximations like e.g. the PearsonVII function is given by the direct parametrisation in terms of the full-width-half-max (FWHM) of the original Gaussian (w_G) and the FWHM of the original Lorentzian (w_L). Thus, if for instance the resolution function of the instrument and hence w_G can be determined independently, the parameter w_G can be fixed in the pattern fit. In order to obtain the integrated intensity, the fit of the diffraction peak with a peak shape function according to equation 2.42 has to be integrated along q_{xy}. It is noteworthy that the Voigt function, like the Lorentzian, exhibits quite extended 'tails' which contain a non-negligible part of the diffraction intensity. Figure 2.12 a) shows a peak function with the intensity axis set to log-scale making the tails of the peak clearly visible. It is evident that integration over a small region, e.g. one FWHM around the center of the peak, would lead to a severe underestimation of the integrated intensity. Figure 2.12 b) displays the ratio of the integrated intensity and the total intensity of the peak shown in panel a) as a function of the integration range in units of FWHMs. To collect about 90% of the peak intensity, it is therefore necessary to integrate over a region of about five times the FWHM around the center of the peak as sketched in panel a).

Modeling of diffraction peak intensities

In the following, the factors which determine the intensity of a diffraction peak will be introduced. In order to model the observed diffraction peak intensities, these factors need to be quantified by analytic functions where the number of free (i.e. a priori not calculable) parameters shall be cut down to a minimum. As GIXD experiments are generally not measuring absolute scattering intensities, relative intensities will be used instead, that is the normalisation of the intensities where usually the most intense one is chosen as a reference.

Structure sensitive factors that effect the relative peak intensities in X-ray powder diffraction are [51] the atomic scattering factor, the structure factor, the polarization factor, the Lorentz factor, the multiplicity of a reflection and the temperature dependent Debye-Waller factor. In contrast, instrument sensitive factors like the detector efficiency or deadtime do in general not change during one set of measurements and do hence not influence the relative peak intensities. Similar, sample sensitive effects like absorption, crystallite size, stress and strain as well as the degree of crystallinity can in general also be assumed to be constant for one set of measurements under constant experimental conditions like e.g. the sample temperature.

The goal of structure factor calculations in standard crystallography is the refinement of the atomic positions Δx, Δy and Δz of the atoms in the unit cells, eventually even taking independent anisotropic atomic displacements Δu_x, Δu_y, Δu_z for the individual atoms into account. However, for the modeling of diffraction peak intensities of organic

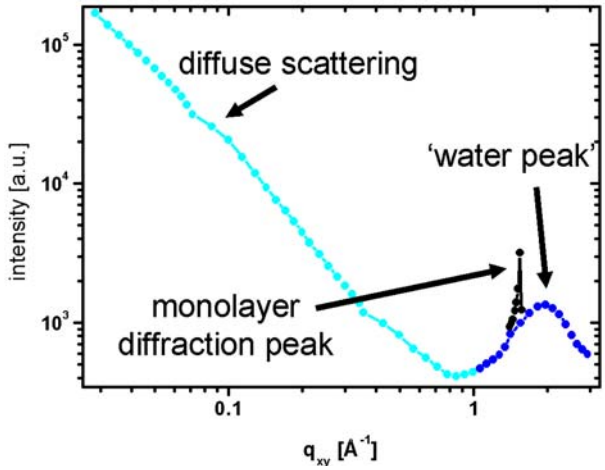

Figure 2.11: Schematic of a GIXD diffraction pattern for an organic monolayer on a liquid subphase. The pattern consists of diffuse scattering, amorphous scattering from the subphase (the so-called 'water peak') and the monolayer diffration peak.

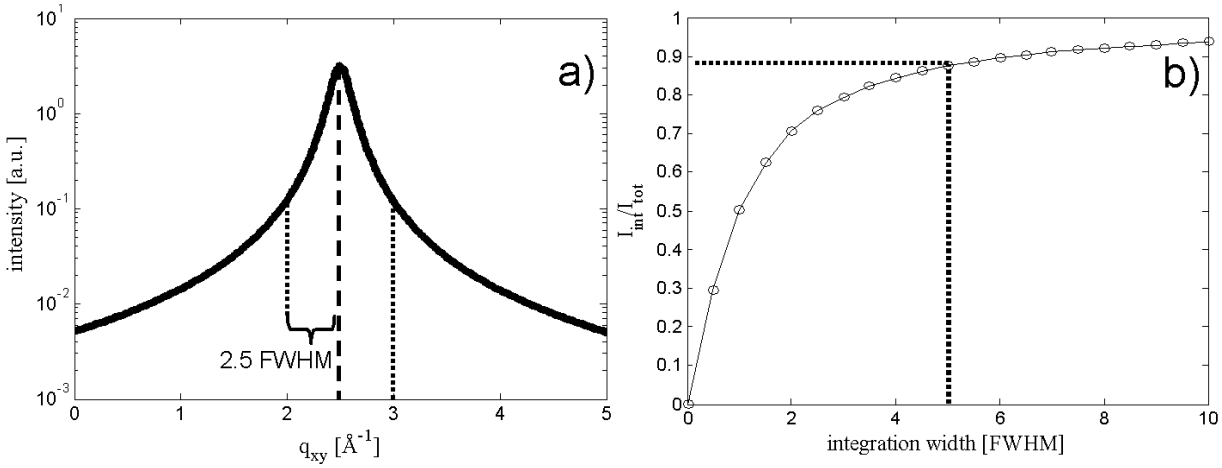

Figure 2.12: Integration of a peak function; a) an integration range of five times the FWHM around the center is indicated; b) integrated intensity over total intensity of the peak as a function of the integration width in units of FWHMs

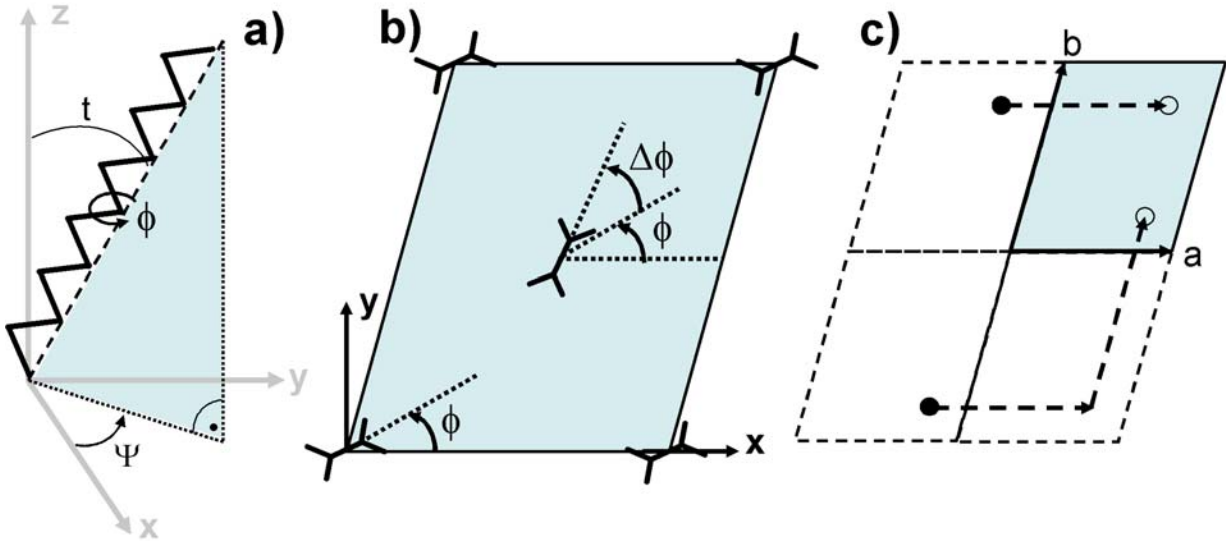

Figure 2.13: a) definition of the twist angle ϕ of an alkane chain around its length axis, $\phi = 0$ corresponds to an alignment of the C-C plane parallel to the hatched plane defined by tilt angle t and tilt direction Ψ; b) definition of the chains twist angle ϕ and phase $\Delta\phi$ for a unit cell containing two alkane chains, note that an upright configuration of the chains is assumed i.e. $\phi = 0$ corresponds to an alignment of the C-C plane parallel to the x-direction; c) sketch of the appliance of periodic boundary conditions: for certain orientations of the alkane chains some atomic coordinates (black dots) might exceed the dimensions of the two-dimensional unit cell (hatched), in that case the appropriate atomic positions (open circles) are obtained after a lattice vector translations (dashed arrows).

monolayers on liquid substrates this approach is rendered impossible by the very limited number of observable reflections. Depending on the lattice structure, usually only the one to three reflections of lowest order can be detected. Even taking only the carbon atoms of e.g. a unit cell containing one C20 alkane chain into account, the refinement of the atomic positions leads to about 60 parameters to be refined with less than ten independent diffraction peak intensities. As this approach would be clearly unpractical, in the following a few assumptions will be made to drastically reduce the number of free parameters while still obtaining more information than within the limitations of the cylinder model. By assuming the alkane chain to be in an all-trans configuration with standard values for the CH2-CH2 bond length (1.54Å) and the bond angle (110°), the positions of the individual atoms are no longer independent. Moreover, with the tilt angle and the tilt direction of the chain known from the position of the Bragg reflections with respect to q_{xy} and q_z, all positions of the atoms of the chain within the unit cell are determined by the twist angle ϕ of the chain around its length axis (see figure 2.13 a)). In agreement with [45] $\phi = 0$ corresponds to the case where the C-C plane of the alkane chain coincides with the plane formed by the molecular length axis and its projection onto the surface (xy-plane). For a non-primitive unit cell, like for instance a centred rectangular one, which contains more than one chain, the twist angles are not necessarily identical. As depicted in figure 2.13 b) for the case of two chains per unit cell this can be described by a shift

$\Delta\phi$ for the twist angle of the second chain with respect to the twist angle of the first one. Assuming an isotropic Debye-Waller factor with only one displacement parameter u (see equation (2.51)), the number of free parameters in the structure factor calculation has been cut down to just one twist angle per alkane chain in the unit cell and one displacement parameter. Thus for a rectangular unit cell the structure factor calculation requires three independent and a priori unknown parameters. The above proposed model tries to compromise between the number of experimentally observable diffraction peak intensities and the number of parameters necessary to model them. The drawback of the model is the loss of independent information about the position of individual atoms as this information is implied by the model assumption. Nevertheless, going beyond the cylinder model, the orientation of the C-C planes of the alkane chains can be revealed. This information plays in particular an important role for the unambiguous detection of the herringbone ordering.

In order to perform the structure factor calculation, first the position of the atoms in the unit cell have to be calculated according to the tilt angle t, the tilt direction Ψ and the assumption of an all-trans configuration. In the following, only the carbon atoms of the alkane chain will be considered while the weakly scattering hydrogens will be neglected for the sake of simplicity. If $\mathbf{c}_i$ denotes the coordinates of the i^{th} carbon atom of the C-C plane which is lying in the zx-plane of the coordinate system, its components are given by

$$\mathbf{c}_i = \begin{pmatrix} (1+(-1)^i)/2 \times 1.54\mathring{A} \times \cos 55^\circ \\ 0 \\ i \times 1.54\mathring{A} \times \sin 55^\circ \end{pmatrix}. \tag{2.43}$$

The adjustment of the tilt angle of the chain relative to the surface normal corresponds to a rotation in the zx-plane around the y-axis. The corresponding rotation matrix is given by

$$\overleftrightarrow{\mathbf{M}}_t = \begin{pmatrix} \cos t & 0 & \sin t \\ 0 & 1 & 1 \\ -\sin t & 0 & \cos t \end{pmatrix}. \tag{2.44}$$

In the same way the tilt direction can be taken into account by a rotation in the yx-plane around the z-axis. The rotation matrix for this operation is

$$\overleftrightarrow{\mathbf{M}}_\Psi = \begin{pmatrix} \cos\Psi & -\sin\Psi & 0 \\ \sin\Psi & \cos\Psi & 0 \\ 0 & 0 & 1 \end{pmatrix}. \tag{2.45}$$

For $t = \Psi = 0$ (thus for untilted chains) the axis $\mathbf{s}$ of rotation of the twist angle ϕ is the z-axis, for tilted chains the rotation axis can be calculated as

$$\mathbf{s} = \begin{pmatrix} s_1 \\ s_2 \\ s_3 \end{pmatrix} = \overleftrightarrow{\mathbf{M}}_\Psi \cdot \left(\overleftrightarrow{\mathbf{M}}_t \cdot \mathbf{e}_z \right) \tag{2.46}$$

with $\mathbf{e}_z$ being a unit vector in z-direction. With the rotation axis given by equation (2.46), the rotation of ϕ around that axis is introduced by the rotation matrix

(2.47)
$$\overleftrightarrow{\mathbf{M}_\phi} = \left[\cos\phi \begin{pmatrix} 1 & 0 & 0 \\ 0 & 1 & 0 \\ 0 & 0 & 1 \end{pmatrix} + (1-\cos\phi) \begin{pmatrix} s_1^2 & s_1 s_2 & s_1 s_3 \\ s_2 s_1 & s_2^2 & s_2 s_3 \\ s_3 s_1 & s_3 s_2 & s_3^2 \end{pmatrix} + \sin\phi \begin{pmatrix} 0 & -s_3 & s_2 \\ s_3 & 0 & -s_1 \\ -s_2 & s_1 & 0 \end{pmatrix}\right].$$

The position $\mathbf{c}_i'$ of the i$^{\text{th}}$ carbon atom after the adjustment of tilt angle, tilt direction and twist angle can then be calculated as

(2.48)
$$\mathbf{c}_i' = \overleftrightarrow{\mathbf{M}_\phi} \cdot \left(\overleftrightarrow{\mathbf{M}_\Psi} \cdot \left(\overleftrightarrow{\mathbf{M}_t} \cdot \mathbf{c}_i\right)\right).$$

With a second chain in the unit cell, the coordinates of its atoms are calculated by replacing the twist angle ϕ in equation (2.47) by $\phi + \Delta\phi$. As the structure factor given by equation (2.8) already contains the lattice sum, the atomic positions need to be expressed in lattice vector units. By defining the lattice vector $\mathbf{a}$ along the x-axis, the y-components of the $\mathbf{c}_i'$'s need to be normalised by the projection $b\sin\gamma_D$ of the lattice vector $\mathbf{b}$ onto the y-axis. After placing the chains in the unit cell, due to twist and tilt some of the atomic positions might exceed the dimensions of the unit cell. As a consequence of the two-dimensional periodic lattice in the xy-plane, periodic boundary conditions have to be applied, ensuring that the normalised coordinates are in the range between zero and one and hence within the 2d unit cell. If that condition is not fulfilled, the atomic positions need to be moved by one lattice vector in the appropriate direction as sketched in figure 2.13 c). With this final atomic coordinates the structure factor can be calculated according to equation (2.21). Thereby the q-dependency of the atomic form factor f^0 has to be taken into account. The atomic form factor can be calculated according to the Cromer-Mann formula [21], an analytic approximation for the atomic form factors calculated in the Hartree-Fock model from numerical atomic wavefunctions:

(2.49)
$$f^0(q_{xy}) = -r_0 \left(\sum_{i=1}^{4} a_i e^{-b_i (q_{xy}/4\pi)^2} + c\right).$$

For a carbon atom the parameters in formula (2.49) are given in table (2.1) [21]. The q_{xy}

a_1	a_2	a_3	a_4	b_1	b_2	b_3	b_4	c
1.930	12.719	1.876	28.650	1.574	0.596	0.371	65.034	0.246

Table 2.1: Cromer Mann coefficients for carbon

dependency of the atomic form factor is depicted in figure 2.14 a) in units of the Thompson scattering length r_0. The scattering ability is maximized for forward scattering ($q_{xy} = 0$) and is decreased for larger scattering angles or larger wavevector transfers q_{xy}, respectively.

The intensity $I(h,k)$ of a reflection in the GIXD geometry at an in-plane wavevector transfer $q_{xy} = G_{hk}$ can be written as

(2.50)
$$I(h,k) \propto L_{powder}(h,k) \times P(h,k) \times F_A(h,k) \times \int_0^{Q_z^{cut-off}} dq_z \left\{ |F(h,k,q_z)|^2 \times D(h,k,q_z) \times |V(q_z)|^2 \right\},$$

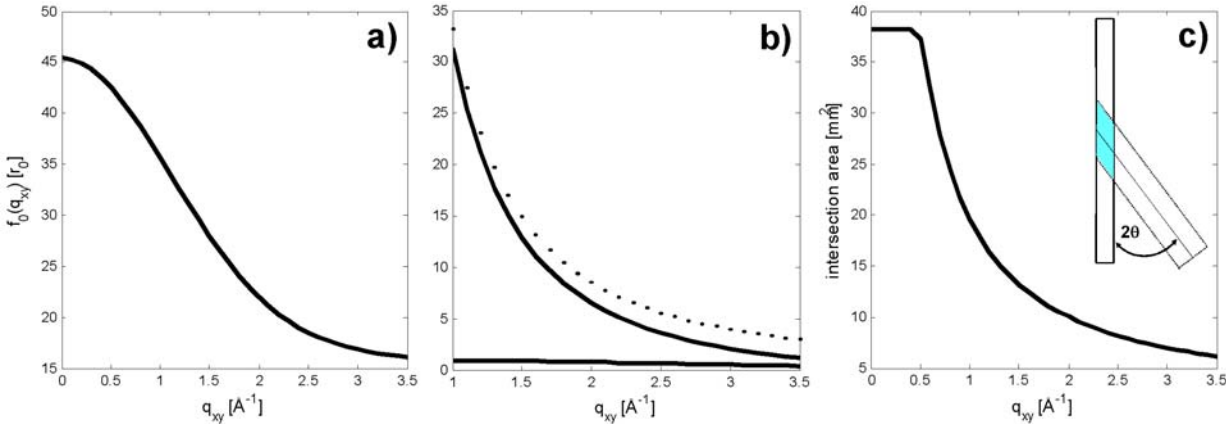

Figure 2.14: a) q_{xy}-dependence of the atomic form factor of carbon according to the Cromer-Mann formula; b) q_{xy}-dependence of the Lorentz-factor (dotted line) for 2d powder diffraction (eq. 2.53), the polarization factor (almost horizontal, according to eq. 2.52) and the product of Lorentz and polarization factor (solid line); c) intersection area of the beam footprint on the sample surface and the detector acceptance for typical experimental values as a function of q_{xy}, inset: sketch of the beam footprint on the sample (solid line), detector acceptance (dashed line) and the intersection area (hatched)

where the structure factor $F(h,k,q_z)$ can be calculated according to equations (2.21) and (2.49), while the transmission function $V(q_z)$ is given by equation (2.23). $D(h,k,q_z)$ denotes the Debye-Waller factor while $L_{powder}(h,k)$ and $P(h,k)$ are the Lorentz and the polarization factor, respectively. The integration of the Bragg rod intensity along q_z up to a certain cut-off limit $Q_z^{cut-off}$ (typically the largest q_z up to which the Bragg rod can be resolved) leads to the in-plane Bragg peaks. The factor $F_A(h,k)$ accounts for the effect that the part of the illuminated footprint on the sample surface which is 'seen' by the detector depends on the scattering angle. This is illustrated in figure 2.14 together with the corresponding detection area as a function of the in-plane wavevector q_{xy} for typical values of the footprint size and the horizontal detector acceptance. The plateau of the curve at small q_{xy} originates from the detector acceptance being typically larger than the width of the beam footprint on the sample. The Debye-Waller factor D describes the diminishing of the diffraction peak intensities due to thermally excited vibrations of the scatterers around their equilibrium position. Expanding the strictly two-dimensional approach [22] to the more realistic case in which the monolayer, despite its lack of periodicity in the z-direction, can nevertheless vibrate normal to its surface, leads to an expression like $D(h,k,q_z) = e^{-2\pi(h^2a^{*2}u_x^2+k^2b^{*2}u_y^2)}e^{-q_z^2u_z^2}$. Here the u_i are the average variances of the scatterer from its equilibrium position for the three spacial directions. However, for upright alkane chains the maximum of the molecular form factor is at $q_z = 0$ and the effect of the second exponential function is marginal and might hence be neglected. Moreover, for a very limited number of observed reflections the information about the average variances for the individual directions is not extractable to a satisfactory level of confidence. In this case the Debye-Waller factor might be assumed to be isotropic with

$u_x = u_y = u$ and may be written in the form

$$D(h,k) = e^{-G_{hk}^2 \cdot u^2}. \tag{2.51}$$

While the polarization factor P for a synchrotron source is unity in the vertical scattering plane and hence not altering the scattering intensity as a function of the scattering angle, for the horizontal geometry the polarisation factor is given by [7]:

$$P(h,k) = \cos^2 2\theta = \cos^2\left(2\arcsin\frac{\lambda G_{hk}}{4\pi}\right). \tag{2.52}$$

It is evident from equation (2.52) that for scattering angles close to $2\theta = 90°$ the observed diffraction intensity is completly supressed by the polarisation factor, independent of the value of the structure factor. The Lorentz factor for a two-dimensional powder can be written in the form

$$L_{powder}(h,k) = \frac{1}{\sin\theta \sin 2\theta} = \frac{4\pi}{\lambda G_{hk} \sin\left(2\arcsin\frac{\lambda G_{hk}}{4\pi}\right)}. \tag{2.53}$$

The influence of polarization and Lorentz factor on the diffraction peak intensity as a function of the in-plane wavevector transfer is depicted in figure 2.14 b).

In order to quantify the agreement between a measured diffraction pattern and the one calculated according to a suggested structure, a measure needs to be defined. A common definition used in crystallography is the so-called R-factor. The original definition by Rietveld [95] generalised for the use of relative intensities instead of structure factor amplitudes reads

$$R \equiv \frac{\sum_{[h,k]} \left| I_{obs}^{rel}([h,k]) - I_{calc}^{rel}([h,k]) \right|}{\sum_{[h,k]} I_{obs}^{rel}([h,k])}. \tag{2.54}$$

Here I_{obs}^{rel} and I_{calc}^{rel} denote the relative intensities of the observed and calculated reflections, respectively, while the sum $\sum_{[h,k]}$ is extended over distinguishable sets of [h,k], i.e. h and k which lead to non-degenerated diffraction peaks. Similar, the R-factor for an individual (possibly degenerated) reflection can be defined as

$$R^{ind} \equiv \frac{\left| I_{obs}^{rel}([h,k]) - I_{calc}^{rel}([h,k]) \right|}{I_{obs}^{rel}([h,k])}. \tag{2.55}$$

A problem for the standard definition of the R-factor according to equation (2.54) is the occurrence of reflections with strongly differing intensities. If one reflection is very intense compared to the others, the total R-factor is approximately equal to the individual R-factor of that reflection as defined by equation (2.55). Thus a structure refinement that seeks to minimise the R-factor would almost exclusively refine the intensity of the outmost strongest reflection. In such a case and in order to weight the residuals of the individual reflections more equally, a total R-factor R_Σ can be defined as the sum of the individual R-factors R^{ind} : $R_\Sigma = \sum_{[h,k]} R^{ind}([h,k])$. By this definition equal weights are assigned to the refinement of all reflections.

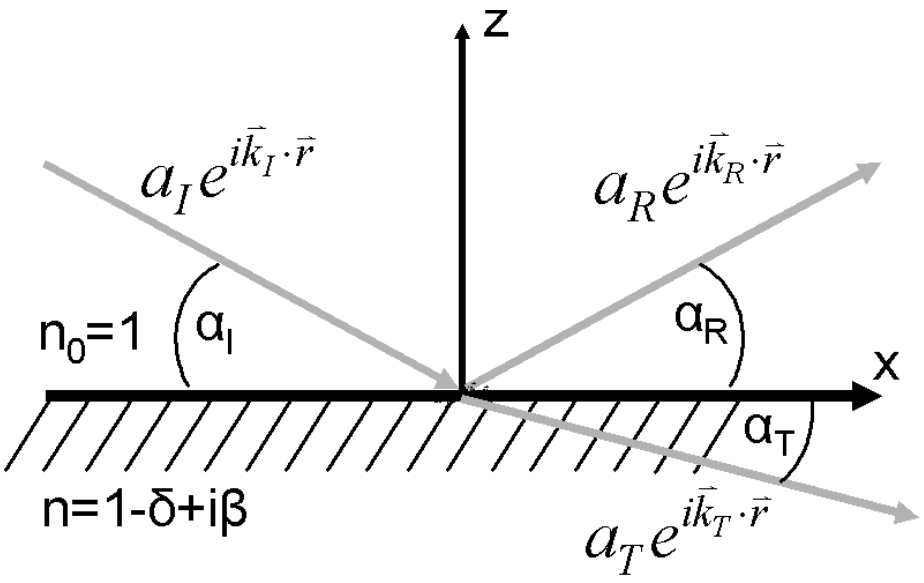

Figure 2.15: Illustration of the reflection of X-rays at a surface: the incoming wave with amplitude a_I and wavevector k_I hits the surface under an incident angle α_I and splits into a reflected wave (index R) and a transmitted wave (index T)

2.2 Gracing Incidence X-ray Scattering out of the Specular Plane (GIXOS)

X-ray specular reflectivity (XSR) is commonly used to investigate the electron density profile of a sample normal to the surface [17, 117]. The obtained structural information include the thickness of layers in a layered system as well as the associated electron or scattering length densities and interface roughnesses. For thin films on liquid surfaces this information can also be provided by the recently developed technique of grazing incidence X-ray scattering out of the specular plane (GIXOS) [123, 126]. Due to the short aquisition times required, GIXOS was applied successfully to monitor time resolved processes [124] or to investigate radiation dose sensitive samples [80, 81]. As part of the theoretical background for XSR and GIXOS are the same, in the following the basis of specular reflectivity will be presented, before adapting the results to the GIXOS technique, which is based on diffuse instead of specular scattering.

The description of the reflection of X-rays at an interface is similar to the description of the reflection and refraction for visible light. Figure 2.15 depicts an electromagnetic wave with amplitude a_I and wavevector k_I impinging onto a surface under an angle α_I. At the interface the wave is split into a transmitted wave with amplitude a_T and wavevector k_T and a reflected wave with amplitude a_R and wavevector k_R. Continuity conditions for the electromagnetic field at the interface lead to the well known Fresnel equations for the

complex reflection and transmission coefficients r and t:

$$r = \frac{a_R}{a_I} = \frac{k_I^z - k_T^z}{k_I^z + k_T^z} \tag{2.56a}$$

$$t = \frac{a_T}{a_I} = \frac{2k_I^z}{k_I^z + k_T^z}. \tag{2.56b}$$

The z component of the wavevector transfer k_T^z is linked to the angle α_T by $k_T^z = n \cdot k \cdot \sin\alpha_T$, where n denotes the refractive index of the medium. The angle α_T between the transmitted wave and the surface follows directly from the incident angle α_I by Snell's law: $\cos\alpha_I = n\cos\alpha_T$. The physical properties of the material enter the formalism via the refractive index n, which can in the case of X-rays and far away from absorption edges be written in the form

$$n = 1 - \delta + i\beta. \tag{2.57}$$

Here δ denotes the dispersion given by $\delta = \frac{2\pi}{k^2}\rho_{av}$ with the average scattering length density ρ_{av}. The absorption β is given by $\beta = \frac{\mu}{2k}$ with the absorption coefficient μ. As both δ and β are smaller than unity, in the X-ray regime the index of refraction is smaller than unity, leading to the phenomenon of total external reflection for incident angles smaller than a certain critical angle α_c. The intensity -and hence the measurable quantity- of the reflected wave is given by the so-called Fresnel reflectivity as the absolute square of the amplitude reflectivity given by equation 2.56a: $R_F = |r|^2$. The Fresnel reflectivity is confined in the specular plane defined by the wavevector of the incident wave and the surface normal and at an exit angle α_R which is equal to the incident angle α_I. While the Fresnel reflectivity holds for a single flat and sharp interface, in the case of a graded interface the altered reflectivity can within the frame of the kinematic (first Born) approximation be written as [13, 50]:

$$R(q_z) = R_F(q_z)\left|\int_0^\infty \left(\frac{d\rho(z)}{dz}\right) e^{iq_z\cdot z} dz\right|^2 = R_F(q_z)S(q_z), \tag{2.58}$$

where $\rho(z)$ describes the normalized scattering length density profile of the interface and S is the accompanied structure factor. As evident from equation (2.58), the observed reflectivity is proportional to the absolute square of the Fourier transform of the gradient of the electron density. Consequently, a contrast in the electron density is needed to make an interface visible in X-ray reflectivity. It can be shown that in the case of a rough surface the reflectivity is altered by a Debye-Waller-like roughness term:

$$R(q_z) = R_F(q_z)e^{-\sigma^2 q_z^2}, \tag{2.59}$$

with the rms roughness σ of the interface[2]. A commonly used algorithm for a system with a free number of interfaces is the Parratt algorithm [84]. It is also noteworthy that the Paratt algorithm serves as an exact solution of the reflectivity from a multilayer system,

[2]In this section the surface tension is denoted with γ to avoid confusion with the rms roughness σ.

while the kinematic approximation provides only satisfactory results for $q_z >> q_c$. The Parratt algorithm considers for the scattering from several sharp interfaces a multilayer stack of N interfaces located at positions $z_j \leq 0$. The vacuum (air) is conventionally the first 'layer' with the interface located at $z_1 = 0$, while the last interface is located at $z_N < 0$. Each layer exhibits a thickness $d_j = z_{j-1} - z_j$ and a refractive index $n_j = 1 - \delta_j + i\beta_j$. T_j and $k_{I,j}$ are the amplitude and the wavevector of the transmitted wave and $k_{R,j}$ and R_j are the corresponding values for the reflected wave. If X_{j+1} denotes the ratio of R_{j+1} and T_{j+1} in the layer $j+1$ then X_j for the layer above may be calculated via [84]:

$$X_j = \frac{R_j}{T_j} = e^{-2ik_j^z \cdot z_j} \frac{r_{j,j+1} + X_{j+1} \exp(2ik_j^z \cdot z_j)}{1 + r_{j,j+1} X_{j+1} \exp(2ik_j^z \cdot z_j)}, \tag{2.60}$$

with the Fresnel coefficient $r_{j,j+1}$ of interface j. With the assumption of a semi-infinite substrate (which is almost always fulfilled to a good approximation due to the limited penetration depth of the X-rays) there is consequently no reflection from the substrate, i.e. R_{N+1} and X_{N+1} may be set to zero as the start of the recursion. The specular reflected intensity is then obtained after N iterations as $R_P(q_z) = |R_1|^2$. In order to account for the interface roughness, the Fresnel coefficients need to be modified [116]. Assuming a Gaussian probability density for the surface roughness, the refractive index profile of the multilayer stack is given by [116]:

$$n_j(z) = \frac{n_j + n_{j+1}}{2} - \frac{n_j - n_{j+1}}{2} \operatorname{erf}\left[\frac{z - z_j}{\sqrt{2}\sigma_j}\right]. \tag{2.61}$$

In the case of a rough surface, the lateral fluctuations give rise to diffuse scattering, which provides information about lateral inhomogeneities of surfaces or interfaces. The first step in the theoretical treatment of the diffuse scattering is the description of the (static) surface by means of statistics via correlation functions. The general definition of the height-height correlation function $C(\mathbf{R})$ of a surface is given by:

$$C(\mathbf{R}) = \frac{1}{A} \int_A d\mathbf{r}_\parallel z(\mathbf{r}_\parallel) \cdot z(\mathbf{r}_\parallel + \mathbf{R}) = \left\langle z(\mathbf{r}_\parallel) \cdot z(\mathbf{r}_\parallel + \mathbf{R}) \right\rangle_{\mathbf{r}_\parallel}. \tag{2.62}$$

Here A denotes a surface area sufficiently large to apply statistical methods, $\mathbf{R}$ and $\mathbf{r}_\parallel$ are lateral in-plane vectors. $z(\mathbf{r}_\parallel)$ denotes the contour function that gives the surface height at each in-plane vector $\mathbf{r}_\parallel$, where the average interface is defined by $\left\langle z(\mathbf{r}_\parallel) \right\rangle_A = 0$. The rms roughness σ of the interface is given by:

$$\sigma^2 = C(\mathbf{0}) = \left\langle z^2(\mathbf{r}_\parallel) \right\rangle_{\mathbf{r}_\parallel}. \tag{2.63}$$

It can be shown that in general the inequality $C(\mathbf{R}) \leq C(\mathbf{0}) = \sigma^2$ holds. For a statistically rough surface the height-height correlation function $C(\mathbf{R})$ decreases in a monotonic fashion until all correlations vanish in the limit $R \to \infty$ (see figure 2.16). Many isotropic solid surfaces can be described by a correlation function of the form [116, 104]:

$$C(R) = \sigma^2 \exp\left\{-\left(R/\xi\right)^{2h}\right\}, \tag{2.64}$$

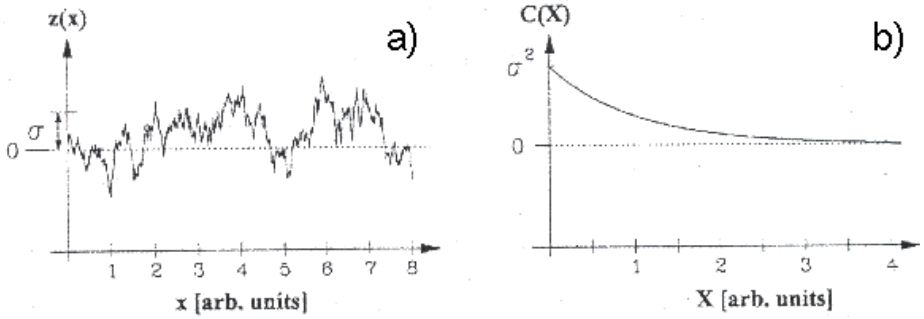

Figure 2.16: a) one dimensional interface contour of a statistical rough surface; b) corresponding height-height correlation function (figure adopted from [116])

where ξ is the lateral length scale on which the surface starts to look rough and $0 \leq h \leq 1$ is the Hurst parameter arising from the assumption of a self-affine surface. Soft matter surfaces like liquid surfaces or thin films like polymers on solid substrates are always decorated with excited waves, called capillary waves, if the effect of surface tension is much larger than the effect of gravity or gravity waves in the inverse case. The height-height correlation function for capillary waves on a liquid or liquid-like surface can be expressed as

$$C(R) = \frac{B}{2} K_0 \left(q_{lc} R\right) \simeq -\frac{B}{2} \left[\ln\left(q_{lc} R/2\right) + \gamma_E\right], \tag{2.65}$$

with $B = k_B T/(\pi\gamma)$ and the lower capillary wavevector cut-off, which is in the order of the gravitational cut-off ($q_{lc} \sim 10^{-8} - 10^{-7} \text{Å}^{-1}$). The logarithmic expression involving Euler's constant γ_E is thereby valid due to the small values of q_{lc}. It is noteworthy that here the determination of the rms roughness σ according to equation (2.63) fails as the expression diverges for $R \to 0$. Instead, σ needs to be determined as an integration over the power spectral density which is Fourier transform of the height-height correlation function. For a layered system, the stochastical description of an interface is in general not complete by a single height-height correlation function. The interface contour of one interface might be at least partially transferred from one layer to the next, which is known as vertically correlated or conformal roughness. The two situations of totally uncorrelated and conformal roughness are depicted in figure 2.17. The stochastical complete description of the interface employs in the case of conformal roughness so-called cross-correlation functions, which give the probability to find two points on the interfaces j and k separated by a lateral vector R having the same position with respect to the mean interface location.

The scattering function $S(\mathbf{q})$ in the kinematical approximation (thus only taking single scattering events into account) is given by the Fourier transform of the scattering length density $\rho(\mathbf{r})$:

$$S(\mathbf{q}) = \iint d\mathbf{r} d\mathbf{r}' \rho(\mathbf{r}) \cdot \rho(\mathbf{r}') e^{i\mathbf{q}(\mathbf{r}-\mathbf{r}')}. \tag{2.66}$$

With the assumption of a density contrast $\Delta\rho$ at the interface whose contour is described by a Gaussian random variable only depending on $X = x - x$' and $Y = y - y$' (with

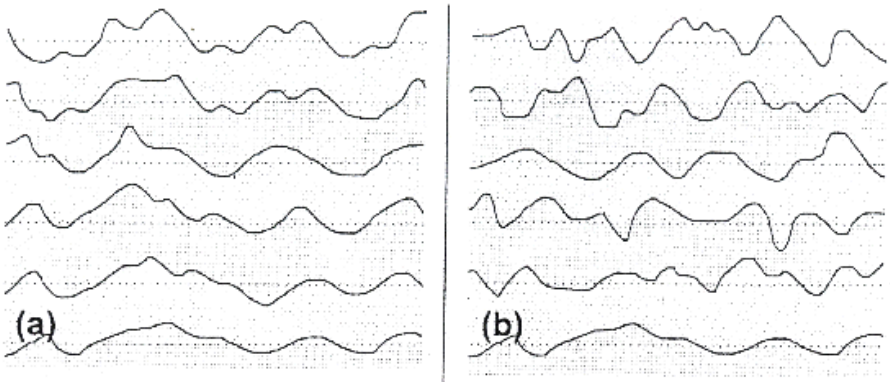

Figure 2.17: a) partially correlated interface roughness; b) uncorrelated roughness (figure adopted from [116])

$R = (X, Y)$), the scattering function can be expressed as

$$S(\mathbf{q}) = \frac{(\Delta\rho)^2}{q_z^2} e^{-q_z^2\sigma^2} \iint dX dY e^{-q_z^2 C(X,Y)} e^{i(q_x X + q_y Y)}. \tag{2.67}$$

For solid surfaces, the correlation function $C(X, Y)$ goes to zero for $X, Y \to \infty$ (compare equation (2.64)), thus the scattering function contains a delta function allowing for the separation of the specular ($q_{xy} = 0$) and diffuse part $S(\mathbf{q}) = S_{spec}(\mathbf{q}) + S_{diff}(\mathbf{q})$, where

$$S_{spec}(\mathbf{q}) = \frac{(\Delta\rho)^2}{q_z^2} e^{-q_z^2\sigma^2} \delta(q_{xy}) \tag{2.68}$$

$$S_{diff}(\mathbf{q}) = \frac{(\Delta\rho)^2}{q_z^2} e^{-q_z^2\sigma^2} \int d\mathbf{R} e^{-q_z^2 C(\mathbf{R})} e^{i(\mathbf{q}_{xy}\mathbf{R})}. \tag{2.69}$$

For soft matter surfaces the separation into a specular and a diffuse part of the scattering function is more subtle, however, the same separation is gained (see [116]). The kinematical theory is not valid in the regions $\alpha_I \approx \alpha_c$ and $\alpha_R \approx \alpha_c$. A theoretical approach to overcome this limitation is the treatment of the diffuse scattering in the framework of the distorted wave Born approximation (DWBA), which is a combination of dynamic and kinematical treatment: The refraction at smooth interfaces is exactly taken into account, while the scattering at lateral inhomogeneities is treated in the kinematic way without considering multiple scattering events. The scattering cross-section is in this framework given by [105]:

$$\left(\frac{d\sigma}{d\Omega}\right)_{\text{diff}} = A_0 \left|T(k_I)\right|^2 \left|T(k_R)\right|^2 S(\mathbf{q}). \tag{2.70}$$

The main difference is that the transmission functions of the incoming and the refracted beams are taken into account. A_0 denotes the illuminated surface area associated with the rough surface. An extension of the result to layer systems was calculated by [47]. It can be shown that by using identical cross-correlation functions and assuming kinematical

scattering the expression for the multilayer system contains exactly the same phase factors as the reflectivity. Therefore, in the case of totally correlated interfaces all oscillations of the specular reflectivity are also found in the diffuse scattering [104]. In the following a simplified approach will be presented and applied to extract information similar about the electron density profile of a layered system from the diffuse scattering.

For the specular reflectivity the scattering function $S(q_z)$ may be expressed according to equation (2.58) as $S(q_z) = R(q_z)/R_F(q_z)$ or by calculating the reflectivity according to the Parratt algorithm as $S(q_z) = R_P(q_z)/R_F(q_z)$. For the case of conformal roughness the information obtained in the diffuse scattering at very small in-plane angles 2θ is similar to the one obtained on the specular path [79]. The scattering function (2.70) might then be replaced by $S(\mathbf{q}) \approx S(q_z) = R_P(q_z)/R_F(q_z)$. The diffuse scattering intensity at small in-plane wavevector transfers is then obtained as

$$I_{\mathrm{diff},q_{xy}\approx 0}(q_z) = I_0 \frac{\Delta\Omega}{A} A_0 \left|T(k_I)\right|^2 \left|V(q_z)\right|^2 \frac{R_P(q_z)}{R_F(q_z)}, \tag{2.71}$$

with the incoming intensity I_0, the area of the beam A and the solid angle $\Delta\Omega$ subtended by the detector at the sample. For fixed incident angle and the use of a position sensitive linear detector for recording the scattered intensity as a function of q_z, the parameters $\Delta\Omega$, A, A_0 and $T(k_I)$ are just constant scaling factors. The transmission function for the refracted beam is given by the Vineyard function $V(q_z)$ (equation 2.23). A main difference between GIXOS and XSR is evident from equation (2.71): the reflectivity as calculated according to the Parratt algorithm is normalised on the Fresnel reflectivity. Consequently, the strong decay of the scattered intensity, which is proportional to q_z^{-4} at large q_z, for the XSR does not apply to the GIXOS technique. For a typical example like a phospholipid monolayer on a water subphase in the case of XSR the specularly reflected intensity decays over eight orders of magnitude in the range $0 \leq q_z \leq 0.5\mathring{A}^{-1}$ while the diffuse scattering as probed by GIXOS is almost constant except for the modulation with the Vineyard transmission function [122]. The following points list some differences between XSR and GIXOS and their adaptation for the investigation of different samples.

- The acquisition times for GIXOS from a liquid surface are in the order of one minute while employing XSR requires about 1.5 hours.
- The GIXOS measurements are carried out in grazing incidence geometry at fixed α_I. Consequently, the beam footprint on the sample surface is constant and no correction as in the case of XSR is required.
- Due to the fixed incident angle and the use of a position sensitive linear detector, for GIXOS no motor movements are needed which could disturb a liquid sample surface.
- For GIXOS the penetration depth into the sample is always the same, but very limited because of the grazing incidence geometry. The applicability of the technique is therefore limited to thin films while with XSR systems up to a total layer thickness of about 100nm can be investigated.

For monolayers of surfactants on a liquid surface the GIXOS technique was applied in this work.

Chapter 3

Static Scattering and Diffraction: Experimental Results

The following chapter is devoted to the presentation of the results of the static scattering and diffraction experiments. First, the sample environment for X-ray studies of surfactant monolayers on liquid subphases under low temperature conditions will be presented. After a short description of the TROIKA II beamline at the ESRF (Grenoble, France), the second part of this chapter is devoted to the presentation of the experimental results from organic monolayers on liquid and solid substrates. An attempt to obtain information beyond the limiting framework of the cylinder model has been undertaken for the highly crystalline phase of eicosanoic acid at low temperature. The deduced characteristic parameters of the different quasi-two-dimensional systems are compared to studies on Langmuir monolayers and to bulk systems such as alkanes and single crystals.

3.1 The Sample Environment

The following part is devoted to the description of a dedicated sample environment that was developed for the investigation of monolayers on liquid subphases at low temperatures by means of X-ray scattering methods. Primed with the knowledge about the freezing points of the different liquids presented in chapter 1, a temperature range between ambient temperature and -60°C is desirable. Because of the phase diagram of a liquid mixture being dependent on the pressure, the experimental conditions should allow for working at ambient atmospheric pressure.

Thermal insulation of the cooled parts of sample environment against the surrounding air atmosphere is necessary to prevent water condensation and freezing. A commonly used set-up for this purpose (see for instance [102]) consists of two chambers, an outer chamber containing an insulation vacuum and an inner chamber containing the sample. For the set-up presented in this work, both outer and inner chamber consists of standard PVC pipes with diameters of 14cm and 10cm, respectively. In the present case, an insulation vacuum accomplished by a membrane pump provides sufficient thermal insulation. A sectional drawing of the sample environment is shown in figure 3.1. The window sizes of the cell are optimized for grazing incidence scattering. Thus, the entrance window

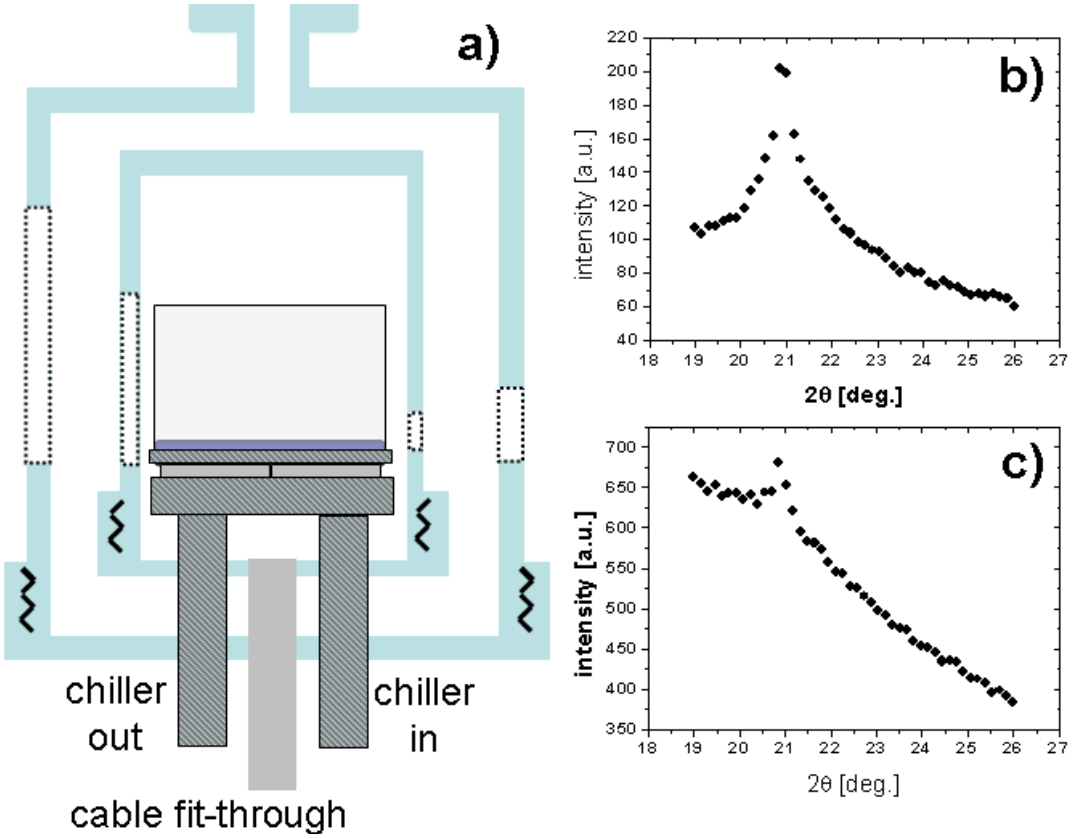

Figure 3.1: a) cross-sectional sketch of the sample cell, consiting of inner and outer chamber, cooling assembly (hatched) and inner aluminum cap (semi-transparent); b) diffraction pattern with helium flow (ambient pressure in the inner cell) and c) with static helium atmosphere (depression in the inner chamber due to helium losses through the Kapton® windows).

for the incident beam is relatively small (1.8×1.8cm^2), while the exit windows covers in-plane angles between -10° and 90° relative to the direct beam. The window height on the exit side allows for out-of plane angles of up to 38°. For an X-ray energy of 8keV this corresponds to an accessible momentum space of -0.7≤ $q_{xy} \leq 5.7\AA^{-1}$ and 0≤ $q_z \leq 2.5\AA^{-1}$. The windows of the inner and outer chamber are sealed with 75μm thick Kapton® foils. The cooling assembly consists of an aluminum trough containing the sample, four peltier elements and a heat exchanger. The heat exchanger cools the hot side of the peltier elements (Supercool, PE-127-10-13), which provide a total cooling power of about 150W at a maximum power input of 240W. The trough sitting on the cold sides of the peltier elements has an outer diameter of 86mm and is fixed by four screws allowing for an easy exchange. Different designs of the trough were realised, adapting to the needs of the different techniques. The standard trough used for GIXD and GIXOS measurements has an inner diameter of 68mm and a depth of 5mm. The XPCS experiments on low viscosity liquids benefit from the use of a shallow trough [11] which effectively damps gravity waves. The trough used for the XPCS experiments has therefore a diameter of 68mm but a reduced depth of 0.5mm. In addition, this trough features a deeper reservoir (about 50mm^2×4mm), which is accessible from the outside of the trough by a 0.55 mm diameter channel. This modification allows the reduction of subphase volume without disturbing the surface by using a syringe with a 0.5mm diameter cannula. For all liquids investigated in the frame of this work the surface tension is sufficient to prevent leakage through the 0.55mm channel so that an additional sealing was unnecessary. The somehow cumbersome option of reducing the subphase volume after the monolayer preparation turned out to be ineluctably as monolayers cannot be spread on the very shallow liquid subphase optimised for XPCS: the surface waves created during the spreading process exhibit an amplitude larger than the depth of the subphase and consequently result in dewetting. Therefore, the trough was filled with the subphase forming a large meniscus and its volume was reduced after the monolayer preparation. The use of Kapton® foils for the X-ray windows does not allow for a tight sealing as Kapton® is partially permeable for helium. By using a static helium atmosphere in the sample chamber, with time a depression is established by a loss of helium gas into the surrounding vacuum of the outer chamber. Figure 3.1 panel b) and c) depict the resulting effect on the diffraction signal: for low pressure conditions in the sample cell the background scattering is drastically increased while the signal to noise ratio is decreased by more than one order of magnitude. Obviously, in the case of a depression in the inner chamber the number of liquid molecules in the gas phase above the surface is increased causing more parasitic scattering. A possible mechanism might involve the boiling point depression as a function of surrounding pressure (e.g. for water: 1bar, 100°C; 30mbar, 26°C): close to the boiling point evaporation is not anymore a pure surface phenomenon, but envolves also bulk molecules so that consequently the number of molecules in the gas phase might be increased. Therefore, the inner chamber was permanently flushed with He gas to maintain an atmospheric pressure. In order to prevent the liquid sample surface from disturbances, the trough is covered by a cap made of 0.5mm thick aluminum foil. Five Pt100 temperature sensors are used to regulate and monitor the temperatures (see also right-hand panel of figure 3.3 for a sketch of locations). One temperature sensor (the corresponding temperature is referred to as T_{trough}) is located at the trough containing the sample, the second one is glued to the bottom of the heat

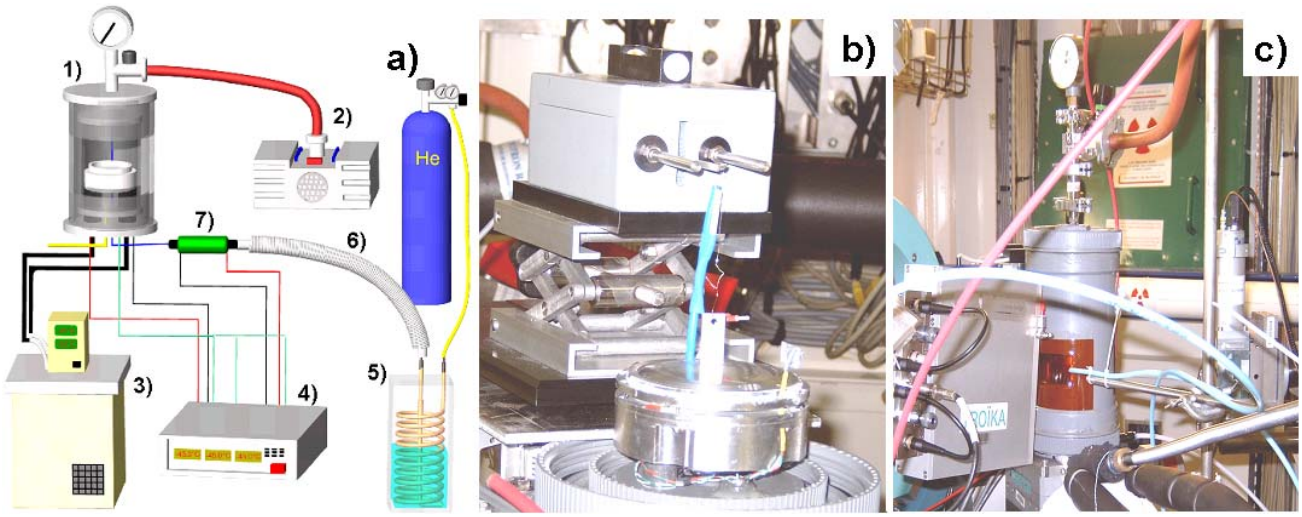

Figure 3.2: a) sketch of the sample cell and the periphery equipment: 1) sample cell, 2) vacuum pump, 3) chiller, 4) temperature controller, 5) copper spiral in liquid nitrogen, 6) vacuum insulated transfer tube, 7) resistive heater; b) open sample cell with tensiometer; c) closed sample cell, mounted on the diffractometer at the TROIKA II beamline

exchanger (T_{chil}) and one (T_{cap}) is attached to the aluminum cap. The temperature of the helium atmosphere is monitored at the exit of the entrance pipe (T_{He}) and with a Pt100 inserted into the aluminum cap, suspended about 10mm above the sample surface (T_{atm}). Figure 3.2 a) gives a schematic outline of the cell assembly with its periphery equipment. The heat exchanger is connected to a chiller (Thermo Haake, K41DC50) running with silicon oil as a cooling agent. The peltier elements where controlled by a PID controller (Watlow SD) using T_{trough} as the input signal. Pre-cooling of the He gas was necessary to minimise the temperature offset between the atmosphere and the sample. Helium cooling was achieved either by flushing He gas from a gas-bottle through a copper spiral immerged into liquid nitrogen or by using liquid helium from a Dewar that was vaporised before entering the sample cell. In both cases the transfer was provided by a vacuum insulated flexible pipe. The temperature stabilisation of the above described assembly is active, i.e. based on a feedback system consisting of a temperature sensor and a PID controller. The mass of the aluminum trough of only 85g and the large cooling power in combination with the fast reaction time of the peltier elements make for a temperature stability better than $\pm 0.05°C$, mainly determined by an appropriate choice of the PID parameters. This approach is contrary to commonly used liquid sample cells [102] where a large block of metal (typically several kilograms) is thermalised and makes for the thermal stability due to its large heat capacity. The chamber itself is not equipped with a surface pressure sensor. Therefore, the surface pressure was monitored during the monolayer spreading process by a standard tensiometer (Nima model ST9002) using a Wilhelmy paper plate. Figure 3.2 b) shows the cell mounted on the diffractometer stage of the ID10A beamline (ESRF, Grenoble, France) with inner and outer cell being removed and the tensiometer being installed on an external support. Figure 3.3 displays the achieved temperatures

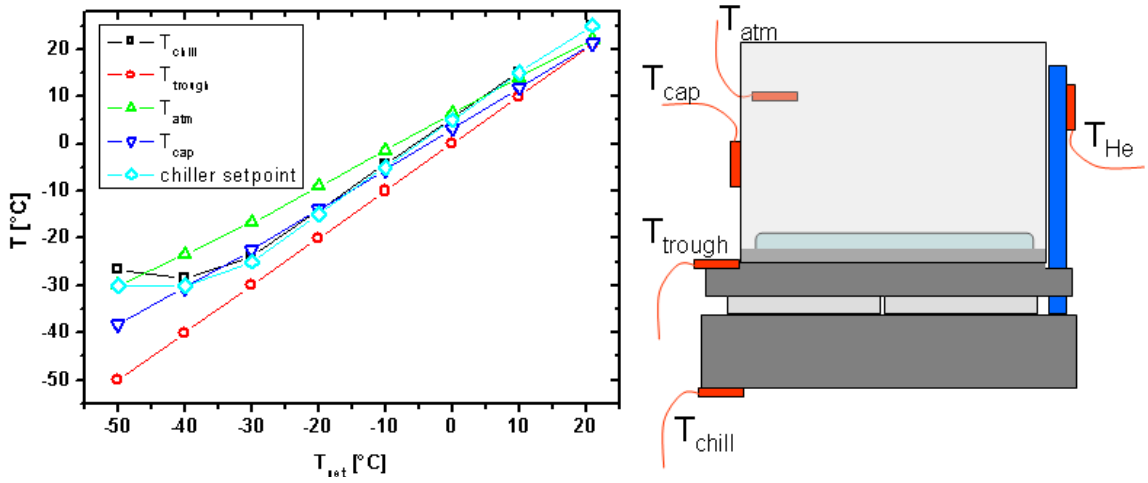

Figure 3.3: left hand panel: temperatures as monitored by the different temperature sensors during a cooling cycle as a function of the set-point temperature; right hand panel: sketch of the locations of the different temperature sensors

at different locations within the cell as a function of the set-point temperature. The temperature of the aluminium cap above the sample (T_{cap}) follows the sample temperature with a small offset. The larger offset of the temperature of the atmosphere (T_{atm}) arises from the data being taken during a test run of the sample chamber without pre-cooling of the exchange gas.

3.2 The TROIKA II (ID10B) Beamline

Scattering (GIXOS) and diffraction (GIXD) experiments were carried out at the Troika II (ID10B) beamline [109] at the European Synchrotron Radiation Facility (ESRF, Grenoble, France). The radiation from up to three undulators is collimated by a primary slit to $1.0\times0.5\text{mm}^2$ (H×V) and monochromatised using a diamond (111) double monochromator, where the first crystal in transmission geometry acts as a beamsplitter. The intrinsic energy resolution of the diamond crystal is $\Delta E/E = 5.9 \cdot 10^{-5}$. A horizontal double mirror (palladium) is used to suppress the higher harmonics and can be used to focus the beam in the vertical direction by bending. The first mirror reflects the beam upwards, while the second one reflects it downwards and is hence also used to adjust the incidence angle for GIXD in the horizontal scattering geometry. A horizontal guard slit before the first mirror re-collimates the beam in the vertical direction. After the double mirror, the beam size can be defined by a pair of horizontal and vertical slits. In the experimental hutch, a deflector stage equipped e.g. with a Ge (111) crystal allows to tilt the beam by up to several degrees with respect to the horizontal for XRR experiments. Optional, the deflector stage can also be equipped with an evacuated flight pass. After the deflector stage, the beam size on the sample is defined by means of another pair of vertical and horizontal slits. An NaI scintillation detector perpendicular to the beam is used as a monitor counter, measuring the intensity of the direct beam via the scattering from a

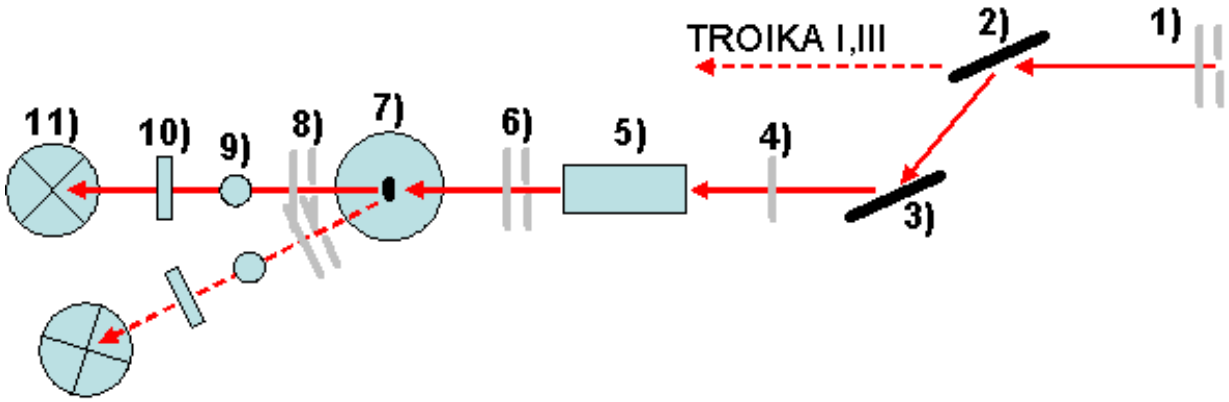

Figure 3.4: Schematic outline (top view) of the TROIKA II beamline at the ESRF. 1) Front end, 2) first monochromator crystal, 3) second monochromator crystal, 4) guard slit, 5) double mirror, 6) optics slits, 7) deflector stage, after the deflector stage the dashed beam path corresponds to the option of using a deflector crystal, 8) slits, 9) monitor counter, 10) absorber wheel, 11) center of rotation of the diffractometer

Kapton® foil. Attenuation of the beam at an X-ray energy at around 8keV can be achieved by a rotating wheel, containing slots with aluminum foils of thicknesses between 0.1 and 1.9mm. With the exception of the second monochromator vessel, which is housed under an helium atmosphere, the whole beam path up to the sample is under vacuum to avoid parasitic air scattering. For the same reason each setup is optimised with respect to the length of the beam path in air. The diffractometer is a 8-circle instrument (Huber), providing horizontal and vertical scattering geometries. The sample chamber was mounted on the horizontal stage of the diffractometer, equipped with an Eulean cradle which was used to adjust the sample surface in the horizontal scattering plane. Translations in z- and x-directions allow to adjust the height of the surface with respect to the incident beam and to change the spot of the sample surface hit by the beam footprint in order to avoid beam damage, respectively. For the diffraction experiments, the detector arm of the diffractometer held a Soller collimator (JJ X-ray, 1.4mrad resolution) to collect diffracted intensity from a larger footprint area and a 150mm position sensitive linear detector (Gabriel), both arranged perpendicular to the sample surface. For the GIXD experiments the Soller collimator was replaced by a pair of vertical slits, separated from each other by a 59cm long evacuated flight pass. Typical slit openings were 0.3 and 0.5mm for the slit after the sample and in front of the detector, respectively. All experiments where carried out at X-ray energies of about 8keV. The GIXD data shown in section 3.3.1 for the monolayer of eicosanoic acid on a liquid subphase were taken using the setup with the Ge deflector, which was aligned slightly off-Bragg in order to achieve an additional suppression of higher energies in the beam. All other data were taken with the evacuated flight pass on the deflector stage. A schematic outline of the beamline is depicted in figure 3.4.

3.3 Experimental Results

3.3.1 Monolayer of Eicosanoic Acid on DMSO/H_2O

GIXOS and GIXD Measurements

Monolayers of eicosanoic acid on a liquid subphase of DMSO/H_2O were prepared by spreading from a chloroform solution at a concentration of 0.05 mg/ml at room temperature. The initial surface pressure for these layers was 4.5 mN/m as determined by *in-situ* maesurements using a tensiometer as described in section 3.1. In order to get the initial states of the monolayers for different experiments as identical as possible, not only identical surface pressure but also identical GIXD diffraction pattern upon monolayer preparation were demanded. A high surface pressure is associated with a dense packing of the molecules, restricting their possibilities to re-organize upon cooling. For this reason the experiments were restricted to an initially low surface pressure state, where according to the isotherms (see chapter 1.3) the monolayer is in a state just above the gas phase with a relatively large overall area per molecule. Unlike common Langmuir experiments, no additional compression of the film, e.g. by means of movable barriers, was used to induce changes in the structure formation. In contrast to the 'excess droplet method' applied for instance for monolayers of alcohols [94], the number of molecules at the surface and within the monolayer is constant under these conditions. Therefore, changes in the conformational ordering can be attributed to a modified interaction between the surfactant molecules and/or the surfactant molecules and the subphase and not to a simple response to an external constraint like compression or excess volume.

In order to obtain information about the electron density (or scattering length density) profile of the layer normal to the surface, GIXOS experiments were performed. This results allow first insights into the stability of the monolayers upon cooling and possible surfactant induced ice formation. The samples were cooled at a rate of 0.5°C/minute and after reaching the requested sample temperature equilibration time was allowed to enable all monitored temperatures (T_{trough}, T_{atm}, $T_{chiller}$) to reach a steady state. The obtained GIXOS curves for an eicosanoic acid monolayer on a subphase of DMSO/H_2O in the eutectic mixing ratio are shown in figure 3.5 panel a). Measurements were performed at temperatures of 22°C (a), 10°C (b), 5°C (c), 0°C (d), -5°C (e), -10°C (f) and -20°C (g). With a horizontal beam width of 0.5mm, horizontal detector slits with a gap of 0.3mm and a sample detector distance of about 900mm, an in-plane angle of $2\theta = 0.5°$, corresponding to an in-plane wavevector transfer of q_{xy}=0.035Å^{-1}, was found to be sufficient to blind out the direct beam from the linear detector. The open circles in figure 3.5 represent the measured data, taken with an acquisition time of 180s. The solid lines are fits according to equation (2.71). It was found that the scattering curves can be well described by a one box model representing the alkane chain of the eicosanoic acid molecule. Considering the small size of the carboxyl group (C-O-O-H) acting as the hydrophilic 'headgroup' of this amphiphile and its relatively similar scattering length density as compared to those of the subphase and the alkane chains, it is plausible that there is no necessity to introduce a second box in the model to represent the carboxyl groups. More precisely, the existence of such a layer cannot be ruled out, but the satisfactory description of the experimental data by a one box model would not justify the introduction of a second box. The parameters

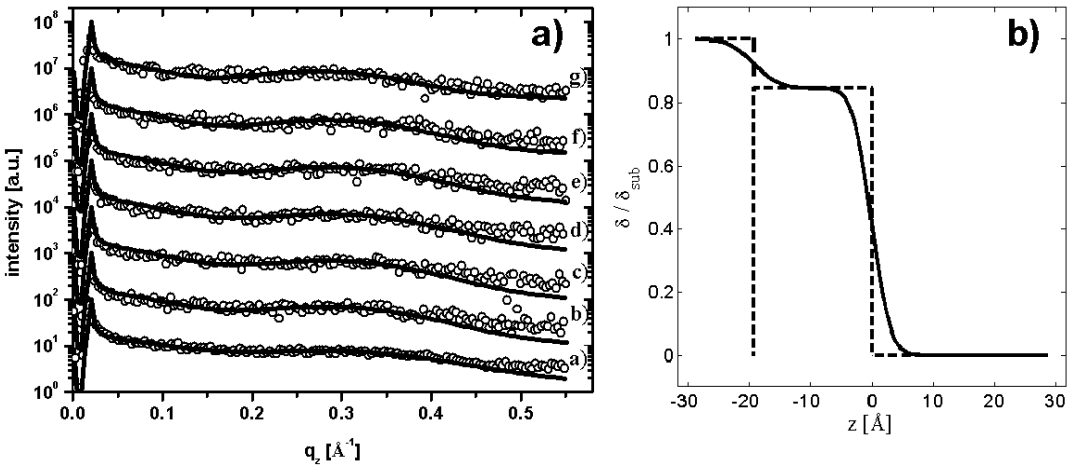

Figure 3.5: Panel a): Measured GIXOS profiles (open circles) and fit to a one box model (solid line) for an eicosanoic acid monolayer on a DMSO/H_2O subphase at temperatures of 22°C (a)), 10°C (b)), 5°C (c)), 0°C (d)), –5°C (e)), -10°C (f)), -20°C (g)); Panel b): box model with zero roughness (dashed line) and erf-model (solid line) for the parameters obtained from the fit of the GIXOS profile at -10°C. The scattering length density is plotted normalised to the scattering lenght density of the subphase; the coordinate z is normal to the layer surface and the origin (z=0) is chosen to coincide with the monolayer/atmosphere interface.

found for the alkane chain layer at the different temperatures are shown in table 3.1: δ_1/δ_{sub} denotes the scattering length density of the layer normalised to the scattering length density of the subphase, d_1 denotes the thickness of the layer and σ_1 is the rms roughness at the alkane chain/helium atmosphere interface. For the fits the scattering length density of the subphase was fixed to its nominal value of about $\delta_{sub} = 1.05 \times \delta_{H_2O}$ as calculated from the chemical composition of the subphase and its density at room temperature (see section 1.2) by means of [49]. Thus minor effects due to the density change of the subphase as a consequence of thermal expansion during the cooling cycle have been neglected. The roughness σ_{sub} of the interface subphase/monolayer was found to be about 3.3Å for the first fitted curves. This reasonable value was fixed afterwards for all the fits to minimise the number of free parameters as the scattering curves are not very richly featured. The evolution of the layer during a cooling cycle shows as the most striking feature an increase of the layer thickness from about 18.1Å at 22°C to about 20.5Å at -20°C. At the same time the scattering length density is dropping from about $0.9 \times \delta_{sub}$ to $0.85 \times \delta_{sub}$. Although qualitatively the scattering length density is decreasing with increasing layer thickness, it reaches an almost constant value at higher temperatures, where the layer thickness is still noticeably increasing. In order to cross-check whether this fit parameters are consistent, the last column of table 3.1 shows the product of $\delta_1/\delta_{sub} \times d_1$, thus the normalised scattering length density in the layer over a unit area. Recalling that the number of surfactant molecules is constant for length scales larger than the characteristic length scales of inhomogeneities due to the particular sample preparation and the absence of compression, it is evident that this value has

T [°C]	δ_1/δ_{sub}	d_1 [Å]	σ [Å]	$\delta_1/\delta_{sub} \times d_1$ [Å]
22 a)	0.896	18.06	2.34	16.18
10 b)	0.855	18.74	2.60	16.02
5 c)	0.849	18.74	2.63	15.91
0 d)	0.852	18.55	2.57	15.80
-5 e)	0.846	18.84	2.53	15.94
-10 f)	0.845	19.19	2.47	16.21
-20 g)	0.850	20.47	2.27	17.40

Table 3.1: Parameters obtained by fitting the GIXOS curves shown in figure 3.5 panel a). The fit parameters of the layer describing the eicosanoic acid monolayer are the scattering length density normalised to the one of the subphase δ_1/δ_{sub}, the layer thickness d_1 and the rms roughness at the layer/atmosphere interface σ_1. The product $\delta_1/\delta_{sub} \times d_1$ is calculated to check the conservation of the scattering length density within the layer as explained in the text.

to be a constant. Except for the parameters extracted at -20°C, the maximum absolute derivation from the average value of 16.01Å amounts to 0.2Å or 1.2%, whereas in the same temperature interval the layer thickness increases by about 1.1Å or 6%. Thus, at least in this temperature range a consistent growth of the layer thickness with a conservation of the overall scattering length density is found. The corresponding scattering length density profile at a sample temperature of -10°C is shown in figure 3.5 panel b). The dashed lines represent the sharp interface positions and corresponding scattering densities for a box model with zero roughness, while the solid line has been calculated according to an erf-profile as given by equation (2.61). The coordinate z is normal to the monolayer surface and its origin (z=0) is chosen to coincide with the interface between the layer and the atmosphere. At -20°C however, the layer thickness is significantly increased compared to the lower sample temperature of -10°C while the scattering length density is almost constant. The roughness σ_1 of the chain/helium interface is found to vary by about 0.14Å around the average value of 2.49Å with a tendency towards decreasing roughness with decreasing temperature below 5°C. However, these variations are too small to draw any conclusions about their physical origin. The GIXOS measurements prove the existence of a well defined monolayer over the entire investigated temperature range. No ice layer underneath the surfactant could be detected. The increase in layer thickness during cooling points towards a tilt angle of the molecules with respect to the surface normal, that is reduced during the cooling process.

Primed with the knowledge about the existance of stable monolayers, their in-plane structure was investigated by means of GIXD. The monolayers were prepared in the same fashion as for the GIXOS measurements and the identical cooling rate of 0.5°C/minute was applied. The development of the diffraction pattern for a range of the in-plane wavevector transfer $q_{xy} = 1.35\ \mathring{A}^{-1}$ to $q_{xy} = 1.85\ \mathring{A}^{-1}$ upon a cooling series from $22°C$ to $-40°C$ is shown in figure 3.6. The corresponding lattice spacings being probed in this q_{xy} range represent the constituting lattice spacings of the unit cell and are hence sufficient to determine the two-dimensional lattice and the alignment of the alkane chains within the framework of the cylinder model. With the exception of the panels c) ($0°C$) and h) (-$40°C$)

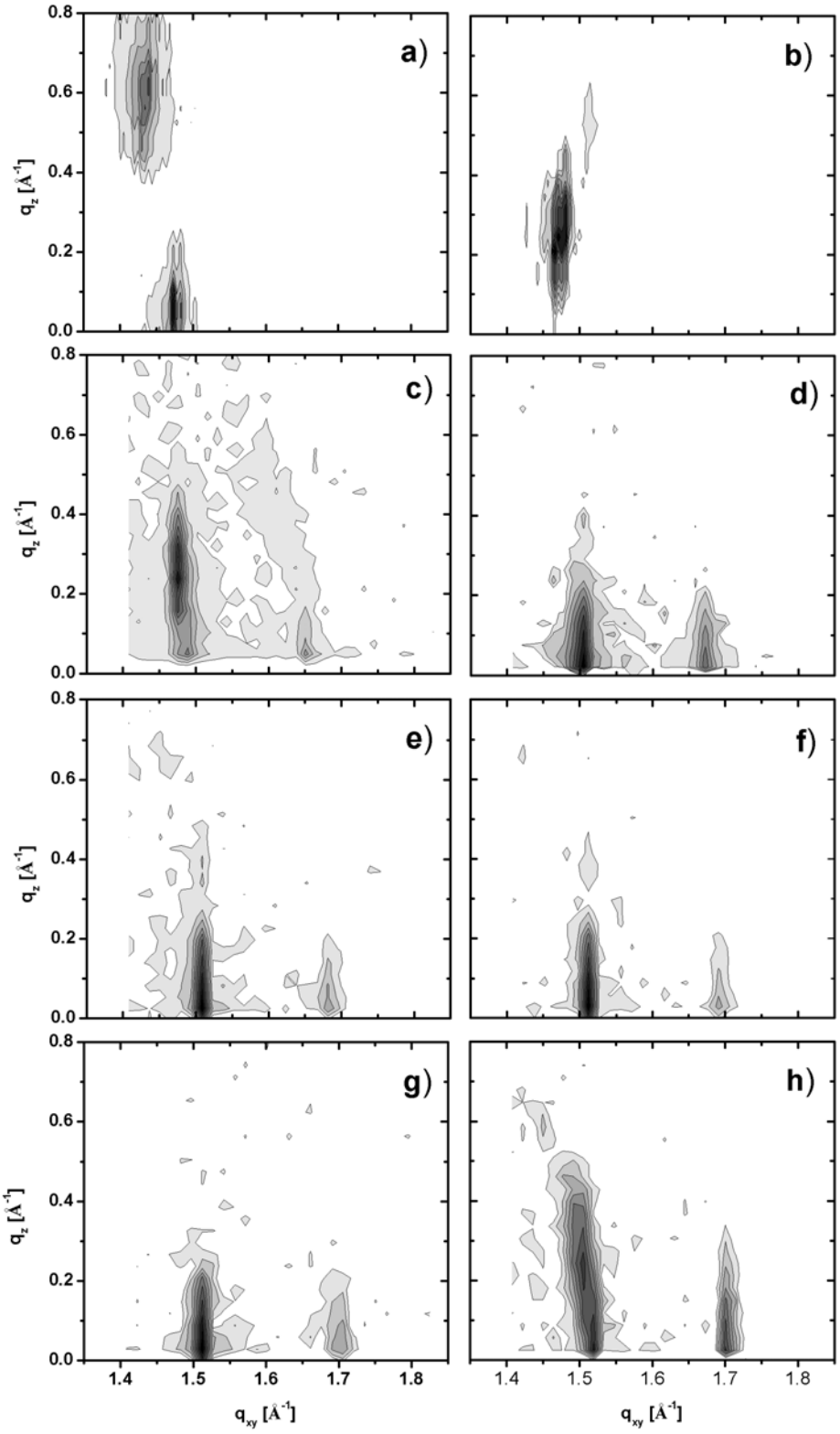

Figure 3.6: Evolution of GIXD patterns for a monolayer of eicosanoic acid at a surface pressure of 4.3 mN/m on DMSO/H_2O during a cooling cycle from 22°C to -40°C. a) 22°C, b) 10°C, c) 0°C, d) -5°C, e) -10°C, f) -15°C, g) -20°C, h) -40°C; grey scale map: intensity increasing from white to black; in order to present as many details of the diffraction pattern as possible, panels a) to c) employ a linear scale for the internsity mapping while log scale is used for panels d) to h).

all diffraction pattern show two separated reflections corresponding to two different lattice spacings. These findings can be qualitatively interpreted as an indicative for a rectangular unit cell. The more complex diffraction patterns c) and d) show up to four reflections which can be attributed to two different phases of the monolayer. The variation of the positions of the reflections with respect to the out-of plane wavevector transfer q_z reflects the change in the conformation of the alkane chains normal to the monolayer surface. The intensity of the diffraction pattern integrated along q_z as a function of q_{xy} is presented in figure 3.7. Starting from two relatively broad reflections exhibiting low peak intensities at $22°C$ (panel a)), upon cooling the diffraction peaks sharpen and their peak intensities increase. At a temperature of about $0°C$ (panel c)) a diffraction peak at larger q_{xy} becomes observable (indicated by an arrow in panel c)), being indicative of the evolution towards a different monolayer phase accompanied by a change in the two-dimensional lattice. While the two diffraction peaks that define the two-dimensional unit cell are close with respect to q_{xy} at higher temperatures (panels a),b)), they become well separated upon cooling. The qualitative interpretation of this finding is the change from a rectangular unit cell that is only slightly distorted from a hexagonal one at higher temperatures towards a rectangular lattice with two strongly differing lattice spacings. The strong asymmetry and broadening of the peak at smaller q_{xy} for dataset h) taken at a temperature of -40°C is caused by the superposition of reflections originating from different monolayer phases as it is evident from figure 3.6 panel h).

A detailed analysis of the two-dimensional monolayer structure and the chain alignment within the unit cell at 22°C is depicted in figure 3.8. Panel a) shows the intensity of the diffraction pattern integrated along q_z in the range $0\ \mathring{A}^{-1} \leq q_z \leq 1\ \mathring{A}^{-1}$. The solid line is a fit to the superposition of two Voigt functions from which the peak centers were determined as $q_{xy}^{a,b} = 1.436\mathring{A}^{-1}$ and $q_{xy}^{ab} = 1.476\mathring{A}^{-1}$. The degeneration of the reflections is clear from their positions with respect to the out-of-plane wavevector transfer q_z. In order to determine these positions, the Bragg rod profiles at the position of the in-plane Bragg peaks have been fitted to equation (2.22) using the molecular form factor $F_{\text{cylinder}}(\mathbf{q})$. The Bragg rods of the eicosanoic acid monolayer were at all temperatures modelled with a standard radius of $0.44\mathring{A}$ for the representing cylinder. The length L of this cylinder was found to be $24\mathring{A}$, contrary to the $25.5\mathring{A}$ suggested by the formula given in section 2.1.3 for a C20 alkane chain in all-trans conformation. Other studies on phospholipids also report a mismatch of about 1.5Å between the length of a scatterer derived from Bragg rod analysis and from theoretical calculations [60]. These findings are nevertheless consistent with results from He-scattering experiments on alkane chain molecules on solid substrates, which suggest that the final methyl group of the chain might be in a liquid-like state at temperatures above $100K$ [15] and would hence not contribute to the GIXD signal. From the obtained parameters like the tilt direction Ψ^* and the tilt angle t the position of the maximum of the molecular form factor can be calculated according to $q_z = q_{xy} \cos\Psi^* \tan t$. The obtained values for the maxima of the reflections with respect to q_z are $0.597\mathring{A}^{-1}$ at $q_{xy} = 1.436\mathring{A}^{-1}$ and $0\mathring{A}^{-1}$ at $q_{xy} = 1.476\mathring{A}^{-1}$, so that according to equation 2.33 the first reflection has to be twice degenerated. Because the solutions obtained for Ψ^* and t by fitting an individual Bragg rod being not necessarily unique, they do not automatically fulfill all the relations given in section 2.1.4. In order to propose a consistent structure, it is therefore indispensable to calculate the parameters $\Psi^*_{a,b,ab}$ and t using equations 2.34,

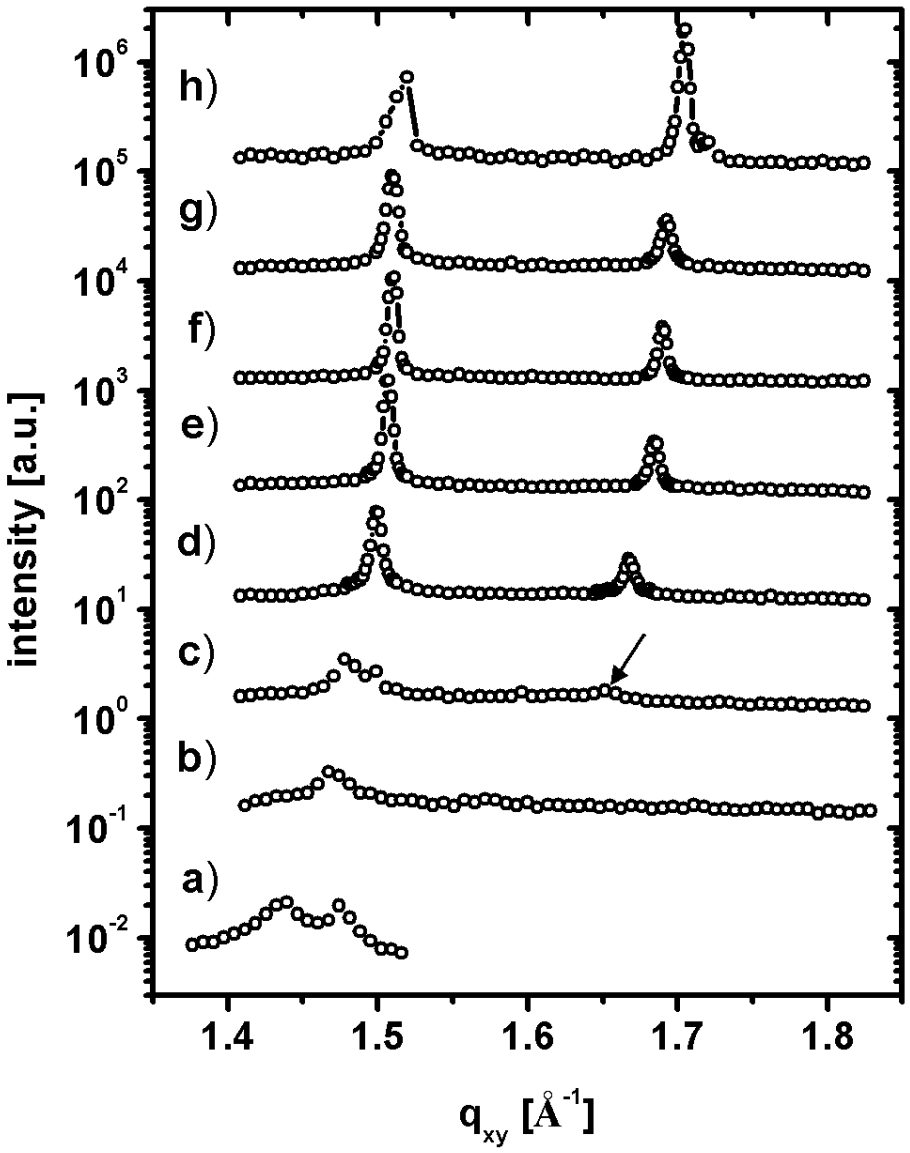

Figure 3.7: Evolution of the diffraction pattern shown in figure 3.6 integrated along q_z upon cooling from 22°C (panel a)) to -40°C (panel h)). The peak profiles have been scaled in intensity for clarity. The arrow in panel c) (0°C) indicates the first appearance of the diffraction peak at larger q_{xy}, being an indicative for a different monolayer phase. Temperatures: a) 22°C, b) 10°C, c) 0°C, d) -5°C, e) -10°C, f) -15°C, g) -20°C, h) -40°C.

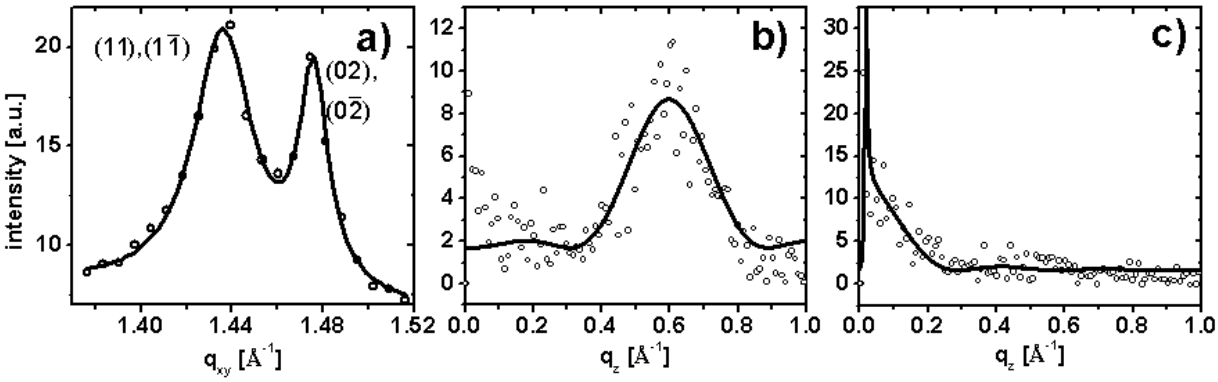

Figure 3.8: Diffraction from the eicosanoic acid monolayer at 22°C; a) in-plane Bragg peaks (open circles), the solid line is a fit to a superposition of two Voight functions; b) measured Bragg rod (open circles) and modelled curve according to the cylinder model (solid line) at $q_{xy} = 1.4356\mathring{A}^{-1}$; c) Bragg rod and model at $q_{xy} = 1.4758\mathring{A}^{-1}$.

2.35, 2.36, 2.37 and the obtained maxima of the reflections with respect to q_{xy} and q_z. Afterwards, the plausibility of the proposed structure can be assured by modeling the Bragg rods with the such obtained parameters and by drawing the unit cell. Figure 3.8 panel b) shows the Bragg rod measured at $q_{xy} = 1.436\mathring{A}^{-1}$ (open circles) and the modelled curve (solid line) according to equation 2.22 for a tilt angle of 25.9° and a tilt direction towards the nearest neighbour (n.n.). The discrepancy between the model curve and the measured data points at small q_z arises from the overlap of the two reflections which result in a superposition of the two Bragg rods. Panel c) of the same figure shows the data (open circles) and the modelled curve (solid line) for the Bragg rod measured at $q_{xy} = 1.476\mathring{A}^{-1}$. The degeneration of the reflections and the obtained parameters for the chain alignment are compatible with a non-primitive centred rectangular cell. With this choice of the unit cell, the tilt direction of the chains becomes the $[\overline{2}0]$ direction (or the [20] direction as there is a 180° symmetry for the tilt direction). The perpendicular direction [20] is therefore the axis of rotation of the molecular form factor around the lattice structure factor. It is hence evident, that both the (02) and the $(0\overline{2})$ reflection exhibit a wavevector transfer with the component $q_z = 0\mathring{A}^{-1}$ and are therefore experimentally observable. In contrast, the $(\overline{1}1)$ and the $(\overline{1}\overline{1})$ reflections exhibit a wavevector transfer component $q_z \leq 0$ so that only the (11) and the $(1\overline{1})$ reflections are observable.

While at 22°C and 10°C the diffraction pattern reveals only two reflections, at around 0°C the pattern is more complex as it is shown in detail in figure 3.9 panel a). Four intensity spots can be distinguished, two of them at $q_z \approx 0\mathring{A}^{-1}$ and two at larger q_z. The first step to analyses the data requires in this case the exact location of the in-plane Bragg peaks, which is hampered by the huge overlap of reflections with respect to q_{xy}, for instance in the case of the two reflections at $q_{xy} \approx 1.5\mathring{A}^{-1}$. A simple fit of the diffraction pattern integrated along the whole q_z range, as done for the data obtained at 22°C, would not allow the determination of the peak centers to a good level of confidence due to the strong overlap of individual Voigt profiles. It is therefore very useful to benefit from the separation of the reflections with respect to q_z by integrating over different regions of

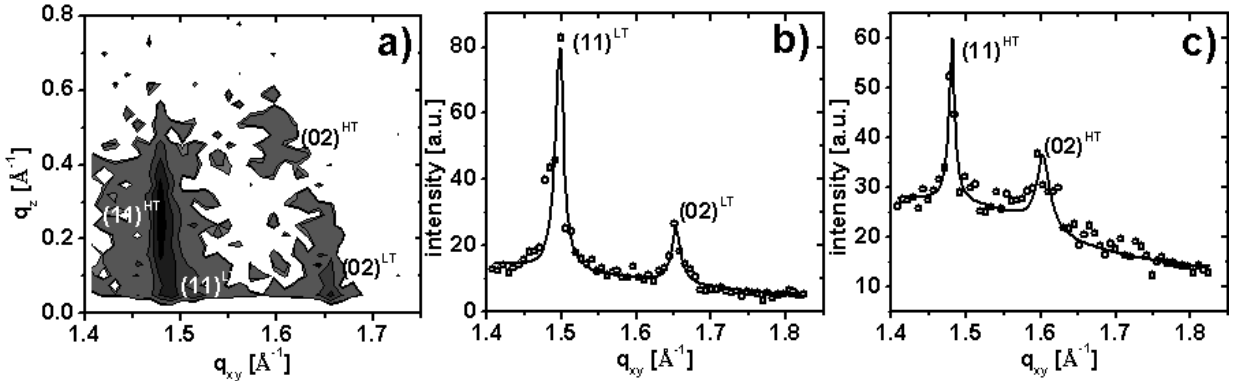

Figure 3.9: a) diffraction pattern for eicosanoic acid on DMSO/H_2O at 0°C, the monolayer exhibits two coexisting ordered phases: a high temperature phase (HT) and a low temperature phase (LT); b) diffraction pattern integrated along q_z over the interval [0,0.1] $Å^{-1}$, the solid line is a fit to a Voigt model to determnine the centers of the Bragg peaks of the (LT) phase; c) diffraction pattern integrated over the interval [0.34,0.67] $Å^{-1}$, the Bragg peaks in this range belong to the (HT) phase. Note: the full indexing of the diffraction peaks is omitted for clarity.

the diffraction pattern. By applying this procedure, the peak intensities might be underestimated due to incomplete integration. Nevertheless, this does not affect the center of the peak being the parameter of interest. Figure 3.9 panel b) shows the diffraction pattern integrated along q_z in the range $0\ Å^{-1} \leq q_z \leq 0.1\ Å^{-1}$ (circles). The fit with a two Voigt model (solid line) reveals two Bragg reflections with their centers located at $q_{xy} = 1.497Å^{-1}$ and $q_{xy} = 1.653Å^{-1}$. Panel c) of the same figure shows the diffraction pattern integrated over the q_z range $0.34\ Å^{-1} \leq q_z \leq 0.67\ Å^{-1}$; the fit leads to peak centers at $q_{xy} = 1.480Å^{-1}$ and $q_{xy} = 1.597Å^{-1}$. The four reflections have been identified as indicative of the coexistence of two centred rectangular phases, a high temperature phase labelled with the index 'HT ', being the evolution of the monolayer phase present at room temperature and a low temperature ('LT') phase which occours upon cooling. The assignment of the reflections to the two different phases will be established in the following. The extraction of the Bragg rods from the diffraction pattern and the fit of their maxima lead to values of $q_z = 0.224\ Å^{-1}$ for the rod belonging to the $(11)^{HT}$ in-plane Bragg peak and $q_z = 0.025\ Å^{-1}$ and $q_z = 0.050\ Å^{-1}$ for the $(11)^{LT}$ and $(02)^{LT}$reflections, respectively. The Bragg rod of the $(02)^{HT}$ reflection appeared to be too weak to determine a sharp maximum by the usual fitting procedure. Nevertheless, it is clear from the log-intensity map plot of figure 3.9 panel a) that the maximum of the rod is somewhere in the range $0.40\ Å^{-1} \leq q_z \leq 0.55\ Å^{-1}$, so that with regard to equation (2.33) a value of $q_z = 0.447\ Å^{-1}$ (corresponding to two times the value found for the $(11)^{HT}$ reflection) is plausible. With these findings for the positions of the reflections with respect to the out-of-plane wavevector transfer, the assignment of the reflection to the two different phases is evident from the q_z-rule (equation 2.33). Nevertheless, it is intuitive to compare the positions of the reflections and the dependent structural parameters at the phase coexistence temperature with other data sets at slightly different temperatures, revealing only one phase

at a time. These parameters for the present data set and the parameters derived from two other measurements at temperatures of -0.5°C and -10°C, respectively, are shown in table 3.2. It is noteworthy, that the data sets at nominal sample temperatures of -0.5°C and -10°C were recorded without pre-cooling of the helium constituting the atmosphere above the sample surface. Under this condition there is a quite large offset between the temperature of the trough and the helium atmosphere, so that the temperature at the position of the sample surface can be estimated to be significantly higher than the trough temperature. Therefore, the nominal temperature of -0.5°C would correspond to a few degrees above zero, while -10°C would correspond to a few degrees below (the offset is increasing with decreasing sample temperature as the cooling of the trough is way more efficient compared to the somehow indirect cooling of the helium atmosphere by the cold sample surface). The parameters for the high and low temperature phase show an excellent agreement with the parameters derived from the data of the individual phases (see table 3.2). For the low temperature phase the position of the reflections with respect to q_{xy} and q_z are almost identical, resulting in very similar values for the tilt angle t, the tilt direction (here characterised by the parameter Ψ^*) as well as the unit cell area and the cross section per alkane chain, A_0 and $A_\perp$, respectively. For the low temperature phase the positions of the reflections with respect to q_z differ noticeable between the two data sets resulting in different tilt angles. Nevertheless, the parameters describing the packing of the alkane chains, A_0 and $A_\perp$, are remarkably close. The peak positions in the high temperature phase are moreover also in accordance with the ones reported for eicoscanoic acid on a water/HCl subphase (pH 2) at a higher surface pressure of 20mN/m [30]. The measured and modelled Bragg rods for the two reflections of the high and the

T [°]	-0.5*)	0 (HT)	-10*)	0 (LT)
q_{xy}^a [Å^{-1}]	1.5845	1.5965	1.6509	1.6529
q_z^a [Å^{-1}]	0.4360	0.4472	0.128	0.050
$q_{xy}^{b,ab}$ [Å^{-1}]	1.4837	1.4798	1.4948	1.4974
$q_z^{b,ab}$ [Å^{-1}]	0.2180	0.2236	0.064	0.025
Ψ_{ab}^* [deg.]	57.7	57.4	56.5	56.5
t [deg.]	15.4	15.6	4.4	1.7
A_0 [Å^2]	19.86	19.85	19.19	19.13
$A_\perp$ [Å^2]	19.15	19.11	19.13	19.12

Table 3.2: Comparison of the peak positions and some derived parameters for the two coexisting phases (HT) and (LT) and two corresponding individual phases found at different temperatures
*) temperatures correspond to the trough temperature of the sample cell, the realistic temperature of the sample surface is higher (see text).

low temperature phase are shown in figure 3.10 panels a), b) and c), d), respectively. The strongly differing tilt angles of 15.6° (n.n.n.) in the high temperature phase and of 1.7° (n.n.) in the low temperature phase are apparent from the Bragg rods. The Bragg rod for the $(02)^{\mathrm{HT}}$ reflection (panel b)) is obviously too weak to be analysed and is hence only shown for the sake of completeness. The small but nevertheless not negligible tilt angle of the alkane chains in the low temperature phase is most evident in the broadening of the

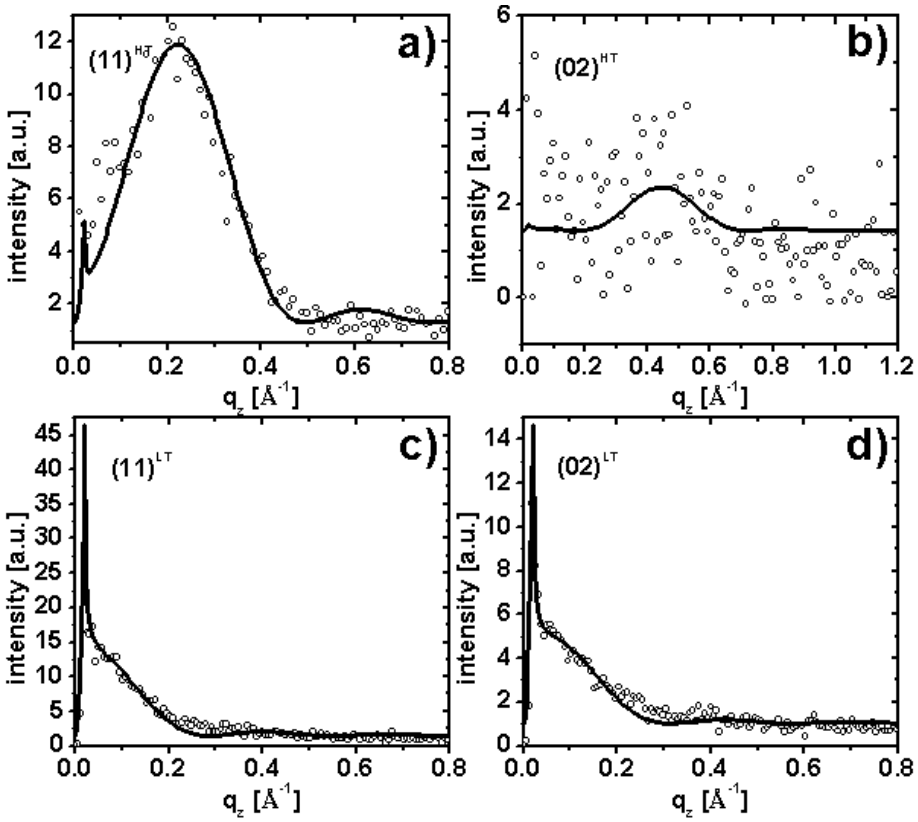

Figure 3.10: Measured Bragg rods (open circles) and modelled curves (solid lines) for the reflections of the high temperature phase (panels a) and b)) and the low temperature phase (panels c) and d)). The rod belonging to the $(02)^{\mathrm{HT}}$ reflection (panel b)) is too weak to extract meaningful parameters. Therefore, its maximum with respect to q_z is assumed to be twice the value found for the $(11)^{\mathrm{HT}}$ reflection in accordance to equation (2.33).

Bragg rod belonging to the $(02)^{\mathrm{LT}}$ reflection (panel c)). The tilt direction of the chains allows in the high temperature phase the observation of the (11), $(1\overline{1})$, (02) reflections, while in the low temperature phase the (11), $(1\overline{1})$, (02) and $(0\overline{2})$ reflections are observable.

At temperatures lower than 0°C only the low temperature phase is present in the diffraction pattern as can be seen from figure 3.6 panel d). The chain configuration within that phase changes from slightly tilted at 0°C to an upright configuration at -5°C. A representative analysis for the pure low temperature phase is shown in figure 3.11 for a sample temperature of -20°C. Panel a) displays the diffraction pattern integrated along q_z in the region $0\ \mathring{A}^{-1} \leq q_z \leq 0.43\ \mathring{A}^{-1}$, leading to two remarkably sharp in-plane diffraction peaks. Fitting of these in-plane Bragg peaks with the superposition of two Voigt function result in center positions of $q_{xy} = 1.510\mathring{A}^{-1}$ and $q_{xy} = 1.693\mathring{A}^{-1}$ for the (11) and (02) reflections, respectively. The fitting of the Bragg rods at the position of the centers of the in-plane Bragg peaks revealed the maxima for the molecular form factor of both reflections being located at $q_z = 0\ \mathring{A}^{-1}$, hence implying the tilt angle of the alkane chains being equal to zero. Because of this upright chain conformation, all reflections

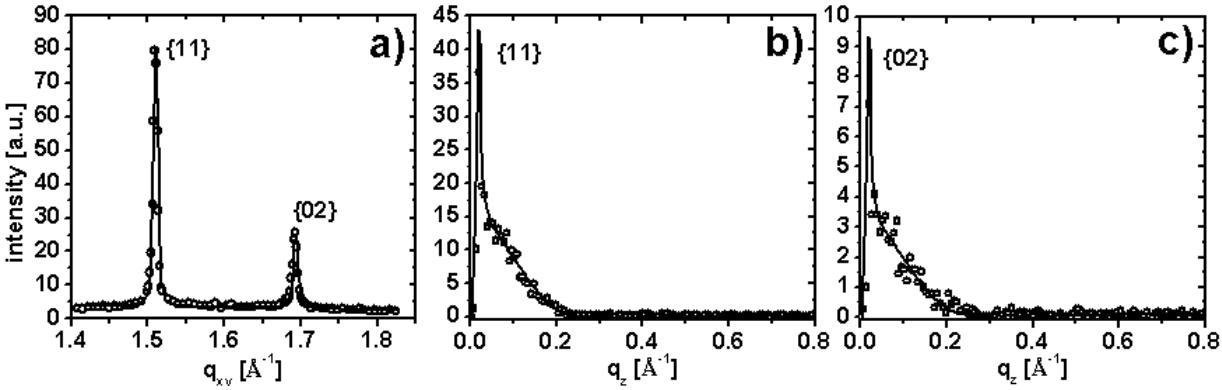

Figure 3.11: Details of the diffraction pattern at a sample temperature of -20°C. a) Diffraction pattern integrated along q_z; b) measured Bragg and modelled curve of the {11} in-plane Bragg peak; c) measured Bragg and modelled curve of the {02} in-plane Bragg peak

belonging to a family of lattice planes are observable; these are the (11), $(\overline{1}1)$, $(1\overline{1})$, $(\overline{11})$ and the (02), $(0\overline{2})$ reflections respectively. These sets of reflections are merged by the notations {11} and {02}. At a sample temperature of -40°C the diffraction pattern is more complicated due to the appearance of an additional phase. A detailed picture of the diffraction pattern is shown in figure 3.12 panel a). Three reflections are clearly visible, the diffraction pattern is somehow similar to the one obtained at 0°C, which could be identified as the fingerprint of the coexistence of two phases. Indeed, the position of the reflection labelled as $(11)^{\mathrm{HT}}$ in panel a is with $q_{xy} = 1.506\mathring{A}^{-1}$ and $q_z = 0.207\mathring{A}^{-1}$ close to the corresponding reflection of the high temperature phase observed at 0°C. In contrast to the data taken at 0°C, in the diffraction pattern for a sample temperature of -40°C neither the in-plane Bragg peak of a $(02)^{\mathrm{HT}}$ reflection nor the corresponding Bragg rod could be resolved. The diffraction pattern integrated along the out-of-plane wavevector transfer q_z in the interval $[0, 0.1]\mathring{A}^{-1}$ is shown in figure 3.12 panel b). The two in-plane reflections belong to the low temperature phase. For the graphic displayed in panel c) the diffraction pattern was integrated along q_z in the interval $[0.1, 0.4]\mathring{A}^{-1}$, in order to locate the position of the resolved in-plane reflection of the high temperature phase. With only one reflection belonging to this phase, it is impossible to extract any further parameters about the lattice or the chain alignment. The conclusion that this reflection in deed belongs to a high temperature phase is therefore mainly based on the comparison of its position with the data taken at 0°C. Nevertheless, some other possibilities to assign that reflection can be ruled out: For instance attributing the reflection to a hexagonal phase seems to be unlikely, because the large tilt angle implied by the position with respect to q_z would be rather unusual for a hexagonal phase where the alkane chains are supposed to be in an upright configuration. In addition, the change of the low temperature configuration from a centred rectangular lattice with two (degenerated) lattice spacings towards an oblique one exhibiting three non-degenerated lattice spacings can be ruled out by considering the q_z positions of the reflections: With two reflections having the maxima of the molecular form factor at $q_z = 0\mathring{A}^{-1}$ and one reflection exhibiting the corresponding maximum at

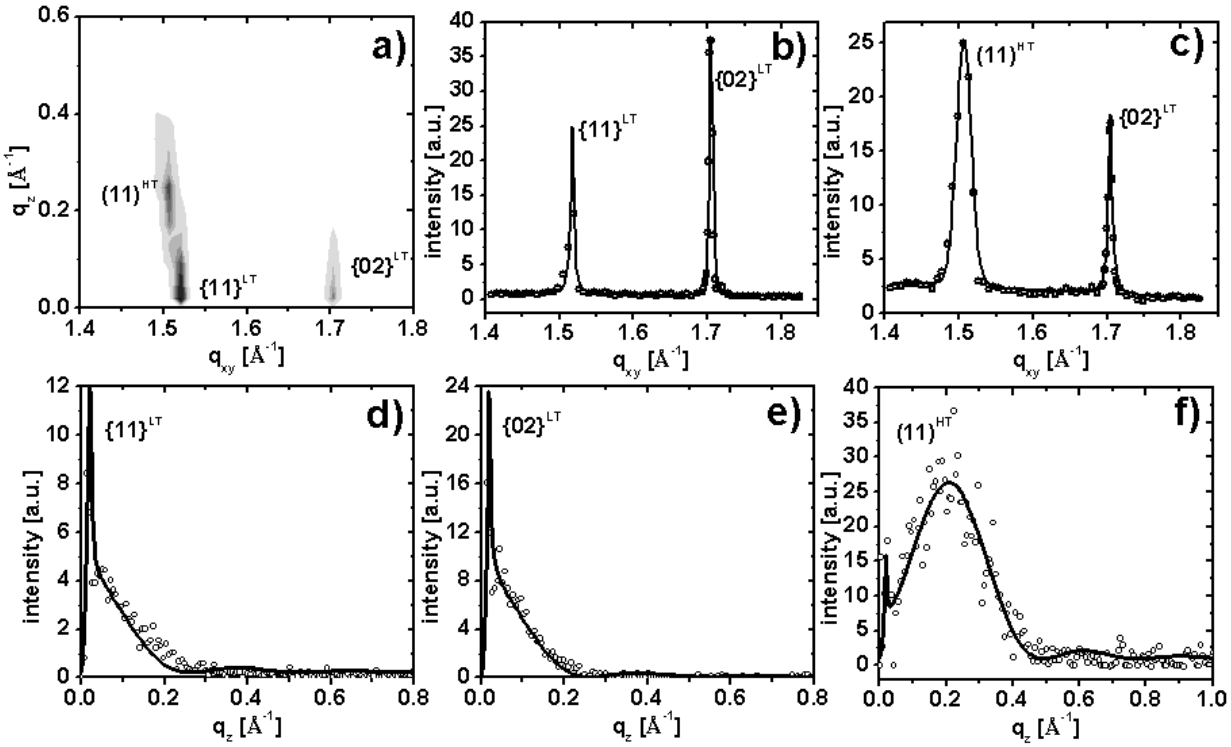

Figure 3.12: a) diffraction pattern of the eicosanoic acid monolayer at a sample temperature of -40°C. b), c) diffraction peaks obtained by integration in the range [0,0.1]Å $^{-1}$ and [0.1,0.4]Å^{-1},respectively, and corresponding fits; d)-f): Bragg rods of the resolved low and high temperature phase reflections, note that from the single Bragg rod of the HT reflection only the diameter and the length of the scatter within the frame of the cylinder model can be determined.

$q_z = 0.207\mathring{A}^{-1}$ the boundary condition given by equation (2.33) cannot be fulfilled. It is therefore most plausible that the $(02)^{\mathrm{HT}}$ reflection, which has also a very low intensity in the data set taken at 0°C, was not resolved, while the phases present in the monolayer are similar to the ones present in the coexisting case at 0°C. A possible mechanism for the appearance of the high temperature phase at -40°C could be the ordering of initially non-ordered surfactant molecules in the voids between the crystalline domains of the quasi-two-dimensional powder constituting the monolayer. This topic will be addressed in more detail below. The measured Bragg rods and modelled curves belonging to the $\{11\}^{\mathrm{LT}}$, $\{02\}^{\mathrm{LT}}$ and $(11)^{\mathrm{HT}}$ are shown in figure 3.12 panels d), e) and f), respectively. It is noteworthy that no parameters can be extracted from the modelling of the single Bragg rod belonging to the $(11)^{\mathrm{HT}}$ shown in figure f) due to the non unique solutions of the model as it has been discussed above. Nevertheless, the good agreement between the shape of the measured Bragg rod and the modelled curve based on the cylinder model provides an independent proof of the reflection originating from the alkane chains of the monolayer rather than being some kind of an artefact.

Comparing the qualitative evolution of the chain tilt as a function of temperature and the corresponding values for the monolayer thickness with the results obtained by

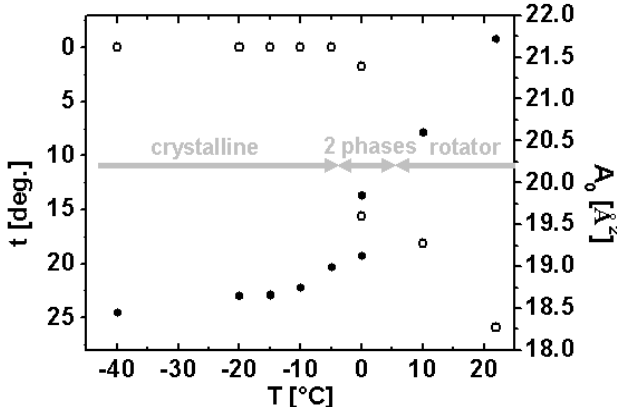

Figure 3.13: Tilt angle t (open circles) and unit cell area per alkane chains A_0 (filled circles) as a function of the sample temperature. At T=0°C two phases have been identified in the diffraction data, resulting in two different values for t and A_0 at the same temperature. The identification of the different phases is explained in the text. The extension of the different phases over certain temperatures intervals is indicated by the horizontal arrows as a guide to the eye without the intention of exact localisation of phase boundaries.

GIXOS, two findings strike out. The first one is the transition of the chains from a tilted towards an upright configuration being according to the Bragg rod measurements already completed at temperatures around -5°C. In contrast, the GIXOS experiments suggest that the change of the layer thickness is not completed even at temperatures of -20°C. A possible mechanism involves again the kinetics of the reorganisation process of the surfactant molecules at the subphase surface: Although time for temperature equilibration was allowed upon each change of the sample temperature, the time for the actual experiment itself is with 180s much shorter for the GIXOS than for the GIXD, where scans at one temperature can last up to several hours depending on scan range and resolution. As a consequence, the time the sample rests at each temperature is drastically reduced during the GIXOS experiments. Moreover, this effect adds up with each temperature step during a cooling cycle. Another reason for this findings might originate from the growth of the crystalline domains during the cooling process. As the crystalline parts of the layer which exhibit upright alkane chains become larger, the averaging over the inhomogeneous layer might lead to a virtual increase of the layer thickness. This averaging over an inhomogeneous monolayer is most plausible also the reason for the second discrepancy between the GIXD and the GIXOS data: As the Bragg rod measurements suggest, the length of the ordered parts of the alkane chains is about 24Å. Calculation of a corresponding layer thickness d_{GIXD}=24Å$\times \cos t$ suggests an increase from 21.77Å at 22°C to 24.00Å at -20°C. These values are about 3.5Å larger as the layer thickness d_1 obtained by GIXOS. Nevertheless, the increase of the layer thickness between these two temperatures is in excellent agreement: about 2.2Å and 2.4Å for GIXD and GIXOS, respectively.

Two characteristic structure parameters, namely the unit cell area per alkane chain A_0 and the tilt angle t, are presented in figure 3.13 as a function of the sample temperature. Both parameters show a distinct change upon approaching a sample temperature of 0°C.

Because two independent monolayer phases have been identified at this particular temperature, there are two values both for the tilt angle and the unit cell area per alkane chain. While the latter one (filled circles) drops by about 0.72Å^2 between the two phases, the tilt angle (open circles) is at the same time reduced from 15.6° to almost zero (1.7°). At lower temperatures (≤-5°C) only the monolayer phase with an upright chain alignment and a smaller unit cell than in the high temperature phase (≥0°C) is present. For the monolayer phases exhibiting a non zero tilt angle also the area per alkane chain normal to the chain axis $A_\perp = A_0 \cos t$, i.e. the chain cross section is a characteristic parameter. At the relatively high temperatures of 22°C and 10°C $A_\perp$ has a value of about 19.6Å^2. According to [60] this value for the chain cross section is about the upper limit for the (hindered) rotation of an alkane chain around its length axis. Therefore, this temperature region has been indicated as the rotator phase regime in figure 3.13. In the two phase coexisting region the cross section per alkane chain is almost identical in the high temperature and the low temperature phase, exhibiting values of 19.11Å^2 and 19.12Å^2, respectively. Nevertheless, the conformational change from a tilted phase with a relatively large unit cell to a smaller unit cell containing upright chains must be energetically favourable for the system. The fact that both phases can be found at the same temperature indicates that the transition between them is not sharp, at least not all over the inhomogenously covered monolayer area probed by the large footprint area of the X-ray beam. A possible mechanism might be a direct consequence of the sample preparation: in contrast to the classical Langmuir method where the macroscopic sample area is reduced during compression, here the average number of molecules per unit area is constant for large length scales. This means in particular that a closer packing of the molecules in parts (domains) of the monolayer must result in a looser packing or even the formation of voids in other parts of the layer. The van der Waals interaction between the alkane chains in this less densely packed regions is reduced so that a further energy reduction is needed to enable (crystalline) structure formation. It is therefore plausible to assume that the two phases are present over an extended temperature interval as indicated in figure 3.13. The same mechanism is most likely the reason for the occurrence of the high temperature phase in the diffraction pattern recorded at a sample temperature of -40°C: the energy of the system as well as the thermal surface fluctuations are reduced such that structure formation in the non-crystalline parts of the monolayer becomes feasible. However, at this stage a possible kinetic mechanism cannot be ruled out: the presence of the high temperature phase with tilted chains as a metastable phase occurring during the cooling process and the formation of crystalline domains. The transition of this metastable phase into the stable crystalline phase with upright chain configuration would depend on the ability of the molecules to reorganise at the surface and thus on their mobility. With decreasing temperature the viscosity of the subhase increases significantly (see section 1.2), so that at the same time the mobility of the molecules is reduced according to [59]. Therefore, at lower temperatures the high temperature phase would be existent on longer time scales than at higher temperatures as for instance -20°C. To shed light on this mechanism, time resolved in-situ scattering experiments [35] would have to be performed during a cooling cycle. At temperatures below the two-phase coexisting region, the cross section area per alkane chain is with a value lower than 19.0Å^2 smaller than the limit for a free or even hindered (≈19.3Å^2 [60]) rotator phase so that the corresponding temperature range is

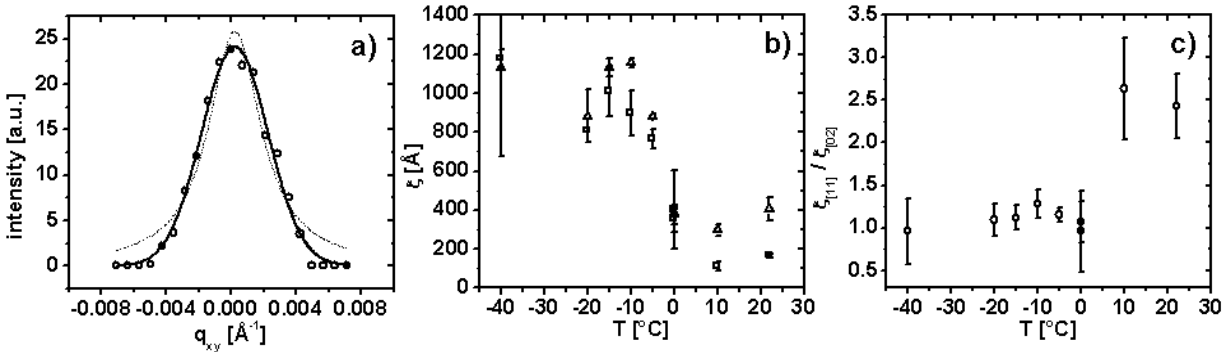

Figure 3.14: a) measured resolution function (open circles), fit to a Gaussian (solid line) and a Lorentzian (dashed line), respectively; b) correlation length according to the Debye-Scherrer formula along the [11] direction (triangles) and the [02] direction (squares); c) ration of the correlation lengths along the [11] and the [02] direction

indicated as crystalline in the phase diagram. Other characteristics of a crystalline phase such as the appearance of reflections of higher Miller indices and the sharpening of diffraction peaks will be discussed below. Section 3.4.1 is devoted to a more detailed analysis of the parameter evolution as a function of the temperature as observed for the different investigated systems, their comparison to the three dimensional pendant such as bulk alkanes and to Langmuir monolayers.

The FWHM Δq_{FWHM} of the diffraction peaks can be related to the size of the crystalline domains within the monolayer via the correlation length ξ, that can be calculated according to the Debye-Scherrer formula [40] as:

$$\boldsymbol{\xi = 0.9 \times \frac{2\pi}{\Delta q_{FWHM}}}. \tag{3.1}$$

Thereby equation (3.1) holds as long as the FWHM of the diffraction peak is larger than the FWHM of the resolution function $\Delta q^{res.}_{FWHM}$. In the case of the used set-up, $\Delta q^{res.}_{FWHM}$ is about $0.004\mathring{A}^{-1}$ as obtained by a fit with a Gaussian line shape (see figure 3.14 a)). The dashed line in figure 3.14 a) represents a best fit to the measured resolution function with a Lorentzian. The better matching with the Gaussian lineshape is evident, thus justifying the use of a Voigt model for the convolution of the intrinsic Lorentzian lineshape of the monolayer diffraction peaks and the instrument resolution. The evolution of the correlation lengths along the [02] direction (open squares) and the [11] direction (open triangles) as a function of the sample temperature are shown in figure 3.14 b). At low temperatures the FWHM of the underlying diffraction peaks approach the resolution limit (e.g. $\Delta q_{FWHM} = (0.0048 \pm 0.0002)\mathring{A}^{-1}$ for the [02] reflection at -40°C), so that the Debye-Scherrer formula might be no longer strictly valid. In addition, extracting peak widths in the coexisting region at 0°C involved integration of the diffraction pattern along different q_z ranges as discussed above. This procedure might cause uncertainties in the FWHM and the corresponding correlation length which exceed the length of the error bar representing just the uncertainty of the lineshape fit. Nevertheless, the increase in the correlation lengths from less than 200Å in the [02] direction to about 1200Å and from

about 400Å in the [11] direction to about 1200Å with decreasing temperature is evident. Thus, the cooling of the monolayer is not only accompanied by a change in the structural conformation involving the two-dimensional lattice and the chain alignment in the unit cell. Moreover, during this cooling process the ordered domains within the layer grow. As already discussed, the particular sample preparation does not exert any additional external constraints like e.g. compression on the monolayer. Therefore, the growth of crystalline domains upon cooling can be attributed to modified interactions within the system. These interactions involve increased net effective van der Waals interactions between the alkane chains in a non-rotator phase as well as reduced thermal fluctuations of the liquid subphase. The growth process might hence be classified as a real self-assembly process, driven only by a change of the (thermal) energy within the system. The ratio $\xi_{[11]}/\xi_{[02]}$ of the correlation lengths along the [11] and the [02] direction is displayed in figure 3.14 c). While at higher temperatures the ratio is close to 2.5, in the crystalline phase at lower temperatures the ratio approaches one. It appears, that in the high temperature phase there is a preferential growth direction, which disappears upon the re-organisation process associated with the cooling of the sample. As the unit cells are rectangular both in the high and the low temperature phase, it seems to be more likely that the preferential growth direction is associated with the horizontal tilt angle of the alkane chain [37]. During the cooling process the alkane chains become upright and thus the preferential direction within the two-dimensional lattice vanishes.

Reflections of higher Miller indices

The crystalline low temperature phase of the eicosanoic acid monolayer is not only characterised by a sharpening of the diffraction peaks associated with a growth of the crystalline domains as discussed above. Like investigations of bulk systems of normal alkanes suggest, the crystalline phase also features a small thermal Debye-Waller factor and an improved organisation of the molecules [27]. Consequently, the maximum wavevector transfer up to which reflections could be observed is increased. At sample temperatures of -20°C and -40°C a systematic search for reflections with higher Miller indices was performed. The obtained diffraction peaks are displayed in figure 3.15 a) and b), respectively. The peak intensities differ quite remarkable as a function of the wavevector transfer q_{xy} due to effects like the q-dependent atomic form factor, Debye-Waller factor and polarization factor (see section 2.1.5). Therefore, the intensities of the diffraction peaks at $q_{xy} \geq 2.4\text{Å}^{-1}$ have been scaled, in order to present all reflections in one graphic. It strikes out that at a sample temperature of -20°C the {11} reflection is the most intensive one, while at -40°C the {02} reflection is more intense. The latter observation is most likely an artefact of the attempt to separate the {11} reflection of the low temperature phase from the coexisting reflection of the high temperature phase (see figure 3.12). As a consequence of the chosen cut-off for the integration along q_z, the intensity of that reflection might be underestimated. The indexing of the reflections at both temperatures is in accordance with a centred rectangular lattice. The high q_{xy} region was not scanned entirely, but the possible positions of additional reflections were calculated from the positions of the {11} and {02} reflections and checked afterwards. The advantage of this strategy over a continuos scan is the limitation of the radiation dose to a minimum, thus avoiding unnecessary beam

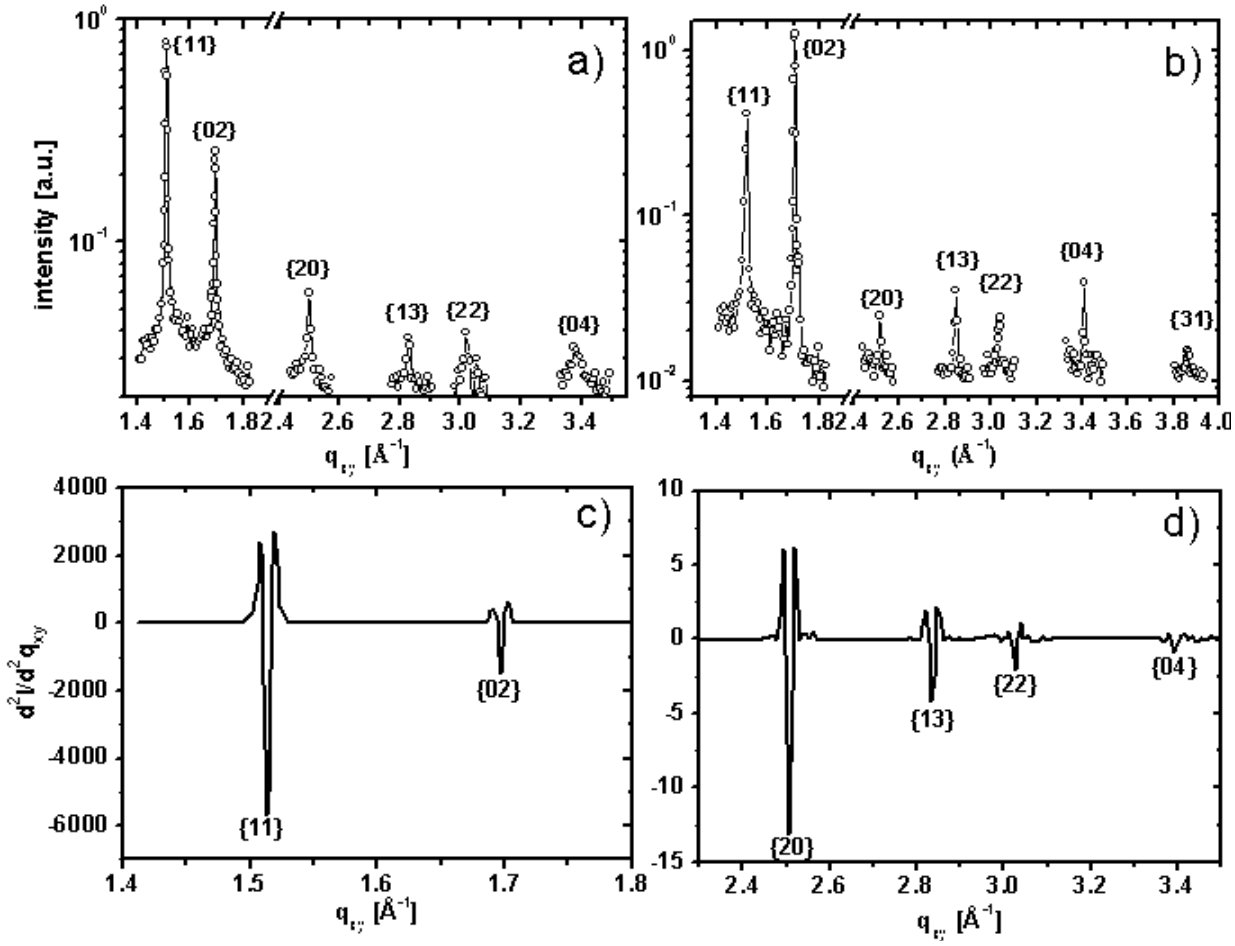

Figure 3.15: All observed reflections for the monolayer of eicosanoic acid at T=-20°C (a)) and T=-40°C (b)) sample temperature; c),d): diffraction peak localisation of the in-plane peaks at -20°C by means of the second derivative

	T=-22°C			T=-40°C		
	q_{xy} [Å^{-1}]	$d_{obs.}$ [Å]	$d_{calc.}$ [Å]	q_{xy} [Å^{-1}]	$d_{obs.}$ [Å]	$d_{calc.}$ [Å]
{11}	1.51003±0.00009	4.1610±0.0002	-	1.5173±0.0004	4.141±0.001	-
{02}	1.6927±0.0004	3.7120±0.0009	-	1.70456±0.00005	3.6861±0.0001	-
{20}	2.5000±0.0005	2.5133±0.0005	2.5122	2.515±0.001	2.498±0.001	2.503
{13}	2.8288±0.0007	2.2211±0.0005	2.2200	2.8468±0.0004	2.2071±0.0003	2.2060
{22}	3.019±0.002	2.081±0.001	2.080	3.0383±0.0004	2.0680±0.0003	2.0705
{04}	3.383±0.002	1.857±0.001	1.858	3.4078±0.0004	1.8438±0.0002	1.8431
{13}	-	-	-	3.865±0.001	1.6257±0.0004	1.6273

Table 3.3: Peak positions with respect to the wavevector transfer q_{xy}, corresponding observed lattice spacing $d_{obs.}$ and calculated lattice spacing $d_{calc.}$ for the reflections at T=-20°C and T=-40°C shown in figure 3.15 a) and b), respectively.

induced degradation of the sample. This becomes particularly crucial as the diffraction peaks are quite narrow and the counting time needed on each point to obtain a reasonable statistic was more than one minute at the largest q_{xy}. However, simultaneous checks on the existence of the 'symmetry forbidden' reflections {21} and {03} revealed no evidence for their existence, implying that their intensity is too weak to make them observable or verifying that the lattice symmetry is indeed centred. A well established method to locate diffraction peaks in a diffraction pattern is the so-called 'second derivative method'. The second derivatives of the diffraction pattern obtained at -20°C at high and low q_{xy} are shown without scaling in the panels c) and d) of figure 3.15, respectively, where the six diffraction peaks are clearly visible. The agreement between the observed peak positions and the theoretically calculated ones is demonstrated by the values given in table 3.3. For each reflection the observed position, the corresponding lattice spacing and the calculated lattice spacing are listed. The latter one was derived from the positions of the first two reflections with the assumption of a rectangular lattice. The excellent agreement between the calculated and the observed lattice spacings is evident. The maximum derivations are about 0.001Å to 0.002Å for both data sets with the exception of the {20} reflection at -40°C, differing by about 0.005Å from its calculated position. This agreement between calculated and measured lattice spacings is of the same order or even better than the agreement found for instance for the rotator phases of bulk alkanes [27].

For most of the reflections listed in table 3.3 not only the in-plane Bragg peaks but also the Bragg rods could be resolved. Figure 3.16 shows the diffraction pattern and the extracted Bragg rods of the {20} (a),b)), {13} (c),d)) and {22} (e),f)) reflections at -20°C. The Bragg rod of the {04} reflection at that temperature could not be resolved; instead the diffraction pattern and the corresponding Bragg rod at a sample temperature of -40°C are shown in panels g) and h). Although the rods at larger q_{xy} become more and more noisy, the match between the measured data (open circles) and the modelled curve (solid line) according to equation (2.22) is satisfactory. It is noteworthy, that with the known tilt angle of the alkane chain ($t = 0\,\mathrm{deg.}$) and length of the representing cylinder ($l = 24$Å) beside a scaling factor there is no additional free parameter in the model.

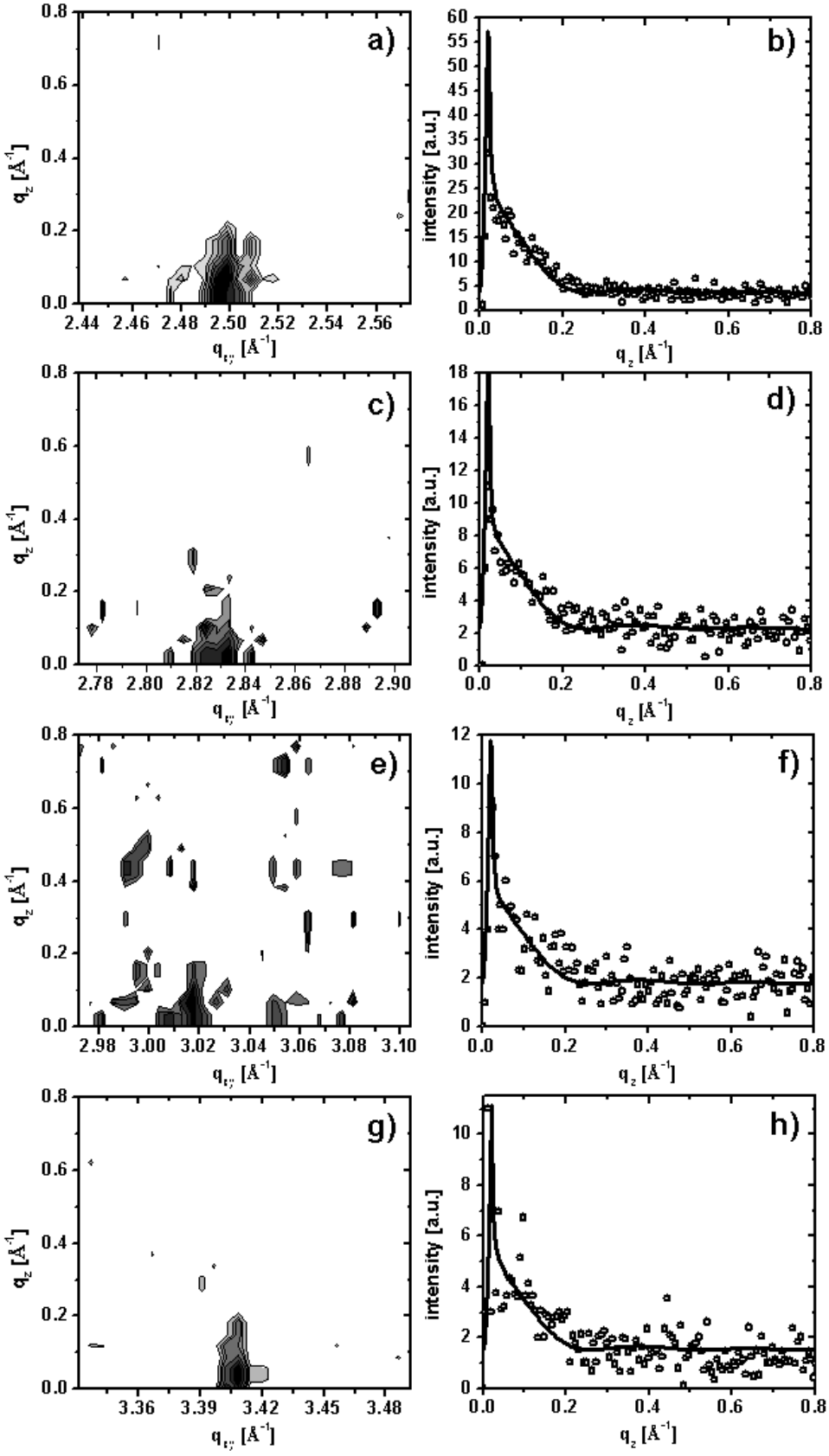

Figure 3.16: Diffraction pattern and corresponding Bragg rods of the reflections {20} (a),b)), {13} (c),d)), {22} (d),f)) of the eicosanoic acid monolayer at T=-20°C; g),h): diffraction pattern and Bragg rod at T=-40°C

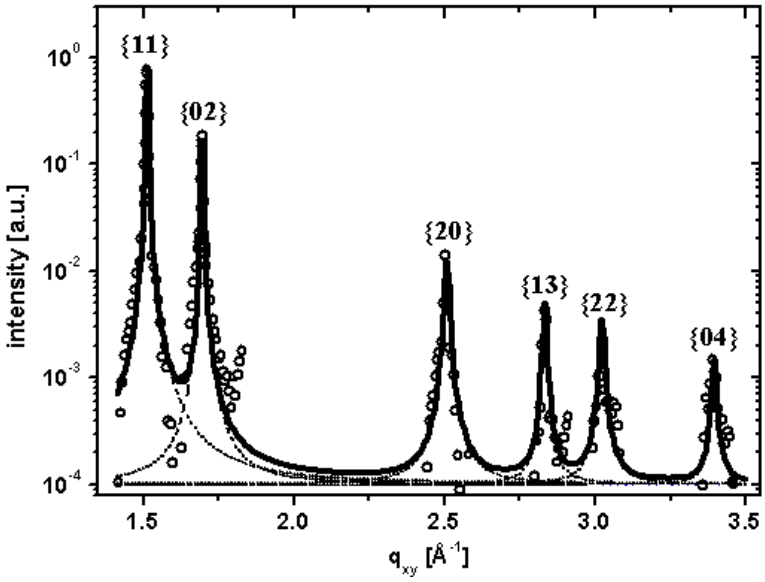

Figure 3.17: Linearised diffraction pattern (open circles) for the monolayer of eicosanoic acid at a sample temperature of -20°C. The solid line is a whole pattern fit using a Voigt line shape function, while the contributions of the individual reflections are given by the dashed lines.

Structure factor calculations

The observability of reflections of higher Miller indices does not only provide a convenient proof of the symmetry of the originating lattice, e.g. by verifying extinction rules, but it also allows for a quantitative analysis of the diffraction peak intensities. As discussed in section (2.1.5), the minimum number of parameters, needed to extract information beyond the scope of the simple cylinder model, is three in the case of a rectangular lattice containing a basis of two scatterers. These parameters are the angle ϕ between an alkane chain C-C plane and a lattice vector, the angle $\Delta\phi$ between the C-C planes of the two alkane chains in the unit cell and an isotropic deplacement parameter u in the Debye-Waller factor. The datasets at -20°C and -40°C provide six and seven diffraction peaks, respectively, to refine the a priori unknown parameters. Thus leading to a ratio diffraction peaks to model parameters of about two. This ratio is smaller than the typical ratio in bulk single crystallography (e.g. refinement of the crystal structure of octadecanoic acid [120]: 2392 measured reflections, 325 refinement parameters, ratio about 7.4), but nevertheless sufficient for a good estimation of the parameters. The peak intensity of the {11} reflection of the crystalline phase at a sample temperature of -40°C is difficult to determine, due to the overlap with the coexisting tilted phase as discussed above. Therefore, the quantitative analysis of the peak intensities is restricted to the dataset taken at a sample temperature of -20°C, despite of the {13} reflection being not observed at that temperature.

The diffraction pattern integrated along q_z in the range $0 \leq q_z \leq 0.43 \mathring{A}^{-1}$ was treated as described in section 2.1.5: The high resolution data containing the {11} and the {02}

reflection were smoothed using a Savitzky-Golay filter with a span of seven data points and a polynomial order of one. For the other datasets a span of five points was employed. Preserving the maxima and widths of the diffraction peaks as accurately as possible is crucial for the application of a lineshape fit in a later step of the data treatment. Therefore, all datasets have been smoothed only in the background region around the sharp diffraction peaks as described in (2.1.5). Background points were identified in the data sets by the algorithm given by Snyder [110] as discussed above. This set of data points was approximated by a polynomial of order seven and subtracted from the integrated diffraction pattern. A whole pattern fit according to equation (2.41) was performed, using a Voigt (equation (2.42)) as the peak shape function and fixing the FWHM of its Gaussian content to the FWHM of the instrumental resolution function (see figure 3.14 a) and accompanying text). The whole pattern lineshape fit of the linearised diffraction pattern is shown in figure 3.17, where the contributions of the single peaks are indicated by the dashed lines while the solid line represents their superposition. The lineshapes of the individual peaks were integrated in a range of five times their FWHM around their center, in order to determine their integrated intensity. The results are shown in the second column of table 3.4 normalised to the intensity of the {11} reflection. As the measurements are not made to determine absolute intensities, the relative intensities will be used for the structure factor modelling as discussed in section (2.1.5). For comparison table 3.4 also lists the relative peak intensities for an integration range of one FWHM around the peak center ($I_{FWHM}/I^{\{11\}}_{FWHM}$), the relative intensities for an integration range extended towards infinity ($I_{\infty}/I^{\{11\}}_{\infty}$) and the relative maximum peak intensities ($I_{\max}/I^{\{11\}}_{\max}$). For the very sharp and intense diffraction peaks like the {02} reflection the peak area is proportional to the peak height so that the different integration ranges do not strongly influence the relative intensities. The exception is the extension of the integration range towards infinity, leading especially in the case of the less intensive diffraction peaks to quite different relative intensities as compared to the other methods. Although the maximum integration range used for this method should provide theoretically the best estimation of a diffraction peak intensity, as it collects all the scattered intensity, this method is not used practically. The reason for this is the large influence of small derivations between the line shape fit and the measured data that might cause huge differences by summing up over the extended integration range. The values are hence only shown for the sake of completeness. The diffraction peaks at larger wavevector transfer q_{xy} appear to be slightly broadened, so consequently their peak height is no longer proportional to the peak area [51]. Therefore, integration of the lineshape profiles becomes a necessity and consequently the relative intensities $I_{5\times FWHM}/I^{\{11\}}_{5\times FWHM}$ are used for the structure factor calculations discussed below. The calculations were performed as a two step process: in a first step the (relative) intensities of the diffraction peaks were calculated as a function of the free refinement parameters. So, in contrast to a classical least-square minimization method, the whole phase space is simulated and afterwards searched for the global minimum. While this procedure is clearly unpractical for the refinement of bulk crystallographical data due to the hundreds of refinement parameters involved, for the current problem with its very limited number of parameters it is affordable in terms of calculation time. Moreover, the possibility to present this low dimensionally phase space graphically allows for a good overview of all global and local minima and the accompanied alignment of the

	$I_{5\times FWHM}/I^{\{11\}}_{5\times FWHM}$	$I_{FWHM}/I^{\{11\}}_{FWHM}$	$I_{\infty}/I^{\{11\}}_{\infty}$	$I_{\max}/I^{\{11\}}_{\max}$
{11}	1	1	1	1
{02}	0.2632	0.2632	0.2632	0.2632
{20}	0.01296	0.0115	0.0316	0.0117
{13}	0.0051	0.0046	0.0105	0.0047
{22}	0.00364	0.0032	0.0095	0.0033
{04}	0.00115	0.00108	0.0038	0.0010

Table 3.4: Relative peak intensities as extracted from the linearised diffraction pattern for the monolayer of eicoscanoic acid. $I_{5\times FWHM}/I^{\{11\}}_{5\times FWHM}$: integration range five times the FWHM around the center of the reflection; $I_{FWHM}/I^{\{11\}}_{FWHM}$ integration range of one FWHM around the center of the reflection; $I_{\infty}/I^{\{11\}}_{\infty}$: integration range extended towards infinity; $I_{\max}/I^{\{11\}}_{\max}$: relative maxima of the diffraction peaks

alkane chains within the unit cell. The peak intensities of the individual reflections were calculated according to equation (2.50) but without taking the in-plane Debye-Waller factor into account. The lattice parameters of the rectangular unit cell were $a = 7.42\mathring{A}^{-1}$ and $b = 5.02\mathring{A}^{-1}$, as obtained from the analysis of the corresponding GIXD dataset. The cut-off out-of-plane wavevector transfer in the integral of equation (2.50)was set to $Q_z^{cut-off} = 0.43\mathring{A}^{-1}$, the same value up to which the experimentally obtained diffraction pattern were integrated. The intensity phase space was simulated as the function of the two angles ϕ (between the C-C plane of the alkane chain in the origin of the unit cell and the lattice vector b) and $\Delta\phi$ (between the C-C plane of the alkane chain in the center of the unit cell and the one in the origin, see figure 2.13) in the range $0 \leq \phi \leq 180°$, $0 \leq \Delta\phi \leq 180°$ with a step width of 2°. Intensity maps of degenerated reflections were superimposed to make up for the multiplicity of the reflection. In a subsequent step the intensities were transformed to relative intensities by normalisation to the {11} intensity map. These intensities multiplied with an in-plane Debye-Waller factor were compared to the experimentally observed ones, where the degree of agreement between the theoretical values and the measured data was quantified by the R-values defined in section 2.1.5. As already discussed therein, the definition of the R-value according to Rietveld (equation 2.54) is not very practical in this context as it puts a too strong weight on the first very intense reflection. Therefore, the sum R_Σ of the individual R-values (equation 2.55) will be used in the following as a reference. In a next step, the displacement parameter u of the Debye-Waller factor was determined by plotting the global minimum of R_Σ as a function of u. The result is shown in figure 3.19 a), leading to a global minimum of $R_\Sigma = 0.9291$ for $u = 0.181\mathring{A}$. This value is smaller than the one of $u = 0.27\mathring{A}$ estimated for a monolayer of phospholipids coupled to the surface of a complex fluid [126]. Taking the denser packing and the higher subphase viscosity of the present system into consideration, a further reduction of the fluctuations as compared to the previously studied system seems plausible. The R-values of the individual reflections R^{ind} and their sum as a function of the two remaining refinement parameters ϕ and $\Delta\phi$ are shown in figure 3.18. The minimum regions of R_Σ are marked by the thick red contour lines. This contour lines were transferred onto the other map plots as a mask, proving that the minimum regions of R_Σ coincide

$\Delta\phi \approx 90°$	$\Delta\phi \approx 270°$
0°-20°	0°-25°
90°-120°	60°-90°
155°-180°	160°-180°

Table 3.5: Intervals for ϕ at fixed $\Delta\phi$ which lead to equivalent minima in the R_Σ matrix

with the minimum regions of the R-values of the individual reflections. The total R-value according to the definition by Rietveld is shown as a function of ϕ and $\Delta\phi$ in figure 3.19 b). Comparison with the individual R factor of the {02} reflection (figure 3.18 top right panel) reveals that the two map plots are almost indistinguishable, thus reflecting that this definition of the R-value almost completely neglects the match between measured and calculated intensities for the weaker reflections. Cuts through the map of R_Σ at constant angle ϕ are shown in figure 3.19 c) for $\phi = 0°$(solid line), $\phi = 45°$ (dashed line) and $\phi = 90°$ All three profiles show minima at around $\Delta\phi = 90°$ and $\Delta\phi = 270°$, indicated by the two dashed vertical lines in the plot. This two angles correspond to the herringbone alignment of the C-C planes of the two alkane chains within the unit cell. This alignment of the two chains relative to each other is a quite robust result of the structure factor calculation. The only two possibilities involve a rotation of the chain around its length axis by 180°. Although this rotation does not lead to identical atomic positions, the differences in the structure factor calculations are way to small to rule out one of the two possibilities. In contrast to the relative alignment of the chains with respect to each other, their absolute orientation within the two-dimensional unit cell as defined by the angle ϕ is less unambiguously determined. The minima in R_Σ at $\phi \approx 0°$ and $\phi \approx 180°$ only imply a rotation of the chain at the origin of the unit cell around its length axis by 180°, while its C-C plane is in both cases oriented parallel to the lattice vector b. As a different possibility, similar minima in the R_Σ and the corresponding cut in figure 3.19 c) can be found for $\phi \approx 90°$ which would imply an orientation of the C-C plane perpendicular to the lattice vector b. In contrast, the classical herringbone alignment would involve a twist angle of about 45 deg . with respect to the lattice vector. However, this alignment leads to larger R_Σ values as can be seen for instance from the profile at constant $\phi = 45°$ (dashed line in figure 3.19 c)): The minima of this curve as a function of $\Delta\phi$ are about 40% larger as compared to the cases of $\phi = 0°$ or $\phi = 90°$. An overview about the parameters ϕ and $\Delta\phi$ which lead to similar values of R_Σ is given in table 3.5. In the following the possible plane groups for the different packings will be discussed. From a strict crystallographic point of view the alkane chain even in an upright configuration does not exhibit a vertical two-fold axis. Nevertheless, as suggested by the above described structure factor calculations, the differences induced by a 180° rotation of the chain around its longitudinal axis are quite small. Therefore, in the following the discussion will be carried out considering a symmetric and an asymmetric chain in parallel. The classical herringbone ordering would result in plane groups p2gg for the case of symmetric chains and in p1g for asymmetric chains. However, these plane groups require the exact values of 45° for ϕ and 90° for $\Delta\phi$ as otherwise the glide mirror symmetries are lost. As $\phi = 45°$ is not a minimum of the R-factor analysis, these two plane groups have to be ruled out. Sketches of the chain alignment within the unit cell for the 'general' case $\phi \approx 20°$ and $\Delta\phi = 90°$ as well as

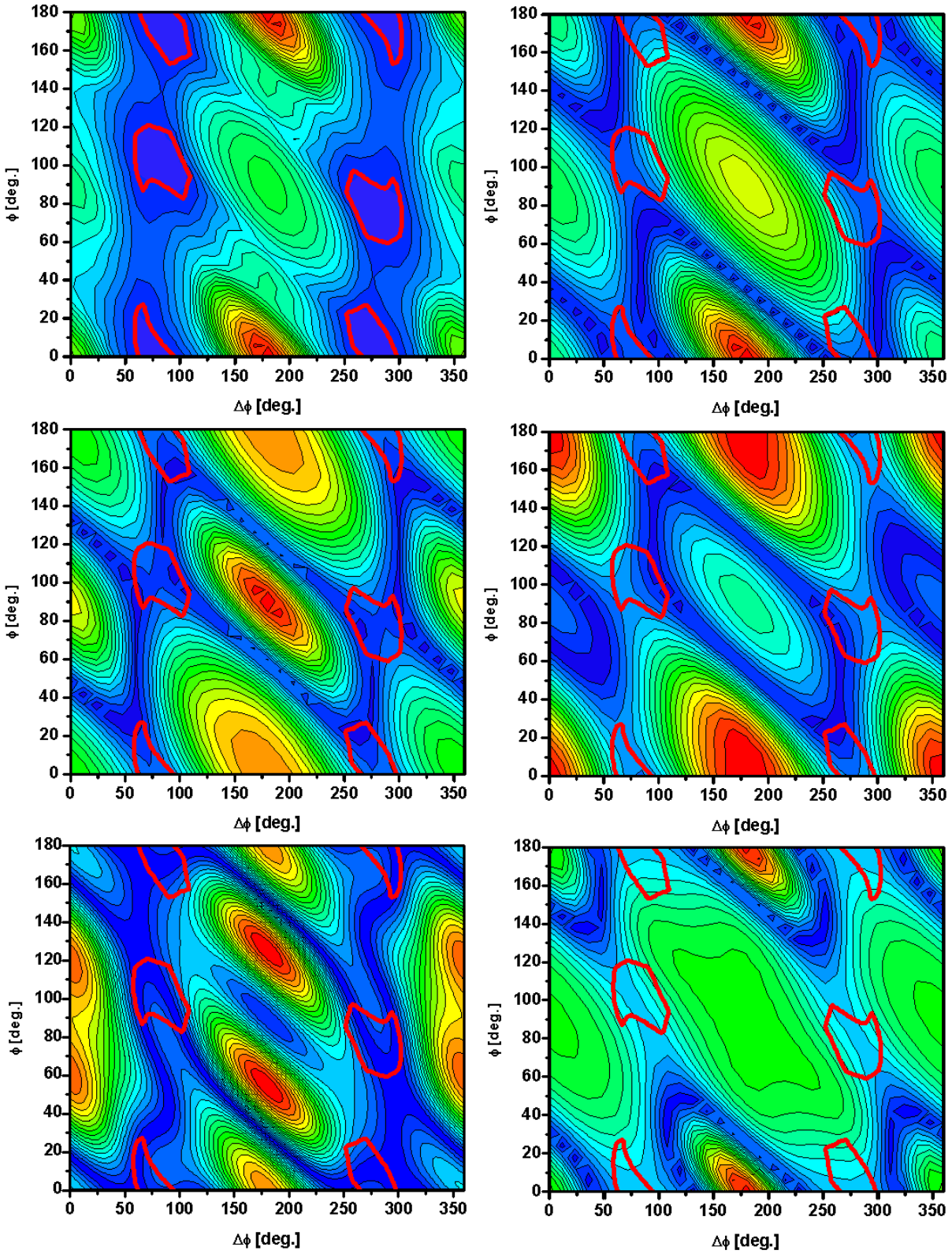

Figure 3.18: R-values of the individual reflections and their sum R_Σ. Left colum: R_Σ, $R_{ind.}^{\{20\}}$, $R_{ind.}^{\{22\}}$ (top to bottom); right colum:$R_{ind.}^{\{02\}}$, $R_{ind.}^{\{13\}}$, $R_{ind.}^{\{04\}}$ (top to bottom) Color mapping: increasing from blue to read in linear scale. Areas surrounded by thick red contour lines in the map plot for R_Σ mark the minimum regions at a level of 0.92 to 1.15. In the other plots these countour lines are superimposed as a mask.

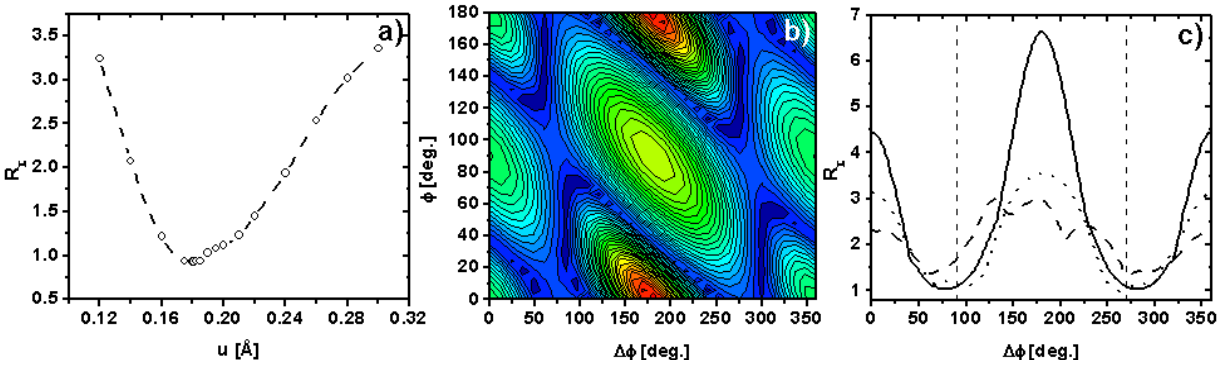

Figure 3.19: a) global minimum of R_Σ as a function of the Debye-Waller displacement parameter u; b) map of the R value according to the original definition by Rietveld; c) cuts through the R_Σ map at constant ϕ, solid line: $\phi = 0°$, dashed line: $\phi = 45°$, dotted line: $\phi = 90°$; the dashed vertical lines indicate $\Delta\phi = 90°$ and $\Delta\phi = 270°$, respectively.

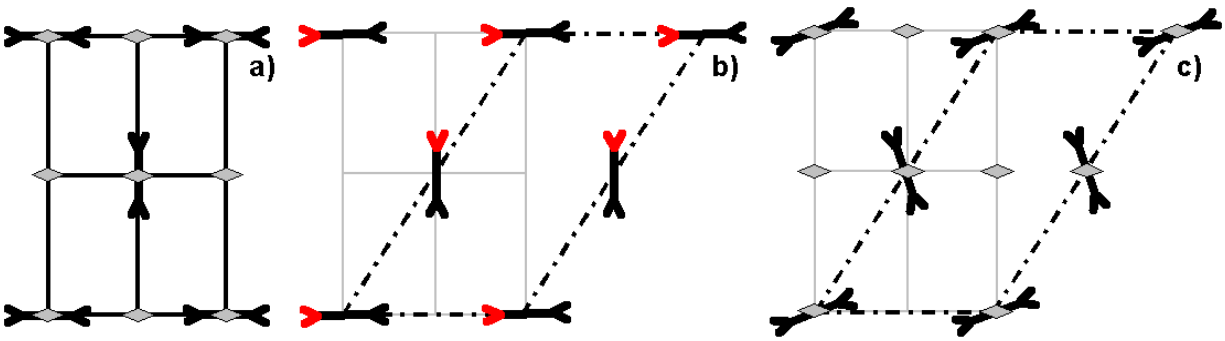

Figure 3.20: Possible chain alignments and corresponding plane groups for the parameters found by structure factor calculations. a) $\phi = 0°$, $\Delta\phi = 90°$, symmetric chains: plane group p2mm. b) $\phi = 0°$, $\Delta\phi = 90°$, asymmetric chains: plane group p1. c) $\phi \approx 20°$, $\Delta\phi = 90°$, symmetric chains: plane group p2. The dashed dotted lines in panel b) and c) show the primitive unit cell with two chains as a basis.

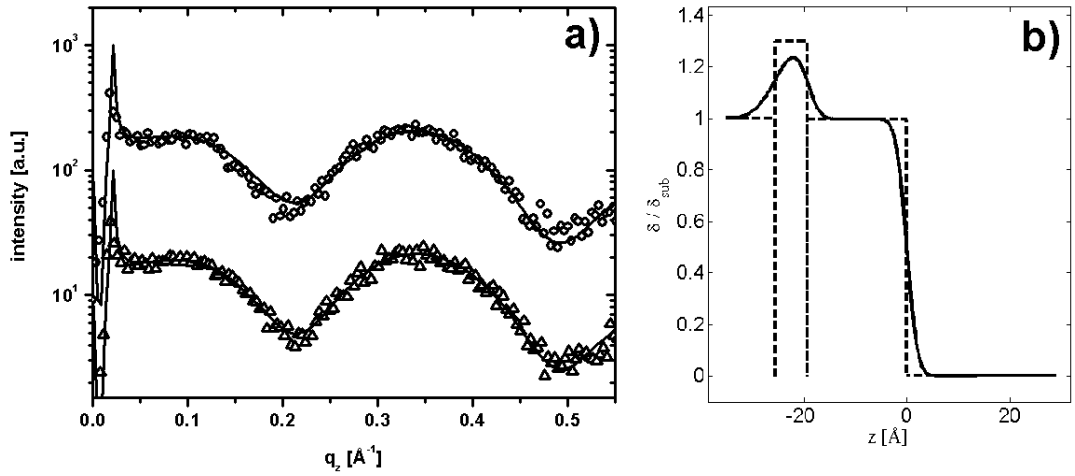

Figure 3.21: a) GIXOS curves for DPPA on DMSO/H_2O at 22°C (open triangles) and -38°C (open circles). The solid lines are fits employing a two box model corresponding to a headgroup and an alkane chain layer. b) Normalised scattering length density profile, dashed line: box model without roughness, solid line: error-function profile

for the particular symmetric case ($\phi = 0°$ and $\Delta\phi = 90°$) are shown in figure 3.20 both for the assumption of symmetric and asymmetric chains. In the case of symmetric chains and $\phi = 0°$, $\Delta\phi = 90°$ (panel a)) the symmetry elements are a two-fold rotation axis and perpendicular mirror lines. As all rotation centers lie on mirror lines, the plane group is identified as p2mm. In the case of asymmetric chains (panel b)), the two-fold rotation axis and the mirror lines disappear. As there is also no glide mirror line, the plane group is in this case identified as p1. In the more general case of $\phi \approx 20°$ and $\Delta\phi = 90°$ (panel c)), the only symmetry element is a two-fold rotation axis with the assumption of symmetric chains. In this case the corresponding plane group is p2, while it is p1 for asymmetric chains as already shown in figure 3.20 b) for the special case of $\phi = 0°$, $\Delta\phi = 90°$.

3.3.2 DPPA Monolayer on DMSO/H_2O

Monolayers of DPPA were prepared on subphases of DMSO/H_2O in a similar way than described for the monolayers of eicosanoic acid (section 3.3.1). The layers were spread from a chloroform/methanol solution at a concentration of 0.17 mg/ml up to a surface pressure of 30mN/m, which was determined *in-situ* by means of a tensiometer. The applied cooling rate at the sample position was 0.5°C/min. and all monitored temperatures were allowed to stabilise prior to data acquisition.

The monolayer structure normal to the surface was investigated by GIXOS measurements. The scattering curves taken in the temperature range between 22°C and -38°C were almost completely superimposable, indicating very little changes of the monlayer structure perpendicular to the surface. Two representative curves measured at temperatures of 22°C (open triangles) and -38°C (open circles) are shown in figure 3.21 a). The solid lines are fits according to equation (2.71), using a two layer model. The first layer in this model corresponds to the headgroup of the phospholipid, while the second one

T [°C]	δ_1/δ_{sub}	d_1 [Å]	σ_1 [Å]	δ_2/δ_{sub}	d_2 [Å]	σ_2 [Å]
22	1.35	5.9	2.2	0.99	19.3	1.7
-38	1.30	6.2	1.9	1.00	19.3	1.7

Table 3.6: Parameters obtained by fitting the GIXOS curves shown in figure 3.21 a). The parameters discribing the DPPA monolayer are the normalised scattering length density of the headgroup layer δ_1/δ_{sub}, its thickness d_1,the roughness at the headgroup/chain interface σ_1, the normalised scattering length density of the alkane chain layer δ_2/δ_{sub}, its thickness d_2 and the roughness of the chain/atmosphere interface σ_2.

represents the alkane chains. The corresponding fit parameters are summarised in table 3.6. The roughness at the subphase/headgroup interface was found to be about 3.3Å at all temperatures. For the alkane chain layer the scattering length densities and layer thicknesses are almost identical at both temperatures. Only for the headgroup layer a small increase in the thickness of about 0.3Å is observed, which might be just due to an artefact or to a slight standing up of the headgroups being packed closer together at lower temperature. Consequently, simultaneous to the increase of the layer thickness, the corresponding scattering length density is decreasing such as the product $\delta_1/\delta_{sub} \times d_1$ remains constant at a value of about 8.0Å. The constant value of this product is thereby a direct consequence of the layer preparation as outlined in section 3.3.1. Like in the case of eicosanoic acid, the GIXOS measurements prove the existance of a defined monolayer over the entire investigated temperature range.

Monolayers of DPPA were prepared for the investigation by GIXD in the same way as for the GIXOS experiments. The evolution of the diffraction pattern as a function of the wavevector transfers q_{xy} and q_z in the temperature range -49°C≤T≤22°C is shown in figure 3.22. In the scanned in-plane range of 1.40Å^{-1} ≤q_{xy} ≤1.83Å^{-1} up to a temperature of -6.0°C only one diffraction peak can be observed. Upon further cooling (panels e)-j)) this diffraction peak splits into two and their separation becomes more and more distinct at lower temperatures. The intensities of the diffraction pattern shown in figure 3.22 integrated along q_z in the range 0≤q_z ≤0.19Å^{-1} are displayed in figure 3.23. The jump of the intense diffraction peak towards smaller q_{xy} values between curves d) (T=-6.0°C) and e) (T=-15.0°C) is evident. This jump in the peak position is accompanied by the occurrence of a second, weaker diffraction peak at larger q_{xy}, indicated by the black arrow in curve e). The qualitative interpretation of this experimental findings is a change of the two-dimensional lattice from a hexagonal one at higher temperatures to a rectangular one at lower temperatures. While the hexagonal lattice exhibits only one constituting lattice spacing, the rectangular lattice exhibits two. While one of these lattice spacings is larger then in the hexagonal case, corresponding to a peak shift towards smaller q_{xy}, the other one is smaller and hence the corresponding in-plane Bragg peaks appears at larger q_{xy}. A more detailed analysis of the structure and the chain alignment is shown in figure 3.24. The center of the Bragg peak corresponding to curve a) in figure 3.23 is $q_{xy} = 1.5172\mathring{A}^{-1}$ as obtained by line profile fitting using a Voigt function. Panel a) displays the measured Bragg rod at the peak position (open circles) and the modelled curve based on the cylinder model according to equation 3.24 (solid line). The parameters used were a length of the chain of $L = 17\mathring{A}$, a standard radius of $0.44\mathring{A}$ for the cylinder representing the alkane

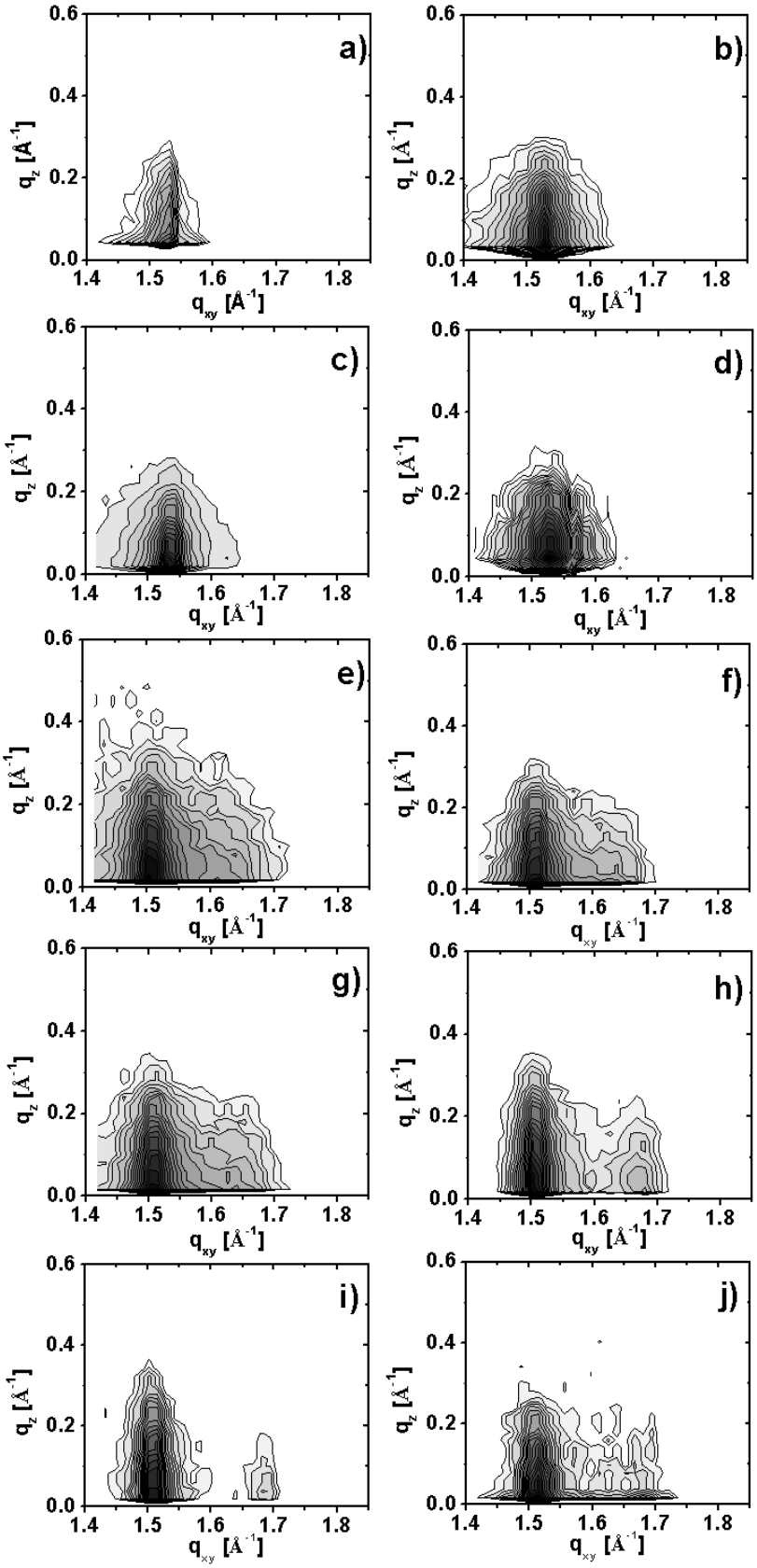

Figure 3.22: Diffraction pattern for a monolayer of DPPA on a subphase of DMSO/H_2O upon cooling. a) 22°C, b) 1.5°C, c) -1.5°C, d) -6°C, e) -15°C, f) -22°C, g) -28°C, h) -30°C, i) -40°C, j) -49°C,

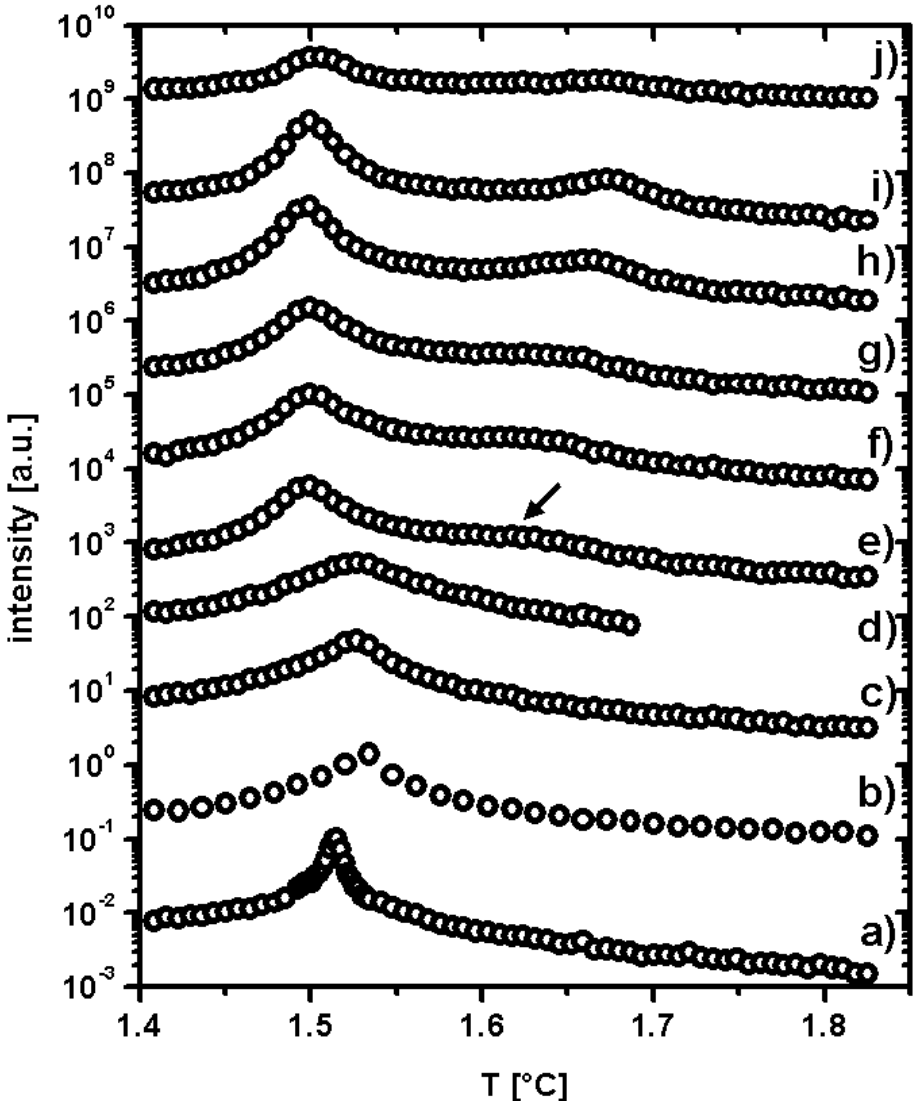

Figure 3.23: Intensity of the diffraction pattern shown in figure 3.22 integrated along q_z. The black arrow indicates the occurrence of a second diffraction peak, indicating a phase change from a hexagonal to a rectangular lattice. At the same time a shift of the more intense diffraction peak towards smaller q_{xy} can be observed.

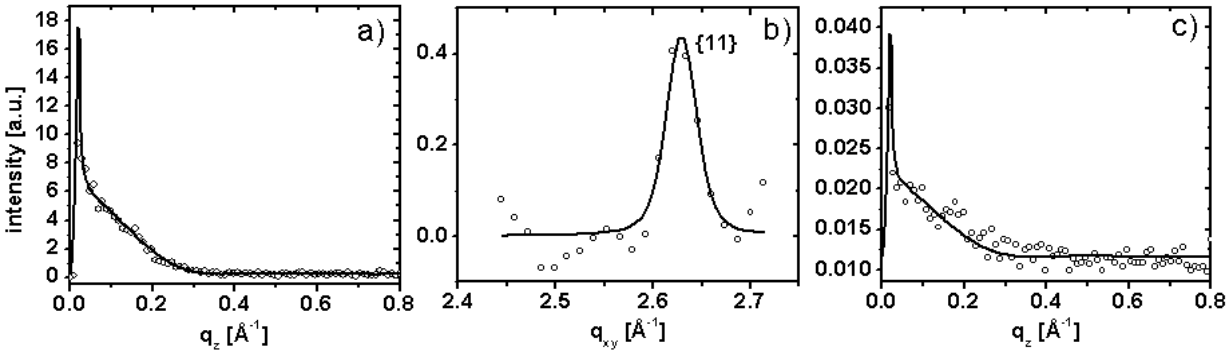

Figure 3.24: Details for the DPPA monolayer at T=22°C. a) Measured Bragg rod (open circles) and modelled curve (solid line) of the {10} Bragg reflection at $q_{xy} = 1.5172\mathring{A}^{-1}$. b) {11} in-plane Bragg peak, the solid line is a fit to a Voigt profile. c) Bragg rod and modelled curve of the {11} Bragg reflection.

chain and a tilt angle $t = 0°$ between the chain and the surface normal. The length of the alkane chain is shorter than the theoretical value of about $20.4\mathring{A}$ for the complete alkane chain in an all-trans conformation or the $19\mathring{A}$ one would expect if the terminal methyl group stays in a liquid like state. Nevertheless, the findings of slightly shorter chains is not unusual for phospholipid monolayers and might be an indication that not all CH_2 groups of the chain are in an ordered state, but the end becomes more liquid-like. The restriction to only one observable Bragg reflection within the scanned q_{xy} region suggests a hexagonal lattice with an upright chain conformation as revealed by Bragg rod analysis. Thus, the reflection is highly degenerated as it consists of the superposition of the (10), (01), $(\overline{1}0)$, $(0\overline{1})$, $(\overline{1}1)$ and $(1\overline{1})$ reflections and is therefore indexed as {10}. The next reflection of higher index for the hexagonal symmetry appears at $\sqrt{3}q_{xy}^{\{10\}} = q_{xy}^{\{11\}}$. An in-plane scan of the region of interest is shown in panel b). The position of the observed Bragg peak as obtained by the fit of a Voigt model (solid line) to the data points is $q_{xy} = 2.6252\mathring{A}^{-1}$, which is in excellent agreement with the calculated position of $2.6278\mathring{A}^{-1}$. Due to the upright chain conformation the {11} Bragg peak comprehends the (11), $(\overline{1}\overline{1})$, $(2\overline{1})$, $(\overline{2}1)$, $(1\overline{2})$ and $(\overline{1}2)$ reflections. The Bragg rod measured at the peak position as well as the modelled curve is shown in figure 3.24c). Beside of a scaling factor and the background there are no free parameters as L, R and t were already determined by the Bragg rod belonging to the {10} reflection. Up to a sample temperature of less than -6°C the structure remains unchanged. In contrast, at -15°C the intense diffraction peak shifts towards smaller q_{xy} and a second peak at larger q_{xy} occurs. A more detailed analysis of the structure at this temperature is shown in figure 3.25. The diffraction pattern integrated along q_z is shown in panel a) as circles, while the solid line represents a pattern fit using Voigt functions to model the diffraction peaks. The peaks were found to be centered at $q_{xy} = 1.5019\mathring{A}^{-1}$ and $q_{xy} = 1.6368\mathring{A}^{-1}$, respectively. The indexing of the diffraction peaks according to a centred rectangular lattice and the degeneration of the diffraction peaks is the same as explained for the crystalline phase with upright chain conformation of the eicosanoic acid monolayer presented in section 3.3.1. The two

Bragg rods measured at the positions of the {11} and {02} in-plane reflections are shown in the panels b) and c), respectively. Modelling of these Bragg rods reveal unchanged parameters for the cylinder length L and the tilt angle t, signifying in particular that the chain conformation in this phase remains upright. An out-of-plane profile taken at the in-plane position $q_{xy} = \sqrt{3}q_{xy}^{\{11\}}$ is shown in figure 3.25 d). The absence of a Bragg rod-like profile indicates the absence of the corresponding Bragg reflection. This findings seem logic with the afore chosen assignation of the diffraction peaks as a rectangular phase, but they are nevertheless important as they rule out the possibility of a coexistence of two hexagonal phases with different lattice spacings. In the case of eicosanoic acid undergoing a phase transition from a rotator to a crystalline phase, the assignment of the diffraction peaks was facilitated by the relationship between their maxima in respect to q_z. For instance, a set of reflections fulfilling the relation (2.33) almost certainly belong to the same phase. Contrary, for an upright chain conformation the main information that can be extracted from the Bragg rod is the length of the cylinder representing the length of the scatterer. Therefore, the disappearance of the {11} reflection of the hexagonal lattice is an important information for the determination of the structure based only on a very limited number of diffraction peaks. The out-of-plane profile rather than a complete in-plane scan was recorded in order to minimise the radiation dose on the sample as each data point in a scan would have required an acquisition time of about one minute for a reasonable statistic. Upon further cooling, the separation of the two diffraction peaks with respect to q_{xy} is increasing. This is an indicative for the unit cell becoming more and more distorted from a hexagonal one. At a sample temperature of -40°C the two in-plane reflections are well separated as can be seen from the integrated diffraction pattern shown in figure 3.26 a). The peak positions as obtained by peak profile fitting are $q_{xy} = 1.503\mathring{A}^{-1}$ and $q_{xy} = 1.678\mathring{A}^{-1}$ for the {11} and the {02} reflections, respectively. The corresponding Bragg rods are shown in the panels b) and c), respectively, confirming the preservation of an upright chain conformation during the phase transition from a hexagonal to a centred rectangular phase. The packing of the alkane chains within the phospholipid monolayer is reduced during cooling from $A_0 = 19.80\mathring{A}^2$ at 22°C to $A_0 = 18.81\mathring{A}^2$ at -49°C. As the chain conformation remains upright over the entire investigated temperature range, no distinction needs to be drawn between the unit cell area A_0 per alkane chain and the chain cross section $A_\perp$. In the temperature range -6°C≤T≤22°C A_0 reduces to $19.60\mathring{A}^2$, thus being compatible with a hindered rotator phase. Contrary, at a temperature of -15°C the lattice is deformed into a rectangular one and at the same time the packing density is increased to $A_0 = 19.15\mathring{A}^2$ per alkane chain, thus being the lower limit for a hindered rotator phase. A more detailed discussion of the evolution of parameters like the lattice vectors upon cooling and a comparison to three dimensional systems is given in section 3.4.1.

The broadening of the in-plane diffraction peaks with decreasing temperature is evident from the curves shown in figure 3.23. For a more quantitative discussion, the correlation lengths as obtained from the FWHM of the diffraction peaks by means of equation 3.1 are shown in figure 3.27. Here ξ refers in the hexagonal phase at high temperatures to the correlation length related to the {10} reflection, while at lower temperatures the {11} reflection of the rectangular lattice serves as a reference. The {02} reflection of the latter phase is in contrast too weak to allow for a precise determination of its FWHM. The cor-

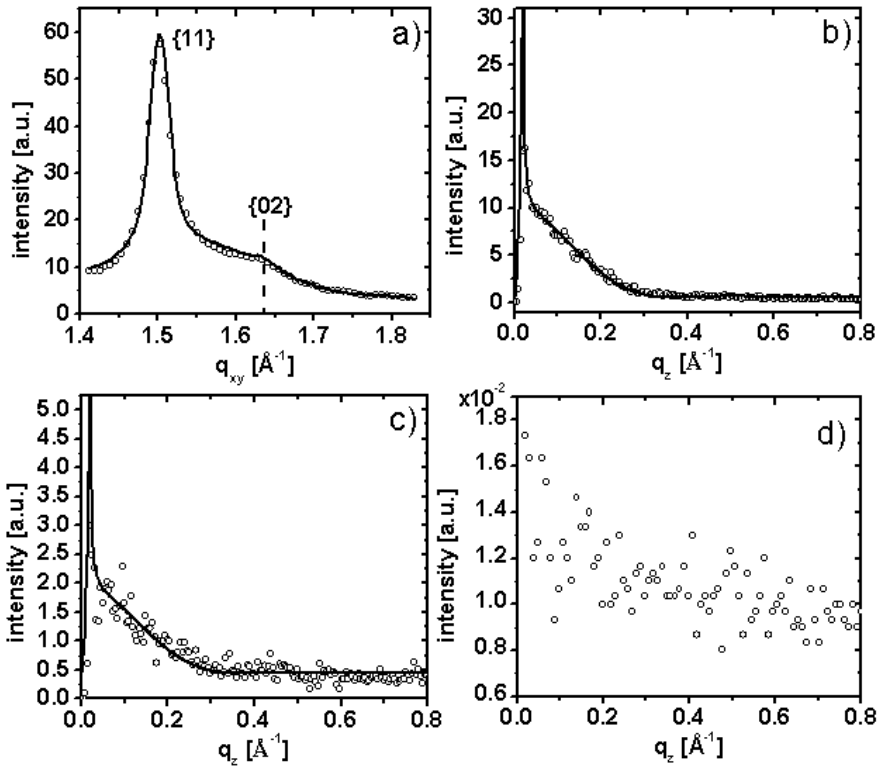

Figure 3.25: Details for the DPPA monolayer on DMSO/H2O at a sample temperature of -15°C. a) diffraction pattern integrated along q_z, the in-plane Bragg peaks were fitted with a superposition of two Voigt profiles, the dashed vertical line marks the center of the {02} reflection. b), c) measured Bragg rods (open circles) and modelled curves according to the cylinder model (solid lines) for the Bragg rods of the {11} and {02} reflection, respectively. d) out-of-plane profile taken at $q_{xy} = \sqrt{3}q_{xy}^{\{11\}}$: the absence of a Bragg rod at this in-plane position confirms the assignment of the two diffraction peaks to a rectangular phase rather than two independent hexagonal once.

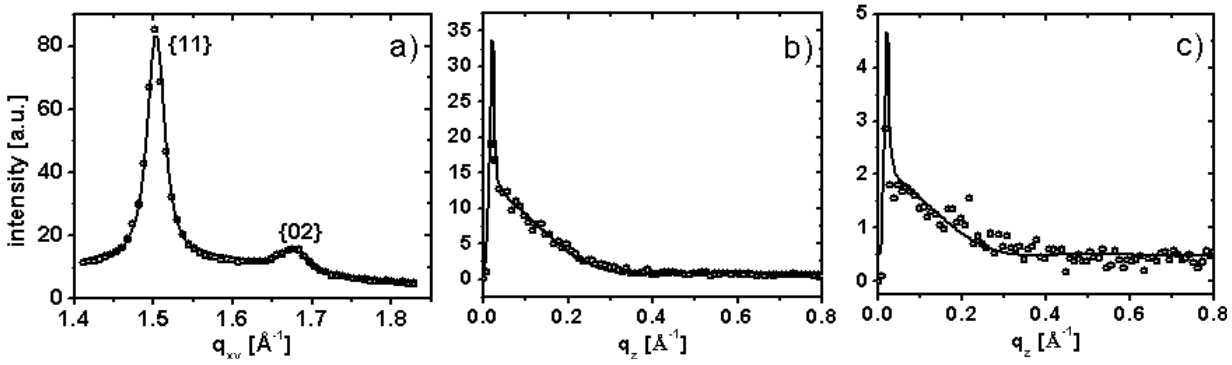

Figure 3.26: a) integrated diffraction pattern at a sample temperature of -40°C and fit to a two superposition of two Voigt functions; b),c): measured Bragg rods and modelled curves according to the cylinder model for the {11} and {02} reflections, respectively.

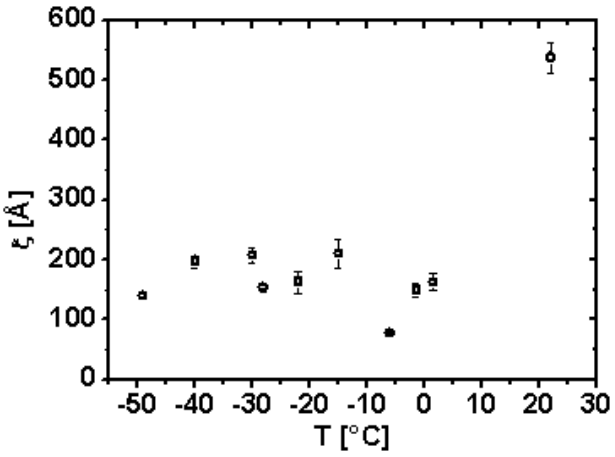

Figure 3.27: Correlation length ξ of the ordered domains in the DPPA monolayer on DMSO/H_2O as a function of temperature.

responding correlation lengths are therefore omitted from the graph. It strikes out, that the largest correlation length of 540Å is obtained at the initial temperature of 22°C, while upon decreasing the temperature the correlation length is reduced to 150Å at -1.5°C. A minimum of 80Å is reached at a temperature of -6°C and upon further temperature decrease the correlation length increases again, reaching values of 150 to 200 Å. A self-evident reason for the occurrence of the minimum at -6°C might be the assumption of two overlapping diffraction peaks belonging to a slightly distorted hexagonal phase. However, the shape of the corresponding diffraction peak was found to be absolutely symmetric, thus contradicting this assumption. Comparing the results for the evolution of the correlation length of the DPPA monolayer with those obtained for eicosanoic acid (see section 3.3.1) a complete different behaviour is found. Instead of a growth of the domains during the phase transition from the rotator to the crystalline phase, the correlation length is reduced by roughly a factor of three. One major difference between the two investigated systems is their initial state: while the eicosanoic acid monolayer was prepared in a state just above the liquid condensed/gas phase transition, the monolayer of DPPA was in a high density LS-phase. It is therefore likely that reorganisation of an already quite densely packed layer results into defects and the break-up of domains into smaller ones. This mechanism is possibly even amplified by the second distinct difference between the two investigated systems: While in the case of eicosanoic acid each molecule exhibits one alkane chain, for DPPA two alkane chains are coupled by the glycerol backbone of the phospholipid. Therefore, the reorganisation of the chains as a reaction to the modified net-effective molecular interactions upon cooling is compromised by this coupling as well as by the more bulky headgroups, resulting in a frustration packing [106] of domains.

3.3.3 LB-Monolayer of Eicosanoic Acid

The rotator-crystalline phase transition as observed for the monolayers of eicosanoic acid and DPPA on a liquid substrate of DMSO/H_2O is accompanied by a structural reorgani-

sation of the molecules within the surface plane. In order to adopt a denser packing of the alkane chains, a certain mobility of the surfactant molecules at the surface is required. In contrast to a liquid surface, the solid surface of a silicon wafer is not decorated by thermally induced capillary waves, but with a static roughness of comparable magnitude of a few Angstroms. The almost complete absence of surface normal fluctuations on a wafer can be considered to favour the van der Waals driven structure formation. In return, the in-plane mobility of the surfactant molecules which are physisorbed to the solid substrate is lower than on a liquid. While the reduced surface normal fluctuations increase the effective interactions between the surfactant molecules, their reduced mobility is supposed to hamper the reorganisation upon a phase change and the corresponding closer packing. In order to investigate how these two contrary mechanisms influence the rotator-crystalline phase transition as well as the corresponding two-dimensional structures, a Langmuir-Blodgett monolayer of eicosanoic acid was investigated by GIXD in the temperature range from about 295K to 30K. The layer was transferred at ambient temperature at a surface pressure of 4mN/m from a $5{\cdot}10^{-4}$M aqueous solution of cadmium chloride onto a hydrophilic silicon wafer as described in section 1.3. The $14{\times}14\text{mm}^2$ samples were mounted horizontally in a liquid helium bath cryostat. The atmosphere around the sample consisted of dry helium gas at a pressure of a few millibars pressure. At an ambient temperature of about 295K only one in-plane Bragg reflection at $q_{xy} = 1.510\text{Å}^{-1}$ could be observed in the range $1.25 \leq q_{xy} \leq 1.85\text{Å}^{-1}$, being indicative of a two-dimensional hexagonal lattice. The observed Bragg rod at the position of the in-plane Bragg peak reveals an upright chain conformation with a chain length of about 22Å. Upon cooling the diffraction peak at around $q_{xy} \approx 1.5\text{Å}^{-1}$ becomes asymmetric with a 'shoulder' towards larger wavevector transfers, indicating an distortion of the hexagonal lattice. At temperatures below 200K a well separated even though weak second diffraction peak is observable corresponding to a rectangular lattice. Figure 3.28 details the diffraction pattern at a sample temperature of 106K. Panel a) shows the intensity distribution as a function of the wavevector transfers q_z and q_{xy}, with the intensity map employing a logarithmic scale. The dashed vertical line is a guide to the eye at the position of the second in-plane reflection. Panel b) displays the diffraction pattern (open circles) integrated along the q_z direction in the range $0 \leq q_z \leq 0.15\text{Å}^{-1}$. The solid line is a fit to a superposition of two Voigt profiles, leading to peak centers of $q_{xy} = 1.518\text{Å}^{-1}$ and $q_{xy} = 1.724\text{Å}^{-1}$, respectively. The peak indexing corresponds to a centred rectangular lattice like the one found for the crystalline phases of DPPA and eicosanoic acid on $DMSO/H_2O$. Modelling of the Bragg rod profiles of the {11} and {02} reflections as shown in figure 3.28 c) and d), respectively, prove that the chains remain in an upright configuration during the cooling process. The FWHM of the diffraction peaks and the corresponding correlation lengths of the crystalline domains were found to vary not systematically as a function of temperature. Like in the case of DPPA on $DMSO/H_2O$, only the relatively intense diffraction peak at smaller q_{xy} allows a reliable determination of a FWHM. For the eicosanoic acid monolayer on silicon the FWHM was found to vary between 0.06 and 0.08 Å^{-1}, corresponding to correlation lengths of 70Å to 94Å. A distinct growth of the crystalline domains upon cooling as discovered on the liquid subphase does hence not occur. In the hexagonal phase at ambient temperature the packing of the alkane chains leads to a chain cross section of $A_\perp = A_0 = 20.01\text{Å}^2$, which reduces upon cooling to a value of 18.44Å^2 at a sample

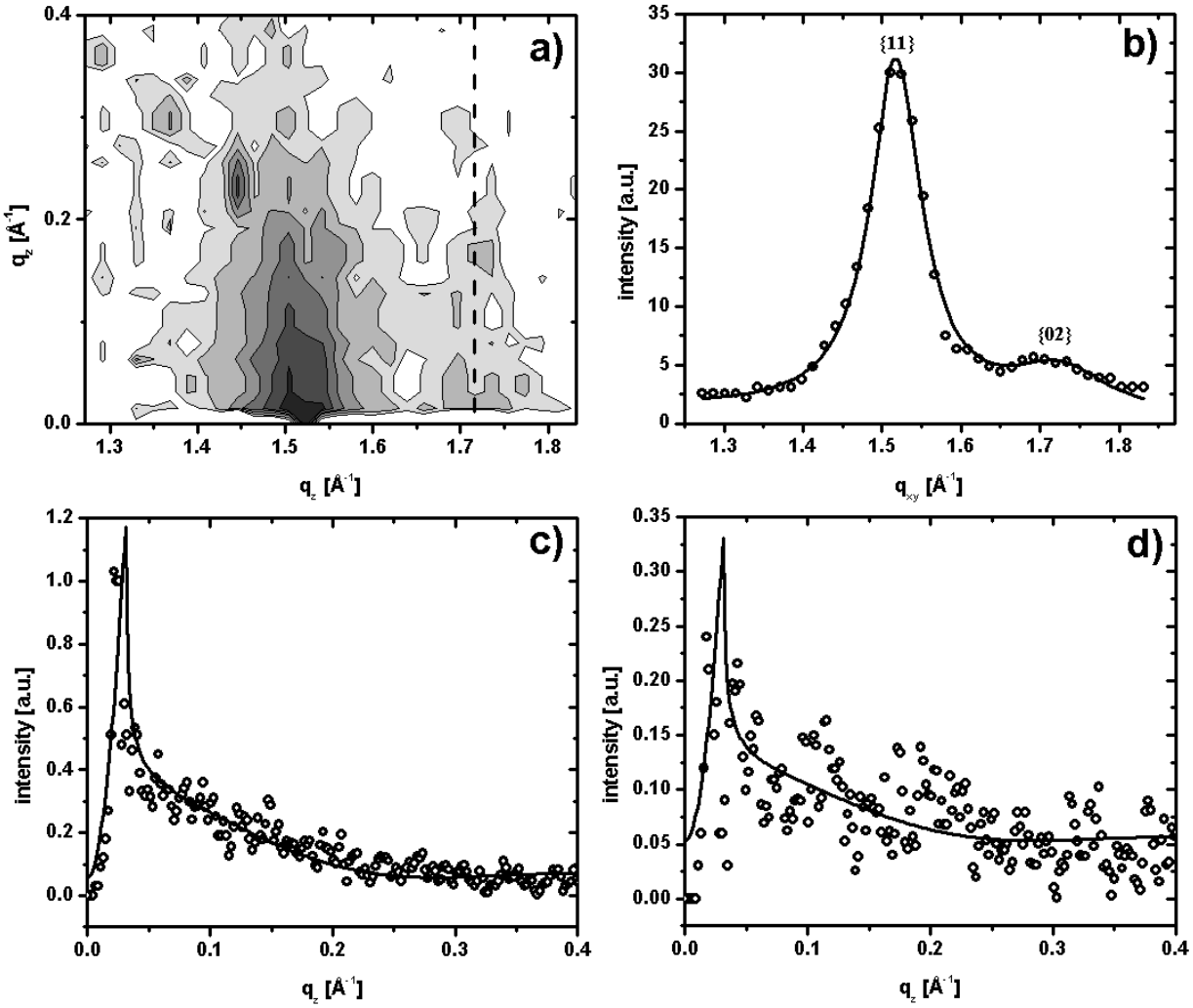

Figure 3.28: Diffraction pattern of a LB monolayer of eicosanoic acid on a silicon wafer recorded at a temperature of 106K. a) intensity distribution as a function of q_z and q_{xy}, intensity mapping employs a logarithmic scale, the dashed line is a guide to the eye at the position of the {02} in-plane reflection; b) diffraction pattern shown in panel a) integrated along q_z (open circles) and fit to a superposition of two Voigt profiles, the indexing corresponds to a centred rectangular lattice. c), d) measured Bragg rods (open circles) of the {11} and {02} reflections, respectively, the solid lines were calculated according to the cylinder model.

temperature of 30K. While the packing density at ambient temperature is compatible with a free rotator (RII) phase of the alkane chains, at T=279.6K the area cross section was found to be reduced to $A_\perp = A_0 = 19.42\mathring{A}^2$, being slightly smaller than the limit for a hindered (RI) rotator phase. This findings imply that the rotator-crystalline phase transition for a LB film of eicosanoic acid takes place at slightly higher temperatures as compared to a liquid subphase. However, as the presented study focusses mainly on the crystalline phase, the very limited number of data points at high temperatures does not allow to determine in detail the phase transition itself. This holds in particular for the question whether the phase transition is of the type RII-RI-crystalline or RII-crystalline. Figure 3.29 a) shows the alkane chain cross section for the LB film of eicosanoic acid (squares) and for the monolayer on the liquid DMSO/H_2O subphase (triangles). Because of the diffraction peaks being less intense and well defined in the case of the LB film, the unit cell parameters as well as the packing density exhibit larger error bars, while for the case of the liquid subphase the error bars are comparable or even smaller than the symbol size. The dashed horizontal line indicates the most dense packing (18.45Å^2) found on the liquid subphase. It strikes out that the phase transition temperature as well as the packing in the crystalline phase are comparable for both investigated systems. On the other hand, the reorganisation in particular in the crystalline phase seems to require much lower temperatures on the solid surface. So a packing density of about 18.75Å^2 is reached at 263K on the liquid subphase, while for the LB film a further temperature reduction down to 150K is required. Consequently, the thermal expansion for the LB fim is with a value of $(0.0038 \pm 0.0007)\mathring{A}^2/K$ for the unit cell area A_0 more than a factor of four smaller than the corresponding value for the liquid subphase (compare table 3.7). Similar findings hold for the lattice parameters a and b of the non-primitive centred rectangular unit cells that are compared in panels b) and c) of figure 3.29. For the lattice vector a both the qualitative evolution as a function of temperature and the absolute values are similar, with an exception for the absolute temperature values which differ in the same way as described for the area cross section. The thermal expansion for the lattice vector a in the crystalline phase is found to be $(0.0022 \pm 0.0004)\mathring{A}/K$, which is about a factor of 2.3 smaller than for the monolayer of eicosanoic acid on DMSO/H_2O. In the case of the lattice vector b the qualitative evolution is even closer to the one of the C21 bulk alkane (see figure 3.32 b)): upon cooling the lattice vector is expanding up to a maximum value and remains almost constant upon a further temperature reduction. The minimum value for b found in the crystalline phase for the LB film and the monolayer on the liquid subphase are identical within the error bars. The ratio of the two lattice vectors a and b of the (pseudo) rectangular cell is compared in figure 3.29 d). For the LB film at ambient temperature the ratio is equal to $\sqrt{3}$ as a consequence of the initial two-dimensional structure being hexagonal. The further evolution upon decreasing the temperature however, resemble the one of the monolayer on the liquid subphase. In particular, the sharp decrease in the ratio at the phase transition temperature as found for DPPA is absent, although all these molecules exhibit a hexagonal rotator phase. The two most striking differences between the structures found for the eicosanoic acid monolayers on silicon and on DMSO/H_2O are therefore the different initial phases at ambient temperature and the lower temperatures needed for the LB sample to obtain equivalent packing densities and lattice parameters. While at a surface pressure of 4mN/m the monolayer of eicosanoic

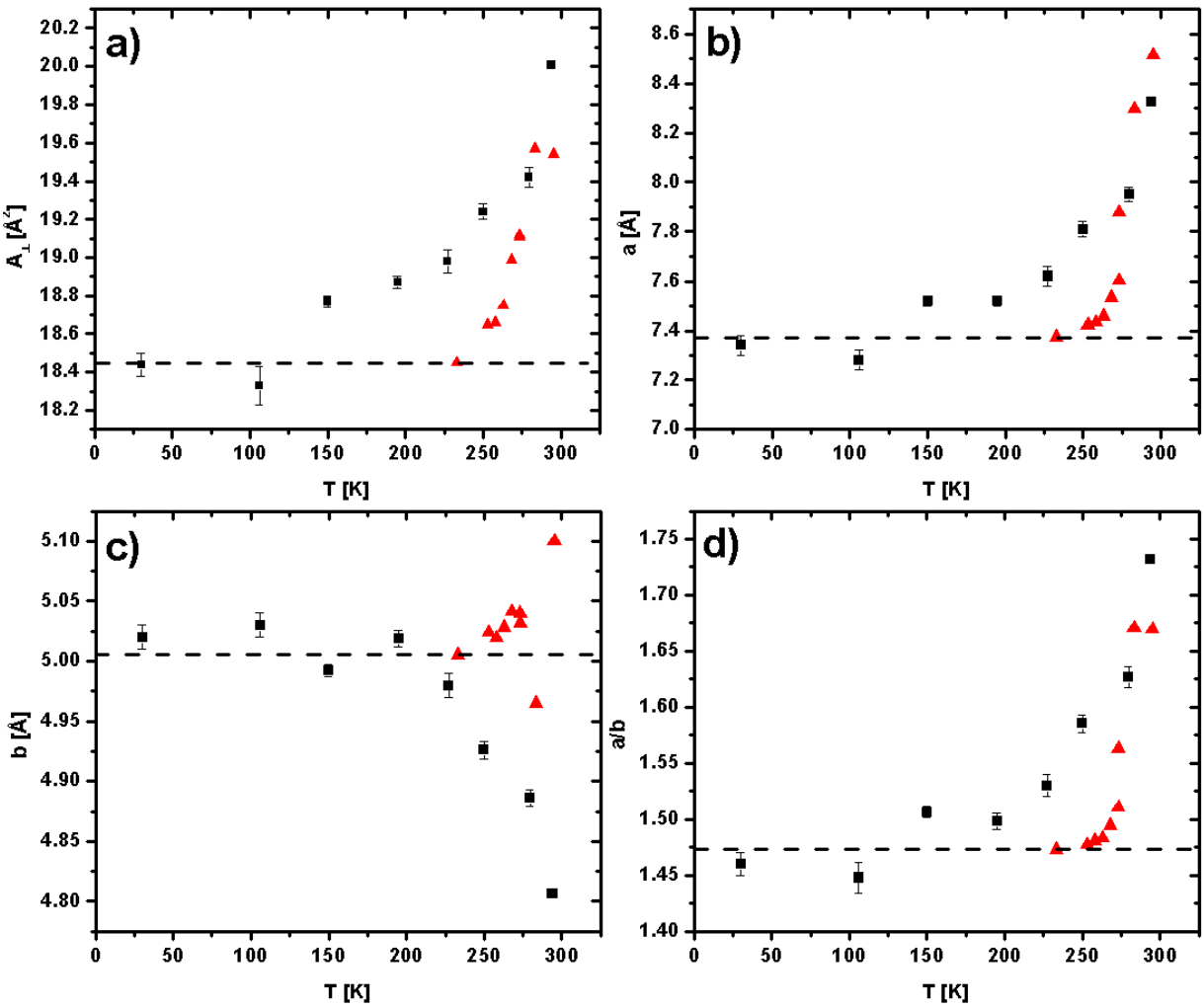

Figure 3.29: a) alkane chain cross section for eicosanoic acid on a silicon wafer (squares) and on a liquid subphase of DMSO/H_2O (triangles); b), c): lattice vectors a and b as a function of temperature for both incestigated systems; d) ratio of the lattice vector a and b. All dashed horizontal lines serve as a guide to the eye and mark the value of the corresponding parameter for Eicosanoic acid on DMSO/H_2O at the lowest investigated temperature

acid on the liquid subphase exhibits a centred rectangular in-plane lattice with tilted chains, the LB film transferred from an aqueous solution of cadmium chloride at the same surface pressure has a hexagonal lattice with upright chains. Two possible mechanisms might lead to such different ordering of the monolayers: One possibility is the change of the structure during the transfer process from the liquid subphase onto the solid substrate. The up stroke of the silicon wafer and the meniscus formed at the liquid/solid interface might alter locally the two-dimensional compression of the molecules and hence the accompanied structure. A second origin of the altered structure might arise from the ion network formed between the headgroups of the surfactant. Although the structure formation is mainly driven by the van der Waals interaction between the alkane chains, the headgroups and ions play nevertheless an important role. Nevertheless, from the pressure area isotherms recorded during the transfer process it seems more plausible that the actual change of the two-dimensional structure takes place during the transfer process itself: even for eicosanoic acid on an aqueous solution of cadmium chloride the increase of the slope of the isotherm associated with the transition towards a hexagonal LS phase with upright chain conformation takes place at surface pressures well above 4mN/m.

Two possible mechanisms or their combination might cause the observed shift towards lower temperatures for the lattice parameters and packing density of the LB film in comparison with the monolayer on a liquid substrate. As the cooling rate was approximately the same for both experiments (about 0.5°C/minute), the observed temperature shift could reflect the slower kinetics of the reorganisation process of the surfactant molecules physisorbed onto the solid substrate. A slightly different mechanism could be the physisorbtion of the surfactant headgroups serving as an additional energy barrier for the reorganisation process: While due to the temperature reduction the net effective interaction between the alkane chains would allow for a closer packing, the reduced in-plane mobility of the headgroups acts as barrier, requiring stronger net-effective interactions between the alkane chains than on a liquid substrate and hence a further temperature reduction. It is noteworthy, that in contrast to results of molecular dynamics simulations for chemisorbed alkane chain molecules (thiols on gold) [45] the molecules do not tilt as their packing density is increased upon cooling. While for chemisorbed molecules the link to the substrate is supposed be too strong to allow for lateral reorganisation processes, these are obviously feasible for the weaker binding via physisorption. As a direct consequence, for the eicosanoic acid molecules undergoing a rotator-crystalline phase transition, the reduced area requirement per molecules is compensated by lateral movements rather than by a molecular tilt.

3.4 Discussion of the Structure Data

3.4.1 Comparison with Bulk Systems

The following part is devoted to the comparison of the structure parameters derived for the monolayers of eicosanoic acid and DPPA and those obtained for bulk systems. The closest 3d system which has been intensively studied are alkanes or paraffins [25, 28, 27, 107, 108, 61]. Despite of the distinct differences of these bulk systems with respect to monolayers, they can be compared to monolayer phases of alkane chain molecules [106]

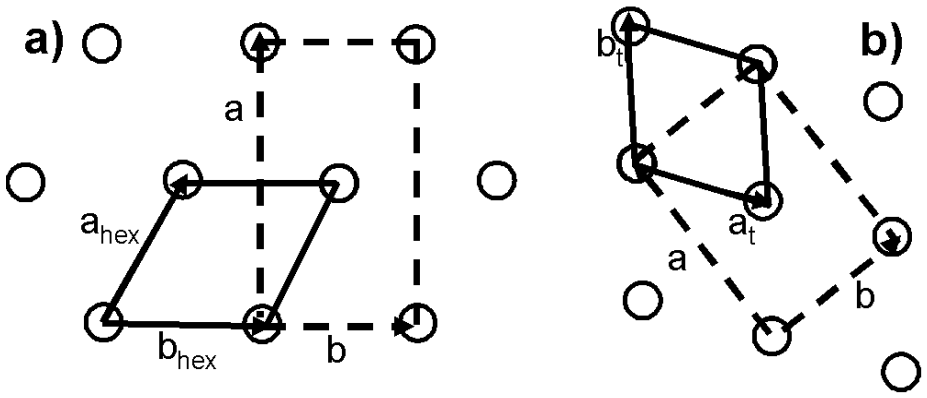

Figure 3.30: Transformation of lattices: a) hexagonal to rectangular; b) 2d layer of a triclinic lattice to a rectangulae one

such as alcohols, fatty acids or phospholipids, as the driving mechanism for structure formation is in both cases given by the van der Waals interaction between the alkane chains. In order to compare molecular packing and the variation of structure parameters such as unit cell vectors during cooling, for the three dimensional systems only the lateral packing of the molecules can be considered. Moreover, the two dimensional packing of the monolayer phases will be compared to the packing within the corresponding subunit of 3d single crystals of similar molecules.

The rotator-crystalline phase transition during temperature variation has been studied in systems of bulk paraffins for various lengths of the normal alkanes ($CH_3(CH_2)_{n\text{-}2}CH_3$). The variation of the chain length generally shifts the phase diagram along the temperature axis due to the modification of the intermolecular interaction. In particular, different behaviours were identified for odd and even numbered paraffins, where the terms 'odd' and 'even' refer to the number of carbon atoms in the chain. Here the results obtained for eicosanoic acid (C20) and DPPA (C16) monolayers on liquid substrates are compared to those of two representative bulk paraffins, namely $C_{21}H_{44}$ and $C_{22}H_{46}$. The reason for choosing these two species, being slightly longer than the alkane chains of the molecules used in the presented monolayer studies, is the fact that for even numbered paraffins $\leq$C20 the rotator phase is only metastable or even not existing [25]. In order to compare consistent sets of data, the longer paraffins were selected, showing very similar qualitative as well as quantitative behaviour as compared to the shorter ones, at least in the temperature range where both exhibit stable phases. The above discussed temperature shift in the phase diagram has no influence on the following discussion: phase transition temperatures of bulk systems and monolayers cannot be directly compared as a consequence of the specific molecular interactions in both systems. This involves for instance in the case of a monolayer the lack of interaction with a neighbouring molecule in one spacial direction or the coupling to the fluctuating surface of a liquid.

In order to facilitate the comparison of the lattice parameters for the four different two and three dimensional systems, it is convenient to chose a common (two dimensional) lattice and to transform the corresponding parameters where necessary. For the eicosanoic acid monolayer on DMSO/H_2O both the rotator and the crystalline phase exhibit a cen-

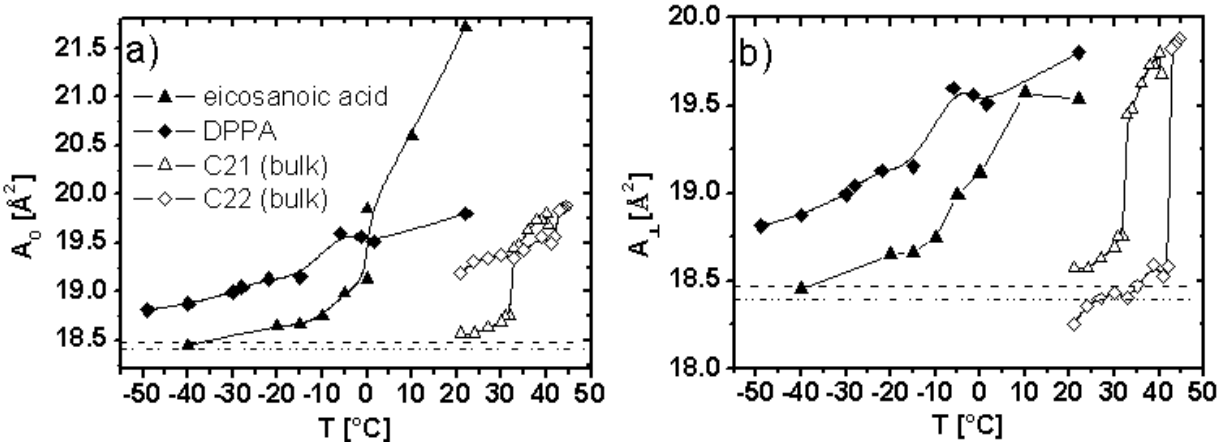

Figure 3.31: Comparison of the unit cell area per alkane chain (A_0, panel a)) and the alkane chain cross-section ($A_\perp$, panel b)) for the monolayers of eicosanoic acid (filled triangles) and DPPA (filled diamonds) as well as for the normal alkane bulk systems C21 (open triangle, [27]) and C22 (open diamonds, [27]). The horizontal dashed and dashed dotted lines lines indicate the corresponding values for the single crystals of the E- and the B-form of octadecanoic acid, respectively [58, 57]. The solid lines connecting the data points are just a guide to the eye.

tred rectangular lattice (see section 3.3.1), while the lattice found for the DPPA monolayer on the same subphase is hexagonal in the rotator and centred rectangular in the crystalline phase (see section 3.3.2). For odd numbered paraffins, like for instance $C_{21}H_{44,}$ the unit cell in the crystalline phase is orthorhombic but not centred, containing two chains in the layer plane which are parallel to the c-axis. Upon heating, the odd numbered paraffins with n$\leq$21 exhibit a RI rotator phase, characterised by orientational disorder of the molecules around their length axis, involving an even number of orientations [27], related by a mirror plane parallel to the lattice vector b. As a consequence of the rotational disorder, the c-face of the cell is centred and the corresponding two dimensional lattice is centred rectangular in the rotator phase with the chains remaining parallel to the c-axis. For the even numbered paraffins like $C_{22}H_{46}$, the three dimensional unit cell is triclinic in the crystalline phase, while they exhibit a RII rotator phase with a hexagonal lattice at higher temperatures. The most convenient choice seems to be therefore the rectangular lattice. In order to transform a primitive 2d hexagonal lattice into a non-primitive rectangular one, the new lattice vectors $\mathbf{a}$ and $\mathbf{b}$ can be calculated from the original ones as $\mathbf{a} = \mathbf{2a}_{hex} - \mathbf{b}_{hex}$ and $\mathbf{b} = \mathbf{b}_{hex}$ (see figure 3.30 a)). Here $\mathbf{a}_{hex}$ and $\mathbf{b}_{hex}$ ($a_{hex} = b_{hex}$) denote the lattice vectors of the original hexagonal lattice. To transform the 2d lattice within the layers of the 3d triclinic form into a pseudorectangular c-centred cell, the lattice vectors of the 2d subcell are given by [25] $\mathbf{a} = \mathbf{a}_t - \mathbf{b}_t$ and $\mathbf{b} = \mathbf{a}_t + \mathbf{b}_t$, where $\mathbf{a}_t$ and $\mathbf{b}_t$ are the lattice vectors of the triclinic unit cell (see figure 3.30 b)).

Unless marked differently, the reference values for the odd and even bulk alkanes used in the following are given in, or have been extracted from, the references [25, 27]. The values of the unit cell area per alkane chain A_0 and the a alkane chain cross section $A_\perp$

are shown as a function of temperature in figure 3.31 a) and b), respectively, for the bulk alkanes C21 and C22 as well as for the monolayer phases of eicosanoic acid and DPPA. The solid lines connecting the data points are spline interpolations, which only serve as a guide to the eye. By definition the values for A_0 and $A_\perp$ are identical for monolayers with an upright chain conformation or a three dimensional system where the c-axis is chosen parallel to the chain length axis. At high temperatures the odd numbered normal alkanes like C21 exhibit a RI rotator phase with a chain alignment parallel to the c-axis of the three dimensional unit cell and typical area values of $A_0 = A_\perp \approx 19.6\mathring{A}^2$ per alkane chain. The variation in the case of C21 at temperatures higher than the rotator-crystalline phase transition amounts from $19.68\mathring{A}^2$ to $19.45\mathring{A}^2$ between 40.5°C and 32.8°C. The high temperature phase of the even numbered normal alkanes like C22 is characterised by an upright chain configuration within a hexagonal two-dimensional sublattice. Typical minimum values needed for this RII rotator phase are lattice parameters like $a = b \approx 4.77\mathring{A}$, $\gamma = 120°$ leading to typical area values of $A_0 = A_\perp \approx 19.7\mathring{A}^2$. In the case of C22, the variations range from $19.88\mathring{A}^2$ $(44.4°C)$ to $19.83\mathring{A}^2$ $(42.8°C)$. Thus, in the rotator phase the area per chain is almost constant. The monolayer of eicosanoic acid exhibits at 22°C a unit cell with an area of $A_0 = 21.72\mathring{A}^2$ and a tilt angle $t = 25.9°$ of the chains relative to the surface normal, leading to an area cross section per alkane chain of $A_\perp = 19.54\mathring{A}^2$. Upon cooling to the two phase coexisting region, these values reduce to $A_0 = 19.85\mathring{A}^2$ and $A_\perp = 19.11\mathring{A}^2$, respectively. These values are certainly to small for a free RII rotator phase. Nevertheless, at least at 22°C a hindered (RI) rotator phase is possible, which gets looked in during the cooling process. The qualitative behaviour of the area values of eicosanoic acid is due to the larger temperature dependence closer to the one of the bulk alkane C21 than to C22. In the high temperature phase of DPPA the area requirement for the upright alkane chain is reduced upon cooling from $A_0 = A_\perp = 19.80\mathring{A}^2$ at 22°C to $19.60\mathring{A}^2$ at -6°C. These findings are compatible with a RII rotator phase at 22°C and a possible transition towards a RI rotator phase upon cooling. The small variation of A_0 of only $0.2\mathring{A}^2$ over the quite extended temperature range of 28°C compares better to the behaviour of the C22 bulk alkane rather than to the temperature dependence found for C21.

In the case of the odd numbered normal alkanes, the area per unit cell is reduced at the phase transition temperature by about $1.5\mathring{A}^2$. In the case of C21 the reduction is $1.4\mathring{A}^2$ per unit cell and $0.7\mathring{A}^2$ per alkane chain, respectively. For the even numbered alkanes the phase transition is accompanied by a change of the three dimensional unit cell from a hexagonal to a triclinic one. Therefore, the conformation of the alkanes is no longer upright with respect to the pseudo-rectangular two-dimensional sublattice and thus the values for A_0 and $A_\perp$ differ. For the C22 alkane the jump of A_0 and $A_\perp$ at the phase transition temperature is $0.51\mathring{A}^2$ and $1.48\mathring{A}^2$, respectively. For both the odd and the even numbered normal alkanes the jump in the area per molecule at the phase transition temperature is very sharp. For the monolayer of eicosanoic acid the chain cross sections $A_\perp$ for the high and the low temperature phases are almost identical at the phase transition temperature as discussed above. Contrary, the unit cell area A_0 shows a discontinues variation of about $0.72\mathring{A}^2$ between the two phases. For DPPA, the areas $A_0 = A_\perp$ change by $0.45\mathring{A}^2$ between -6°C and -15°C, however, the sharpness of the accompanied phase transition is difficult to judge due to the large temperature step in

the data. Nevertheless, the value for the area difference found for DPPA compares well with the step found for A_0 for the even numbered alkane C22.

For the odd numbered paraffins in the crystalline phase, like e.g. C21 at 24°C, the lattice parameters are $a = 7.48\mathring{A}$ and $b = 4.97\mathring{A}$, which are typical values for the crystalline phase [76, 51]. As the alkane conformation for C21 in this phase is upright with respect to the two-dimensional sublattice, the corresponding cross section and unit cell area per molecule are identical: $A_0 = A_\perp = 18.59\mathring{A}^2$. For C21 this values range from $18.75\mathring{A}^2$ at 31.9°C to $18.57\mathring{A}^2$ at 21.0°C. In the triclinic packing of the even numbered alkanes in the crystalline phase, like for instance C22 at 20°C, the molecules are tilted by about 18 deg . with respect to the normal of the two-dimensional subunit. The values for the alkane cross section and the unit cell area per molecule in the corresponding pseudo-rectangular lattice range here from $A_0 = 19.56\ \mathring{A}^2$ and $A_\perp = 18.58\mathring{A}^2$ (at 41.9°C) to $A_0 = 19.19\mathring{A}^2$ and $A_\perp = 18.26\mathring{A}^2$ (at 20.8°C). The specific tilt angle of 18° was interpreted as a direct consequence of steric arguments: at this angle the Zig-Zags of the alkane chains are locked-in, thus enabling closest packing. The packing of the alkanes within the two-dimensional sub-unit differs for the odd and even numbered ones: while the odd numbered alkanes exhibit a herringbone configuration, the molecular planes of the even numbered alkanes in the triclinic structure are parallel. It strikes out that the packing of the even numbered normal alkanes is therewith denser than for the odd numbered ones. For the bulk alkanes this finding was explained by the Kitaigorodskii theory [62] as a direct consequence of molecules' symmetry: while for the even numbered alkanes a triclinic packing is allowed, this denser packing is 'symmetry forbidden' for the less symmetric odd numbered alkanes, which therefore arrange in an orthorhombic structure.

The values found for the chain cross section and the unit cell area per molecule in the low temperature phase of eicosanoic acid are ranging from $A_0 \approx A_\perp = 19.12\mathring{A}^2$ at 0°C to $A_0 = A_\perp = 18.45\mathring{A}^2$ at -40°C, thus reaching an even closer packing than the odd numbered alkane C21. In the following an attempt is made to compare the packing of the alkane chains of the crystalline phase of the eicosanoic monolayer to bulk single crystals of comparable fatty acids. The dashed and dashed-dotted lines in figure 3.31 a) and b) indicate the area values for three dimensional single crystals of the E-form ($A_0 = A_\perp = 18.47\mathring{A}^2$, [57, 56]) and the B-form ($A_0 = A_\perp = 18.39\mathring{A}^2$, [58]) of octadecanoic acid ($CH_3(CH_2)_{16}COOH$). Both polymorphs crystallise in an orthorhombic unit cell containing eight molecules, two in the a-b plane stacked in double layers along the c-direction. The straight part of the alkane chain constructs an orthorhombic polyethylene subcell with perpendicular arrangement of the skeletal planes. The subcell parameters like $a = 7.36\mathring{A}$ and $b = 5.01$ (E-form) compare well to the values of $a = 7.37\mathring{A}$ and $b = 5.01\mathring{A}$ found for the monolayer of eicosanoic acid at a sample temperature of -40°C. It is noteworthy, that under these conditions the packing within the two-dimensional layer is as dense as the lateral packing of the bulk single crystal. Only modified fatty acids like silver salts of octadecanoic acid ($CH_3(CH_2)_{16}COOAg$) [119] exhibit distinct smaller cross-sections per alkane chain: in the triclinic lattice the alkane chains are tilted by 17.95° with respect to the c-axis, leading to values of $A_0 = 18.76\mathring{A}^2$ and $A_\perp = 17.85\mathring{A}^2$, respectively.

For the investigated monolayer of DPPA the area requirement per alkane chain in the crystalline phase varies from $A_0 = A_\perp = 19.15\mathring{A}^2$ at -15°C to $A_0 = A_\perp = 18.81\mathring{A}^2$ at -49°C. Despite of the large headgroup and the glycerol backbone of this molecule acting

	a [Å/°C]	b [Å/°C]	A_0 [Å^2/°C]	$A_\perp$ [Å^2/°C]
C21 (bulk)	0.003	0.0015	0.045	0.045
C22 (bulk)	0.0044±0.0004	0.0010±0.0004	0.015±0.002	0.014±0.002
eicos. acid	0.005±0.001	0.009±0.002	0.016±0.003	0.016±0.003
DPPA	0.006±0.001	-0.0012±0.0080	0.011±0.001	0.011±0.001

Table 3.7: Thermal expansion corresponding to the lattice parameters a and b of the (pseudo) rectangular lattices, the unit cell area per alkane chain (A_0) and the chain cross-section ($A_\perp$); data are given for the bulk systems C21 [27] and C22 (extracted from [25]) and the monolayers of eicosanoic acid and DPPA.

as 'spacers' in the two-dimensional structure, their influence on the alkane chain lattice is smaller than one might anticipate. So the value found for the closest packed DPPA monolayers are only about 0.06 to 0.23$\AA^2$ larger than the loosest crystalline packing found for the C21 and C22 normal alkanes in the bulk, respectively. Nevertheless, it might seem more natural to compare the packing of the crystalline phase of the DPPA monolayer to the packing of three dimensional phospholipid single crystals. An overview about crystal structures of membrane lipids can be found in [85]. The crystal structure of DMPA (monosodium 1,2-dimyristoyl-sn-glycerophosphate) was solved by Harlos et al.[44], revealing a packing density of $A_\perp = 18.6\AA^2$. The paking is thus slightly denser in the bulk crystal, although the alkane chains of this compound are shorter (C14) than those of DPPA. For a phopholipid with C16 alkane chains but an ethanolamine headgroup (3-palmytoyl-DL-glycerol-phosphoryl-ethanolamin) a chain cross section $A_\perp = 18.69\AA^2$ is reported [86]. These cross sections are hence smaller than the ones found for DPPA on the liquid subphase, in contrast to the case of eicosanoic acid.

The thermal expansion in the crystalline phase for the lattice parameters a and b of the (pseudo) rectangular lattices, the unit cell area per molecule and the chain cross-section for the C21 and C22 bulk systems as well as for the monolayers of eicosanoic acid and DPPA are summarised in table 3.7. The values for the C21 bulk alkane have been given directly in reference [27], while for the other substances the values given in table 3.7 are based on linear fits of the corresponding parameters. For the monolayer of eicosanoic acid the excellent agreement with the data for the C22 bulk systems within the error bars is evident not only for the lattice parameters, but also for A_0 and $A_\perp$. In comparison to the C21 bulk system, the thermal expansion for the vectors a and b appear to be similar, with the qualitative difference that the lattice of the eicosanoic acid monolayer is shrinking stronger along the **a** direction than along **b**. In contrast, the thermal expansion for the areas A_0 and $A_\perp$ differ by about a factor of three. For the DPPA monolayer the thermal expansion does not only differ quantitatively but also qualitatively from the alkane bulk systems. The most striking feature is the appearance of a negative thermal expansion for the lattice parameter **b**, although the large error bar of this particular parameter has to be borne in mind. It appears that the large thermal expansion of the lattice vector **a**, being about a factor of two larger as in comparison to C21, allows the lattice vector **b** to relax, while the parameters A_0 and $A_\perp$ decrease upon cooling as expected. Reasons for this puzzling thermal expansion might be steric hindrances like the coupling of two alkane chains by the glycerol backbone or the larger headgroup size as compared to

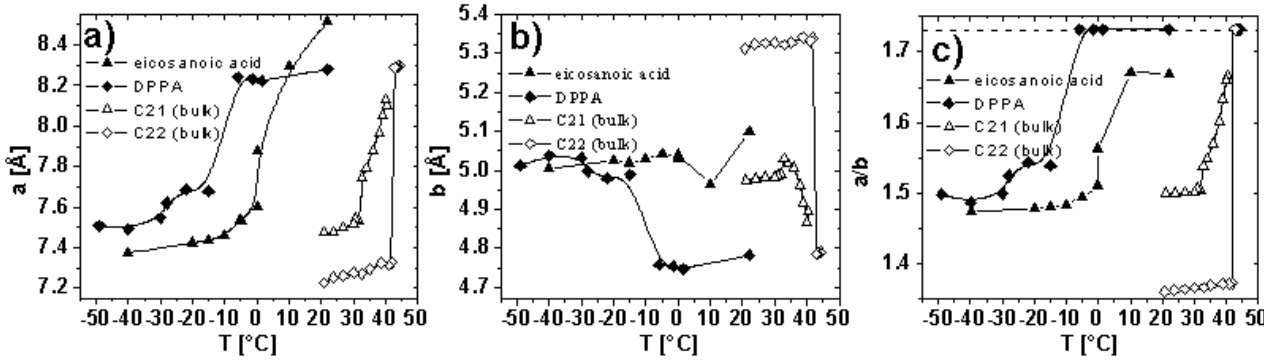

Figure 3.32: lattice parameters a (panel a)), b (panel b)) and their ratio a/b (panel c)) for the monolayers of eicosanoic acid and DPPA and for the bulk systems of the normal alkanes C21 and C22. The dashed line in panel c) indicates a ratio a/b equal to $\sqrt{3}$, corresponding to a hexagonal cell.

the carboxyl group of the fatty acid. In order to investigate possible mechanisms in more detail, information of the chain alignment would be needed on a sub-molecular level. This would involve a data analysis beyond the limitations of the cylinder model. Unfortunately, the very limited number of diffraction peaks observed for DPPA does not allow structure factor calculations as performed for eicosanoic acid.

The evolution of the lattice parameters a and b as a function of temperature is shown in figure 3.32 a) and b), respectively. For the odd numbered normal alkanes like C21, at the transition from the rotator to the crystalline phase the lattice parameters a and b decrease. While in the case of a the decrease is quite sharp at the phase transition temperature, the parameter b increases within the rotator phase, passes through a maximum and decreases afterwards in the crystalline phase as a function of temperature. The values of b are smaller in the rotator phase than in the crystalline phase. For the lattice parameter a of the eicosanoic acid monolayer the behaviour upon reaching the rotator crystalline phase transition compares to the one of the C21 bulk system, although the slope in temperature range corresponding to the rotator phase is contrary. The evolution of the lattice vector b starts with a rapid decrease between 22°C and 10°C, but beside this first data point the progression is similar to the one of C21. For DPPA the evolution of both a and b qualitatively match very well that of the C22 bulk system with the exception of the already discussed negative thermal expansion coefficient for the parameter b in the crystalline phase. The ratio of the lattice vectors a and b for the systems under discussion is shown in figure 3.32 c). For the odd numbered normal alkanes the ratio a/b is nearly constant in the rotator phase (≈ 1.5) and increases progressively in the rotator phase, such that its upper limit becomes closer to $\sqrt{3} \approx 1.73$ (indicated as a dashed line in figure 3.32 c)), the theoretical value corresponding to a hexagonal cell. For the even numbered bulk alkanes there is a distinct jump of the ratio a/b at the phase transition temperature, where in the case of C22 the value drops from $\sqrt{3}$ to about 1.37. For the eicosanoic acid monolayer in the crystalline phase the ratio is almost constant at a value of about 1.49, which increases in the rotator phase up to a value of 1.67. Again, the qualitative as well

as the quantitative agreement with the corresponding data for the C21 bulk system is evident. Contrary, the behaviour of a/b for the DPPA monolayer compares better to the one of the C22 bulk system. In particular the hexagonal rotator phase and the extended discrete jump from $\sqrt{3}$ to an average of 1.52 compare well, although the absolute values differ with ratios of 1.52 for DPPA and 1.37 for C22 quite strongly in the crystalline phase. A possible explanation might be packing restrictions for the alkane chains of the DPPA molecule due to steric hindrances as discussed above.

Summarising the comparison between the monolayer and the bulk systems, in terms of the packing density the eicosanoic acid monolayer is comparable to the C21 bulk alkane system. Contrary, for the DPPA monolayer the packing density in the rotator phase is similar to the one of C22, while it is less dense in the crystalline phase, where only the unit cell areas A_0 compare. In the crystalline phase both the packing of the eicosanoic acid and the DPPA monolayer compare to bulk single crystals of similar molecules. The evolution of the lattice parameters a and b are determined by the initial configuration of the lattice: the eicosanoic acid monolayer and the C21 bulk system both exhibit rectangular lattices in the rotator and crystalline phase. Consequently, the corresponding parameters for the DPPA monolayer are much closer to the C22 bulk system, as both exhibit a hexagonal lattice in the rotator phase which turns into a (pseudo) rectangular lattice in the crystalline phase.

3.4.2 Comparison with Langmuir Layers

Most investigations of amphiphilic monolayers at the liquid/gas interface employ the traditional Langmuir technique either for the measurement of pressure-area isotherms or to prepare monolayers for the investigation by other methods. Contrary, studies like the presented one, where at constant macroscopic area and without external compression only the influence of temperature on the monolayer phase behaviour and morphology is studied, are rare. Bommarito et al. [10] investigated the L2"-L2' phase transition by what they called 'temperature scans': at a constant trough area the X-ray structures and the surface pressure were recorded as the temperature was increased. This corresponds from a macroscopic point of view to an isochore measurement, however, this term might be misleading as the microscopic area requirement per molecule is changing. They found upon temperature rise an increasing surface pressure and the conformational change indicating the L_2"- L_2' phase transition predicted by the generic phase diagram. Their technique of monolayer preparation is probably the closest reported match to the preparation technique used in the present study. In default of a sufficent number of equilibrium studies, in the following the obtained results will be compared to data obtained from standard Langmuir monolayer experiments.

Primed with the knowledge about the existing generic phase diagram (see section 1.1.2), in the following the phase sequence of eicosanoic acid at a constant surface pressure of 4.5mN/m upon cooling -as investigated in the present study- will be identified. Because of the experiments were not made to locate phase boundaries (large temperature steps between individual measurements), the question about the order of phase transition will not be addressed. After preparation and equilibration at 22°C, a rectangular phase with tilted chains and a tilt azimuth towards the nearest neighbour was observed. At about

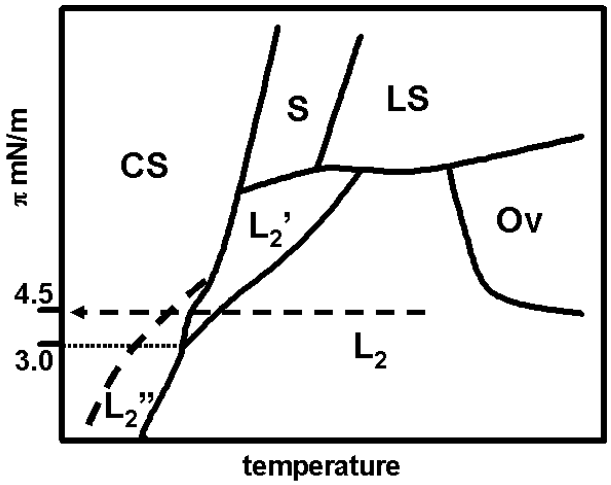

Figure 3.33: proposed path (dashed arrow) opon cooling through a modified phase diagram: the location of the L_2-L2'-L2 " triple point at 3mN/m follows the work of Bommarito et al. [10], the suggested L2 "-CS phase boundary (dashed line) is similar to the L2-CS boundary in diagram a), allowing for the existance of a CS phase at low surface pressure. The other phase boundaries are adopted from the phase diagram b) for the sake of completeness. As the presented experiments were not made to map the phase boundaries, a scale on the temperature axis is abandoned.

10°C the tilt direction was found to be changed towards the next nearest neighbour, while the unit cell remained rectangular. Upon further cooling, the low temperature phase identified at 0°C exhibits a tilt direction which had returned to the nearest neighbour direction. At the same time the width of the diffraction peaks is decreased in a way such that the correlation lengths double. This result could be interpreted as the onset of crystallinity with the appearance of this phase. Upon further cooling the tilt angle of the chains is reduced to zero and the characteristic herringbone order of the crystalline phase was revealed by structure factor calculations. The phase sequence would therefore be: L_2 at 22°C, L_2' at 10°C, L_2" at about 0°C ('low temperature' phase) and CS for lower temperatures. Comparing this phase sequence to the reported phase diagram for eicosanoic acid as well as to the generic phase diagram of fatty acids, three points strike out:

- the crystalline phases of eicosanoic acid have up to now not been reported
- in the generic phase diagram (fig. 1.1 b)) the CS phase does not extend to surface pressures as low as 4.5 mN/m, neither does the L_2' phase
- according to the slope of the L_2"-CS phase boundary in the generic phase diagram, the transition between these two phases should not be accessible by cooling without compression of the monolayer

The first point is owed to the chain length of eicosanoic acid, rendering the van der Waals interaction between them too weak to stabilise a crystalline phase against the

competing surface fluctuations. The reasons for the crystalline phase, insetting at about 0°C in the presented study, not being observed in the experiments carried out by Durban et al. [30] may be twofold: First, the pH value of the subphase (pH=2 in their study) changes the headgroup dissociation and might hence alter the phase behaviour. Second, without an additional cooling of the atmosphere the effective temperature at the interface is higher than the subphase temperature.

Addressing the second point requires to take the preparation procedure of the monolayer into account. As pointed out before, in the present study the monolayer is in an equilibrium state and all changes in phase behaviour and morphology are only induced by a reduction of entropy via the temperature. In contrast, compressed monolayers are not necessarily in an equilibrium state, moreover, it is a subject under discussion, whether in particular the high pressure phases are thermodynamically stable or not. Kjaer et al. [66] report a study on eicosanoic acid on pure water and salt solutions investigated by GIXD and specular reflectivity. At a surface pressure of 25mN/m the monolayer was found to collapse and the surface pressure could only be held constant by continuous compression. Schlossman et al. [100] found relaxation and re-entrant appearance of phases in a monolayer of tetracosanoic acid (C24). They report a collapse of the monolayer along a 21°C isotherm for surface pressures above 12.5mN/m with relaxation times in the order of hours. A rigorous study of the relaxation phenomena and their impact on the phase diagram was performed by Bommarito et al. [10], who studied behenic acid (C22) in the temperature range from 3°C to 20.6°C by means of GIXD and BAM. Besides some temperature scans at fixed macroscopic area (see above) they employed isothermal compression, but allowed for the relaxation of the monolayer after each incremental compression step until a stable surface pressure was reached. Comparing relaxation isotherms with constant compression isotherms, remarkable differences for the maximum reachable surface pressure were found: for relaxation isotherms the surface pressure prior to collapse varies between 11 to 20mN/m, depending on temperature, while by constant compression 60mN/m can be reached. Consequently, in constant compression isotherms features like kinks or plateaus (and thus phase transitions) are observed for pressures larger than the collapse pressure of a relaxed monolayer. Despite the smaller surface pressure range covered by the relaxation isotherms, the corresponding phase diagram exhibits most of the phases found in the generic phase diagram. Only at a temperature above 12°C a few phases at high surface pressure were found to be 'missing'. Below 12°C, the effects of relaxation and lower collapse pressure do not result in a truncation of the generic phase diagram, but rather in its 'compression' into a smaller pressure range. In particular, the L_2"-L_2'-L_2 triple point was located at a surface pressure of about 3mN/m, contrary to the 10 to 15mN/m as reported from constant compression measurements. With this findings and the parallels between the monolayer preparation in relaxation isotherm measurements and the present study, the phase sequence L_2-L_2'-L_2" upon cooling and without external compression becomes plausible.

According to the generic phase diagram of Ställberg-Stenhagen and Stenhagen [111], the crystalline CS phase with upright chain configuration is the common low temperature phase, independent of the surface pressure. Moreover, in their publications the authors predict, that this phase should be achievable for many substances, where the cross section of the headgroup is smaller than that of the chain and the chains are sufficiently long

π [mN/m]	T [°C]	$A_\perp$ [Å^2]	subphase	reference
4.5	15.8	19.377	H_2O	[88]
3.5	21.1	19.479	H_2O	[88]
4.8	24.4	19.575	H_2O	[88]
21	-	19.8	H_2O	[115]
0	9	18.85	H_2O/CdCl	[71]
5.3	0	20.00$^{+)}$	HCl, pH2	[30]
20	0	19.39$^{+)}$	HCl, pH2	[30]
25	-	19.8	H_2O	[66]
35$^{*)}$	18.5	19.45	H_2O	unpublished

Table 3.8: Reference values for Langmuir monolayers of eicosanoic acid. $^{+)}$ values calculated from peak positions given in the publication; $^{*)}$layer was found to be not stable at that surface pressure so continous re-compression was applied

or the temperature sufficiently low [111]. In contrast, the later accepted generic phase diagram features the L_2" phase as the low temperature/low surface pressure configuration. In addition, the slope of the CS-L_2" phase boundary as mapped by Schwarz and Knobler [101] implies that a transition between the two phases can only be achieved by compression. However, the slope of this phase boundary might as well be an artifact of the investigation of constant compression isotherms: the authors state explicitly in their study, that they did not investigate the issues of stability and relaxation. This explanation would fit with the findings of Bommarito et al. [10] whose experiments on relaxed monolayers suggest qualitatively the opposite slope, thus allowing for the CS-L_2" transition by cooling at constant pressure. Although the presented experiments on monolayers of eicosanoic acid are obviously not made to construct a phase diagram, the obtained results point nevertheless towards a revised phase diagram containing a CS phase at low surface pressure and low temperature. Figure 3.33 sketches a possible phase diagram and the dashed line indicates the path through it as observed in the presented experiments.

A characteristic parameter that can be used to distinguish rotator from crystalline phases is the alkane chain cross section. Table 3.8 lists surface pressure, subphase, subphase temperature and chain cross section for reported Langmuir monolayer studies. Without the exception of enhancing the crystallinity of the monolayer by the presence of ions [71], the cross section is distinct larger than 19Å^2. Fatty acids with shorter alkane chains exhibit even larger cross sectional areas, e.g. about 23Å^2 for nonadecanoic acid (C19) at T=30°C and a surface pressure of 15mN/m [29]. Similar dense packing densities at low surface pressures like 18.45Å^2 observed at -40° on the present study were only observed for much longer alkane chains, e.g. triaccontanoic acid (C30) at zero surface pressure and 5°C subphase temperature [72]. The phases with a cross section of about 19.8Å^2 can be considered as rotator phases, despite of a tilt angle ('tilted rotator phase') and a distortion from a hexagonal lattice [88]. The chain cross section of 19.58Å^2 at a surface pressure of 4.8mN/m and a subphase temperature of 24.4°C as reported by Peterson and co-workers [88] corresponds well to the value of 19.54Å^2 found in the presented study for a surface pressure of 4.5mN/m and a subphase temperature of 22°C.

Another characteristic of a crystalline phase is the herringbone ordering. Contrary to the rotator phase, the two scatterers within the unit cell are not related by translational symmetry and consequently the reflection condition h+k=2n does not hold any longer. Durbin et al. [31] were the first to search successfully for the (12) reflection in ordered phases of heneicosanoic acid (C21). The observation of this reflection in the CS and L_2" phases demonstrated their long-range herringbone ordering. Within of the presented study no systematic search for the 'forbidden' herringbone-reflections were performed. However, the calculated position (about q_{xy}=2.54Å^{-1}) of the (03) peak was within a mapped q_{xy} region, but no significant evidence for the existence of this reflection could be found in the data. Calculating the peak intensity of this reflection using the backbone orientations as obtained from structure factor calculations of the observed peak intensities revealed that the intensity of this reflection would be way too small to be observed.

A low compressibility is another characteristic of the crystalline phases and moreover an important parameter for the transfer of surfactant films from the liquid to a solid surface via the Langmuir-Blodgett technique [9]. The microscopic linear compressibility of behenic acid (C22) was investigated by Fradin et al. using X-ray structures taking along an isotherm during a compression cycle [37]. However, this parameter is not accessible in the present study as experiments were carried out under constant surface pressure conditions. It might be therefore more natural to compare the thermal expansion of the phase to those of bulk alkanes like described in section 3.4.1.

Going from single chain amphiphilic molecules to multichain molecules like phospholipids, one can expect to find the same structures as discussed for fatty acids, albeit with some restrictions [54]. Nevertheless, studies of phospholipid phase diagrams including the location of phase boundaries and the identification of X-ray structures are barely available. A major difference as compared to fatty acids is the coupling of two chains to a single headgroup via a hydrophilic backbone, resulting in a hindrance of lateral motion of the whole molecule and a disabling of the chain rotation around its longitudinal axis. Nevertheless, typical packing modes and structural features found for phospholipid monolayers are similar to the rotator phases S and LS of fatty acids. With the assumption that a free rotation of the chains is not possible, the 'rotation' manifests itself in this case as a static disorder that provides on average a large cross section of the chains [54]. The phase behaviour of the phospholipids does not only depend on the chain length, but also on the headgroups. For the phospholipids with the etnanolamine head group, the area per molecule as derived from pressure-area isotherms is comparable to the area of two alkane chains. Hence the size of the headgroup is sufficiently small and does not impede chain ordering. Monolayers of C18 (DSPE) and C14 (DMPE) diacylethanolamines were studied at the air water surface by Kenn et al. [60]. They found phases exhibiting analogies with the rotator phases of fatty acids such as hexagonal lattices without tilt, rectangular lattices with n.n. tilt and oblique lattices. However, even for the stiffest film at high compression and low temperatures, no structures were observed, which could be compared to hindered rotator or crystalline phases of single chain molecules. For DSPE at 13°C in the highest compression phase they report a chain cross section of about 19.5Å^2, thus well above the lower limit of a hindered rotator phase. Replacing the phosphoethanolamine by a phosphatidic acid group, a pressure induced transition from a centred rectangular structure with n.n. tilt to a hexagonal lattice with upright chains is enabled [24]. Re-

ported chain cross sections for DPPA on water subphases are 19.8Å^2 and 19.78Å^2 at a surface pressure of 35mN/m at ambient temperature ([24] and [122], respectively), thus both comparable to packing densities in the free rotator phase of fatty acids. These values are compatible with the area requirement in a free rotator phase and to the 19.80Å^2 found in the present study for DPPA in DMSO/H2O at a surface pressure of 30mN/m and ambient temperature. In the present study of DPPA at the phase transition temperature of -15°C, the chain cross section of 19.15Å^2 is much smaller than even those for ethanolamines, but nevertheless still larger than the absolute lower limit of 19.0Å^2 for a hindered rotator phase. At a sample temperature of -49°C however, the cross section is with a value of 18.81Å^2 not any longer compatible with a rotator phase. To the best knowledge, this is the densest packing achieved for phospholipid monolayers on a liquid subphase. In addition, the phase transition from a hexagonal to a rectangular lattice, both exhibiting an upright chain conformation, points towards a LS-S phase transition also not yet reported for comparable molecules. A rectangular unit cell with upright chains would be also compatible with a crystalline CS phase. However, the rather broad diffraction peaks point towards a meso- and therefore an S-phase. The broadening of diffraction peaks in Langmuir monolayers of phospholipids upon compression is commonly observed and attributed to a frustration packing of the molecules caused by backbone disorder. In contrast to single chain molecules, the phase transitions in phospholipid monolayers resemble glass transitions where disorder is frozen-in [60]. The other characteristic feature distinguishing the CS from the S phase is long range herringbone order. Due to the limited number of diffraction peaks and their rather low intensity, unfortunately no structure factor calculations can be carried out to address this question.

Chapter 4

Theory of Surface Dynamics and XPCS

In this chapter the dynamics of a bare liquid/gas interface and a monolayer covered liquid surface will be described. The theory follows the framework of dynamic light scattering, which was first employed to get information about the viscoelastic constants of monolayers at a liquid surfaces. An adaptation of the theory to the X-ray regime and a description of the technical aspects of X-ray photon correlation spectroscopy (XPCS) will be given in last section of the chapter. This technique will be applayed in fifth chapter for the first time to determine the surface dynamics of a liquid surface covered by an organic monolayer. The X-ray technique is supposed to be suited for this purpose, as it allows to enhance the surface sensitivity by working under grazing incidence conditions.

4.1 Surface Dynamics

The following section is devoted to the description of a liquid/gas interface employing the hydrodynamic parameters. Both the case of a free and a monolayer covered surface will be discussed. The theory follows the description given in [11]. The surface of a liquid, either covered by a surfactant monolayer or not, is always decorated with so-called thermally capillary waves also known as ripples. The vertical displacement ζ of a point on the surface at the location $\mathbf{r}$ at a time t can be written as the sum of its Fourier components:

$$\zeta(\mathbf{r},t) = \sum_{\mathbf{q}} \zeta_{\mathbf{q}}(t) e^{i\mathbf{q}\mathbf{r}}. \tag{4.1}$$

Thereby the displacement is defined in a way that its average value vanishes: $\overline{\zeta(\mathbf{r},t)} = 0$. Because the space-time correlation function $\overline{\zeta(\mathbf{r},t)\cdot\zeta(\mathbf{r}+\boldsymbol{\delta}\mathbf{r},t+\tau)}$ has to fulfill the principles of invariance with respect to space and time, it only depends on $\boldsymbol{\delta}\mathbf{r}$ and τ. According to a hypothesis of Onsager, the evolution of a state variable like $\zeta_{\mathbf{q}}$ can be predicted by assuming that the evolution obeys the macroscopic equations relevant to describe the fluid. In this case, these are the linearised hydrodynamic equations, which

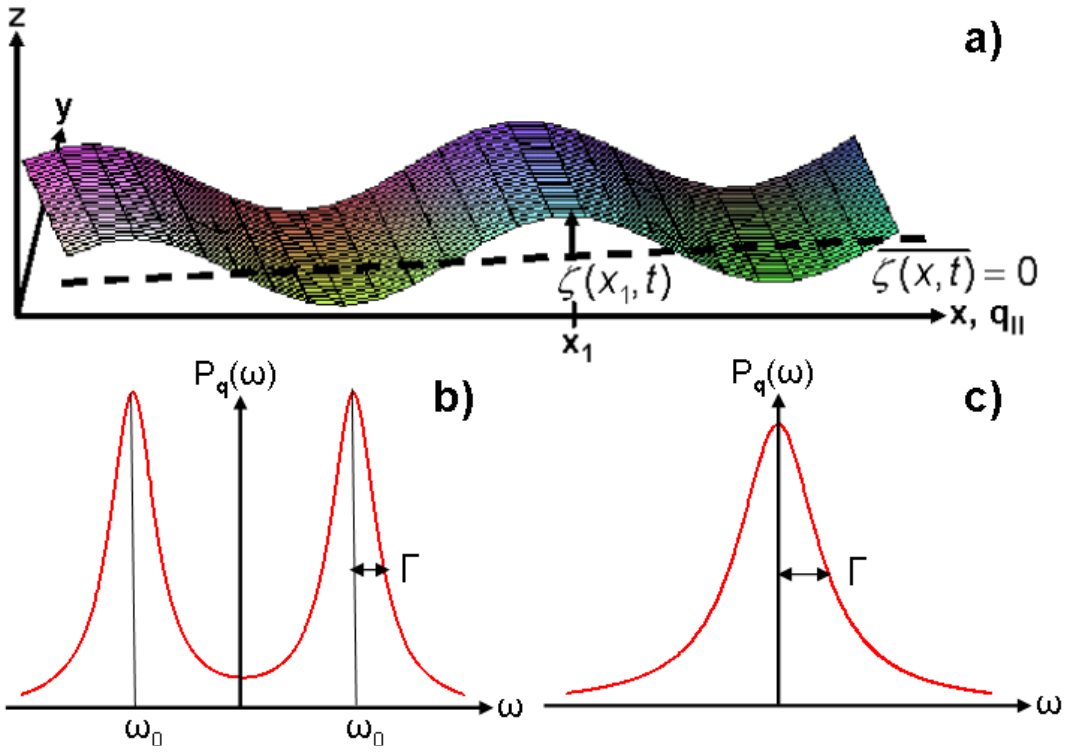

Figure 4.1: a) definition of the surface displacement of a two-dimensional surface wave; b) power spectrum in the case of propagating capillary waves; c) power spectrum in the case of overdamped capillary waves

express mass and momentum conservation in a liquid volume:

$$\mathbf{div}\ \mathbf{v} = 0 \tag{4.2a}$$

$$\frac{\partial \mathbf{v}}{\partial t} = -\frac{1}{\rho}\mathbf{grad}\ p + \frac{\eta}{\rho}\mathbf{\Delta v}, \tag{4.2b}$$

where $\mathbf{v}$ is the fluid velocity, ρ is its density, p the pressure and η the viscosity. In equation 4.2b the non-linear term $(\mathbf{v}\ \mathbf{grad})\mathbf{v}$ of the general hydrodynamic equation is already omitted by considering only surface waves whose amplitudes are very small as compared to the wavelength. Moreover, the term giving rise to gravity waves is also absent, as those waves are dominant on length scales much larger than the wave length of capillary waves (which are typically of the order of a few milimeters). The boundary conditions that have to be fulfilled are that the stress exerted normally and tangentially on an interface element are identical at both sides of the surface. These boundary conditions (valid at the surface) can be expressed for the case of two-dimensional waves on a plane liquid surface (see figure 4.1 a)) in the form:

$$-p + 2\eta\frac{\partial \mathbf{v}_z}{\partial z} - \sigma\frac{\partial^2 \zeta}{\partial x^2} = -p_0 \tag{4.3a}$$

$$\eta\left(\frac{\partial \mathbf{v}_x}{\partial z} + \frac{\partial \mathbf{v}_z}{\partial x}\right) = 0, \tag{4.3b}$$

with the surface tension σ and the pressure p_0 in the gas phase above the liquid. The Ansatz of Levich [73] to find solutions of this initial value problem is the seeking for solutions in form of a periodic function of the coordinate x and exponential functions of time and depth (corresponding to the z-direction). For the vertical displacement ζ the solution is the real part of the function of type

$$\zeta = \sum_{j=1,2} \exp(-iq_{\parallel}x + S_j t/\tau_0)\frac{\tau_0}{S_j}\left(A_j + \frac{q_{\parallel}}{m_j}B_j\right), \tag{4.4}$$

with the wavevector transfer $q_{\parallel}$ along the x-axis, and

$$\tau_0 = \frac{\rho}{2\eta q_{\parallel}^2}, \tag{4.5a}$$

$$m_j = \sqrt{q_{\parallel}^2 + 2S_j}, \tag{4.5b}$$

$$\frac{A_j}{B_j} = -\frac{m_j^2 + q_{\parallel}^2}{2q_{\parallel}m_j}. \tag{4.5c}$$

The parameter S_j has to fulfill simultaneously the dispersion equation

$$y + (S+1)^2 - \sqrt{1+2S} = 0 \tag{4.6}$$

and the condition Re$\{S\}$<0, where $y = \frac{\sigma\rho}{4\eta^2 q_{\parallel}}$. Solutions for S are real for $y < 0.145$ and complex imaginary conjugates for $y > 0.145$ (free surface of water, $q_{\parallel} = 450cm^{-1}$: $y = 400$). The corresponding evolutions of the systems are aperiodic and periodic, respectively. The solution of the dispersion equation in the periodic (propagating) case is given by

$$\omega(q_{\parallel}) = \underbrace{\sqrt{\frac{\sigma}{\rho}}q_{\parallel}^{3/2}}_{\omega_0} - \underbrace{i2\frac{\eta}{\rho}q_{\parallel}^2}_{\Gamma}, \tag{4.7}$$

with the propagation frequency ω_0 and the damping constant Γ. In the aperiodic (overdamped) case, the damping is given by

$$\Gamma = \frac{\sigma q_{\parallel}}{2\eta}. \tag{4.8}$$

It is noteworthy, that the approach of Levich does not constitute a general resolution of the hydrodynamic initial value problem. The applicability of the solution strongly depends upon the damping. In the case of weak or strong damping the solutions are satisfactory, while for critical damping conditions (at the transition from periodic to aperiodic behaviour) the approach results in an unreasonable partially correlation between the fluid velocity in the bulk and the surface vertical displacement [11].

The presence of monolayers at the liquid/gas interface changes the response of the surface with respect to external excitation due to its viscoelastic behaviour. In this case the dispersion equation takes the form

$$D(\omega) = [\widetilde{\varepsilon}q_{\parallel}^2 + i\omega\eta(m+q_{\parallel})][\widetilde{\sigma}q_{\parallel}^2 + i\omega\eta(m+q_{\parallel}) - \omega^2\rho/q_{\parallel}] + \omega^2\eta^2(m-q_{\parallel})^2 = 0, \tag{4.9}$$

where

$$m = q_{\parallel}\sqrt{1+\frac{i\omega\rho}{\eta q_{\parallel}^2}}, \tag{4.10a}$$

$$\widetilde{\varepsilon} = \varepsilon + i\omega\kappa, \tag{4.10b}$$

$$\widetilde{\sigma} = \sigma + i\omega\mu. \tag{4.10c}$$

The viscoelastic constants are here ε, κ and μ, while σ is the actual surface tension in the presence of the monolayer. The complex moduli in equations (4.10b) and (4.10c) arise from classical viscoelastic theory, where the response of the system to a periodic deformation is described by an elastic modulus (real part) and the dissipative viscosity (imaginary part). The parameter ε denotes the compressional elasticity, while κ is the compressional viscosity. The surface tension σ is in fact an equilibrium property of the system and can hence not be treated as a response function. The complex part of the surface tension related to the parameter μ was therefore introduced from pure symmetry considerations. The physical meaning of this parameter is related to the relaxation process associated with the vertical displacement of the surface. For instance, just after the distortion the tilt angle of the surfactant molecules with respect to the surface normal might have been changed. The return process to their equilibrium position is accompanied by a viscous loss.

4.2 Correlation Function and Power Spectrum

(X)PCS measurements give access either to the first-order time correlation function of the surface displacement parameter

$$G_{\mathbf{q}}^{(1)}(\tau) = \left\langle \zeta_{\mathbf{q}}(t)\zeta_{\mathbf{q}}^{*}(t+\tau)\right\rangle_t \tag{4.11}$$

or to its Fourier transform, the surface fluctuation power spectrum:

$$P_{\mathbf{q}}(\omega) = \frac{1}{2\pi}\int_{-\infty}^{+\infty} d\tau G_{\mathbf{q}}^{(1)}(\tau)e^{i\omega\tau}. \tag{4.12}$$

In the case of a simple low viscosity liquid, the power spectrum exhibits two Lorentzian components corresponding to the frequencies of propagating capillary waves (figure 4.1 b)). For large viscosities and/or small surface tension, the spectrum consists of a single Lorentzian profile (figure 4.1 c)), corresponding to overdamped capillary waves. In this two extreme cases the analysis of either the spectrum or of the time correlation function involves the determination of the two characteristic parameters (frequency and width or damping constant, respectively), which can be related to physical properties of the system via the dispersion relation (4.7). In the intermediate viscosity range or in the presence of an adsorbed monolayer at the surface, the variation of the spectrum from a Lorentzian is not negligible and the exact spectrum (or its Fourier transform) need to be employed for the analysis of the measured data.

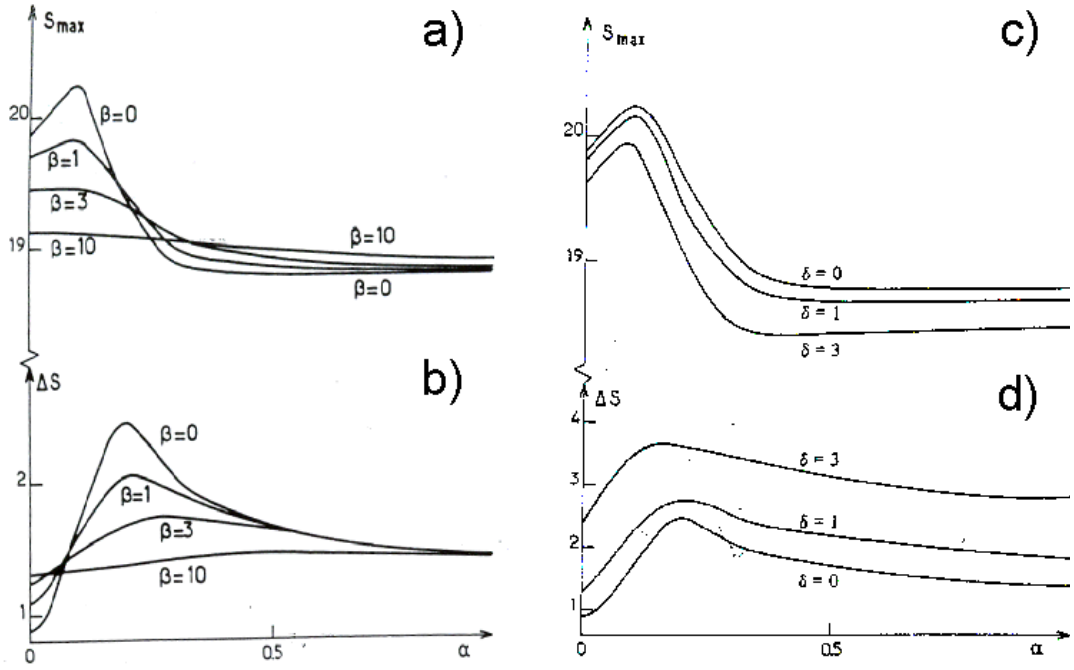

Figure 4.2: a), b) reduced peak frequency $S_{\max}$ and half-width ΔS versus reduced compressional elasticity α for different reduced compressional viscosities β; c), d) reduced peak frequency and half-width versus α for different reduced transvers shear viscosities δ.(figures from [68])

By introducing the reduced dimensionless variables

$$\alpha = \frac{\varepsilon}{\sigma}; \quad \beta = \frac{\kappa q_{\parallel}}{2\eta}; \quad \delta = \frac{\mu q_{\parallel}}{2\eta} \tag{4.13}$$

the dispersion equation (4.9) takes the form

$$\widetilde{D}(\omega) = [(\sigma\alpha+2i\omega\eta\beta/q_{\parallel})q_{\parallel}^2+i\omega\eta(q+m)][(\sigma+2i\omega\eta\delta/q_{\parallel})q_{\parallel}^2+i\omega\eta(q+m)-\frac{\rho\omega^2}{q_{\parallel}}]-[i\omega\eta(m-q_{\parallel})]^2 = 0. \tag{4.14}$$

By combining the results obtained by [68] and [20] the power spectrum of a liquid/gas interface in the presence of a monolayer can be written as:

$$\widetilde{P}_{q_{\parallel}}(\omega) = \frac{k_B T}{\pi\omega} \operatorname{Im}\left\{\frac{i\omega\eta(m+q) + (\sigma\alpha + 2i\omega\eta\beta/q_{\parallel})q_{\parallel}^2}{\widetilde{D}(\omega)}\right\}, \tag{4.15}$$

with the Boltzmann constant k_B and the temperature T in Kelvin. By setting $\alpha = \beta = \delta = 0$, the power spectrum given by equation (4.15) applies also to the case of a free liquid surface. The influence of the reduced compressional and shear transverse viscosities on the frequency and peak width of the power spectra are shown in figure 4.2 a) - d) as a function of the reduced compressional viscosity. Both the compressional elasticity and the viscosity have similar effects on the spectra: peak shift and broadening. The maximum

effect in terms of frequency shift and peak broadening is observed for $\alpha \approx 0.1 - 0.2$. In this region the frequencies of the capillary and compression waves are about equal and a maximum in the coupling occurs. For large values of α and β the spectra become more or less independent of these parameters. Physically this reflects a strongly reduced compressibility of the monolayer, which behaves like a solid plate, and the frequency and the damping of the capillary waves do not depend any more on the compressional parameters. In contrast, there is no limit for the influence of the shear transverse viscosity. Neither an upper limit for the increase of the width nor for the frequency decrease of the spectrum exists. Moreover, for large δ the capillary waves can even become completely damped.

4.3 X-ray Photon Correlation Spectroscopy (XPCS)

This section is devoted to the description of the principles of XPCS. The observable quantity in an XPCS experiment are intensity fluctuations, which can be related to the dynamics of the system via the correlation function as described in the first subsection. The second subsection summarises how partially coherent sources in the X-ray regime can be realised. The last part of this section deals with the finite resolution of an experimental setup and the accompanied coherence effects that need to be taken into account for the analysis of the data.

4.3.1 Speckle Pattern and Correlation Function

The principle of (X)PCS is based on the speckle pattern that arises from the coherent superposition of electromagnetic waves from different scattering centers of a sample. The intensity of the speckles depend strongly on the relative positions of the scattering centers with respect to each other. The microstructure of a sample is modified by its dynamics, which in turn results in a fluctuation of the speckle pattern. For X-rays, surface sensitive conditions can be established under grazing incidence conditions. Due to the limited penetration depth of the X-rays into the sample, the observed dynamics of the speckle pattern originates from the dynamic changes of the surface conformation. The length scale on which the dynamics is observed depends thereby on the wavevector transfer or the scattering angle, respectively. Thus, by accessing different scattering angles, the Fourier image of the surface is constructed, where each wavevector is related to one Fourier component of the surface deformation (compare equation (4.1)).

The observable in an XPCS experiment are the time dependent intensity fluctuations of the speckle pattern. These intensity fluctuations are proportional to the height displacement parameter: $I_{\mathbf{q}}(t) \propto \zeta_{\mathbf{q}}(t)\zeta^*_{\mathbf{q}}(t)$[1].The correlation between the surface displacement at wavevector $\mathbf{q}$ at times t and $t + \tau$ can be obtained under the assumption of Gaussian

[1]This relation, almost always valid in the case of light scattering, does not generally hold in the X-ray regime. As evidenced by the description of the diffuse scattering (see equation 2.69), the expansion $S_{diff}(\mathbf{q}) \sim \zeta_{\mathbf{q}}$ only holds in the limit $q\sigma \ll 1$. However, with a typical surface roughness of the order $\sigma \approx 3\mathring{A}$ and wavevector transfers which are in a typical surface XPCS experiement of the order of $5 \times 10^{-6}\mathring{A}^{-1}$, this condition is met.

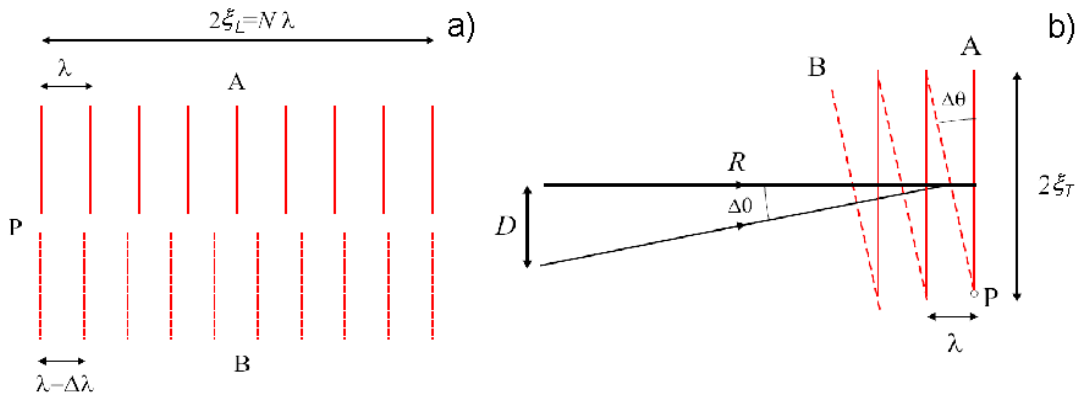

Figure 4.3: a) longitudinal coherence length ξ_L; b) transversal coherence length ξ_T (adapted from [7]).

fluctuations and a sufficiently large coherent volume via the Siegert relation [19]:

(4.16)
$$G^{(2)}_{\mathbf{q}}(\tau) = \left\langle \zeta_{\mathbf{q}}(t)\zeta^*_{\mathbf{q}}(t)\zeta_{\mathbf{q}}(t+\tau)\zeta^*_{\mathbf{q}}(t+\tau)\right\rangle_t = 1 + \left|\left\langle \zeta_{\mathbf{q}}(t)\zeta^*_{\mathbf{q}}(t+\tau)\right\rangle_t\right|^2 = 1 + \left|G^{(1)}_{\mathbf{q}}(\tau)\right|^2,$$

where $G^{(2)}_{\mathbf{q}}(\tau)$ denotes the second-order correlation function.

4.3.2 Coherent X-ray Radiation

In the optical wavelength regime lasers are powerful sources of coherent electromagnetic radiation with excellent energy resolution. In the X-ray regime, up to date no fully coherent sources are operational. The coherence of a (electromagnetic) wave describes the ability to interfere with itself or with a different wave. The coherence length is defined as the distance over which the phase relation of two waves differ by less than 180°. The longitudinal coherence length ξ_L (or temporal coherence) depends on the energy or wavelength resolution of the source, respectively (see figure 4.3 a)). For a wavelength spectrum ranging from λ to $\lambda + \Delta\lambda$, with $\Delta\lambda << \lambda$, the following expression for the longitudinal coherence length holds [7]:

(4.17)
$$\lambda = (N+1)\Delta\lambda \approx N\Delta\lambda \Longrightarrow \xi_L = \frac{N\lambda}{2} = \frac{\lambda}{2}\frac{\lambda}{\Delta\lambda},$$

where N>>1 is an integer number. It is evident, that a good energy or wavelength resolution ($\Delta\lambda/\lambda << 1$) is needed to obtain a useful longitudinal coherence, in particular as ξ_L scales with λ which is of the order of one Angstrom in the X-ray regime. The transverse coherence length ξ_T depends on the angular divergency $\Delta\theta$ of the incoming wave, which in turn depends on the size D of the source and its distance R to the sample. The transverse coherence length can be expresses as (see figure 4.3 b)):

(4.18)
$$\frac{\lambda}{2\xi_T} = \tan\Delta\theta = \frac{D}{R} \Longrightarrow \xi_T = \frac{\lambda R}{2D}.$$

X-ray radiation from an insertion device like an undulator is only partially coherent, meaning that the transverse coherence length is smaller than the usual beam size. In addition, the width of the intrinsic energy spectrum results in a longitudinal coherence length much smaller than the length scales under investigation. The first problem is usually overcome by collimating the beam to a size smaller than the transverse coherence length, while ξ_L is improved by increasing the energy resolution via the insertion of crystal monochromators and mirrors. Both measures are account of the photon flux, which is therefore a limiting parameter.

4.3.3 The Resolution problem

In contrast to the theoretical case treated in section (4.3.1), for an experimental setup the q-resolution is always limited. Among technical reasons, the finite coherence length of the incident radiation and the approximation of Frauenhofer scattering, which is hard to meet in the hard X-ray regime, cause coherence effects which alter the functional form of the correlation function and the corresponding power spectrum, respectively. In the grazing incidence geometry coherence effects may enter in a more complicated way than a simple contrast variation [75]. But it can lead to the observation of homdyne-heterodyne mixing, i.e. the occurrence of both first and second order correlation functions in the intensity autocorrelation function and an increased effective damping constant [41]. The relation between the second order correlation function $G^{(2)}_{\mathbf{q}}(\tau)$ and the first order correlation function $G^{(1)}_{\mathbf{q}}(\tau)$ is thereby given by equation (4.16). The physical interpretation

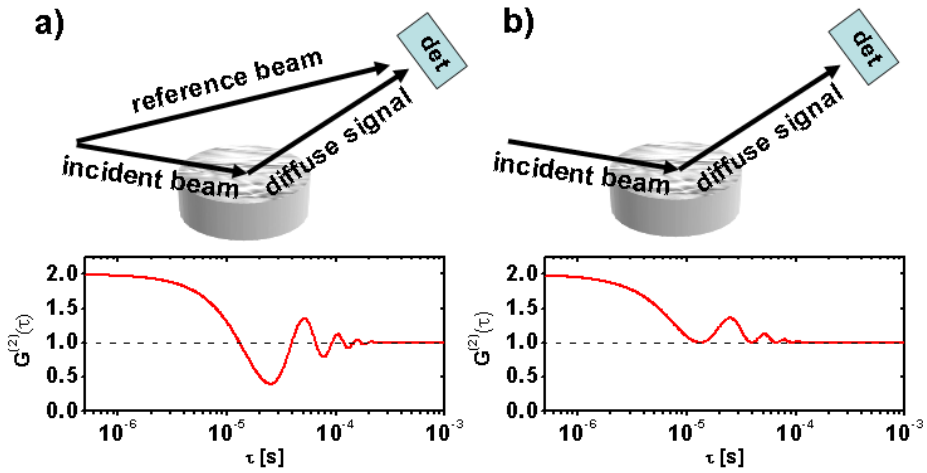

Figure 4.4: a) principle of the heterodyne detection scheme and the corresponding correlation function: the detected signal is the superposition of a reference beam with the diffuse scattering from the sample surface. In praxis, the heterodyne mixing occuring in the experiments arises most probably from a mixing between the specular reflected beam and the diffuse scattering. The functional shape of the correlation function is (in the most simple case) a damped cosine. b) homodyne detection scheme: The signal observed in the detector is solely the diffuse scattering from the sample. In this case the functional form of the correlation function is the abolute square of a damped cosine.

of a homodyne signal is the detection of an electromagnetic wave that arises solely from scattering at the sample surface (see figure 4.4 b)). In the heterodyne case (see figure 4.4 a)) this signal is superimposed with a reference beam which does not contain the diffuse signal. In praxis, this reference beam might be constituted by the direct or the specular beam. The rigorous mathematical calculations of the coherence effects due to the finite q-resolution [38] and [41] are quite cumbersome and employ the calculation of the evolution of the mutual coherence function as the incident coherent beam passes the optical elements and the sample in the experimental setup. A simplified approach to take the finite resolution and the accompanied coherence effects into account can be found in [34]. The intensity autocorrelation function is then given as

$$G_q^{(2)}(\tau) \propto \left| R(q) + \frac{k_B T}{\sigma} \int_0^\infty d^2q' G_q^{(1)}(\tau) R(q-q') \right|^2 , \tag{4.19}$$

with the surface tension σ and a generalised resolution function R. The first term describes the specular reflection, while the convolution integral accounts for the diffuse scattering from the sample. The convolution of the surface height-height correlation function $G_q^{(1)}(\tau)$ with the resolution function R causes a broadening of the corresponding power spectrum which is equivalent to an additional damping. In addition, the convolution might also cause a shift of the mean frequency of the spectrum. Furthermore, the first term on the right hand side of equation (4.19) can act as a reference term, playing a role similar to the systematic mixing of a reference beam with the diffuse scattering of the sample. Therefore, depending on the resolution, switching between the hetero- and homodyne detection scheme can occur. In principle, the resolution function R can be theoretically calculated, if the exact influence of each optical element within the beam pass (including the sample itself) is known. However, in praxis this situation is not realistic and the resolution function or its parameters remain as free fit parameters in the data analysis procedure. Within the framework of the present work, the resolution function is assumed to be Gaussian.

In general, the dependency of the functional shape of the correlation function and the corresponding physical parameters (in particular the bulk viscosity) is much larger in the case of propagating capillary waves. This behaviour arises from the superposition of (in the most simple case) Lorentzian profiles with different integrated intensities and mean frequencies (compare figure 4.1 b)). This situation is matched for instance for low viscosity liquids with high surface tension like water. By neglecting resolution effects the damping constants were found to lead to values for the bulk viscosity which were too high compared to accepted literature values [42]. Contrary, in the overdamped case for large viscosities and/or low surface tensions the resolution corrections have a minor influence on the physical parameters deduced from the spectra. So the values obtained by XPCS measurements for the viscosity of glycerol compare well to tabulated values even without taking resolution effects in the analysis of the XPCS data into account [103].

There are other techniques available to determine the viscosity or surface tension of simple liquids with a higher precision than light or X-ray scattering methods. By studying the free surface of simple liquids, the resolution parameters of the used setup can be therefore determined, if the physical parameters like surface tension, bulk viscosity

and density are known from independent measurements. By applying this procedure, the resolution parameters can be determined, so that in the investigation of an unknown sample the physical parameters are the only refineable variables.

Chapter 5

Surface Dynamics: Experimental Results

The current chapter is devoted to the results of the investigation of the surface dynamics of free and monolayer covered liquid surfaces by means of XPCS. After the description of the beamline at which the experiments were performed, the results for pure water and the bare subphase will be presented. These measurements serve also as a calibration from which the setup dependent resolution parameters can be determined. Primed with the knowledge of the achievable resolution, the sensitivity of the method with regard to the elastic constants in the presence of a monolayer will be discussed. The following sections of this chapter are dedicated to the presentation of the results obtained for the DMSO/water surface covered by monolayers of eicosannoic acid and DPPA, respectively, followed by a discussion of the dynamics measurements.

5.1 The Troika I (ID10A) Beamline

The surface XPCS measurements were carried out at the Troika I (ID10A) beamline (ESRF, Grenoble). A schematic outline of the beamline is shown in figure 5.1 a). The X-ray energy was 7.98keV, using all three undulators of the beamline. The Troika beamline is located in a so-called high-β section of the ESRF storage ring, i.e. it provides a small beam divergence (h×v: $28\times17\mu\text{rad}^2$) at the cost of a larger source size of about (h×v) $928\times23\mu\text{m}^2$). The beam passing through the first monochromator of the Troika II branch (see chapter 3) is focussed in the vertical direction by beryllium compound refractive lenses and collimated by a pair of perpendicular slits. Afterwards it is pre-monochromatised by means of a double mirror setup. Before hitting the Si111 single bounce monochromator, the beam is again collimated by a pair of perpendicular slits. The Si111 monochromator provides an intrinsic energy resolution of $\frac{\Delta E}{E} \approx 6 \cdot 10^{-5}$. After the monochromator a single mirror is used to tilt the beam down to establish grazing incidence conditions (in this case $\alpha_I = 0.12°$). The beam can be attenuated by an absorber wheel after the mirror. A secondary source is established by means of a perpendicular pair of roller-blade slits acting as a pinhole and were used at an opening of $10\times10\mu\text{m}^2$. The typical transvers and longitudinal coherence lengths which are achieved with this setup are $\xi_T \approx 10\mu m$

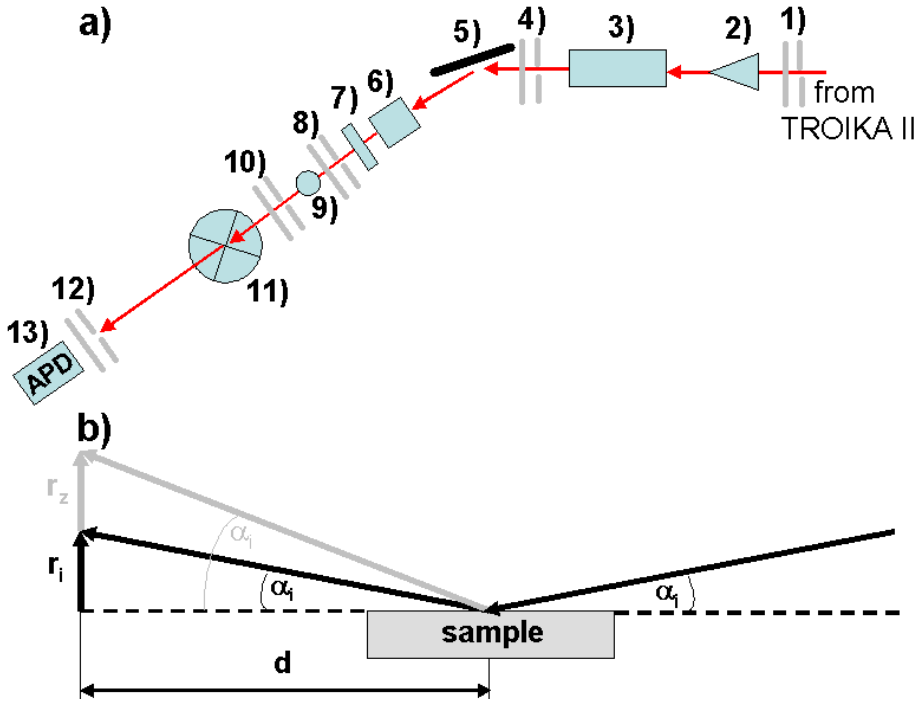

Figure 5.1: a) schematic outline of the Troika I beamline (ID10A): 1), 4) pairs of horizontal and vertical slits, 2) Be compound refractive lenses for vertical focussing, 3) double mirror, 5) Si111 monochromator, 6) mirror, 7) absorber, 8) roller-blade slits (acting as a pinhole), 9) monitor counter, 10) guard slits, 11) sample position, 12) detector aperture, 13) detector; b) scattering geometry:α_i, α_f incident and exit angles, respectively, r_i, r_z: corresponding detector aperture offsets, d: sample detector distance

and $\xi_L \approx 1\mu m$. The intensity of the incoming beam is monitored by the scattering of a capton foil in the beam path and a NaI scintillation detector. A set of guard slits after the roller-blade slits are used to suppress Frauenhofer fringes from the roller-blade slits. The sample is mounted in liquid surface geometry on a versatile six circle diffractometer. After the sample, the beam passes through a 2m long evacuated flight pass before it hits the detector. A crossed pair of μm controlled slits were used to define the detector aperture (typically (h×v): 20×20 to 50×50μm^2). An avalanche photo diode (APD) was used as a detector, being capable of detecting high flux with a high signal to noise ratio down to short time scales in the ns range. Time correlations were recorded with a digital Flex01-08D multiple τ correlator, providing an intrinsic time resolution of 8ns.

Correlation functions were recorded in the specular plan at exit angles $\alpha_f \neq \alpha_i$ by moving the aperture offset r_z with respect to the specular beam. The scattering geometry is depicted in figure 5.1 b). The modulus of the wavevector transfer $q_{\|}$ parallel to the sample surface is given by

$$q_{\|} = \frac{2\pi}{\lambda} \left(\cos \alpha_f - \cos \alpha_i\right), \tag{5.1}$$

where α_i is the incidence angle of the incoming beam and α_f the exit angle, under which

the diffuse scattering from the sample is detected and λ is the X-ray wavelength. The exit angle α_f can be expressed in terms of the detector aperture offsets r_i at the position of the specular beam, r_z at the position of the diffuse scattering belonging to the scattering angle α_f and the sample detector distance d (d=2275mm in the used setup) as:

$$\alpha_f = \arctan\left(\frac{d\tan\alpha_i + r_z}{d}\right). \tag{5.2}$$

The sample environement and the sample preparation procedure were identical to the ones described in sections 3.1 and 3.3.1.

5.2 Pure Liquids

5.2.1 Calibration Measurements with Water

As outlined in section 4.3.3, especially for propagating capillary waves the resolution has a non neglegible influence on the power spectrum and the corresponding correlation function. In particular, the width of the power spectrum, related to the damping of the capillary waves via the bulk viscosity of the liquid, is altered. It is hence indispensable to determine the resolution by measuring a test liquid with known physical characteristics so that the resolution related parameters are the only unknowns in the data refinement process. For this work, capillary waves on the surface of pure water were measured as a calibration. Although pure water is not easy to measure due to its high surface tension and small bulk viscosity, the obtained correlation functions are in turn very sensitive to coherence effects conditional upon the resolution. In addition, its physical properties like surface tension, bulk viscosity and density are widely studied by various techniques and well tabulated. Figure 5.2 shows the correlation function obtained for pure water at a temperature of 22.2°C and a parallel wavevector transfer of 503cm^{-1}. Panel a) displays the power spectra according to equation (4.15) where in the case of a simple liquid $\alpha = \beta = \delta = 0$ holds. The dashed line represents the theoretical spectrum for an infinite resolution, while the solid line was calculated by taking resolution effects via the convolution with a Gaussian resolution function (see equation 4.19) into account. The broadening of the spectrum due to this convolution is evident, while the shift of the mean frequency is less distinct. Figure 5.2 b) shows the corresponding autocorrelation functions (dashed and solid lines for infinite and finite resolution, respectively) and the measured data (open circles). As the convolution with the resolution function is an integral over $q_\parallel$ while the Fourier transform between the power spectrum and the correlation function (eq. 4.12) is an integral over ω, the resolution can be accounted for in the power spectrum before the transformation to the time domain. The obtained correlation function was shifted along the y-axis by a constant baseline and scaled by a contrast factor.

It is noteworthy that in this low damping regime the experimental data can be equally well described by the commonly used exponentially damped cosine function, leading to identical resolution parameters.

Correlation functions for pure water recorded in the $q_\parallel$-range from 335 to 901cm^{-1} are shown in figure 5.3 a). The solid lines were calculated using the Fourier transformed

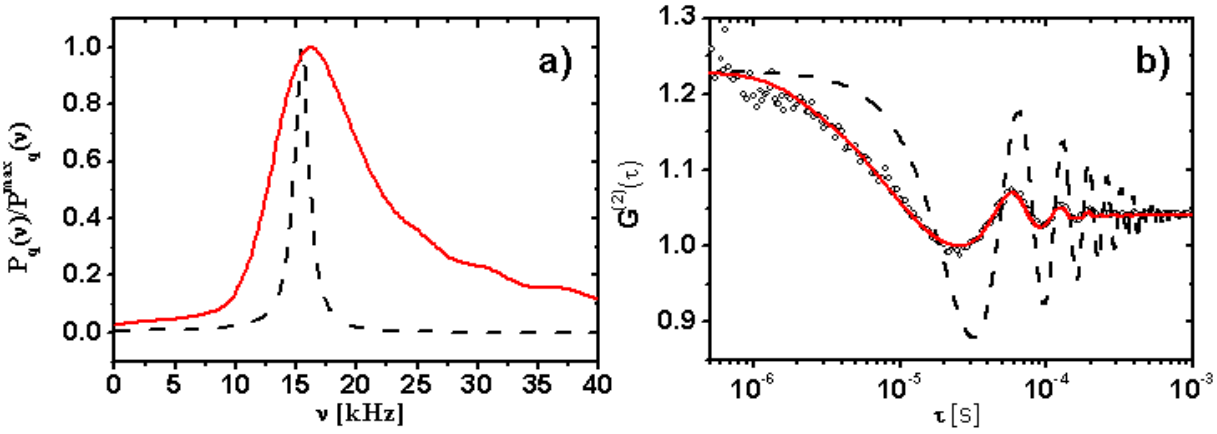

Figure 5.2: a) power spectra for pure water at a wavevector transfer of 503cm^{-1} with infinite (dashed line) and finite (solid line) resolution; b) corresponing correlation functions and measured data (open circles)

power spectrum (equation 4.15) and literature values of $\sigma = 72mN/m$, $\eta = 1mPas$ and $\rho = 1000kg/m^3$. The correlation functions are predominantly heterodyne (compare section 4.3.3) with the exception of the function recorded at the largest wavevector transfer $q_{\|} = 900cm^{-1}$, which is about at the transition from heterodyne to homodyne. The shift of the first minimum of the correlation function towards faster time scales with increasing $q_{\|}$ reflects the quadratic dependency of the propagation frequency of the wavevector transfer (see equation 4.7) The refinement of the curves employed exclusively the resolution parameters. While a constant spread of a $\Delta q_y \approx 4.0 \cdot 10^{-5}\mathring{A}^{-1}$ can be assumed in the horizontal direction, the spread Δq_x was found to be in general of the order $10^{-7}\mathring{A}^{-1}$ but to vary linear as a function of the parallel wavevector transfer $q_{\|}$. The obtained values for the resolution parameter Δq_x are shown in figure 5.3 b) as open circles. The solid line is a linear fit of the data points that can also serve as an interpolation to get the resolution parameter corresponding to a $q_{\|}$ for which no calibration measurement was performed. Both the constant behaviour of Δq_y and the linear variation of Δq_x are in accordance with the more rigerous mathematical treatments of the resolution problem [41]. Moreover, from the magnitude of these two parameters reasonable coherence length of $\xi_x \approx 25\mu m$ and $\xi_y \approx 15\mu m$ can be deduced. Thus, although introduced via an oversimplified approach of the resolution problem, magnitude and $q_{\|}$-dependence of these parameters seems reasonable. The further strategy of the data analysis is therefore to assume that these parameters are only setup dependent and can hence be used to evaluated all measurements carried out with the same setup. As in the frame of this work also the temperature dependent surface dynamics of the pure subphase DMSO/H_2O was investigated, these data sets can be used as a cross-check of this strategy.

5.2.2 Temperature Dependent Surface Dynamics of DMSO/H_2O

The surface dynamics of bare DMSO/H_2O mixtures were investigated in the temperature range between 22°C and -40°C. The values or interpolation formulas for the surface

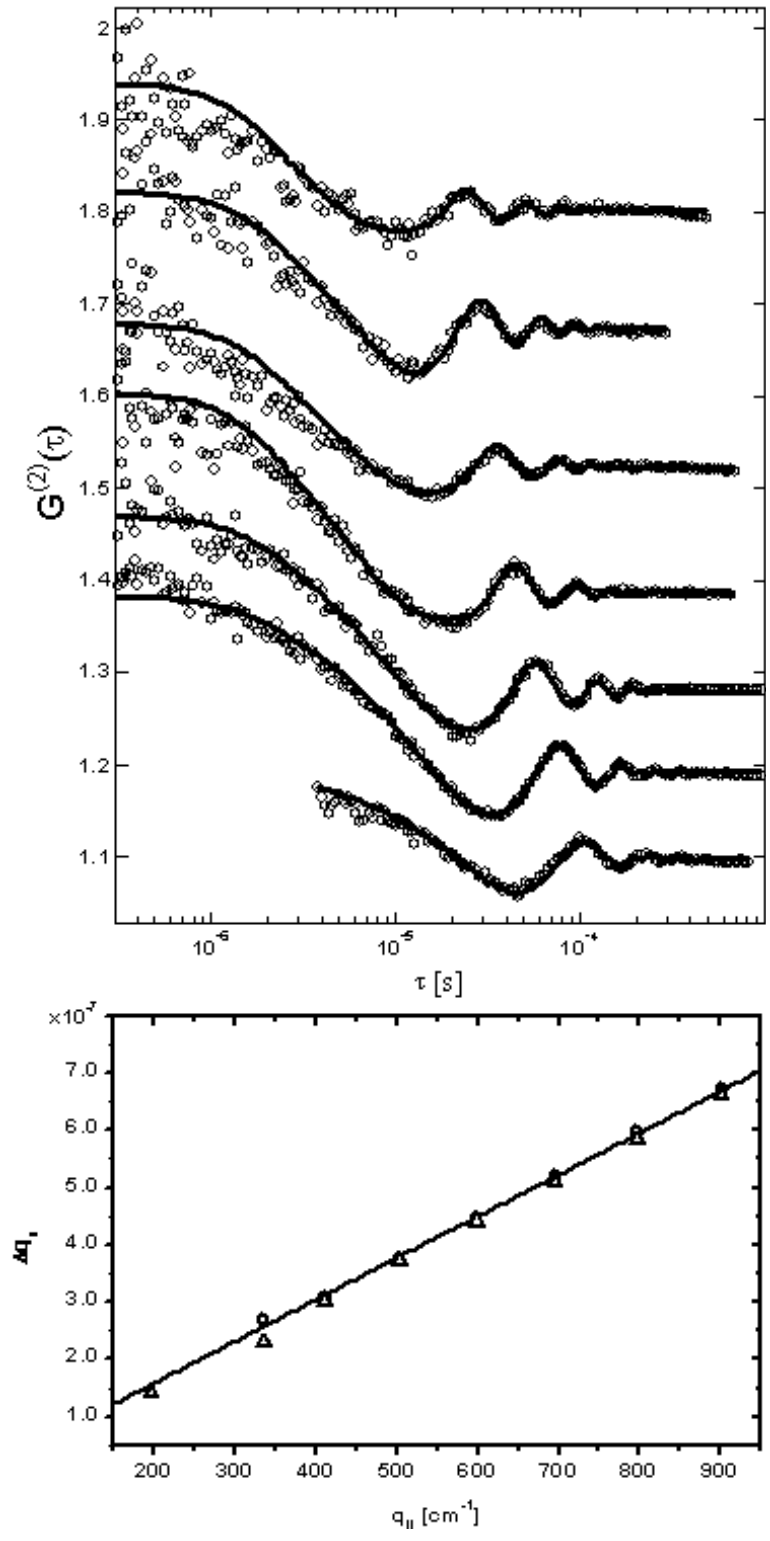

Figure 5.3: a) correlation functions and fits including resolution effects for pure water at 22.2°C at wavevector transfers $q_{\|} = 335$, 411, 503, 598, 696, 797 and $901 cm^{-1}$ (bottom to top), the correlation functions have been scaled in contrast and shifted along the y-axis for clarity; b) resolution parameter Δq_x as a function of the parallel wavevector transfer $q_{\|}$: open circles: values obtained by fitting the correlation functions in panel a), solid line: linear fit of these values, open triangles: values from fitting DMSO/H_2O at 22°C

tension, bulk viscosity and density of the eutectic mixture in this temperature range can be found in section 1.2. Assuming the validity of the resolution parameters found in the calibration measurement for pure water, besides of the contrast and the baseline there are no refinable parameters to describe the measured correlation functions. Figure 5.4 a) shows the correlation functions recorded at 22.0°C in the $q_{\|}$-range from 196 to 901cm^{-1}. The curves were modeled with the values $\sigma = 51mN/m$, $\eta = 4mPas$ and $\rho = 1080kg/m^3$. Using the resolution parameters found for pure water already a qualitatively good descritption of the data was achieved. Further refinement of the resolution parameter Δq_x only let to marginal changes as can be seen from figure 5.3 were the refined resolution parameters are plotted as open triangles but in most cases overlap with the ones found for water. The most striking difference between the correlation functions of pure water and DMSO/water at 22°C is that the latter ones show a homodyne behaviour. The switching between hetero- and homodyne is automatically reproduced, demonstrating that the convolution with the resolution function is capable of accounting for this coherence effect. In contrast, at a sample temperature of -40°C the capillary waves are completely overdamped as can be seen from the correlation functions in figure 5.4 b). These correlation functions were fitted with values of $\sigma = 63mN/m$, $\eta = 93mPas$, $\rho = 1145kg/m^3$ and resolution parameters identical to the ones obtained for water at 22.2°C. The transition from

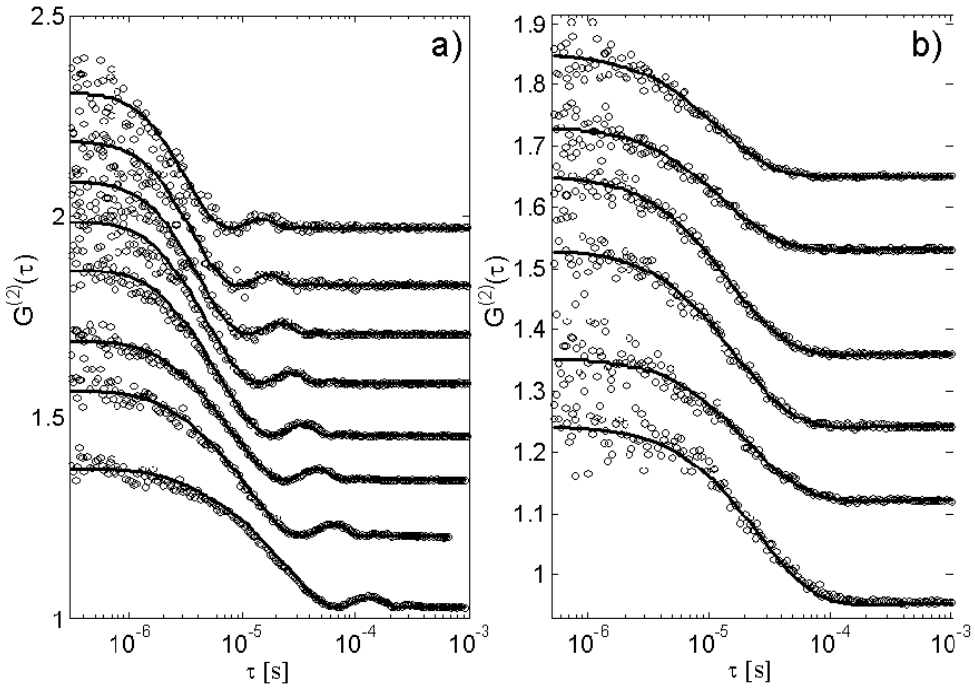

Figure 5.4: a) correlation functions for DMSO/water in the eutectic mixing ratio at 22.2°C for parallel wavevector transfers $q_{\|}$ = 196, 323, 411, 503, 598, 696, 797, 901cm^{-1} (bottom to top); b) correlation functions at -40°C measured at $q_{\|}$ = 411, 503, 598, 696, 797, 901cm^{-1} (bottom to top)

propagating to overdamped capillary waves as a function of temperature is evident from figure 5.5. Here the measured correlation functions (open circles) and the corresponding

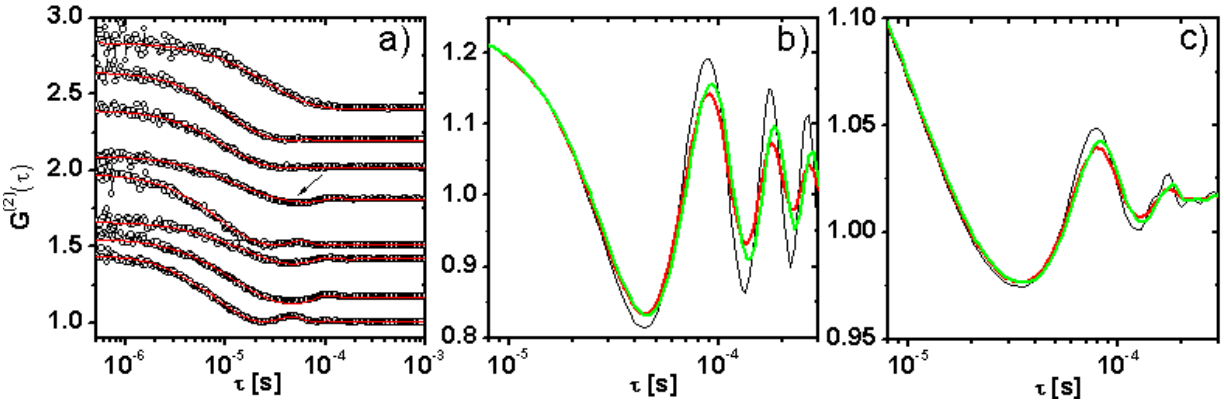

Figure 5.5: a) correlation functions for DMSO/water taken at $q_{\|} = 411\mathring{A}^{-1}$ at temperatures of 22°C, 10°C, 5°C, 0°C, -5°C (arrow), -10°C, -20°C, -40°C (bottom to top), the correlation functions have been scaled in contrast and shifted along the y-axis for clarity b) simulated correlation functions for $q_{\|} = 400cm^{-1}$, $\sigma = 72mN/m$, $\eta = 1mPas$, $\beta = \delta = 0$, black line: $\alpha = 0$, red line: $\alpha = 0.2$, green line: $\alpha = 0.5$ (infinite resolution) c) identical correlation function as in b) but taking the finite resolution into account. Contrast and baseline are identical for the curves in panels b) and c), the correlation functions are only displayed partially to enhance visability.

fits (solid lines) are shown as a function of temperature for a constant parallel wavevector transfer of $q_{\|} = 411\mathring{A}^{-1}$. Although the correlation functions change between homodyne and heterodyne as the physical parameters change with temperature, it is clearly evident that at a sample temperature of -5°C the capillary waves are still propagating, while at -10°C they are overdamped. Strictly speaking, this behaviour is $q_{\|}$ dependent, as the damping increases with increasing $q_{\|}$ (see equation 4.7).

5.2.3 Some Remarks on the Resolution

After the experimental determination of the resolution parameters and their cross-check by measuring the temperature dependent dynamic of the pure DMSO/H_2O subphase, some conclusions can be drawn how the viscoelastic constants of a monolayer manifest themself in the correlation functions. It is evident from the spectra and the correlation functions shown in figure 5.2 that the contribution of the finite resolution to the broadening of the power spectrum and the shift of the mean frequency is not negligible. In order to compare the influence of the resolution and the viscoelastic constants, correlation functions were calculated using the bulk properties for pure water ($\sigma = 72mN/m$, $\eta = 1mPas$, $\rho = 1000kg/m^3$) and modified by varying the parameters α, β and δ. The results are shown in figure 5.5 b) for the theoretical case of infinite resolution and in panel c) for a finite resolution identical to the one determined by the calibration sample analysed in section 5.2.1. For the curves calculated with infinite resolution the derivation from $\alpha = 0$ is evident as an additional damping of the oscillation. In the case of finite resolution, the damping is already drastically increased for $\alpha = 0$. Although the relative additional

damping for e.g. $\alpha = 0.2$ is almost identical in both cases, the absolute reduction of the oscillation amplitude e.g. at around $\tau \approx 10^{-4}$ is 80% smaller in the case of finite resolution. The frequency shift induced by $\alpha \neq 0$ becomes clearly visible as a shift of the oscillations at longer correlation times τ in the case of infinite resolution. However, in the case of finite resolution very often only the first two oscillations are distinct before they get damped out. Hence, both α and β cause mainly an increased damping, while the accompanied frequency shift is not easy to detect in the correlation functions. For the parameter β, the additional damping is even smaller than for α, while the magnitude of the frequency shift is comparable. The additional damping induced by a non-zero value of the parameter δ is even more distinct than that caused by $\alpha \neq 0$ in the case of infinite resolution. Taking the finite resolution into account, the effect of δ is superimposed with the according broadening of the spectrum and hence less destinct. In contrast to α and β the parameter δ can in extrem cases cause the transition from propagating to overdamped capillary waves. The most favourable sensitivity to this parameter can therefore be expected in a region of critical damping. Contrary, the influence of α and β on the damping is quite similar in the correlation functions so that an independent determination of these two parameters is not favourable. As δ also increases the damping, its influence superimposes with the ones of α and β. The impact of a finite resolution and the accompanied coherence effects are less important in the case of overdamped capillary waves. The sensitivity of overdamped correlation functions in the case of infinite and finite resolutions was simulated using the paramaters for the DMSO/H_2O mixture at a temperature of -40°C. In both cases the curves for α and β unequal to zero superimpose exactly with the ones for $\alpha = \beta = 0$, so that a determination of these parameters from overdamped correlation functions is not feasible. Because there is no upper limit for δ, its influence becomes visible even in the overdamped correlation functions.

5.3 Surface Dynamics of Monolayers on DMSO/H_2O

5.3.1 Eicosanoic Acid

Monolayers of eicosanoic acid were prepared for the investigation by XPCS in the same way as described in sections 3.1 and 3.3.1. Upon cooling down to a temperatures of 0°C, the correlation functions reveal the presence of propagating capillary waves on the sample surface. Moreover, in the temperature range between 22°C and 0°C the correlation functions could be described by the same parameters as the pure DMSO/H_2O subphase, despite of the adjustment of the surface tension for which the reduction by the surface pressure of the layer was taken into account. As discussed in section 5.2.3, the finite resolution and accompanied coherence effects limit the sensitivity to the viscoelastic parameters α, β and δ. Therefore, non-zero values of this parameters in this temperature range cannot be excluded. Figure 5.6 a) shows the correlation function for eicosanoic acid at 22°C and a parallel wavevector transfer $q_{\parallel} = 411 cm^{-1}$. The lower curve (open squares) is superimposed by a model curve for which the viscoelastic parameters were set to $\alpha = 0.2$, $\beta = 8$ and $\delta = 0.5$. The upper curve (open triangles) is superimposed by a model curve using $\alpha = \beta = \delta = 0$. Hence, a satisfactory agreement between the data and the model is already achied without taking the viscoelastic constants of the monolayer

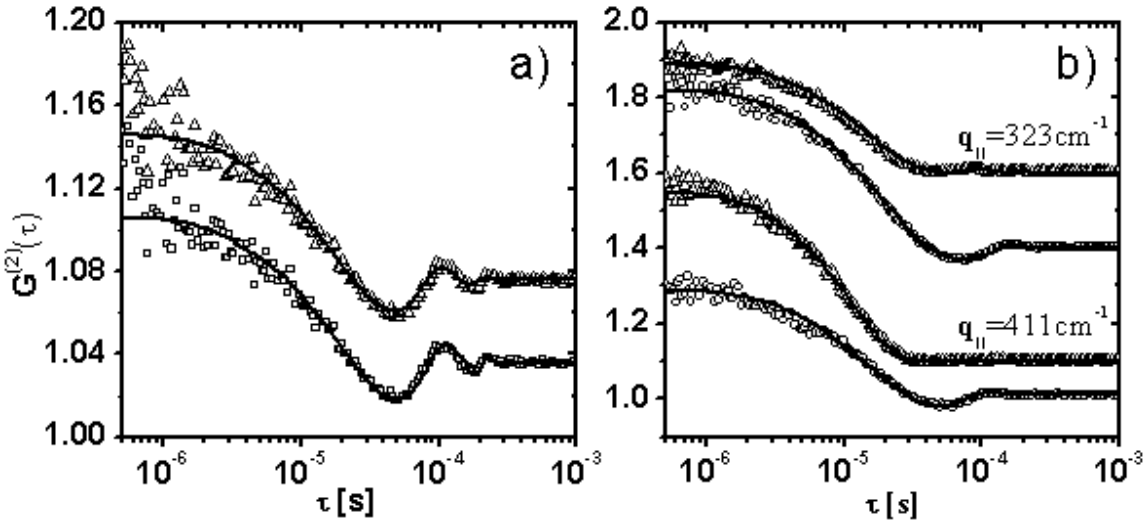

Figure 5.6: a) correlation functions of eicosanoic acid on DMSO/H_2O at T=22°C and $q_{||} = 411cm^{-1}$: modeled with $\alpha = 0.2$, $\beta = 8$ and $\delta = 0.5$ (open squares) and with $\alpha = \beta = \delta = 0$ (open triangles). b) Correlation functions for the bare (open circles) and monolayer covered (open triangles) DMSO/H_2O surface at $q_{||} = 323cm^{-1}$ and $q_{||} = 411cm^{-1}$. In the presence of the monolayer the switching to an overdamped behaviour was achieved by increasing the parameter δ to 2.5. Correlation functions have been shifted along the y-axis for clarity.

into account. Thus, only an upper limit for the parameter δ can be given, which was found to be $\delta < 1$. A somehow different situation is met at a sample temperature of -5°C: while for wavevector transfers up to 696cm^{-1} the bare DMSO/H_2O surface is according to the correlation functions decorated with propagating capillary waves, in the presence of the eicosanoic acid monolayer the capillary waves are overdamped. Thus, here the system is close to a critical damping behaviour, where subtile changes lead to a switching between propagating and overdamped behaviour. Figure 5.6 b) displays the correlation functions at two different wavevector transfers for the pure subphase (open circles) and in the presence of the monolayer (open triangles). In the case of the monolayer covered surface, the solid lines represent a model, where $\delta = 2.5$. The switching to an overdamped behaviour could not be induced by varying the parameters α and β alone. However, the sensitivity of these parameters is too low to determine their values, so that they were set to zero instead and the increased damping was achieved by solely increasing δ. It is noteworthy, that even by a varying the resolution sensitive parameter Δq_x no simultaneous agreement in terms of characteristic time scale and damping could be achieved with δ set to zero. At even lower temperatures both the bare and the monolayer covered subphase were found to be decorated by overdamped capillary waves. Therefore, as discussed above, the sensitivity of the correlation functions to the viscoelastic parameters is further reduced. Nevertheless, the measured correlation functions at temperatures below -5°C are compatible with a value of δ=2.5. At a temperature of -40°C the upper limit of δ being compatible with the obtained correlation functions was determined to be about 2.8.

Although the model itself would in principle allow for a detailed insight into the viscoelastic behaviour of the monolayer, it is clear that from the performed measurements and obtained results only qualitative conclusions can be drawn. This holds in particular, as the additional damping in the presence of the monolayer was only modeled using one parameter and was hence treated as an additional effective damping. It strikes out, that the critical damping appears at a temperature close to the appearance of the crystalline phase of the monolayer as determined by X-ray diffraction. Two self-energizing effects are plausible: Due to the increasing viscosity of the subphase, the system is at that temperature already close to an overdamped behaviour. The reduced dynamics of the surface can in turn favour the structure formation of the surfactant molecules. With the appearance of crystalline domains the viscoelasticity of the monolayer becomes visible in the dynamics. Furthermore one might think about an damping effect of the crystalline domains similar to ice floes on the ocean, but need to bear in mind that the monolayer is highly inhomogeneous and the average domain size in the crystalline phase is with about 100nm small compared to the length scales $x_0 = 2\pi/q_{\|}$ probed in the experiment.

5.3.2 DPPA

Monolayers of DPPA were prepared on DMSO/H_2O in a similar way as for the static scattering and diffraction experiments. The surface dynamics was studied at temperatures of 22°C, 0°C, -10°C and -20°C in the $q_{\|}$-range between 323 and 797 cm^{-1}. At a sample temperature of 22°C the correlation functions showed all a homodyne detection scheme and the characteristics of propagating capillary waves. Representative curves at a wavevector transfer of $q_{\|}$=503cm^{-1} are shown in figure 5.7 a) Comparing the correlation functions in the presence of the monolayer (open triangles and squares) with the one obtained for the bare subphase (open circles), a distinct shift in the propagation frequency of the capillary waves is evident. This shift arises from the presence of the monolayer, whose surface pressure of 30mN/m noticeably reduces the effective surface tension of the subphase. According to equation (4.7) this effect results in a reduction of the capillary waves' propagation frequency. Taking only this reduced surface tension into account and setting the viscoelastic constants of the monolayer all to zero leads to the curve shown with the data as open squares in figure 5.7. Especially at faster time scales of about 10^{-5}s, the discrepancy between the model curve and the data points become visible. Taking an additional damping in the presence of the monolayer into account, the match between data and model can be substantially improved. The curve shown with the data as open triangles takes an additional damping via the parameter $\delta = 0.5$ into account. At a temperature of 0°C all correlation functions are found to show overdamped behaviour, in contrast to the pure DMSO/H_2O subphase (see figure 5.7 b)). In contrast to the case of the eicosanoic acid monolayer, the switching from propagating to overdamped can be reproduced with the model already with $\alpha = \beta = \delta = 0$ (curve belonging to the data shown as open squares). But like at 22°C a value of δ of about 0.5 is needed to obtain a satisfactory matching between the experimental data and the modelled correlation function. At -20°C (see figure 5.7 panel c)) both the capillary waves of the bare and the monolayer covered surface are overdamped. Although in this situation the sensitivity with respect to the viscoelastic parameters is in general poor, a minimum value of about 0.5 for δ was

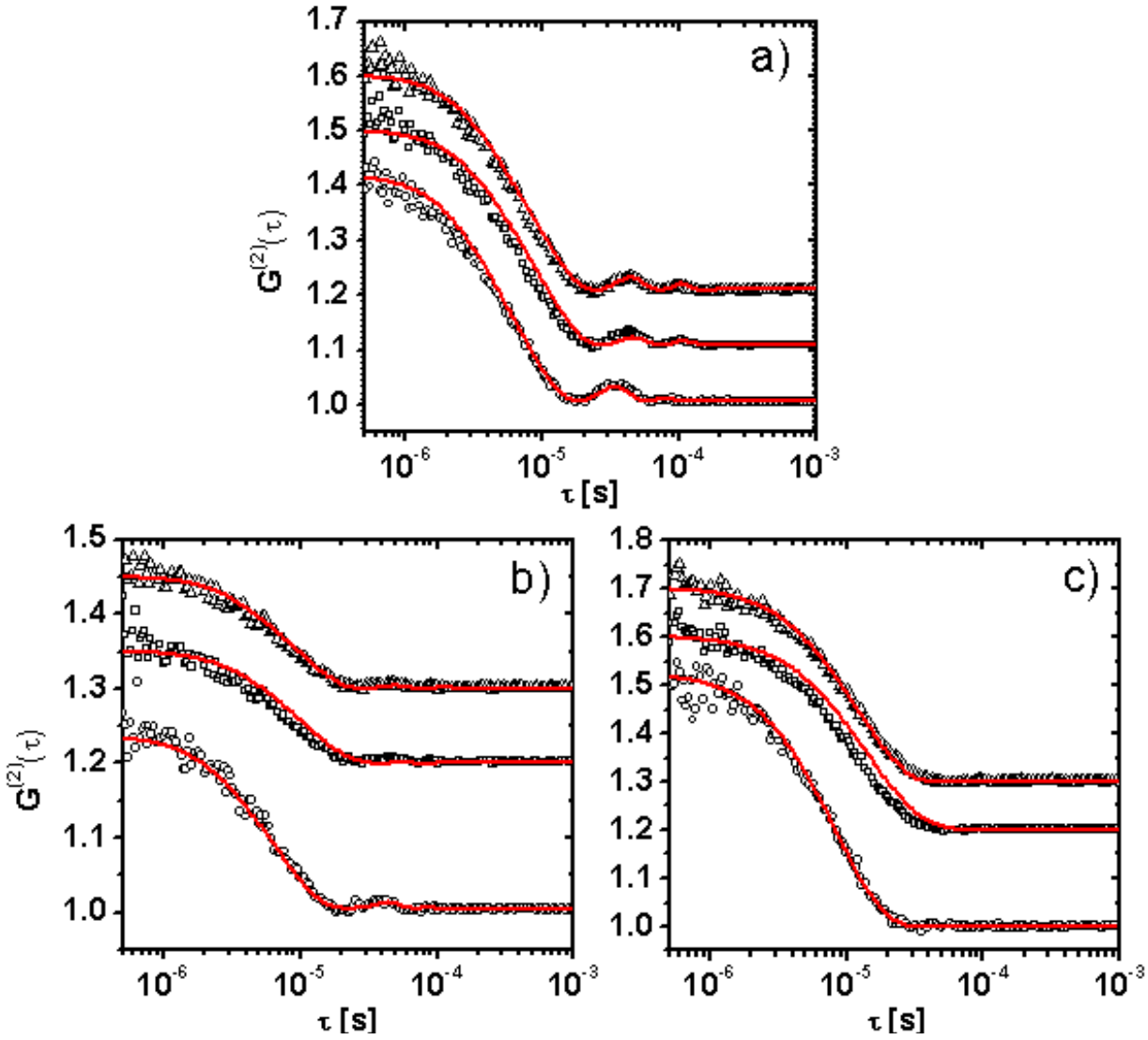

Figure 5.7: Correlation functions for the pure (open circles) and monolayer covered (open squares, triangles) $DMSO/H_2O$ subphase for a wavevector transfer $q_{\parallel} = 503cm^{-1}$. The model correlation functions (solid lines) approximating the data points presented as open squares use zero values for all viscoelastic constants of the monolayer. In contrast, the model curve approximating the data shown as open triangles introduce an additional damping via the parameter δ. a) T=22°C, b) T=0°C, c) T=-20°C. Correlation functions have been shifted along the y-axis for clarity.

found to be necessary to describe the measured data. An estimation of an upper limit for this parameter at -20°C revealed a value of about 1.5. An increase of this parameter accompanied with the phase transition at a temperature of about -15°C can hence not be ruled out, but is not deducible from the experimental data, neither.

5.4 Discussion of the Results

The resolution parameters for the used grazing incidence XPCS setup were determined in a semi-empirical way by measuring a test liquid (water) with known physical parameters. The obtained ($q_{\parallel}$-dependent) resolution parameters were used as fixed parameters in the data analysis of the temperature dependent measurements of the bare DMSO/H_2O subphase. The excellent agreement with reported literature values of for the (temperature dependent) surface tension, bulk viscosity and density as well as the reproduction of coherence effects like the switching from a hetero- to a homodyne detection scheme prove the applicability of the procedure. The dynamics of the bare subphase is found to undergo a transition from propagating to overdamped capillary waves at a temperature between -5°C and -10°C. Comparing these temperatures to the phase transition temperatures found for monolayers of eicosanoic acid and DPPA by static diffraction, it appears that this change in the dynamics arises at temperatures slightly below or above the phase transition, respectively. Nevertheless, the surface dynamics might be related to the structure formation of the monolayer by a coupling mechanism: reduced surface fluctuations favour the reorganisation into more densely packed domains as the driving forces for structure formation compete with surface fluctuations. Moreover, in the presence of a monolayer the surface dynamics is altered due to the viscoelastic properties of the film. The influence of the resolution on the measured correlation functions is not negligible and constitutes partially even a dominant contribution, hampering the determination of individual values for the three viscoelastic parameters. The influence of the monolayer on the correlation function is hence accounted for in terms of a modified surface tension and an additional effective damping. Nevertheless, close to critical damping conditions, the influence of the monolayer becomes observable. For the case of eicoscanoic acid, the additional damping is responsible for the switching from propagating to overdamped capillary waves. This transition appears in the presence of the monolayer at temperatures between 0°C and -5°C, similar to the structural phase transition in the monolayer.

The most distinct difference between surface dynamics in the presence of the eicosanoic acid and the DPPA monolayer is the finding, that for DPPA even at ambient temperature the elastic properties of the layer influence the dynamics. Taking into account, that this layer prepared in a high density phase which is much more homogeneous than the fatty acid monolayer, a possible mechanism is evident: the fatty acid monolayer consists of densely packed domains embedded into presumable liquid-like regions. Thus the monolayer exhibits on length scales like the ones probed by XPCS a quite heterogenous response to the surface fluctuations. In particular the possibly stiff crystalline domains do not remarkably damp the surface fluctuations, because their diameter of the order of 100nm is about three orders of magnitude smaller than the capillary wavelengths probed in the experiment. Contrary, the DPPA monolayer can be supposed to be much more

homogenous (as judged from the areas per molecule obtained by a macroscopically averaging technique like Langmuir isotherms and diffraction data with Angstrom resolution). Thus, despite of the ordered domains being even smaller than in the case of the fatty acid, a larger impact on the surface dynamics as observed can be expected. In general, an improved sensitivity of the method would be desirable, allowing for an accurate determination of the relevant parameters, which could in return be related to monolayer properties on a molecular length scale.

Conclusions and Outlook

In the presented thesis the low temperature phase behaviour of two model systems for organic monolayers, namely a fatty acid and a phospholipid, has been investigated. The monolayers were cooled down on a liquid cryoprotective subphase to temperatures of $-50°C$. In the case of the fatty acid a transition from a weakly ordered to a crystalline phase could be observed. Comparing the evolution of the structure parameters with those of bulk systems like alkanes, an excellent agreement with the rotator-crystalline phase transition of these three dimensional systems is found. For the quasi two-dimensional monolayer the phase transition is accompanied by a growth of crystalline domains and the occurrence of higher order reflections in the X-ray diffraction pattern. The characteristic herringbone ordering in the crystalline phase was proven by structure factor calculations, taking benefit from the large number of observable in-plane reflections. The phase transition was induced by a pure reduction of entropy in the system via the thermal energy. Upon preparation of the monolayer in a state slightly above the liquid-liquid condensed phase transition, no external constraints like compression were applied. The growth of crystalline domains under these circumstances can hence be considered as a real self-assembly process under equilibrium conditions. These results on the structure formation of a completely relaxed monolayer are also made to shed some new light on the low pressure/low temperature region of the generic phase diagram of fatty acids. In order to generalise the principle, its applicability to a more complex molecule like a phospholipid was investigated. While the problem of frustration packing, arising from the coupling of two alkane chains to one headgroup, cannot be overcome, the achieved packing density of the low temperature phase constitutes the first observed non rotator-phase-like packing of a phospholipid. Relating the surface dynamics of the studied systems to the static structure data, it appears that for both systems the appearance of the crystalline phase follows the switching from propagating to overdamped capillary waves, underlining the role of surface dynamics for the organisation of the monolayer.

Still open questions which arose during the thesis project concern the further amelioration of the crystalline phase, its conservation at ambient temperature and the kinetics of the self-assembly process. The domains in the monolayer grow upon approaching the rotator-crystalline phase transition temperature. With the exact location of this temperature annealing processes become practical, where temperature cycles are used to minimise defects and induce a further growth of existing domains. Such studies would explore the limits towards the fabrication higly ordered monolayers with low defect densities. In order to preserve the self-assembled crystal structures at higher temperatures, one might think of two possible mechanisms. One possibility involves the transfer of the high density phase at low temperatures to a solid substrate, where the organic molecule is either physisorbed or chemically bounded. A different route of structure preservation at high temperatures involves the use of chemically modified molecules which can be polymerised at low temperatures in the self-assembled crystalline phase. In particular for the inhomogeneous system of the fatty acid monolayer the question about the kinetics of the domain growth arose, where time resolved grazing incidence diffraction would allow for the *in-situ* observation of the process.

By improving the resolution in grazing incidence XPCS, a detailed investigation

of the viscoelastic properties of a monolayer on a liquid subphase would become possible.

Bibliography

[1] *The Merck Index.*
Merck & Co., Inc., Whitehouse Station (New Jersey), 12. edition, 1996.

[2] *The CRC Handbook of Chemistry and Physics.*
CRC Press, Boca Raton (Florida), 85. edition, 2004.

[3] M. Abramowitz and I. Stegun.
Handbook of Mathematical Functions.
Dover, New York, 1968.

[4] A. Adamson.
Physical Chemistry of Surfaces.
Wiley & Sons, New York, 1976.

[5] O. Albrecht, H. Gruler, and E. Sackmann.
Polymorphism of phospholipid monolayers.
Journal De Physique, 39(3): p.301–313, 1978.

[6] J. Als-Nielsen and K. Kjaer.
X-ray reflectivity and diffraction studies of liquid surfaces and surfactant monolayers.
In T. Riste and D. Sherrington, editors, *Phase Transitions in Soft-Condensed Matter*, pages 113–138. Plenum Press, New York, 1989.

[7] J. Als-Nielsen and D. McMorrow.
Elements of Modern X-ray Physics.
John Wiley & Sons, Ltd, Chichester, 2001.

[8] N. Ashcroft and N. Mermin.
Solid State Physics.
Thompson Learning, Inc., Florence, 1976.

[9] A. M. Bibo and I. R. Peterson.
Phase-diagrams of monolayers of the long-chain fatty-acids.
Advanced Materials, 2(6-7): p.309–311, 1990.

[10] G. M. Bommarito, W. J. Foster, P. S. Pershan, and M. L. Schlossman.
A determination of the phase diagram of relaxed langmuir monolayers of behenic acid.
Journal of Chemical Physics, 105(12): p.5265–5284, 1996.

[11] M. A. Bouchiat.

The spectral shape problem.
In D. Langevin, editor, *Light Scattering by Liquid Surfaces and Complementary Techniques*, volume 41 of *Surfactant Science Series*, pages 35–59. Marcel Dekker, inc., New York, 1992.

[12] W. Bragg.
Proceedings of the Royal Society A, 88:428–438, 1913.

[13] F. P. Buff, R. A. Lovett, and Stilling.Fh.
Interfacial density profile for fluids in the critical region.
Physical Review Letters, 15(15): p.621–623, 1965.

[14] C. Buzano, A. Pelizzola, and M. Pretti.
Herringbone ordering and lattice distortions in a planar-molecule model for langmuir monolayers.
Physical Review E, 62(4): p.5230–5241, 2000.

[15] N. Camillone, C. E. D. Chidsey, G. Y. Liu, T. M. Putvinski, and G. Scoles.
Surface-structure and thermal motion of normal-alkane thiols self-assembled on au(111) studied by low-energy helium diffraction.
Journal of Chemical Physics, 94(12): p.8493–8502, 1991.

[16] S. Cantin.
Interface mixte: Structuration et ségrégation (habilitation à diriger des recherches), 2006.

[17] E. Chason and T. M. Mayer.
Thin film and surface characterization by specular x-ray reflectivity.
Critical Reviews in Solid State and Materials Sciences, 22(1): p.1–67, 1997.

[18] Y. M. Chen and A. J. Pearlstein.
Viscosity temperature correlation for glycerol water solutions.
Industrial & Engineering Chemistry Research, 26(8): p.1670–1672, 1987.

[19] B. Chu.
Laser Light Scattering.
Academic Press, New York, 1991.

[20] P. Cicuta and I. Hopkinson.
Recent developments of surface light scattering as a tool for optical-rheology of polymer monolayers.
Colloids and Surfaces a-Physicochemical and Engineering Aspects, 233(1-3): p.97–107, 2004.

[21] J. Cromer and B. Mann.
X-ray scattering factors computed from numerical hartree-fock wave functions.
Acta Cryst., A24: p.321–324, 1963.

[22] D. W. J. Cruickshank.
The determination of the anisotropic thermal motion of atoms in crystals.
Acta Crystallographica, 9(8): p.747–753, 1956.

[23] D. Düchs and F. Schmid.
Phase behaviour of amphiphilic monolayers: theory and simulation.
Journal of Physics-Condensed Matter, 13(21): p.4853–4862, 2001.

[24] K. de Meijere, G. Brezesinski, and H. Möhwald.
Polyelectrolyte coupling to a charged lipid monolayer.
Macromolecules, 30(8): p.2337–2342, 1997.

[25] I. Denicolo, J. Doucet, and A. F. Craievich.
X-ray study of the rotator phase of paraffins(iii) - even-numbered paraffins c18h38, c20h42, c22h46, c24h50, and c26h54.
Journal of Chemical Physics, 78(3): p.1465–1469, 1983.

[26] W. F. Dong, R. M. Wang, G. Z. Mao, and H. Möhwald.
Self-assembled molecular patterns of fatty acid on graphite in the presence of metal ions.
Soft Matter, 2(8): p.686–692, 2006.

[27] J. Doucet, I. Denicolo, and A. Craievich.
X-ray study of the rotator phase of the odd-numbered paraffins c17h36, c19h40, and c21h44.
Journal of Chemical Physics, 75(3): p.1523–1529, 1981.

[28] J. Doucet, I. Denicolo, A. Craievich, and A. Collet.
Evidence of a phase-transition in the rotator phase of the odd-numbered paraffins c23h48 and c25h52.
Journal of Chemical Physics, 75(10): p.5125–5127, 1981.

[29] M. K. Durbin, A. Malik, R. Ghaskadvi, M. C. Shih, P. Zschack, and P. Dutta.
X-ray-diffraction study of a recently identified phase-transition in fatty-acid langmuir monolayers.
Journal of Physical Chemistry, 98(7):1753–1755, 1994.

[30] M. K. Durbin, A. Malik, A. G. Richter, R. Ghaskadvi, T. Gog, and P. Dutta.
Transitions to a new chiral phase in a langmuir monolayer.
Journal of Chemical Physics, 106(19): p.8216–8220, 1997.

[31] M. K. Durbin, A. G. Richter, C. J. Yu, J. Kmetko, J. M. Bai, and P. Dutta.
Backbone orientational order in fatty acid monolayers at the air-water interface.
Physical Review E, 58(6): p.7686–7690, 1998.

[32] P. Dutta.
Grazing incidence x-ray diffraction.
Current Science, 78(12):1478–1483, 2000.

[33] P. Ewald.
Zeitschrift für Kristallographie, 14:129–156, 1921.

[34] R. Fendt.
Coherent X-ray Scattering From Soft-Matter Surfaces.
PhD thesis, Universität Dortmund, 2006.

[35] P. Fontaine, M. Goldmann, M. Bordessoule, and A. Jucha.
Fast and adjustable-resolution grazing-incidence x-ray liquid surface diffraction.
Review of Scientific Instruments, 75(10): p.3097–3106, 2004.
Part 1.

[36] C. Fradin, A. Braslau, D. Luzet, D. Smilgies, M. Alba, N. Boudet, K. Mecke, and J. Daillant.
Reduction in the surface energy of liquid interfaces at short length scales.
Nature, 403(6772): p.871–874, 2000.

[37] C. Fradin, J. Daillant, A. Braslau, D. Luzet, M. Alba, and M. Goldmann.
Microscopic measurement of the linear compressibilities of two-dimensional fatty acid mesophases.
European Physical Journal B, 1(1): p.57–69, 1998.

[38] T. Ghaderi.
X-ray Intensity Correlation Spectroscopy from Fluid Surfaces.
PhD thesis, Universität Dortmund, 2006.

[39] V. I. Gordeliy, M. A. Kiselev, P. Lesieur, A. V. Pole, and J. Teixeira.
Lipid membrane structure and interactions in dimethyl sulfoxide/water mixtures.
Biophysical Journal, 75(5): p.2343–2351, 1998.

[40] A. Guinier.
X-ray diffraction in crystals, imperfect crystals, and amorphous bodies.
W.H. Freeman, San Francisco, 1963.

[41] C. Gutt.
to be published.

[42] C. Gutt, T. Ghaderi, V. Chamard, A. Madsen, T. Seydel, M. Tolan, M. Sprung, G. Grubel, and S. K. Sinha.
Observation of heterodyne mixing in surface x-ray photon correlation spectroscopy experiments.
Physical Review Letters, 91(7), 2003.

[43] T. Hahn, editor.
International Tables For Crystallograpgy, volume 4 Space-group Symmetry.
D. Reichel Publishing Company, Dordrecht, Holland / Boston, USA, 1983.

[44] K. Harlos, H. Eibl, I. Pascher, and S. Sundell.
Conformation and packing properties of phosphatidic-acid - the crystal-structure of monosodium dimyristoylphosphatidate.
Chemistry and Physics of Lipids, 34(2): p.115–126, 1984.

[45] J. Hautman and M. L. Klein.
Molecular-dynamics simulation of the effects of temperature on a dense monolayer of long-chain molecules.
Journal of Chemical Physics, 93(10):7483–7492, 1990.

[46] C. A. Helm, H. Möhwald, K. Kjaer, and J. Alsnielsen.
Phospholipid monolayers between fluid and solid states.
Biophysical Journal, 52(3): p.381–390, 1987.

[47] V. Holy and T. Baumbach.
Nonspecular x-ray reflection from rough multilayers.
Physical Review B, 49(15): p.10668–10676, 1994.

[48] http://www.avantilipids.com/.

[49] http://www.ncnr.nist.gov/resources/sldcalc.html.

[50] R. James.
The Optical Principles of the Diffraction of X-rays.
Ox Bow, Woodbridge, CT, 1982.

[51] R. Jenkins and R. L. Snyder.
Introduction to X-ray Powder Diffractometry, volume 138 of *Chemical Analysis.*
John Wiley & Sons, Inc., New York, 1996.

[52] L. B. A. Johansson, B. Kalman, G. Wikander, A. Fransson, K. Fontell, B. Bergenstahl, and G. Lindblom.
Phase-equilibria and formation of vesicles of dioleoylphosphatidylcholine in glycerol water mixtures.
Biochimica Et Biophysica Acta, 1149(2): p.285–291, 1993.

[53] V. M. Kaganer and E. B. Loginov.
Symmetry and phase-transitions in langmuir monolayers - the landau theory.
Physical Review E, 51(3): p.2237–2249, 1995.

[54] V. M. Kaganer, H. Möhwald, and P. Dutta.
Structure and phase transitions in langmuir monolayers.
Reviews of Modern Physics, 71(3): p.779–819, 1999.

[55] V. M. Kaganer, I. R. Peterson, R. M. Kenn, M. C. Shih, M. Durbin, and P. Dutta.
Tilted phases of fatty-acid monolayers.
Journal of Chemical Physics, 102(23): p.9412–9422, 1995.

[56] F. Kaneko, M. Kobayashi, Y. Kitagawa, and Y. Matsuura.
Structure of stearic-acid e-form.
Acta Crystallographica Section C-Crystal Structure Communications, 46: p.1490–1492, 1990.

[57] F. Kaneko, H. Sakashita, M. Kobayashi, Y. Kitagawa, Y. Matsuura, and M. Suzuki.
Double-layered polytpic structure of the e-form of octadecanoic acid, c18h36o2.
Acta Crystallographica Section C-Crystal Structure Communications, 50: p.247–250, 1994.

[58] F. Kaneko, H. Sakashita, M. Kobayashi, Y. Kitagawa, Y. Matsuura, and M. Suzuki.
Double-layered polytypic structure of the b-form of octadecanoic acid, c18h36o2.
Acta Crystallographica Section C-Crystal Structure Communications, 50: p.245–247, 1994.

[59] Y. S. Kang and M. Majda.
Headgroup immersion depth and its effect on the lateral diffusion of amphiphiles at the air/water interface.
Journal of Physical Chemistry B, 104(9): p.2082–2089, 2000.

[60] R. M. Kenn, K. Kjaer, and H. Möhwald.
Non-rotator phases in phospholipid monolayers?
Colloids and Surfaces a-Physicochemical and Engineering Aspects, 117(1-2): p.171–181, 1996.

[61] H. E. King, E. B. Sirota, H. Shao, and D. M. Singer.
A synchrotron x-ray-scattering study of the rotator phases of the normal-alkanes.
Journal of Physics D-Applied Physics, 26(8B): p.133–136, 1993.

[62] A. Kitaigoradskii.
Organic Chemical Crystallography.
Consultants Bureau, New York, 1961.

[63] C. Kittel.
Introduction to Solid State Physics.
John Wiley & Sons, New York, 5. edition, 1976.

[64] K. Kjaer.
Some simple ideas on x-ray reflection and grazing-incidence diffraction from thin surfactant films.
Physica B, 198(1-3): p.100–109, 1994.

[65] K. Kjaer, J. Alsnielsen, C. A. Helm, L. A. Laxhuber, and H. Möhwald.
Ordering in lipid monolayers studied by synchrotron x-ray-diffraction and fluorescence microscopy.
Physical Review Letters, 58(21):2224–2227, 1987.

[66] K. Kjaer, J. Alsnielsen, C. A. Helm, P. Tippmankrayer, and H. Möhwald.
Synchrotron x-ray-diffraction and reflection studies of arachidic acid monolayers at the air-water-interface.
Journal of Physical Chemistry, 93(8): p.3200–3206, 1989.

[67] I. Kuzmenko, V. M. Kaganer, and L. Leiserowitz.
Packing of hydrocarbon chains and symmetry of condensed phases in langmuir monolayers.
Langmuir, 14(14): p.3882–3888, 1998.

[68] D. Langevin.
Adsorbed monolayers.
In D. Langevin, editor, *Light Scattering by Liquid Surfaces and Complementary Techniques*, volume 41 of *Surfactant Science Series*, pages 161–201. Marcel Dekker, inc., New York, 1992.

[69] I. Langmuir.
Journal of the American Chemical Society, 39: p.1848, 1917.

[70] M. Laue.
Physikalische Zeitung, 39: p.1075–1079, 1913.

[71] F. Leveiller, C. Bohm, D. Jacquemain, H. Möhwald, L. Leiserowitz, K. Kjaer, and J. Alsnielsen.
2-dimensional crystal-structure of cadmium arachidate studied by synchrotron x-ray-diffraction and reflectivity.

Langmuir, 10(3): p.819–829, 1994.

[72] F. Leveiller, D. Jacquemain, L. Leiserowitz, K. Kjaer, and J. Alsnielsen.
Toward a determination at near atomic resolution of 2-dimensional crystal-structures of amphiphilic molecules on the water-surface - a study based on grazing-incidence synchrotron x-ray-diffraction and lattice energy calculations.
Journal of Physical Chemistry, 96(25): p.10380–10389, 1992.

[73] V. Levich.
Physicochemical Hydrodynamics.
Prentice-Hall International Series in the Physical and Chemical Engineering Sciences. Prentice-Hall, inc., Englewood Cliffs, 1962.

[74] M. Lundquis.
Relation between polymorphism in 2-dimensional monomolecular films on water to polymorphism in 3-dimensional state, and formation of multimolecular films on water .2. ethyl-esters of aliphatic acids.
Chemica Scripta, 1(5): p.197ff, 1971.

[75] A. Madsen, T. Seydel, M. Tolan, and G. Grübel.
Gracing-incidence scattering of coherent x-rays from a liquid surface.
Journal of Synchrotron Radiation, 12(Part 6): p.786–794, 2005.

[76] W. M. Mazee.
Some properties of hydrocarbons having more than 20 carbon atoms.
Recueil Des Travaux Chimiques Des Pays-Bas-Journal of the Royal Netherlands Chemical Society, 67(4): p.197–213, 1948.

[77] H. Moewald.
Phospholipid monolayers.
In R. Lipowsky and E. Sackmann, editors, *Structure and Dynamics of Membranes*, volume 1A of *Handbook Of Biological Physics*, pages 161–211. Elsevier, Amsterdam, 1995.

[78] A. F. Moodie and H. J. Whitfield.
Friedels law and noncentrosymmetric space-groups.
Acta Crystallographica Section A, 51: p.198–201, 1995.

[79] S. Mora, J. Daillant, D. Luzet, and B. Struth.
X-ray surface scattering investigation of langmuir films: Phase transitions and elastic properties.
Europhysics Letters, 66(5): p.694–700, 2004.

[80] S. M. O'Flaherty, L. Wiegart, O. Konovalov, and B. Struth.
Observation of zinc phthalocyanine aggregates on a water surface using grazing incidence x-ray scattering.
Langmuir, 21(24): p.11161–11166, 2005.

[81] S. M. O'Flaherty, L. Wiegart, and B. Struth.
Grazing incidence x-ray scattering to probe the self-assembly of phthalocyanine nanorods on a liquid surface.
Journal of Physical Chemistry B, 110(39): p.19375–19379, 2006.

[82] G. Oradd, G. Wikander, G. Lindblom, and L. B. A. Johansson.
Effect of glycerol on the translational and rotational motions in lipid bilayers studied by pulsed-field gradient h-1-nmr, epr and time-resolved fluorescence spectroscopy.
Journal of the Chemical Society-Faraday Transactions, 90(2): p.305–309, 1994.

[83] G. A. Overbeck and D. Mobius.
A new phase in the generalized phase-diagram of monolayer films of long-chain fatty-acids.
Journal of Physical Chemistry, 97(30): p.7999–8004, 1993.

[84] L. G. Parratt.
Surface studies of solids by total reflection of x-rays.
Physical Review, 95(2): p.359–369, 1954.

[85] I. Pascher, M. Lundmark, P. G. Nyholm, and S. Sundell.
Crystal-structures of membrane-lipids.
Biochimica Et Biophysica Acta, 1113(3-4): p.339–373, 1992.

[86] I. Pascher, S. Sundell, and H. Hauser.
Polar group-interaction and molecular packing of membrane-lipids - the crystal-structure of lysophosphatidylethanolamine.
Journal of Molecular Biology, 153(3): p.807–824, 1981.

[87] J. B. Peng, G. T. Barnes, I. R. Gentle, G. J. Foran, T. H. Le, and M. J. Crossley.
X-ray scattering studies of mixed langmuir monolayers and langmuir-blodgett films of a noncentrosymmetric porphyrin with cadmium arachidate.
Langmuir, 17(6): p.1936–1940, 2001.

[88] I. R. Peterson, R. M. Kenn, A. Goudot, P. Fontaine, F. Rondelez, W. G. Bouwman, and K. Kjaer.
Chiral and herringbone symmetry breaking in water-surface monolayers.
Physical Review E, 53(1): p.667–673, 1996.

[89] M. Petty.
Langmuir-Blodgett films.
University Press, Cambridge, 1996.

[90] J. Pignat, J. Daillant, L. Leiserowitz, and F. Perrot.
Grazing incidence x-ray diffraction on langmuir films: Toward atomic resolution.
Journal of Physical Chemistry B, 110(44): p.22178–22184, 2006.

[91] R. Popovitzbiro, J. L. Wang, J. Majewski, E. Shavit, L. Leiserowitz, and M. Lahav.
Induced freezing of supercooled water into ice by self-assembled crystalline monolayers of amphiphilic alcohols at the air-water-interface.
Journal of the American Chemical Society, 116(4): p.1179–1191, 1994.

[92] G. Porod.
In O. Glatter and O. Kratky, editors, *Small Angle X-ray Scattering*, pages 32–36. Academic Press Inc. Ltd., London, 1982.

[93] J. P. Rabe, S. Buchholz, and L. Askadskaya.

Scanning tunneling microscopy of several alkylated molecular moieties in monolayers on graphite.
Synthetic Metals, 54(1-3): p.339–349, 1993.

[94] A. Renault, J. F. Legrand, M. Goldmann, and B. Berge.
Surface diffraction studies of 2d crystals of short fatty alcohols at the air-water-interface.
Journal De Physique Ii, 3(6): p.761–766, 1993.

[95] H. M. Rietveld.
A profile refinement method for nuclear and magnetic structures.
Journal of Applied Crystallography, 2: p.65–71, 1969.

[96] S. Riviere, S. Henon, J. Meunier, D. K. Schwartz, M. W. Tsao, and C. M. Knobler.
Textures and phase-transitions in langmuir monolayers of fatty-acids - a comparative brewster-angle microscope and polarized fluorescence microscope study.
Journal of Chemical Physics, 101(11): p.10045–10051, 1994.

[97] S. Riviere-Cantin, S. Henon, and J. Meunier.
Phase transitions in langmuir films of fatty acids: L(2)-l(2)'-l(2)" triple point and order of the transitions.
Physical Review E, 54(2): p.1683–1686, 1996.

[98] S. Schichman and R. L. Amey.
Viscosity and local liquid structure in dimethyl sulfoxide-water mixtures.
Journal of Physical Chemistry, 75(1): p.98–102, 1971.

[99] M. Schlenker.
Neutron and synchrotron radiation for condensed matter studies.
In J. Baruchel, J. Hodeau, M. Lehmann, J. Regnard, and C. Schlenker, editors, *Theory, instruments and methods*, volume 1. Springer Verlag, Heidelberg, 1993.

[100] M. L. Schlossman, D. K. Schwartz, P. S. Pershan, E. H. Kawamoto, G. J. Kellogg, and S. Lee.
Relaxation and the reentrant appearance of phases in a molecular monolayer.
Physical Review Letters, 66(12): p.1599–1602, 1991.

[101] D. K. Schwartz and C. M. Knobler.
Direct observations of transitions between condensed langmuir monolayer phases by polarized fluorescence microscopy.
Journal of Physical Chemistry, 97(35): p.8849–8851, 1993.

[102] T. Seydel, A. Madsen, M. Sprung, M. Tolan, G. Grubel, and W. Press.
Setup for in situ surface investigations of the liquid/glass transition with (coherent) x rays.
Review of Scientific Instruments, 74(9): p.4033–4040, 2003.

[103] T. Seydel, A. Madsen, M. Tolan, G. Grubel, and W. Press.
Capillary waves in slow motion.
Physical Review B, 6307(7):art. no.–073409, 2001.

[104] S. K. Sinha.

X-ray diffuse-scattering as a probe for thin-film and interface structure.
Journal De Physique Iii, 4(9): p.1543–1557, 1994.

[105] S. K. Sinha, E. B. Sirota, S. Garoff, and H. B. Stanley.
X-ray and neutron-scattering from rough surfaces.
Physical Review B, 38(4): p.2297–2311, 1988.

[106] E. B. Sirota.
Remarks concerning the relation between rotator phases of bulk n-alkanes and those of langmuir monolayers of alkyl-chain surfactants on water.
Langmuir, 13(14): p.3849–3859, 1997.

[107] E. B. Sirota, H. E. King, G. J. Hughes, and W. K. Wan.
Novel phase-behavior in normal alkanes.
Physical Review Letters, 68(4): p.492–495, 1992.

[108] E. B. Sirota, H. E. King, D. M. Singer, and H. H. Shao.
Rotator phases of the normal alkanes - an x-ray-scattering study.
Journal of Chemical Physics, 98(7): p.5809–5824, 1993.

[109] D. M. Smilgies, N. Boudet, B. Struth, and O. Konovalov.
Troika ii: a versatile beamline for the study of liquid and solid interfaces.
Journal of Synchrotron Radiation, 12: p.329–339, 2005.

[110] R. L. Snyder.
The renaissance of x-ray powder diffraction.
In D. Rossington, R. Condrate, and R. Snyder, editors, *Advances in Material Characterization*, pages p.449–464. plenum, New York, 1983.

[111] S. Ställberg-Stenhagen and E. Stenhagen.
Phase transitions in condensed monolayers of normal chain carboxylic acids.
Nature, 156(3956): p.239–240, 1945.

[112] B. Struth.
Strukturcharakerisierung von Monoschichten und waessrigen Dispersionen chemisch modifizierter Phospholipide.
Phd thesis, Gutenberg-Universitaet, 1996.

[113] B. Struth, E. Scalas, G. Brezesinski, H. Möhwald, F. Bringezu, W. G. Bouwman, and K. Kjaer.
Influence of a hydrophilic spacer on the structure of a phospholipid monolayer.
Nuovo Cimento Della Societa Italiana Di Fisica D-Condensed Matter Atomic Molecular and Chemical Physics Fluids Plasmas Biophysics, 16(9): p.1545–1550, 1994.

[114] E. Teer, C. M. Knobler, C. Lautz, S. Wurlitzer, J. Kildae, and T. M. Fischer.
Optical measurements of the phase diagrams of langmuir monolayers of fatty acid, ester, and alcohol mixtures by brewster-angle microscopy.
Journal of Chemical Physics, 106(5): p.1913–1920, 1997.

[115] P. Tippmannkrayer and H. Möhwald.
Precise determination of tilt angles by x-ray-diffraction and reflection with arachidic acid monolayers.
Langmuir, 7(10): p.2303–2306, 1991.

[116] M. Tolan.
X-ray Scattering from Soft-Matter Thin Films, volume 148.
Springer Tracts in Modern Physics, Berlin, Heidelberg, 1999.

[117] M. Tolan and W. Press.
X-ray and neutron reflectivity.
Zeitschrift Fur Kristallographie, 213(6): p.319–336, 1998.

[118] J. Torrent-Burgues, M. Pla, L. Escriche, J. Casabo, A. Errachid, and F. Sanz.
Characterization of langmuir and langmuir-blodgett films of a thiomacrocyclic ionophore by surface pressure and afm.
Journal of Colloid and Interface Science, 301(2): p.585–593, 2006.

[119] V. Vand, A. Aitken, and R. K. Campbell.
Crystal structure of silver salts of fatty acids.
Acta Crystallographica, 2(6): p.398–403, 1949.

[120] G. Vanderkooi.
Multibilayer structure of dimyristoylphosphatidylcholine dihydrate as determined by energy minimization.
Biochemistry, 30(44): p.10760–10768, 1991.

[121] G. H. Vineyard.
Grazing-incidence diffraction and the distorted-wave approximation for the study of surfaces.
Physical Review B, 26(8): p.4146–4159, 1982.

[122] L. Wiegart.
Thermodynamic and structural properties of lipid monolayers on sol surfaces.
Diploma thesis, University of Dortmund, 2004.

[123] L. Wiegart, S. O'Flaherty, and B. Struth.
Nanocrystal induced organization of a langmuir phospholipid monolayer.
Langmuir, 21(5): p.1695–1698, 2005.

[124] L. Wiegart, S. M. O'Flaherty, P. Terech, and B. Struth.
Observation of the desorption of mineral nanoparticles from a hybrid langmuir monolayer: an in situ grazing incidence x-ray (gixos) study.
Soft Matter, 2(1): p.54–56, 2006.

[125] L. Wiegart and B. Struth.
Geometric boundary condition for the chain alignement in lipid monolayers.
Physica B, 357(1-2): p.126–129, 2005.

[126] L. Wiegart, B. Struth, M. Tolan, and P. Terech.
Thermodynamic and structural properties of phospholipid langmuir monolayers on hydrosol surfaces.
Langmuir, 21(16): p.7349–7357, 2005.